

THESIS FOR THE DEGREE OF DOCTOR OF PHILOSOPHY

# Kinetic modelling of runaways in plasmas

OLA EMBRÉUS

Department of Physics  
CHALMERS UNIVERSITY OF TECHNOLOGY  
Göteborg, Sweden, 2019

Kinetic modelling of runaways in plasmas  
OLA EMBRÉUS  
ISBN 978-91-7597-840-6

© OLA EMBRÉUS, 2019

Doktorsavhandlingar vid Chalmers tekniska högskola  
Ny serie nr 4521  
ISSN 0346-718X

Department of Physics  
Chalmers University of Technology  
SE-412 96 Göteborg  
Sweden  
Tel: +46 (0) 31 772 1000

Cover: Momentum-space contours of the electron distribution function on a logarithmic scale. Steady-state solution of the spatially homogeneous kinetic equation in the presence of a constant electric field, collisions and bremsstrahlung losses.

Printed in Sweden by  
Reproservice  
Chalmers Tekniska Högskola  
Göteborg, Sweden, 2018

# Kinetic modelling of runaways in plasmas

Ola Embréus

Department of Physics

Chalmers University of Technology

## Abstract

The phenomenon of runaway occurs in plasmas in the presence of a strong electric field, when the accelerating force overcomes the collisional friction acting on the charged particles moving through the plasma. Runaway is observed in both laboratory and space plasmas, and is of great importance in fusion-energy research, where the energetic runaway electrons can damage the plasma-facing components of fusion reactors.

In this thesis, we present a series of papers which investigate various aspects of runaway dynamics. We advance the kinetic description of electron runaway by deriving and analyzing a fully conservative large-angle collision operator suitable for studying runaway dynamics, and explore its impact on runaway generation and decay. We also present a generalization of the Landau-Fokker-Planck equation to describe screening effects in partially ionized plasmas, providing improved capability of modelling the effect of runaway mitigation schemes in fusion devices.

The emission of synchrotron and bremsstrahlung radiation are important energy-loss mechanisms for relativistic runaway electrons, and they also provide essential diagnostic tools. We demonstrate the need for a stochastic description in order to accurately describe the effect of bremsstrahlung radiation losses on the electron motion. Synchrotron radiation is often emitted at visible and infrared wavelengths in tokamaks, allowing the emission to be readily observed. We have developed a synthetic radiation diagnostic tool, SOFT, which provides new insight into how features of the runaway distribution can affect the observed emission patterns.

Finally, we have investigated the runaway dynamics of ions and of positrons which are generated during runaway. The runaway description in these cases differs from regular electron runaway due to the high mass of the ions, and the fact that positrons are created with a large momentum antiparallel to their direction of acceleration.

**Keywords:** plasma, runaway, Boltzmann equation, Fokker-Planck equation, bremsstrahlung, synchrotron radiation, tokamak, positrons

# Publications

This thesis is based on the work contained in the following papers, which can be found appended at the end of the thesis:

- A** O. Embréus, A. Stahl and T. Fülöp,  
*On the relativistic large-angle electron collision operator for runaway avalanches in plasmas*,  
Journal of Plasma Physics **84**, 905840102 (2018).  
<https://doi.org/10.1017/S002237781700099X>
- B** O. Embréus, A. Stahl and T. Fülöp,  
*Effect of bremsstrahlung radiation emission on fast electrons in plasmas*,  
New Journal of Physics **18**, 093023 (2016).  
<https://doi.org/10.1088/1367-2630/18/9/093023>
- C** O. Embréus, L. Hesslow, M. Hoppe, G. Papp, K. Richards and T. Fülöp,  
*Dynamics of positrons during relativistic electron runaway*,  
Journal of Plasma Physics **84**, 905840506 (2018).  
<https://doi.org/10.1017/S0022377818001010>
- D** O. Embréus, S. Newton, A. Stahl, E. Hirvijoki and T. Fülöp,  
*Numerical calculation of ion runaway distributions*,  
Physics of Plasmas **22**, 052122 (2015).  
<https://doi.org/10.1063/1.4921661>
- E** L. Hesslow, O. Embréus, M. Hoppe, T. C. DuBois, G. Papp, M. Rahm and T. Fülöp,  
*Generalized collision operator for fast electrons interacting with partially ionized impurities*,  
Journal of Plasma Physics **84**, 905840605 (2018).  
<https://doi.org/10.1017/S0022377818001113>
- F** M. Hoppe, O. Embréus, R. A. Tinguely, R. S. Granetz, A. Stahl and T. Fülöp,  
*SOFT: A synthetic synchrotron diagnostic for runaway electrons*,  
Nuclear Fusion **58**, 026032 (2018).  
<https://doi.org/10.1088/1741-4326/aa9abb>

## Statement of contribution

**Paper A:** I derived the new theory (most notably equations (2.23-24)) and implemented it in the numerical kinetic solver. I performed all simulations, produced all figures, and prepared the draft of sections 2 and 3. I contributed with finalizing the manuscript together with the co-authors.

**Paper B:** I was responsible for all calculations as well as their numerical implementation, I performed the simulations and prepared all figures. I wrote the draft of the second and third sections, as well as contributed to the preparation of the final version of the manuscript.

**Paper C:** I carried out all the calculations and derivations in the paper, participated in the numerical implementation of the theory and produced the results shown in figures 1, 2 and 4. I prepared the entire draft of the manuscript, excluding parts of the introduction and conclusions, and I was involved in finalising the text for publication.

**Paper D:** I was responsible for all simulations and calculations, as well as developed the CODION tool. I wrote all parts of the text presenting new calculations or results, and produced all the figures.

**Paper E:** Throughout the project I was involved with exploring and developing ideas and calculations for the paper. In particular, I was mainly responsible for the calculations presented in section 4 and appendix B. I assisted in finalizing the manuscript for publication.

**Paper F:** I was involved with the design of the SOFT tool, and derived the theory presented in section 2.1 and 2.3. I contributed with analysis and interpretation to all results presented. I assisted in finalizing the manuscript for publication.

## Related publications, not included in the thesis

- G** A. Stahl, E. Hirvijoki, J. Decker, O. Embréus and T. Fülöp,  
*Effective critical electric field for runaway electron generation*,  
Physical Review Letters **114**, 115002 (2015).  
<http://doi.org/10.1103/PhysRevLett.114.115002>
- H** E. Hirvijoki, I. Pusztai, J. Decker, O. Embréus, A. Stahl and T. Fülöp,  
*Radiation reaction induced non-monotonic features in runaway electron distributions*,  
Journal of Plasma Physics **81**, 475810502 (2015).  
<http://doi.org/10.1017/S0022377815000513>
- I** E. Hirvijoki, J. Decker, A. Brizard and O. Embréus,  
*Guiding-center transformation of the Abraham-Lorentz-Dirac radiation reaction force*,  
Journal of Plasma Physics **81**, 475810504 (2015).  
<http://doi.org/10.1017/S0022377815000744>
- J** E. Hirvijoki, J. Candy, E. Belli and O. Embréus,  
*The Gaussian Radial Basis Function method for plasma kinetic theory*,  
Physics Letters A **379**, 2735 (2015).  
<https://doi.org/10.1016/j.physleta.2015.08.010>
- K** J. Decker, E. Hirvijoki, O. Embréus, Y. Peysson, A. Stahl, I. Pusztai and T. Fülöp,  
*Numerical characterization of bump formation in the runaway electron tail*,  
Plasma Physics and Controlled Fusion **58**, 025016 (2015).  
<http://doi.org/10.1088/0741-3335/58/2/025016>
- L** A. Stahl, O. Embréus, G. Papp, M. Landreman and T. Fülöp,  
*Kinetic modelling of runaway electrons in dynamic scenarios*,  
Nuclear Fusion **56**, 112009 (2016).  
<http://doi.org/10.1088/0029-5515/56/11/112009>

- M** A. Stahl, O. Embréus, M. Landreman, G. Papp and T. Fülöp,  
*Runaway-electron formation and electron slide-away in an ITER post-disruption scenario*,  
Journal of Physics: Conference Series **775**, 012013 (2016).  
<http://doi.org/10.1088/1742-6596/775/1/012013>
- N** A. Stahl, M. Landreman, O. Embréus and T. Fülöp,  
*NORSE: A solver for the relativistic non-linear Fokker-Planck equation for electrons in a homogeneous plasma*,  
Computer Physics Communications **212**, 269 (2017).  
<https://doi.org/10.1016/j.cpc.2016.10.024>
- O** L. Hesslow, O. Embréus, A. Stahl, T. C. DuBois, G. Papp, S. L. Newton and T. Fülöp,  
*Effect of partially screened nuclei on fast-electron dynamics*,  
Physical Review Letters **118**, 255001 (2017).  
<https://doi.org/10.1103/PhysRevLett.118.255001>
- P** M. Hoppe, O. Embréus, C. Paz-Soldan, R. A. Moyer and T. Fülöp,  
*Interpretation of runaway electron synchrotron and bremsstrahlung images*,  
Nuclear Fusion **58**, 082001 (2018).  
<https://doi.org/10.1088/1741-4326/aaae15>
- Q** R. A. Tinguely, R. S. Granetz, M. Hoppe and O. Embréus,  
*Measurements of runaway electron synchrotron spectra at high magnetic fields in Alcator C-Mod*,  
Nuclear Fusion **58**, 076019 (2018).  
<https://doi.org/10.1088/1741-4326/aac444>
- R** L. Hesslow, O. Embréus, G. J. Wilkie, G. Papp and T. Fülöp,  
*Effect of partially ionized impurities and radiation on the effective critical electric field for runaway generation*,  
Plasma Physics and Controlled Fusion **60**, 074010 (2018).  
<https://doi.org/10.1088/1361-6587/aac33e>
- S** R. A. Tinguely, R. S. Granetz, M. Hoppe and O. Embréus,  
*Spatiotemporal evolution of runaway electrons from synchrotron images in Alcator C-Mod*,  
Plasma Physics and Controlled Fusion **60**, 124001 (2018).  
<https://doi.org/10.1088/1361-6587/aae6ba>

## Conference contributions

- T** O. Embréus, S. Newton, A. Stahl, E. Hirvijoki and T. Fülöp,  
*Numerical calculation of ion runaway distributions*,  
Proceedings of 42nd EPS Conference on Plasma Physics, Lisbon,  
P1.401 (2015).  
<http://ocs.ciemat.es/EPS2015PAP/pdf/P1.401.pdf>
- U** O. Embréus, A. Stahl and T. Fülöp,  
*Effect of bremsstrahlung emission on fast electrons in plasmas*,  
Proceedings of 43rd EPS Conference on Plasma Physics, Prague,  
O2.402 (2016).  
<http://ocs.ciemat.es/EPS2016PAP/pdf/02.402.pdf>
- V** L. Hesslow, O. Embréus, G. Wilkie, T. C. DuBois, G. Papp and  
T. Fülöp,  
*Fast-electron dynamics in the presence of weakly ionized impurities*,  
Proceedings of 44th EPS Conference on Plasma Physics, Prague,  
O4.118 (2017).  
<http://ocs.ciemat.es/EPS2017PAP/pdf/04.118.pdf>
- W** A. Stahl, O. Embréus, G. Wilkie, M. Landreman, G. Papp and  
T. Fülöp,  
*Self-consistent nonlinear kinetic modeling of runaway-electron dynamics*,  
Proceedings of 44th EPS Conference on Plasma Physics, Prague,  
P2.150 (2017).  
<http://ocs.ciemat.es/EPS2017PAP/pdf/P2.150.pdf>
- X** O. Embréus, A. Stahl and T. Fülöp,  
*Effect of bremsstrahlung emission on fast electrons in plasmas*,  
Proceedings of 44th EPS Conference on Plasma Physics, Prague,  
O2.402 (2017).  
<http://ocs.ciemat.es/EPS2016PAP/pdf/02.402.pdf>
- Y** M. Hoppe, O. Embréus, P. Svensson, L. Unnerfelt and T. Fülöp,  
*Simulations of bremsstrahlung and synchrotron radiation from runaway electrons*,  
Proceedings of 45th EPS Conference on Plasma Physics, Prague,  
O5.J603 (2018).  
<http://ocs.ciemat.es/EPS2018PAP/pdf/05.J603.pdf>

**Z** O. Embréus, K. Richards, G. Papp, L. Hesslow, M. Hoppe and T. Fülöp,  
*Dynamics of positrons during relativistic electron runaway*,  
Proceedings of 45th EPS Conference on Plasma Physics, Prague,  
P5.4011 (2018).  
<http://ocs.ciemat.es/EPS2018PAP/pdf/P5.4011.pdf>

## Acknowledgements

I would first like to express my gratitude towards my supervisor Tünde Fülöp – who has mostly been patient with me, against all odds – for providing such a creative work environment and for allowing me into the runaway family. Thanks for always having me pursue the ideas that I have felt the most excited about.

I would like to thank my assistant supervisors Håkan Smith, for his hospitality during my visit to Greifswald, and to Geri Papp, for the lovely email physics conversations, his meticulous attention to detail and for all of our delightful interactions over the years.

Also thanks to Sarah Newton, for showing me the ropes in plasma physics and for the good times in Oxford during my visit. Additionally, I would like to direct my gratitude towards Eero Hivijoki and Joan Decker, who have been there since the start and have inspired me ever since.

Thanks to the entire Chalmers Plasma Theory family, who made this work a pure joy. In particular to Linnea Hesslow, for always striving for perfection, for always challenging my beliefs and for the countless discussions of the intricacies of runaway theory; and to Mathias Hoppe, for the thrilling roller-coaster ride of SOFT development. You have both provided some of my most cherished memories from this time.

Finally, to Brita and Frasse, for all the encouragement and love, and for keeping me reminded of what I do this for.

Ola Embréus, Göteborg, Dec 13, 2018

# Contents

<b>Abstract</b>	<b>i</b>
<b>Publications</b>	<b>ii</b>
<b>Acknowledgements</b>	<b>viii</b>
<b>1 Introduction</b>	<b>1</b>
1.1 Runaway generation . . . . .	3
1.2 Runaway in tokamaks . . . . .	6
1.3 Ion runaway . . . . .	9
1.4 Outline . . . . .	10
<b>2 The kinetic equation</b>	<b>11</b>
2.1 BBGKY hierarchy and the kinetic equation . . . . .	13
2.2 The Boltzmann collision operator . . . . .	15
2.3 The Fokker-Planck collision operator . . . . .	20
2.4 Effects of screening on the collision operator . . . . .	23
2.5 CODE . . . . .	26
<b>3 Radiation from runaways</b>	<b>29</b>
3.1 Bremsstrahlung radiation reaction . . . . .	30
3.2 Synthetic radiation diagnostic . . . . .	33
<b>4 Positively charged runaway</b>	<b>37</b>
4.1 Positron runaway . . . . .	37
4.2 Ion runaway . . . . .	39
<b>5 Summary and outlook</b>	<b>45</b>
<b>Bibliography</b>	<b>51</b>



# Chapter 1

## Introduction

A plasma is an ionized gas, sufficiently hot that the electrons have detached from the atoms that carried them. Because it consists of free charges, rather than neutral atoms, a plasma behaves differently to the familiar gases and fluids encountered in everyday life. The addition of electric and magnetic forces between the particles creates a rich interplay, allowing a wide range of strange and wonderful phenomena to occur. Some of these are well-known to most: lightning, electric sparks, fluorescent lamps, the Sun and the stars, and even the *aurora borealis* – the northern lights – are examples of plasmas. In fact, a majority of the visible matter in the universe is in the plasma state. The study of plasmas is a vast field of research, ranging from astrophysical research and space physics, through fusion-energy research to various industrial and medical applications.

Runaway is a phenomenon which occurs in any plasma in the presence of a sufficiently strong electric field. It is a process related to dielectric breakdown, which occurs when electric sparks are created. Runaway breakdown occurs in laboratory plasmas, such as those in tokamak fusion devices [1], as well as in lightning discharges during thunderstorms [2], and in astrophysical plasmas, such as solar flares [3]. In these scenarios, a subpopulation of particles – typically electrons, which are the lightest – are accelerated by the electric field to energies significantly higher than the thermal energy, at which point they will emit large amounts of radiation that will be visible to an observer.

The phenomenon of runaway can be understood by considering the frictional drag force due to collisions which acts on a charged particle moving through a plasma that is near thermodynamic equilibrium. Fric-

tion in plasmas is a non-monotonic function of speed: at low speed, the drag steadily grows in magnitude as the speed increases; however, above the thermal speed of the particles, the drag force will instead decrease in magnitude as the speed increases further. In the absence of an electric field, the friction force on the thermal particles will be balanced by velocity-space diffusion induced by collisions, which tends to increase the width of the velocity distribution. An equilibrium between friction and diffusion is reached when the distribution takes the Maxwellian form,  $f_M = n(m/2\pi T)^{3/2} \exp(-mv^2/2T)$ , where  $m$ ,  $n$  and  $T$  are the mass, number density and temperature (in energy units, throughout this work) of the species, and  $v$  is the speed.

In the presence of an electric field which acts to accelerate charged particles, an electron with sufficiently high initial speed will experience an unbounded acceleration to highly relativistic energies, where the electrons move at close to the speed of light. At these energies, competing physical effects become important, such as radiation losses caused by the rapidly accelerated motion experienced by the particles when moving in electromagnetic fields (leading to synchrotron radiation) or in collisions (causing bremsstrahlung emission). Figure 1.1 illustrates the forces which act on a runaway electron.

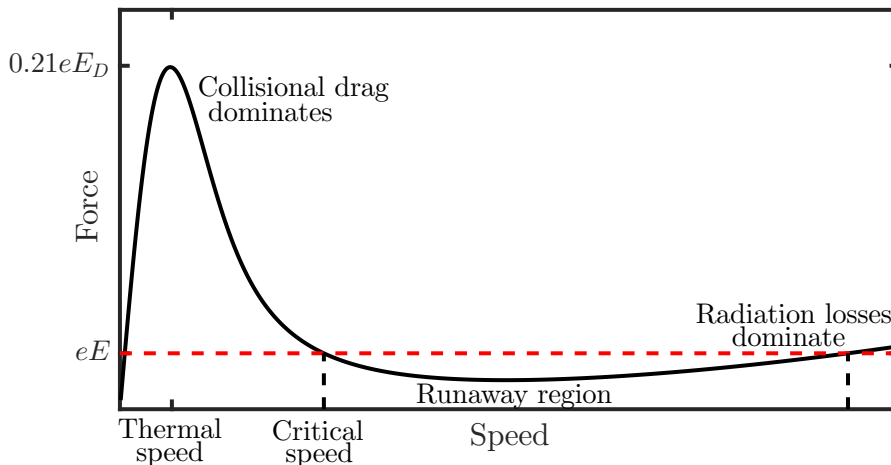


**Figure 1.1:** The speed-dependent force acting on a particle in a plasma, showing friction due to collisions and radiation (solid, black) and acceleration by an electric field (dashed, red). Not to scale (the speed where radiation losses become important can be thousands of times larger than the thermal speed).

## 1.1 Runaway generation

Historically, the basic runaway phenomenon was first encountered by Wilson in the early 20th century, who considered the acceleration of  $\beta$ -rays moving through a medium under the influence of a strong DC electric field [4, 5], having electron acceleration in thunderclouds in mind. He demonstrated that in a sufficiently strong constant electric field, energetic electrons would gain kinetic energy at an increasing rate as they accelerate. In 1926, in *The Internal Constitution of the Stars*, Eddington coined the term “runaway” electron to describe this “Wilson effect” [6].

### Primary generation

Among the earliest<sup>1</sup> theoretical studies of runaway in plasmas was the work by Dreicer [8] in 1959. He considered the total friction force between two Maxwellian particle species moving uniformly with a given speed relative to each other. When accelerated by a sufficiently strong electric field, of order of the so-called Dreicer field

$$E_D = \frac{n_e e^3 \ln \Lambda}{4\pi \varepsilon_0^2 T_e},$$

the electric force overcomes the maximum frictional force, and he concluded that the particles would “run away” towards infinite energy (given infinite time). The Coulomb logarithm  $\ln \Lambda$  is a plasma parameter which typically takes values 10-20 in the applications we consider [9].

In 1964, Kruskal and Bernstein [10] rigorously treated the runaway problem with an analytic solution to the kinetic equation (albeit using a simplified model for collisions). They solved the kinetic equation with an asymptotic technique, matching approximate solutions across five regions in momentum space, thereby obtaining expressions for the shape of the velocity distribution of runaway electrons and the rate at which new runaways are generated (here called the runaway growth rate). It was found that all electrons moving with a velocity above a critical velocity  $v_c$  – the velocity above which the electric field becomes stronger than friction – will run away towards infinite energy. In addition, diffusion would supply the runaway region ( $v > v_c$ ) with new particles from the bulk at a constant rate. This mechanism of runaway generation is referred to as primary generation, or *Dreicer generation*.

---

<sup>1</sup>Earlier efforts have been briefly reviewed by Harrison [7].

Early work on runaways primarily considered the initial generation of runaways at relatively low, non-relativistic speeds. A full description of electron runaway requires the use of a relativistic kinetic equation, a scenario which was first analyzed by Connor and Hastie [11] in 1975. They extended the method of Kruskal and Bernstein to account also for relativistic effects. Unlike the case of non-relativistic runaway, where the frictional force appears to tend towards zero for large speeds, the friction in the relativistic model attains a minimum value, corresponding to a critical (Connor-Hastie) electric field

$$E_c = \frac{n_e e^3 \ln \Lambda}{4\pi \varepsilon_0^2 m_e c^2}.$$

This electric field is smaller than the Dreicer field by the factor  $T/m_e c^2$ . The result of the Connor-Hastie analysis is an explicit expression for the primary runaway growth rate  $\gamma = (\partial n_{\text{RE}}/\partial t)_{\text{primary}}$ , given by

$$\begin{aligned} \gamma &= C \frac{n_e}{\tau_{ee}} \left( \frac{E}{E_D} \right)^{-\frac{3}{16}(1+Z_{\text{eff}})h} \exp \left[ -\lambda \frac{E_D}{4E} - \sqrt{\eta \frac{(1+Z_{\text{eff}})E_D}{E}} \right], \quad (1.1) \\ \lambda &= 8 \frac{E^2}{E_c^2} \left[ 1 - \frac{1}{2} \frac{E_c}{E} - \sqrt{1 - \frac{E_c}{E}} \right], \\ \eta &= \frac{1}{4} \frac{E^2}{E_c(E-E_c)} \left[ \frac{\pi}{2} - \arcsin \left( 1 - \frac{2E_c}{E} \right) \right]^2, \\ h &= \frac{1}{3} \frac{1}{\frac{E}{E_c} - 1} \left[ \frac{E}{E_c} + 2 \left( \frac{E}{E_c} - 2 \right) \sqrt{\frac{E}{E-E_c}} - \frac{Z_{\text{eff}} - 7}{Z_{\text{eff}} + 1} \right]. \end{aligned}$$

The prefactor  $C$  is an order-unity parameter which is undetermined by the asymptotic analysis, but tends to be nearly constant  $C \sim 0.3$  [14]. The three parameters  $\lambda$ ,  $\eta$  and  $h$  all approach unity when  $E/E_c$  becomes large, so that the non-relativistic limit  $E \gg E_c$  is obtained by setting  $\lambda = \eta = h = 1$ , correctly reducing to the Kruskal-Bernstein result. The effective charge of the plasma is denoted  $Z_{\text{eff}} = \sum_i n_i Z_i^2 / n_e$ , and  $\tau_{ee} = 4\pi \varepsilon_0^2 m_e^2 v_{Te}^3 / (n_e e^4 \ln \Lambda)$  is the electron thermal collision time, with the electron thermal speed  $v_{Te} = \sqrt{2T_e/m_e}$ . It is found that the runaway growth rate is exponentially sensitive to the electric field, the dominant scaling following approximately  $\gamma \propto \exp(-E_D/4E)$ . Unless the electric field is a significant fraction of the Dreicer field  $E_D$  – typically a few percent – the primary generation mechanism will accelerate only a negligible number of runaways.

## Secondary generation

Another mechanism for runaway generation was originally proposed by Sokolov [12] in 1979, which is often referred to as *secondary, avalanche* or *knock-on* generation of runaways. For a given electric field  $E > E_c$ , there is a critical speed  $v_c$  above which electrons will almost certainly become runaway accelerated. Whereas in the primary generation mechanism, thermal electrons are fed into the runaway region  $v > v_c$  by a nearly continuous collisional diffusion, the secondary generation mechanism supplies fast electrons through single large-angle collisions between existing runaways and the thermal population. Since the rate at which this occurs is directly proportional to the number of runaways present, one may expect that in a knock-on-dominated discharge the number of runaways will grow exponentially in time, hence being referred to as a runaway avalanche.

In a seminal paper by Rosenbluth and Putvinski [13] in 1997 (following notable developments by Jayakumar *et al.* [14]), the effect of large-angle collisions on the runaway rate was detailed. By solving the kinetic equation in various limits, whilst including a source term describing the momentum-space distribution of knock-on electrons, they obtained an avalanche growth rate  $\Gamma = n_{\text{RE}}^{-1} (\partial n_{\text{RE}} / \partial t)_{\text{secondary}}$  given by the asymptotically-matched formula

$$\Gamma = \frac{1}{\tau_c \ln \Lambda} \sqrt{\frac{\pi \rho}{3(Z_{\text{eff}} + 5)}} \frac{\frac{E}{E_c} - 1}{\sqrt{1 - \frac{E_c}{E} + \frac{4\pi(Z_{\text{eff}}+1)^2}{3\rho(Z_{\text{eff}}+5)(E^2/E_c^2+4/\rho^2-1)}}}, \quad (1.2)$$

$$\rho = \frac{3}{4} \int_0^1 \frac{\lambda d\lambda}{\oint \sqrt{1 - \lambda b(\theta)} d\theta / 2\pi} \approx \frac{1}{1 + 1.46\sqrt{\frac{r}{R}} + 1.72\frac{r}{R}}.$$

Here,  $\tau_c = 4\pi\varepsilon_0^2 m_e^2 c^3 / (n_e e^4 \ln \Lambda)$  is the relativistic electron collision time, and the neoclassical function  $\rho$  represents the effects of an inhomogeneous magnetic field, with the approximate equality corresponding to the large-aspect ratio limit  $r \ll R$  in a tokamak. In the important limit  $E/E_c \gg \sqrt{1 + Z_{\text{eff}}}$  and large aspect ratio, the avalanche growth rate takes the relatively simple form

$$\Gamma \approx \frac{1}{\tau_c \ln \Lambda \sqrt{Z_{\text{eff}} + 5}} \left( \frac{E}{E_c} - 1 \right). \quad (1.3)$$

The total rate at which a runaway population grows, given by the

sum of primary and secondary generation, is

$$\frac{dn_{\text{RE}}}{dt} = \gamma + n_{\text{RE}}\Gamma.$$

In a constant electric field, the generation rate will initially be dominated by primary generation, so that  $n_{\text{RE}} \approx \gamma t$ . Avalanche generation will become dominant once  $\gamma = n_{\text{RE}}\Gamma \approx \gamma t\Gamma$ , i.e. after approximately one avalanche time  $t_{\text{ava}} = 1/\Gamma$ . Note that the net force acting on a runaway electron is approximately  $dp/dt = e(E - E_c)$ , meaning that in one avalanche time a runaway has time to accelerate to a momentum

$$p = e(E - E_c)t_{\text{ava}} \approx m_e c \ln \Lambda \sqrt{Z_{\text{eff}} + 5},$$

which is independent of the electric-field strength [14]! Consequently, by the time that the fastest electron in the plasma has reached an energy of  $\frac{1}{2} \ln \Lambda \sqrt{Z_{\text{eff}} + 5}$  MeV, avalanche is the dominant runaway generation mechanism. As a corollary, in runaway discharges where significant avalanche multiplication occurs the runaway electron population is always ultrarelativistic with average energies in the 10 MeV range, unless there are energy loss mechanisms that can compete with the electric field without deconfining the runaways.

## 1.2 Runaway in tokamaks

Runaways are of particular interest in magnetic-fusion research, where they pose a great threat to the successful operation of tokamaks [15, 16]. The tokamak is a promising concept for fusion-energy reactors [17, 18], which confine a plasma by a magnetic field and heat it to several hundred million Kelvin. At these temperatures nuclear fusion reactions spontaneously occur, releasing large amounts of energy which is then available for generation of electricity. The magnetic field is partially generated by driving a strong current of several mega-ampere through the plasma, with the downside that this is then available for conversion into a runaway-carried current. The mechanism for this conversion is the runaway breakdown, which typically occurs during so-called disruptions [15, 19, 20] which are sudden events where heat confinement is lost. During these disruptions the plasma loses its energy and cools rapidly on a timescale of milliseconds [18] in a thermal quench, sometimes to less than one-thousandth of its original temperature. Due to its size, in a tokamak the total plasma current cannot change on the thermal-quench

time scale. The temperature reduction is associated with a massive decrease in the electrical conductivity of the plasma, thereby inducing strong electric fields in the vessel and plasma in order to maintain the current. These fields are often large enough to enable runaway breakdown to occur. The occurrence of runaway in tokamaks was first pointed out in the literature by Gibson [21] in 1959, and has since been regularly observed and studied in a large number of tokamaks.

Avalanche runaway multiplication will often dominate the runaway generation, although initiation of the avalanche requires the presence of an initial seed population of runaways. This can be provided either by Dreicer generation, as described above, or by so-called hot-tail generation [22, 23, 24, 25, 26]. This third generation mechanism is enabled by the rapid temperature change that occurs during disruptions. If the cooling is sufficiently fast – comparable to the thermal collision time of the plasma – the fastest particles in the tail of the thermal distribution (which experience a weaker drag force) will maintain their initial energy. During the cooling their speeds may at some point exceed the critical speed for runaway generation, and thus they can become runaway accelerated.

It can be shown that, if there is an initial seed population  $n_{\text{RE},0}$  of runaways, avalanche multiplication will increase this number to approximately  $n_{\text{RE}} \sim \exp(2.5I[\text{MA}]) n_{\text{RE},0}$  before the electric field has decayed [15], where  $I[\text{MA}]$  is the original plasma current in MA. While the multiplication factor is fairly small in present-day experiments (of order  $10^4$  [15] in the JET tokamak [27, 28], the biggest experiment to date), in future tokamaks such as ITER [29] this implies a devastating number of  $10^{16}$  or greater [15]. Because of this immense number, runaway-electron dynamics and disruption mitigation are fields of active study. Recent reviews can be found in Refs. [30, 31, 32, 33, 34]. The avalanche multiplication factor is exponentially sensitive to the avalanche growth rate  $\Gamma$ , and in order to accurately predict the final runaway current the large-angle collisions must be modelled precisely. In Paper A we therefore present a linearized Boltzmann operator which generalizes the knock-on models that have previously been used, allowing more accurate generation rates to be calculated than was previously possible.

At highly relativistic (multi-MeV) energies, additional effects such as radiation losses become important for the dynamics of the fast electrons. These effects only weakly impact runaway generation which typically occurs at non-relativistic speeds, but are particularly important during

the termination phase of a runaway beam where the current decays with time. Accurate models for radiation losses are then needed in order to understand the energy distribution of the runaway population, as well as the threshold electric field below which runaways slow down. This motivated the study presented in Paper B, where a model for bremsstrahlung losses treated as binary large-angle collisions is introduced.

The qualitative features of the basic runaway phenomenon in plasmas can thus be summarized as:

- Runaway is only possible for electric fields exceeding the critical field,  $E > E_c$ .
- Primary (Dreicer) runaway generation is exponentially sensitive to electric field, and only gives an appreciable growth rate when  $E \gtrsim 0.03E_D$ .
- Secondary (avalanche) runaway generation depends weakly on electric field and is caused by knock-on collisions, requiring a population of runaways to already be present in the plasma. When avalanche generation is significant the average runaway energy is in the 10 MeV range, and vice versa.
- Hot-tail runaway generation occurs during a rapid temperature drop, and describes significant conversion of previously thermal electrons into runaways even when  $E \lesssim 0.01E_D$  at all times.
- Once the entire plasma current is carried by runaways, the system tends to be at marginal stability where the electric field must be near the avalanche threshold field ( $E_c$  in the ideal theory) wherever the current density is non-vanishing [35]. This sets the decay time of a runaway beam in a tokamak to roughly  $dI/dt \sim (10 \text{ kA/s}) \times \ln \Lambda n / (10^{20} \text{ m}^{-3})$  in the absence of radial particle transport, where  $n$  is the electron density.

## Disruption mitigation

Due to the expected detrimental effect of a large unmitigated runaway beam in reactor-scale tokamaks, electron runaway is a question of critical importance for the ITER programme [15]. The demands of the disruption mitigation system are multifaceted [36]: during the thermal quench, where the plasma rapidly releases its thermal energy, the energy flux density to the wall must be kept below a certain threshold

by distributing the energy loads in space and time. During the current quench that follows, the poloidal magnetic energy of the plasma is released, either directly into the first wall via eddy currents that are induced or radiated from the plasma, or into the formation of a runaway electron beam. The current quench must be sufficiently rapid that significant halo currents causing large electromagnetic forces are avoided, but sufficiently slow that excessive runaway generation is also avoided; the energy transferred to runaway electrons is of particular concern, because it will eventually be deposited into the wall both locally and within a short time interval. As a result, runaways can cause immense localized damage to plasma-facing components, forcing extensive (and expensive) maintenance of the tokamak.

The current disruption mitigation plan for ITER revolves around massive material injection where large amounts of high- $Z$  matter is injected into the plasma, which will reduce the current-quench time and contribute to radiating the energy content of the plasma. Large uncertainties still surround the formation of the runaway beam during disruptions [16], however, calling for an urgent need to develop more accurate models for runaway as well as disruption dynamics. This spurred the study presented in Paper E, where we describe a model for electron collisions with partially ionized impurities, which is essential in order to predict the generation and decay rate – and indeed the distribution function – of runaway electrons in tokamak disruption scenarios.

### 1.3 Ion runaway

Runaway acceleration of ions – instead of the nowadays more commonly studied electron runaway – was first invoked in order to explain experimental observations at the Zeta device [21] in 1959. In 1972, Furth and Rutherford [37] used an asymptotic technique similar to that used for electron runaway in order to obtain an analytic solution of the ion drift-kinetic equation. Their treatment, however, provided only limited information about the runaway growth rate in most scenarios due to the more complicated structure of the ion kinetic equation. A limited time-dependent solution of the ion kinetic equation was more recently developed in order to explain observations at the Mega Ampere Spherical Tokamak [38, 39, 40, 41]. Simpler test-particle methods have also been used to study the ion runaway phenomenon in astrophysical contexts [42]. The lack of widely applicable analytic results has motivated

a numerical study of the ion drift-kinetic equation, which is presented in Paper D. Experimentally observed ion acceleration in the Madison Symmetric Torus reversed-field pinch has lead to recent work where similar methods have been employed [43, 44].

## 1.4 Outline

Chapter 2 contains an introduction to the kinetic theory of plasmas, which describes the phase-space dynamics of charged particles. The theory presented here covers the physics required to understand the basic runaway phenomenon, but is also the foundation upon which further extensions of the theory can be developed. In chapter 3, we discuss the radiation emitted by runaways. We develop the runaway kinetic theory by describing a model for the effect of bremsstrahlung emission based on the Boltzmann collision operator. We also present a synthetic diagnostic for the radiation that a runaway population will emit, focusing on synchrotron radiation and bremsstrahlung. The method predicts what a radiation detector would measure when observing a tokamak plasma containing runaway electrons. The theory for the runaway of positively charged particle species requires a modified treatment compared to electron runaway; the theory for runaway of ions and positrons is summarized in chapter 4. Finally the thesis is summarized in chapter 5, where we also present an outlook for future work in the field of runaway.

## Chapter 2

# The kinetic equation

A detailed study of runaway particles requires the resolution of their momentum-space structure, accounting for the randomizing collisions in an accurate way. This is achieved using a kinetic equation, which provides a full description of the time evolution of the distribution function  $f_a(t, \mathbf{x}, \mathbf{p})$  of a particle species  $a$ , where  $t$  is time,  $\mathbf{x}$  is the particle position,  $\mathbf{p} = m_a \mathbf{v} / \sqrt{1 - v^2/c^2}$  is the momentum and  $\mathbf{v}$  is the velocity, with  $v = |\mathbf{v}|$ . The distribution function is the particle density function in phase space, defined such that  $n_a(t, \mathbf{x}) = \int d\mathbf{p} f_a(t, \mathbf{x}, \mathbf{p})$  is the number density, and  $N_a(t) = \int d\mathbf{x} n_a(t, \mathbf{x})$  is the total number of particles of species  $a$ . In the absence of collisions, the distribution function describes particles moving along trajectories  $\mathbf{x} = \mathbf{x}(t)$  and  $\mathbf{p} = \mathbf{p}(t)$ , governed by the equations of motion for a charged particle

$$\begin{aligned}\frac{d\mathbf{x}}{dt} &= \mathbf{v}, \\ \frac{d\mathbf{p}}{dt} &= q_a(\mathbf{E} + \mathbf{v} \times \mathbf{B}),\end{aligned}$$

where  $q_a$  is the electrical charge of species  $a$ ,  $\mathbf{E}$  the electric field and  $\mathbf{B}$  the magnetic field. The continuity equation in phase space is [45]

$$0 = \frac{df_a}{dt} = \frac{\partial f_a}{\partial t} + \mathbf{v} \cdot \frac{\partial f_a}{\partial \mathbf{x}} + q_a(\mathbf{E} + \mathbf{v} \times \mathbf{B}) \cdot \frac{\partial f_a}{\partial \mathbf{p}}, \quad (2.1)$$

where the electric and magnetic fields are given by the charge and current distribution of the plasma according to Maxwell's equations,

$$\begin{aligned}\mathbf{E}(t, \mathbf{x}) &= -\nabla\phi - \frac{\partial \mathbf{A}}{\partial t}, \\ \mathbf{B}(t, \mathbf{x}) &= \nabla \times \mathbf{A}.\end{aligned}$$

When the time variations of the plasma are slow compared to the transit time of light across its extent, the electromagnetic potential functions are given by

$$\phi(t, \mathbf{x}) = \frac{1}{4\pi\epsilon_0} \int d\mathbf{x}' \frac{\rho(t, \mathbf{x}')}{|\mathbf{x} - \mathbf{x}'|},$$

$$\mathbf{A}(t, \mathbf{x}) = \frac{\mu_0}{4\pi} \int d\mathbf{x}' \frac{\mathbf{j}(t, \mathbf{x}')}{|\mathbf{x} - \mathbf{x}'|},$$

where the charge  $\rho$  and current  $\mathbf{j}$  within the plasma are in turn determined by the distribution functions,

$$\rho(t, \mathbf{x}) = \sum_b q_b \int d\mathbf{p} f_b(t, \mathbf{x}, \mathbf{p}),$$

$$\mathbf{j}(t, \mathbf{x}) = \sum_b q_b \int d\mathbf{p} \mathbf{v} f_b(t, \mathbf{x}, \mathbf{p}),$$

with the sum taken over all particle species  $b$  present in the plasma. In order to obtain a useful kinetic equation, Eq. (2.1) needs to be ensemble-averaged over macroscopically equivalent systems. The distribution function will then become a smooth function, but the microscopic interactions between the discrete particles in the plasma will need to be accounted for by the addition of a new term [46], which is called the *collision operator*  $C$ , or the collision integral (as it generally takes the form of an integral operator). The kinetic equation then takes the form

$$\frac{\partial f_a}{\partial t} + \mathbf{v} \cdot \frac{\partial f_a}{\partial \mathbf{x}} + q_a (\mathbf{E} + \mathbf{v} \times \mathbf{B}) \cdot \frac{\partial f_a}{\partial \mathbf{p}} = \sum_b C_{ab} \{f_a, f_b\}, \quad (2.2)$$

where  $\mathbf{E}$  and  $\mathbf{B}$  now denote the macroscopic fields, not including fluctuations caused by individual particles which are instead captured by the collision operator  $C$ . Throughout this thesis, we mainly focus on the simplest scenario that exhibits the runaway phenomenon: an infinite homogeneous plasma with an electric field in a constant direction (although allowed to vary in amplitude with time). In this case we can suppress the space variables and write  $f_a = f_a(t, \mathbf{p})$ , and introduce a spherical momentum coordinate system  $(p, \theta, \varphi)$  aligned with the electric field, in which the azimuthal angle  $\varphi$  is referred to as the gyroangle and the longitudinal angle  $\theta$  is referred to as the pitch-angle. The kinetic equation then becomes

$$\frac{\partial f_a}{\partial t} + q_a E \left( \xi \frac{\partial f_a}{\partial p} + \frac{1 - \xi^2}{p} \frac{\partial f_a}{\partial \xi} \right) = \sum_b C_{ab} \{f_a, f_b\}, \quad (2.3)$$

where  $\xi = \cos \theta = \mathbf{p} \cdot \mathbf{E}/pE$ . This equation allows us to study the effects of various contributions in the collision operator  $C$  on the dynamics of the runaway particles. The model also approximately describes the local dynamics of runaways near the magnetic axis in a tokamak, if  $E$  is taken to be the component of the electric field parallel to the magnetic field and the pitch  $\xi$  is defined relative to the magnetic field.

An essential part of the description of runaway electrons is the collision operator. This term in the kinetic equation describes the effect of microscopic particle-particle interactions, in contrast to the macroscopic interactions with the electromagnetic field set up by the charge distribution in the plasma or by external sources. The collisions drive the particle distributions towards thermal equilibrium by always increasing entropy in the system, and this is the restoring effect which needs to be overcome by the electric field in order to generate runaway particles. Therefore the details of the collision operator can be expected to strongly influence the description of the runaway process.

In this chapter we will provide a detailed discussion of the collision operator, revealing a unified picture of small-angle collisions, knock-on collisions and bremsstrahlung radiation in the same framework. We shall begin by presenting in more detail how the collision operator can be obtained.

## 2.1 BBGKY hierarchy and the kinetic equation

A systematic framework for obtaining kinetic equations was initially developed by Bogolyubov, Born, Green, Kirkwood and Yvon (BBGKY) [47, 48, 49, 50, 51]. The starting point of their analysis is the Liouville theorem [52], which deterministically describes the time evolution of an  $N$ -body system according to Hamiltonian mechanics. The system is fully described by the phase space density function  $f_N(t, \mathbf{x}_1, \mathbf{p}_1, \dots, \mathbf{x}_N, \mathbf{p}_N)$  giving the location and momentum of all its constituents. A kinetic equation describes the time evolution of the distribution function, which is defined as  $f(t, \mathbf{x}, \mathbf{p}) = \int d\mathbf{x}_2 d\mathbf{p}_2 \cdots d\mathbf{x}_N d\mathbf{p}_N f_N(t, \mathbf{x}, \mathbf{p}, \mathbf{x}_2, \mathbf{p}_2, \dots, \mathbf{x}_N, \mathbf{p}_N)$ . Note that, while this definition appears to single out the particle with subscript 1 as special, the particles described by the phase-space density function are identical, and hence it is symmetric in all indices. That is, non-identical particle species are each described by their own distribution function.

The Liouville equation [53] for a species interacting pair-wise with a

central potential  $V_{ij} = V(|\mathbf{x}_i - \mathbf{x}_j|)$ , with the force on particle  $i$  being  $\mathbf{F}_i = -\sum_{(j \neq i)=1}^N \partial V_{ij} / \partial \mathbf{x}_i$  (for simplicity assuming a single species and no magnetic interaction, which would require a generalized form of the potential), is given by

$$\frac{\partial f_N}{\partial t} + \sum_{i=1}^N \frac{\mathbf{p}_i}{m_a} \cdot \frac{\partial f_N}{\partial \mathbf{x}_i} - \sum_{i=1}^N \sum_{(j \neq i)=1}^N \frac{\partial V_{ij}}{\partial \mathbf{x}_i} \cdot \frac{\partial f_N}{\partial \mathbf{p}_i} = 0.$$

By integrating over all but  $s$  particle coordinates, a *reduced* phase space density, or the *s-particle correlation function*, can be defined as  $f_s = \int d\mathbf{x}_{s+1} d\mathbf{p}_{s+1} \cdots d\mathbf{x}_N d\mathbf{p}_N f_N$ . Here,  $s = 1$  gives the distribution function in which we are most interested, and  $s = N$  returns the full  $N$ -particle phase space density. When performing such an integration over the Liouville equation, an equation for the time-evolution of the reduced distribution function is obtained; however, the equation for  $\partial f_s / \partial t$  invariably contains  $f_{s+1}$  due to the pair-wise interaction term. Thus, the time-evolution of the distribution function depends on the two-particle correlation function  $f_2$ , which in turn is affected by  $f_3$ , and so on. This set of coupled partial differential equations is called the BBGKY hierarchy. A systematic approximation scheme to close this set of equations was developed by Frieman [54], Sandri [55] and collaborators, which takes the form of a perturbation expansion in two parameters  $\mu$  and  $\eta$ . These appear naturally when normalizing the equation to characteristic values of particle separation  $r_0$ , velocities  $v_0$  and interaction strength  $V_0$ , and are given by

$$\mu = \frac{1}{nr_0^3},$$

$$\eta = \frac{V_0}{mv_0^2} \sim \frac{e^2}{4\pi\varepsilon_0 Tr_0}.$$

Here  $1/\mu$  is the number of particles in the interaction region (defined by a characteristic range  $r_0$ ), and  $\eta$  is a measure of the strength of the interaction (described by the potential function  $V_0$ ) compared to the kinetic energy. There are three domains of primary interest [56, 57] which can be described as (1) “dilute, short-range”, (2) “weak coupling” (small momentum transfer) and (3) “long-range”. These, respectively,

correspond to the choices (with  $\epsilon$  a small expansion parameter)

- (1)  $\mu = \mathcal{O}(\epsilon^{-1}), \quad \eta = \mathcal{O}(1),$
- (2)  $\mu = \mathcal{O}(1), \quad \eta = \mathcal{O}(\epsilon),$
- (3)  $\mu = \mathcal{O}(\epsilon), \quad \eta = \mathcal{O}(\epsilon).$

These lead, in turn, to (1) the so-called Boltzmann equation, (2) the Fokker-Planck equation and (3) the Balescu-Lenard (or Bogolyubov-Lenard-Balescu) equation. Plasmas are particularly pathological, as no specific ordering applies to the entire phase space. The long-range Coulomb interaction allows for collisions where any of the orderings may apply, depending on the impact parameter.

An analysis shows that the Balescu-Lenard operator takes a similar form to the Fokker-Planck operator, but where the dielectric constant of the plasma appears in the collision integral. This factor accounts for *dynamical screening* in the plasma, which ensures that collisions with impact parameter of order the Debye length  $\lambda_D = \sqrt{\epsilon_0 T / ne^2}$  or greater are exponentially damped. This effect demonstrates the well-known behavior of Debye screening [17], where the electric field from a point charge in a plasma will be exponentially damped on a length scale  $\lambda_D$  by the rearrangement of the surrounding plasma. The Fokker-Planck collision operator diverges in the contribution from large-impact-parameter collisions, but by following Landau's prescription from the original derivation [58] to cut the integration off at impact parameters  $\lambda_D$  (which can be motivated by the Balescu-Lenard equation), one obtains a convergent integral. The contribution from small-angle collisions in the Fokker-Planck operator is then found to be larger than the contribution from large-angle collisions in the Boltzmann operator by a factor  $\ln n \lambda_D^3 \simeq \ln \Lambda$ , the so-called Coulomb logarithm.

In this chapter we will not pursue a detailed analysis of the BBGKY hierarchy of equations. Instead, we will derive the Boltzmann and Fokker-Planck collision operators with heuristic arguments, based on an analysis of binary collisions. This method gives the same result as the more rigorous derivation from first principles, and also provides some physical insight into how we may view collisions in a plasma.

## 2.2 The Boltzmann collision operator

The Boltzmann equation was originally derived by Ludwig Boltzmann in the late nineteenth century [59, 60] in order to study the dynamics of

gases. As we indicated in the previous section, the Boltzmann equation for a plasma is valid when describing those large-angle collisions where the impact parameter is much smaller than the mean distance between particles in the plasma, that is for  $\mu \gg 1$ . The Boltzmann collision operator describes the rate-of-change of the distribution function due to binary collisions, and we shall briefly derive it here in a form that will be suited to our applications.

We describe a binary interaction with a differential cross-section  $d\sigma_{ab}(\mathbf{p}_1, \mathbf{p}_2; \mathbf{p}, \mathbf{p}')$  for particles  $a$  and  $b$  to be taken from initial momenta  $\mathbf{p}$  and  $\mathbf{p}'$ , respectively, to final momenta  $\mathbf{p}_1$  and  $\mathbf{p}_2$ , respectively. The cross-section is defined such that the total differential change of the phase-space particle density  $dn_a(t, \mathbf{x}, \mathbf{p}) = f_a(t, \mathbf{x}, \mathbf{p})d\mathbf{p}$  due to these interactions in a time interval  $dt$  is

$$[dn_a(\mathbf{p})]_{c,ab} = f_a(\mathbf{p}_1)f_b(\mathbf{p}_2)g_\phi(\mathbf{p}_1, \mathbf{p}_2)d\sigma(\mathbf{p}, \mathbf{p}'; \mathbf{p}_1, \mathbf{p}_2)d\mathbf{p}_1d\mathbf{p}_2dt \\ - f_a(\mathbf{p})f_b(\mathbf{p}')g_\phi(\mathbf{p}, \mathbf{p}')d\sigma(\mathbf{p}_1, \mathbf{p}_2; \mathbf{p}, \mathbf{p}')d\mathbf{p}d\mathbf{p}'dt, \quad (2.4)$$

where  $\mathbf{p}_1$  and  $\mathbf{p}_2$  are related to  $\mathbf{p}$  and  $\mathbf{p}'$  by the conservation of energy and momentum. The relativistic generalization of the relative speed  $v_{\text{rel}} = |\mathbf{v} - \mathbf{v}'|$ , is the Møller relative speed  $g_\phi(\mathbf{p}, \mathbf{p}') = \sqrt{(\mathbf{v} - \mathbf{v}')^2 - (\mathbf{v} \times \mathbf{v}')^2/c^2}$  [61]. The collision operator can formally be defined as

$$C_{ab}\{f_a, f_b\} \equiv \left( \frac{\partial^2 n_a}{\partial t \partial \mathbf{p}} \right)_{c,ab} \\ = \int d\mathbf{p}_1 f_a(\mathbf{p}_1) \int d\mathbf{p}_2 f_b(\mathbf{p}_2) g_\phi(\mathbf{p}_1, \mathbf{p}_2) \frac{\partial \sigma(\mathbf{p}, \mathbf{p}'; \mathbf{p}_1, \mathbf{p}_2)}{\partial \mathbf{p}} \\ - f_a(\mathbf{p}) \int d\mathbf{p}' f_b(\mathbf{p}') g_\phi(\mathbf{p}, \mathbf{p}') \sigma(\mathbf{p}, \mathbf{p}'), \quad (2.5)$$

where the total cross-section  $\sigma(\mathbf{p}, \mathbf{p}')$  is defined as

$$\sigma(\mathbf{p}, \mathbf{p}') = \int d\mathbf{p}_1 \frac{\partial \sigma(\mathbf{p}_1, \mathbf{p}_2; \mathbf{p}, \mathbf{p}')}{\partial \mathbf{p}_1}.$$

A symmetric form is obtained in the special case of elastic collisions by utilizing the *principle of detailed balance* [61], which is a symmetry relation for the cross-section stating that

$$g_\phi(\mathbf{p}_1, \mathbf{p}_2)d\sigma(\mathbf{p}, \mathbf{p}'; \mathbf{p}_1, \mathbf{p}_2)d\mathbf{p}_1d\mathbf{p}_2 = g_\phi(\mathbf{p}, \mathbf{p}')d\sigma(\mathbf{p}_1, \mathbf{p}_2; \mathbf{p}, \mathbf{p}')d\mathbf{p}d\mathbf{p}'.$$

Using this relation, which is valid for classical particles interacting with a central potential and also in the first order spin-averaged Born approximation in quantum mechanics [62, 63], Eq. (2.4) leads to

$$C_{ab}\{f_a, f_b\} = \int d\mathbf{p}' d\sigma(\mathbf{p}_1, \mathbf{p}_2; \mathbf{p}, \mathbf{p}') g_\phi(\mathbf{p}, \mathbf{p}') \times \times \left( f_a(\mathbf{p}_1) f_b(\mathbf{p}_2) - f_a(\mathbf{p}) f_b(\mathbf{p}') \right). \quad (2.6)$$

This is the operator which is typically referred to as the Boltzmann operator, although we shall apply the term more generally here to any integral operator of the form of Eq. (2.5). In Eqs. (2.4), (2.5) and (2.6) the first – the gain term – describes the rate at which particles  $a$  of initial momentum  $\mathbf{p}_1$  are scattered into  $\mathbf{p}$ , while the second – the loss term – describes the rate at which particles scatter away from  $\mathbf{p}$ .

### Large-angle collision operator for runaways

The description of large-angle collisions is essential in order to understand runaway dynamics. The reason is that when the electric field is far below the Dreicer field  $E_D = n_e \ln \Lambda e^3 / (4\pi \varepsilon_0^2 T_e)$ , no thermal electrons will spontaneously be runaway accelerated through the primary (Dreicer) mechanism. Large-angle collisions between highly energetic runaways and the bulk population can, however, even under such circumstances generate a significant number of new runaways. The electron-electron Boltzmann operator for collisions between runaways and thermal electrons must therefore be included in the kinetic equation in order to capture the runaway avalanche.

Two main approximations allow a significantly simpler collision operator to be obtained:

- (i) The runaways are assumed to be few in number, so that the operator can be linearized around the thermal background. This is often the case; due to their high speed, runaways would carry a massive current whenever their number density is comparable to that of the bulk plasma (giga-ampere scale in tokamaks).
- (ii) The thermal electrons are treated as stationary, which can be motivated by the fact that the operator is mainly important when  $E \ll E_D$ , at which point runaway speeds will far exceed the thermal speed.

In that case, the linearized electron-electron collision operator takes the form

$$C_{ee} = n_e \int d\mathbf{p}_1 v_1 \frac{\partial \sigma_{ee}}{\partial \mathbf{p}} f_e(\mathbf{p}_1) - n_e v \sigma_{ee}(\mathbf{p}) f_e(\mathbf{p}) - n_e \delta(\mathbf{p}) \int d\mathbf{p}_1 v_1 \sigma_{ee}(\mathbf{p}_1) f_e(\mathbf{p}). \quad (2.7)$$

The differential cross-section for relativistic electron-electron collisions is given by the Møller cross-section, which in the laboratory frame takes the form [62]

$$\frac{\partial \sigma_{ee}}{\partial \mathbf{p}}(\mathbf{p}, \mathbf{p}'; \mathbf{p}_1, \mathbf{p}_2) = \frac{\delta(\cos \theta_s - \xi^*(\gamma, \gamma_1))}{2\pi p \gamma} \frac{\partial \sigma_{ee}}{\partial \gamma}(\gamma, \gamma_1), \quad (2.8)$$

$$\begin{aligned} \frac{\partial \sigma_{ee}}{\partial \gamma}(\gamma, \gamma_1) = & \frac{2\pi r_0^2 \gamma_1^2}{(\gamma_1^2 - 1)(\gamma - 1)^2(\gamma_1 - \gamma)^2} \left( (\gamma_1 - 1)^2 \right. \\ & \left. - \frac{(\gamma - 1)(\gamma_1 - \gamma)}{\gamma_1^2} \left[ 2\gamma_1^2 + 2\gamma_1 - 1 - (\gamma - 1)(\gamma_1 - \gamma) \right] \right). \end{aligned} \quad (2.9)$$

Here, we have introduced the angles

$$\begin{aligned} \xi^*(\gamma, \gamma_1) &= \sqrt{\frac{\gamma_1 + 1}{\gamma_1 - 1} \frac{\gamma - 1}{\gamma + 1}}, \\ \cos \theta_s &= \frac{\mathbf{p}_1 \cdot \mathbf{p}}{p_1 p}, \end{aligned} \quad (2.10)$$

and the delta function of the differential cross-section, relating the scattering angle  $\theta_s$  to the energy transfer, arises due to the conservation of momentum and energy in elastic collisions. The classical electron radius is denoted  $r_0 = e^2/(4\pi \varepsilon_0 m_e c^2) \approx 2.8 \cdot 10^{-15}$  m. The collision operator can then be further simplified under the additional assumption that

(iii) The runaway population is cylindrically symmetric in momentum space, fulfilling the conditions under which Eq. (2.3) was derived.

Expanding the electron distribution function in Legendre polynomials,

$$f_e(\mathbf{p}) = \sum_L f_L(p) P_L(\cos \theta), \quad (2.11)$$

then allows the linearized large-angle collision operator to be written

$$\begin{aligned}
 C_{ee}(\mathbf{p}) &= \sum_L C_L(p) P_L(\cos \theta), \quad (2.12) \\
 C_L(p) &= \frac{(m_e c)^{-3}}{2\tau_c \ln \Lambda} \frac{1}{\gamma p} \int_{q_0}^{\infty} dp_1 \frac{p_1^3}{\gamma_1} f_L(p_1) P_L(\xi^*) \Sigma(\gamma, \gamma_1) \\
 &\quad - \frac{1}{4\tau_c \ln \Lambda} \frac{v}{c} f_L(p) \int_{\gamma_m}^{\gamma+1-\gamma_m} d\gamma_1 \Sigma(\gamma_1, \gamma) \\
 &\quad - \frac{(m_e c)^{-1}}{4\tau_c \ln \Lambda} \delta_{L,0} \frac{\delta(p)}{p^2} \int_{q_0}^{\infty} dp' \frac{p'^3}{\gamma'} f_0(p') \int_{\gamma_m}^{\gamma'+1-\gamma_m} d\gamma_1 \Sigma(\gamma_1, \gamma'), \\
 q_0 &= m_e c \sqrt{(\gamma + \gamma_m - 1)^2 - 1}, \\
 \frac{1}{\tau_c} &= \ln \Lambda \frac{n_e}{4\pi} \frac{e^4}{\varepsilon_0^2 m_e^2 c^3}.
 \end{aligned}$$

Here, we have truncated the collision operator so that it only accounts for those collisions where the secondary electron receives a kinetic energy greater than  $m_e c^2(\gamma_m - 1)$ , corresponding to a cut-off momentum  $p_m = m_e c \sqrt{\gamma_m^2 - 1}$ . This operator, which is derived in Paper A, still identically conserves electron density, momentum and energy. In Paper A we study its predictions for runaway avalanche generation and compare it to previous studies which have imposed further assumptions on the distribution function. One such example is the widely used model studied by Rosenbluth and Putvinski [13], where the runaway electron distribution is taken as a delta function at infinite momentum and zero pitch angle in the evaluation of the Boltzmann operator. In that case, the linearized electron-electron Boltzmann collision operator reduces to the remarkably simple form

$$C_{RP}(\mathbf{p}) = n_{RE} \frac{\delta[\cos \theta - \xi^*(\gamma, \infty)]}{4\pi \tau_c \ln \Lambda} \frac{(m_e c)^3}{p^2} \frac{\partial}{\partial p} \frac{1}{1 - \gamma}, \quad (2.13)$$

$$n_{RE} = \int_{p > p_c} f_e d\mathbf{p}. \quad (2.14)$$

This operator refers explicitly to the runaway density and to the critical momentum which defines a runaway; in practice, the details of the definition are often unimportant as long as  $p_c$  is chosen to be significantly larger than the thermal momentum but negligible compared to the average runaway momentum.

## 2.3 The Fokker-Planck collision operator

When the interaction distance is significant compared to the mean particle separation, but the interaction is weak, the appropriate collision term is the Fokker-Planck operator, rather than the Boltzmann operator. However, as we will now show, the Fokker-Planck operator can in fact be derived from the Boltzmann operator in the limit of small momentum transfers in the collisions. That the seemingly opposite description of weak interactions in the Fokker-Planck picture can be contained in the Boltzmann picture of binary collisions appears counter-intuitive. It can, however, be physically understood by the fact that the small momentum transfers described by the Fokker-Planck operator only negligibly change the particle momentum in a single collision; then the net effect of the many-body interaction can be viewed as a linear superposition of pairwise momentum transfers [64].

The procedure is as follows: a general integral moment of the Boltzmann operator of a test function  $\phi$  is given by

$$J[\phi] = \int d\mathbf{p} \phi(\mathbf{p}) C_{ab} = \int d\mathbf{p} \int d\mathbf{p}' d\sigma(\mathbf{p}_1, \mathbf{p}_2; \mathbf{p}, \mathbf{p}') f_a(\mathbf{p}) f_b(\mathbf{p}') \times g_\phi(\mathbf{p}, \mathbf{p}') [\phi(\mathbf{p}_1) - \phi(\mathbf{p})],$$

which is most easily seen by integrating Eq. (2.4) and switching names of the dummy variables  $\mathbf{p}_1$  and  $\mathbf{p}_2$  in the first term with  $\mathbf{p}$  and  $\mathbf{p}'$ , respectively. For convenience we will suppress the arguments of  $d\sigma$  and  $g_\phi$  as they will remain unchanged for the rest of the calculation. Here we introduce the small-momentum-transfer argument: the integral is assumed to be dominated by the contribution from  $\mathbf{p}_1 \approx \mathbf{p}$ . We then Taylor expand

$$\phi(\mathbf{p}_1) - \phi(\mathbf{p}) \simeq (\mathbf{p}_1 - \mathbf{p}) \cdot \frac{\partial \phi(\mathbf{p})}{\partial \mathbf{p}} + \frac{(\mathbf{p}_1 - \mathbf{p})(\mathbf{p}_1 - \mathbf{p})}{2} : \frac{\partial \phi(\mathbf{p})}{\partial \mathbf{p} \partial \mathbf{p}},$$

where we use dyadic notation such that the rank-2 tensor  $\mathbf{T} = \mathbf{a}\mathbf{b}$  has components  $T_{ij} = a_i b_j$ . By introducing the quantities

$$\Delta\mathbf{p} = \mathbf{p}_1 - \mathbf{p}, \quad \mathbf{A} = \int d\mathbf{p}' g_\phi f_b(t, \mathbf{p}') \int d\sigma \Delta\mathbf{p}, \quad (2.15)$$

$$\mathbf{D} = \int d\mathbf{p}' g_\phi f_b(t, \mathbf{p}') \int d\sigma \Delta\mathbf{p} \Delta\mathbf{p}, \quad (2.16)$$

integrating by parts twice yields

$$J[\phi] = \int d\mathbf{p} \phi(\mathbf{p}) \left[ \frac{\partial}{\partial \mathbf{p}} \cdot \left( -\mathbf{A}(t, \mathbf{p}) f_a(t, \mathbf{p}) + \frac{1}{2} \frac{\partial}{\partial \mathbf{p}} \cdot [\mathbf{D}(t, \mathbf{p}) f_a(t, \mathbf{p})] \right) \right].$$

As this equality holds for any  $\phi$ , the small-momentum-transfer assumption therefore leads to the well-known Fokker-Planck operator [65, 66]

$$C_{ab}\{f_a, f_b\} = \frac{\partial}{\partial \mathbf{p}} \cdot \left[ -\mathbf{A}_{ab}(t, \mathbf{p}) f_a(t, \mathbf{p}) + \frac{1}{2} \frac{\partial}{\partial \mathbf{p}} \cdot (\mathbf{D}_{ab}(t, \mathbf{p}) f_a(t, \mathbf{p})) \right]. \quad (2.17)$$

For relativistic elastic electron-electron collisions, the Fokker-Planck operator was first given by Beliaev and Budker [67], with a direct derivation from Eqs. (2.15), (2.16) and (2.17) later given by Akama [68]. This Fokker-Planck operator can conveniently be expressed in the form

$$C_{ee}\{f_e, f_e\} = \frac{\partial}{\partial \mathbf{p}} \cdot \int d\mathbf{p}' \mathcal{E} \cdot \left( \frac{\partial f_e(\mathbf{p})}{\partial \mathbf{p}} f_e(\mathbf{p}') - \frac{\partial f_e(\mathbf{p}')}{\partial \mathbf{p}} f_e(\mathbf{p}) \right), \quad (2.18)$$

where the collision kernel  $\mathcal{E}$  is the symmetric rank-2 tensor [69]

$$\mathcal{E} = 2\pi \left( \frac{e^2}{4\pi\epsilon_0} \right)^2 \ln \Lambda \frac{\gamma' \gamma (1 - \mathbf{v}' \cdot \mathbf{v}/c^2)^2}{c \{ [\gamma' \gamma - \mathbf{p}' \cdot \mathbf{p}/(m_e c)^2]^2 - 1 \}^{3/2}} \times \left\{ \begin{aligned} & \left[ \left( \gamma' \gamma - \frac{\mathbf{p}' \cdot \mathbf{p}}{m_e^2 c^2} \right)^2 - 1 \right] \mathbf{I} - \frac{\mathbf{p} \mathbf{p} + \mathbf{p}' \mathbf{p}'}{m_e^2 c^2} + \left( \gamma' \gamma - \frac{\mathbf{p}' \cdot \mathbf{p}}{m_e^2 c^2} \right) \frac{\mathbf{p}' \mathbf{p} + \mathbf{p} \mathbf{p}'}{m_e^2 c^2} \end{aligned} \right\},$$

where  $\mathbf{I}$  is the unit tensor and  $\gamma = \sqrt{1 + (p/m_e c)^2}$  is the relativistic Lorentz factor. In this expression, only the leading-order term in  $\ln \Lambda$  has been retained, which corresponds to the small-angle contribution to the integrals (2.15) and (2.16).

## General Fokker-Planck equation for stationary targets

The general Fokker-Planck operator given by (2.17) can be given in a more explicit form when considering collisions with stationary targets – which is often an appropriate approximation for runaways – and for isotropic collision processes which only depend on the energy transfer and deflection angle. In that case, it can be expressed as [70]

$$C_{ei} = \frac{\nu_D^{ei}(p)}{2} \frac{\partial}{\partial \xi} \left[ (1 - \xi^2) \frac{\partial f_e}{\partial \xi} \right] + \frac{1}{p^2} \frac{\partial}{\partial p} \left[ p^3 \left( \nu_s^{ei} f_e + \frac{\nu_{\parallel}^{ei} p}{2} \frac{\partial f_e}{\partial p} \right) \right], \quad (2.19)$$

where  $\nu_D$  can be identified as the rate of deflection in pitch angle,  $\nu_s$  the slowing-down frequency (so that the dynamical friction is given by  $-\mathbf{p}\nu_s$ ) and  $\nu_{\parallel}$  the rate of energy diffusion. For an arbitrary binary interaction, they are explicitly given by

$$\begin{aligned}\nu_s &= \left\langle -\frac{\mathbf{p} \cdot \Delta\mathbf{p}}{p^2} \right\rangle - \nu_D + \nu_{\parallel} + \frac{1}{2} \frac{\partial(p\nu_{\parallel})}{\partial p}, \\ \nu_{\parallel} &= \frac{1}{p^4} \langle (\mathbf{p} \cdot \Delta\mathbf{p})^2 \rangle, \\ \nu_D &= \frac{1}{2p^2} \langle |\Delta\mathbf{p}|^2 - \frac{1}{p^2} (\mathbf{p} \cdot \Delta\mathbf{p})^2 \rangle.\end{aligned}\quad (2.20)$$

The bracket  $\langle A \rangle$  denotes the average rate of change of a quantity  $A = A(\mathbf{p}, \mathbf{p}_1)$  in a collision, and is for stationary targets defined by

$$\langle A \rangle(\mathbf{p}) = nv \int d\mathbf{p}_1 \frac{\partial \sigma_{ei}}{\partial \mathbf{p}_1} A(\mathbf{p}, \mathbf{p}_1), \quad (2.21)$$

In terms of the scattering angle  $\cos \theta_s = \mathbf{p}_1 \cdot \mathbf{p} / p_1 p$  we obtain the explicit expressions

$$\begin{aligned}\nu_s &= \frac{1}{p^2} \langle p^2 - p_1 p \cos \theta_s - \frac{1}{2} p_1^2 \sin^2 \theta_s \rangle + \frac{1}{2p^2} \frac{\partial}{\partial p} [p \langle (p - p_1 \cos \theta_s)^2 \rangle], \\ \nu_D &= \frac{1}{2p^2} \langle p_1^2 \sin^2 \theta_s \rangle, \\ \nu_{\parallel} &= \frac{1}{2p^2} \langle (p - p_1 \cos \theta_s)^2 \rangle.\end{aligned}\quad (2.22)$$

If we then write  $p_1 = p(1 - \epsilon)$  and expand to second order in  $\theta_s$ , we find

$$\begin{aligned}\nu_s &= \langle \epsilon - \frac{1}{4} \epsilon^2 \theta_s^2 \rangle + \frac{1}{2p^2} \frac{\partial}{\partial p} [p^3 \langle \epsilon^2 + \theta_s^2 \epsilon (1 - \epsilon) \rangle] \\ \nu_D &= \frac{1}{2} \langle (1 - \epsilon)^2 \theta_s^2 \rangle, \\ \nu_{\parallel} &= \frac{1}{2} \langle \epsilon^2 + \theta_s^2 \epsilon (1 - \epsilon) \rangle.\end{aligned}\quad (2.23)$$

Since the Fokker-Planck operator was obtained in the first place as a second-order expansion in  $\Delta\mathbf{p}$ , we can consistently neglect terms which are cubic or higher in  $\epsilon$  and  $\theta_s$ , which finally yields the general Fokker-Planck coefficients for an arbitrary binary interaction with stationary

targets (elastic as well as inelastic),

$$\nu_s = \frac{1}{p} \langle p - p_1 \rangle + \frac{1}{2p^2} \frac{\partial}{\partial p} \left[ p \langle (p - p_1)^2 \rangle \right],$$

$$\nu_D = \langle 1 - \cos \theta_s \rangle, \quad (2.24)$$

$$\nu_{\parallel} = \frac{1}{2p^2} \langle (p - p_1)^2 \rangle. \quad (2.25)$$

We discover that the parallel diffusion frequency  $\nu_{\parallel}$  is a higher-order term in the expansion than  $\nu_s$  and will therefore tend to be negligible, since the validity of the equation requires small momentum transfers to dominate. In that case, we may approximate  $\langle (p - p_1)^2 \rangle \approx 0$ . At highly relativistic speeds, we then see that  $\nu_s = \langle p - p_1 \rangle / p \approx \langle \gamma - \gamma_1 \rangle m_e c^2 / (vp)$  with a relative error of order  $1/\gamma^2$ . In that case, the dynamical friction  $F$  is given by

$$F = p \nu_s = \frac{1}{v} \langle m_e c^2 (\gamma - \gamma_1) \rangle = n \int d\sigma m_e c^2 (\gamma - \gamma_1) \equiv - \frac{\partial E}{\partial x} \Big|_{\text{stopping}}$$

equalling the stopping power of the interaction. In fact, with this form of  $\nu_s$ , the energy moment of the Fokker-Planck operator coincides exactly with that of the original Boltzmann operator even for non-relativistic speeds, as well as having the exact transport cross section (i.e. the  $(1 - \cos \theta)$ -moment) thanks to the form of  $\nu_D$ . We therefore propose the following Fokker-Planck coefficients to describe binary interactions with stationary targets which are dominated by small momentum transfers:

$$\begin{aligned} \nu_s &= \frac{m_e c^2}{vp} \langle \gamma - \gamma_1 \rangle, \\ \nu_D &= \langle 1 - \cos \theta_s \rangle, \\ \nu_{\parallel} &= 0. \end{aligned} \quad (2.26)$$

Note that this model is only meant to describe the dynamics of the already-generated runaway electrons; to describe the generation of the seed population, in particular Dreicer generation, the non-vanishing speeds of the thermal population must be kept, which will lead (among other things) to a non-negligible energy-diffusion coefficient.

## 2.4 Effects of screening on the collision operator

Using the general Fokker-Planck equation derived in the previous section, given by Eqs. (2.19) and (2.26), we will now describe the collision

## 2.4. EFFECTS OF SCREENING ON THE COLLISION OPERATOR

model that we propose in Paper E to model collisions between fast electrons and partially ionized ions. This requires us to calculate the collision frequencies  $\nu_D$  and  $\nu_s$ ; unlike the regular Landau-Fokker-Planck equation where these are evaluated for a pure Coulomb interaction, they must now account for the screening effect of the bound electrons as well as the effect of ionizing collisions.

The determination of the slowing-down frequency  $\nu_s$  is in practice the simpler task, as it only requires knowledge of the collisional stopping power. This is well known for an electron passing through a medium, and is described by the Bethe formula [71], yielding

$$\nu_s = \frac{e^4}{4\pi\epsilon_0^2 m_e c^2} \frac{c^2}{pv^2} \sum_j n_j \left[ Z_{0j} \ln \Lambda + N_{ej} \left( \ln \frac{cp\sqrt{\gamma-1}}{I_j} - \frac{v^2}{c^2} \right) \right]. \quad (2.27)$$

Here, the sum is taken over all ion species  $j$  (where different charge states are considered different species),  $Z_j$  denotes the atomic number,  $Z_{0j}$  the charge number (i.e. the net charge of the ion) and  $N_{ej} = Z_j - Z_{0j}$  the number of bound electrons. Then, the slowing-down frequency is completely determined for any ion species  $j$  in terms of the three parameters  $Z_j$ ,  $Z_{0j}$  and the mean-excitation energy  $I_j$ , which must be determined experimentally or by comprehensive atomic simulations. In our work we have used tabulated values from Sauer *et al.* [72] which have been given for all ionization degrees of some ion species, including the experimentally relevant argon and neon. The first term of the sum in Eq. (2.27) represents the contribution to the slowing-down frequency from elastic collisions with the free electrons, which can be treated as usual with the ideal theory yielding the familiar Coulomb logarithm  $\ln \Lambda$ .

In the determination of the deflection frequency  $\nu_D$ , contributions will be obtained both from elastic collisions with the ion where its internal state does not change (which do not contribute significantly to  $\nu_s$  since  $\gamma - \gamma_1$  in such reactions is of the order of the mass ratio  $m_e/m_i \ll 1$ ) as well as the inelastic collisions where the bound electrons are excited or ionized. In this case the elastic collisions provide the dominant contribution to  $\nu_D$ , since the associated cross-section is of the order of  $Z_j^2 r_0^2$ . Conversely, the inelastic collisions – consisting mainly of incoherent interactions with individual bound electrons – scale as  $(Z_j - Z_{0j}) r_0^2$ , and also tend to be more strongly peaked in the forward direction than the elastic collisions [73]. Therefore, for the highly charged ion species ( $Z_j \gg 1$ ) in which we are primarily interested, such as neon and argon, the contribution is obtained by evaluating  $\langle 1 - \cos \theta \rangle$  using only the dominant

elastic scattering cross-section.

In the Born approximation, the elastic differential cross section is given by

$$d\sigma_j = |Z_j - F_j(\mathbf{p}_1 - \mathbf{p})|^2 d\sigma_0, \quad (2.28)$$

where  $d\sigma_0$  is the electron-proton differential cross-section, given in the lab-frame by [62]

$$\frac{\partial\sigma_0}{\partial\cos\theta} = \frac{\pi r_0^2}{2(p/m_ec)^4} \frac{1 + (p/m_ec)^2 \cos^2(\theta/2)}{\sin^4(\theta/2)}. \quad (2.29)$$

The *atomic form factor*  $F_j$ , which completely describes the screening effect of the bound electrons, is given by

$$F_j(\mathbf{p}_1 - \mathbf{p}) = \int n_j(\mathbf{x}) \exp\left[\frac{i}{\hbar} \mathbf{x} \cdot (\mathbf{p}_1 - \mathbf{p})\right] d\mathbf{x}, \quad (2.30)$$

where  $n_j(\mathbf{x})$  is the number density of the bound electrons of ion species  $j$ , normalized such that  $\int n_j(\mathbf{x}) d\mathbf{x} = N_{ej} = Z_j - Z_{0j}$  is the number of bound electrons, and the integration is taken over all space. For a spherically symmetric bound-electron density  $n_j = n_j(r)$ , it is found that the form factor only depends on the magnitude  $q = |\mathbf{p}_1 - \mathbf{p}| = 2p \sin(\theta_s/2)$  of the momentum transfer;

$$F_j(q) = \frac{4\pi}{q} \int_0^\infty dr r n_j(r) \sin qr. \quad (2.31)$$

The contribution to the deflection frequency from a single ion species is then given by

$$\begin{aligned} \nu_{Dj} &= 2n_j v \int d\sigma_0 \sin^2 \frac{\theta_s}{2} |Z_j - F_j(q)|^2 \\ &= 4\pi r_0^2 n_j c \frac{\gamma}{(p/m_ec)^3} \int_{1/\Lambda}^1 dx \frac{1 - x^2 v^2/c^2}{x} |Z_j - F_j(2px)|^2, \end{aligned} \quad (2.32)$$

where  $x = \sin(\theta_s/2)$ , and the integral is taken from the minimum scattering angle  $\theta_{s,\min} = 2/\Lambda \ll 1$  corresponding to Debye-length interaction distances. In Paper E, we show that in the high-energy limit  $p \gg \hbar/a_0$  where  $a_0$  is the Bohr radius (i.e. approximately the size of the ion), the diffusion coefficient takes the explicit form

$$\nu_D = \frac{4\pi c r_0^2 \gamma}{(p/m_ec)^3} \sum_j n_j \left[ Z_j^2 \ln \Lambda + (Z_j^2 - Z_{0j}^2) \ln \left( \frac{pa_j}{\hbar} \right) - \frac{2}{3} (Z_j - Z_{0j})^2 \right], \quad (2.33)$$

where the ion properties are again completely captured by three parameters  $Z_j$ ,  $Z_{0j}$  as well as the new parameter  $a_j$  which defines an effective ion radius given by an integral over the bound-electron density  $n_j(r)$ . In Paper E we have tabulated values for  $a_j$  for He, Be, C, N, Ne, Ar, Xe and W, where  $n_j$  was determined through density-functional-theoretical calculations using the tools EXCITING [74] and GAUSSIAN [75]. To give an indication of the magnitude of the effective ion radii, a few explicit values normalized to the Bohr radius as produced by the simulations are:  $a_j/a_0 \approx 0.81$  for neutral neon Ne; 0.70 for neutral argon Ar; and 0.32 for  $\text{Ar}^{+9}$ .

From the above expressions for  $\nu_s$  and  $\nu_D$ , we find that the modifications to the Fokker-Planck coefficients are sensitive to the runaway energy. In the low-energy limit, the completely screened situation is retrieved where the electrons only sense the net charge of the ions; however, significant departures are demonstrated already at runaway energies exceeding 100 eV. For characteristic runaway energies in the 10 MeV range, and for high- $Z$  impurities of low ionization degree, the pitch-angle deflection rate is typically reduced to approximately 60% of its non-screened value, and the dynamical friction typically by 20-30%. At lower energies of  $\sim 1$  MeV, the screening effect tends to be of the order of 70% and 50% for deflection and friction, respectively.

## 2.5 CODE

An approximate Fokker-Planck collision operator to study runaway electrons was developed in Ref. [76]. It is an asymptotic matching of the linearized Beliaev-Budker operator (2.18) in the high-energy limit with the non-relativistic collision operator [58, 77] (corresponding to Eq. (2.18) for  $v \ll c$ , linearized with a cold bulk of thermal velocity  $v_{Te} = \sqrt{2T_e/m_e} \ll c$ ). The operator is, in terms of Eq. (2.19), given by

$$\begin{aligned} A(p) &= \frac{m_e^2 c^2}{\tau_c} \frac{c}{vp} G\left(\frac{v}{v_{Te}}\right), \\ \nu_s(p) &= \frac{2}{p} \frac{m_e c}{\tau_c} \frac{c^2}{v_{Te}^2} G\left(\frac{v}{v_{Te}}\right), \\ \nu_D(p) &= \frac{m_e^2 c^2}{\tau_c} \frac{c}{v} \left[ Z_{\text{eff}} + \phi\left(\frac{v}{v_{Te}}\right) - G\left(\frac{v}{v_{Te}}\right) + \frac{1}{2} \frac{v_{Te}^2}{c^2} \frac{v^2}{c^2} \right]. \end{aligned}$$

Here we have introduced the error function  $\phi(x) = 2\pi^{-1/2} \int_0^x ds \exp(-s^2)$  and the Chandrasekhar function  $G(x) = (\phi(x) - x\phi'(x))/2x^2$ . A term

proportional to the plasma effective charge  $Z_{\text{eff}} = \sum_i n_i Z_i^2 / n_e$  (the sum taken over all ion species in the plasma) has been added to the pitch-angle scattering operator coefficient, which corresponds to the contribution from ions in the plasma, taken to be stationary. This collision operator was implemented in the numerical tool CODE [78], with more recent improvements to the model described in Paper L. CODE obtains solutions to the kinetic equation (2.3) treated as an initial-value problem, but has been extended during this thesis with additional terms to describe the effect of synchrotron and bremsstrahlung losses as well as of large-angle collisions. By representing the distribution function in terms of Legendre polynomials in pitch-angle cosine and a finite-difference discretization of the momentum coordinate, a flexible and computationally efficient scheme is obtained. The model contains the essential physics needed in order to study a wide range of momentum-space runaway dynamics, making it highly suited for studies such as those presented in this thesis.

A separate numerical tool, NORSE (NOn-linear Relativistic Solver for Electrons), has also been developed which solves the electron kinetic equation using the full non-linear relativistic Fokker-Planck equation (2.18). The tool is presented in Paper N, and is also freely available to download<sup>1</sup>. The method must be used whenever the deviations from a local Maxwellian distribution are large; this may for example be the case when the runaway population is comparable in number to the thermal population, or when the thermal energy of the distribution varies on a time-scale comparable to the collision time. The latter may be important during the thermal-quench phase of a disruption, and non-linear effects could plausibly have an influence on hot-tail runaway generation. A case study of the former situation was analyzed in Paper M, where NORSE was applied to investigate slide-away runaway generation in a post-disruption plasma.

---

<sup>1</sup>Original published version available at <http://doi.org/10.17632/86wmqj758w.1>, with an updated version at <https://github.com/hoppe93/NORSE>.



## Chapter 3

# Radiation emitted by runaway electrons

Radiation is essential in order to understand electron runaway. When electrons emit radiation, they transfer a fraction of their kinetic energy to the electromagnetic field. This affects their phase-space dynamics, and radiation losses can for example limit the maximum energy achievable in a given accelerating electric field, where the dominant energy-loss channels are through synchrotron radiation as well as bremsstrahlung. In the classical theory of radiation reaction [79, 80, 81], it is assumed that a charged particle undergoes smooth accelerated motion. Maxwell's equations for a point source then yields the rate at which momentum is gained by the electromagnetic field; by imposing the conservation of momentum, this yields an associated average radiation reaction force experienced by the particle which is given by the Abraham-Lorentz-Dirac force

$$\mathbf{F}_{\text{ALD}} = \frac{e^2 \gamma^2}{6\pi \varepsilon c^3} \left[ \ddot{\mathbf{v}} + \frac{3\gamma^2}{c^2} (\mathbf{v} \cdot \dot{\mathbf{v}}) \dot{\mathbf{v}} + \frac{\gamma^2}{c^2} \left( \mathbf{v} \cdot \ddot{\mathbf{v}} + \frac{3\gamma^2}{c^2} (\mathbf{v} \cdot \dot{\mathbf{v}})^2 \right) \mathbf{v} \right]. \quad (3.1)$$

For runaways in magnetized plasmas, this force tends to be dominated by the synchrotron radiation reaction due to the rapid gyration of the electrons at the cyclotron frequency  $\Omega_B = eB/(\gamma m_e)$  [82]. The effects on runaways of including the synchrotron-reaction force in the kinetic equation is explored in-depth in Papers G, H, I and K. In particular, Paper I includes the full guiding-center transformation to first order of the ALD force for energetic electrons in magnetized plasmas.

Radiation is also one of few ways in which a runaway beam can be passively diagnosed, since it is typically emitted at such short wave-

lengths that the plasma is optically thin to this radiation; particularly in tokamaks is this generally the case. Observation of the emission provides insight into the runaway distribution function, which allows the validity of runaway models to be assessed.

### 3.1 Bremsstrahlung radiation reaction

When charged particles collide, the resulting emission is referred to as *bremsstrahlung* (German for “braking radiation”, as it causes the particles to decelerate) [83, 84]. Unlike synchrotron radiation, as discussed above, the bremsstrahlung emission is not emitted due to smooth macroscopic motion, but rather in bursts during the brief microscopic interactions of runaways colliding with the background plasma. As such, a statistical approach can be taken where we consider only the *total momentum*  $\mathbf{k}$  lost to the electromagnetic field in each collision (in the classical picture corresponding to the time-integrated radiation reaction force), and consider the differential cross-section  $\partial\sigma_{\text{br},j}/\partial\mathbf{p}$  for runaways of momentum  $\mathbf{p}_1$  incident on a target of species  $j$  to end up with momentum  $\mathbf{p}$  after the collision. Then, since the microscopic interactions are dominated by binary collisions, the bremsstrahlung radiation reaction is governed by a Boltzmann collision operator of the form given in Eq. (2.5), which for stationary targets is given by

$$C_{\text{br}} = \sum_j n_j \int d\mathbf{p}_1 v_1 f_e(\mathbf{p}_1) \frac{\partial\sigma_{\text{br},j}(\mathbf{p}; \mathbf{p}_1)}{\partial\mathbf{p}} - v f_e(\mathbf{p}) \sum_j n_j \sigma_{\text{br},j}(\mathbf{p}). \quad (3.2)$$

In the classical theory of bremsstrahlung one finds that the frequency  $\omega$  of the bremsstrahlung radiation becomes large enough that the total energy  $c|\mathbf{k}|$  emitted in individual collisions becomes comparable to the photon energy  $\hbar\omega$  [83]. Hence the classical theory breaks down, and only quantum theory can describe the bremsstrahlung process. The differential cross-section  $\partial\sigma_{\text{br},j}/\partial\mathbf{p}$  was given for interactions with stationary ions in the Born approximation in Refs. [85, 86]. From the differential cross-section it is found that relativistic electrons on average lose a significant fraction of their kinetic energy in each bremsstrahlung emission, indicating that a Fokker-Planck equation for bremsstrahlung losses is inadequate. We reproduce the dominant single-photon bremsstrahlung

differential cross section given in Ref. [86], which can be written as

$$\begin{aligned} \frac{\partial \bar{\sigma}_{ab}}{\partial \mathbf{p}} &= Z_b^2 \alpha r_0^2 \frac{2k}{p_1 \gamma} W(p; p_1, \cos \theta_s) \\ W(p; p_1, \cos \theta_s) &= \frac{2\gamma_1 \gamma + (\gamma_1^2 + \gamma^2 - 1)\lambda - \lambda^2}{k^2 \lambda^2 \sqrt{\lambda(\lambda + 2)}} \ln \left( 1 + \lambda + \sqrt{\lambda(\lambda + 2)} \right) \\ &\quad - \frac{2\gamma_1 \gamma - \lambda}{k^2 \lambda^2} - \frac{3(\gamma_1^2 \gamma^2 - 1)^2}{\lambda^2 p_1^4 p^4} \\ &\quad + \frac{4(\gamma_1^2 \gamma^2 - \gamma_1 \gamma + 1) - \gamma_1 \gamma (p_1^2 + p^2) + (\gamma_1^2 + \gamma^2 + \gamma_1 \gamma - 1)\lambda}{2\lambda^2 p_1^2 p^2} \\ &\quad + \left( 2 \frac{\gamma_1 \gamma - 1}{\lambda^3} - \frac{k^2}{\lambda^4} \right) \frac{2(\gamma_1^2 + \gamma^2 - \gamma_1 \gamma) p_1^2 p^2 + 3k^2 (\gamma_1 + \gamma)^2}{p_1^4 p^4} \\ &\quad + \frac{l}{p^3} \left[ \frac{\gamma + 2\gamma^3}{\lambda^2 p^2} + \frac{2\gamma^4 + 2p_1^2 p^2 + \gamma_1(\gamma_1 + \gamma) - (\gamma_1 \gamma + p^2)\lambda}{2k \lambda^2} \right. \\ &\quad \left. + \gamma \left( 2 \frac{\gamma_1 \gamma - 1}{\lambda^3} - \frac{k^2}{\lambda^4} \right) \frac{2\gamma_1 p^2 - 3k\gamma^2}{kp^2} \right] \\ &\quad + \frac{l_1}{p_1^3} \left[ \frac{\gamma_1 + 2\gamma_1^3}{\lambda^2 p_1^2} - \frac{2\gamma_1^4 + 2p_1^2 p^2 + \gamma(\gamma_1 + \gamma) - (\gamma_1 \gamma + p_1^2)\lambda}{2k \lambda^2} \right. \\ &\quad \left. - \gamma_1 \left( 2 \frac{\gamma_1 \gamma - 1}{\lambda^3} - \frac{k^2}{\lambda^4} \right) \frac{2\gamma p_1^2 + 3k\gamma_1^2}{kp_1^2} \right]. \end{aligned} \quad (3.3)$$

In the expression for  $W$ , the electron momenta  $p_1$  and  $p$ , and photon momentum  $k$ , have been normalized to  $m_e c$  for clarity. The fine-structure constant is denoted  $\alpha = e^2/(4\pi \varepsilon_0 \hbar c) \approx 1/137$ , and  $r_0 = e^2/(4\pi \varepsilon_0 m_e c^2) \approx 2.8 \cdot 10^{-15}$  m is again the classical electron radius. We have also introduced the auxiliary quantities

$$\begin{aligned} l &= \ln(\gamma + p), \\ l_1 &= \ln(\gamma_1 + p_1), \\ \lambda &= \gamma_1 \gamma - p_1 p \cos \theta_s - 1, \end{aligned}$$

where the full angular dependence of the cross-section is captured in  $\lambda$ .

In the context of runaway in magnetic-fusion plasmas, the effects of bremsstrahlung losses have been studied within the approximation that runaways experience only the mean force [87, 88, 89]

$$\mathbf{F}_{\text{br}}(\mathbf{p}) = -\hat{v} \sum_j n_j c \int_0^{\gamma-1} (kc) \frac{\partial \sigma_{\text{br},j}}{\partial k} dk, \quad (3.4)$$

where  $\partial\sigma_{\text{br},j}/\partial k$  is the cross-section for a photon of energy  $k$  to be emitted, and describes the average energy loss in the sense that

$$\int d\mathbf{p} m_e c^2 (\gamma - 1) C_{\text{br}}(\mathbf{p}) = \int \mathbf{v} \cdot \mathbf{F}_{\text{br}}(\mathbf{p}) f_e(\mathbf{p}) d\mathbf{p}. \quad (3.5)$$

The model is equivalent to using the Fokker-Planck operator (2.19) with coefficients (2.26) to describe the bremsstrahlung reaction, taking  $\nu_D = 0$ . In these studies it was found that bremsstrahlung emission could play an important role in limiting the maximum achievable energy for a runaway being accelerated in an electric field near the threshold value  $E_c$ . It was found to be particularly important for high plasma charge  $Z$  [88], and also that its relative importance compared to synchrotron loss increases with density [87]. It was concluded that in a range of typical tokamak disruption scenarios, bremsstrahlung losses would play an important role in limiting the runaway kinetic energy.

In Paper B, we extend the model used in previous studies of bremsstrahlung emission during electron runaway to utilize the full statistical description of Eq. (3.2) for the bremsstrahlung energy loss. In the mean-force picture of the previous studies, for a given accelerating electric field there will be a well-defined kinetic energy above which the bremsstrahlung radiation loss will exceed the force due to the electric field, thus setting a sharp upper boundary for the runaway energy. Conversely, in the statistical description there is a non-zero probability that a runaway will be accelerated for an arbitrarily long time before emitting a photon in a bremsstrahlung reaction. One could thus expect that the energy distribution of runaways exhibits a tail that extends beyond the critical energy where the *average* energy loss balances the electric field. Indeed, this behavior was found in Paper B from numerical solutions of the kinetic equation; a main result of the study is that in the statistical model using a Boltzmann operator, approximately 10% of the total runaway kinetic energy in steady state is carried by electrons with energy at least 80% higher than the theoretical prediction in the mean-force model.

Paper B also explores the pitch-angle deflection of fast electrons during bremsstrahlung emission. In the study, we found that this effect can generally be neglected for those reactions where the photon energy is comparable to the electron energy, which are responsible for the majority of the total energy loss. However, the contribution to pitch-angle scattering is found to increase rapidly as the photon energy approaches zero, and the total bremsstrahlung-assisted pitch angle scattering rate can become significant compared to ordinary (elastic) collisional pitch

angle scattering for fast electrons with energy in the GeV range. For runaways, which are generally in the 10-100 MeV energy range, the effect tends to be minor.

### 3.2 Synthetic radiation diagnostic

On the other side of the coin is the question of the characteristics of the emitted radiation. Interpreting the synchrotron and bremsstrahlung radiation emitted by a plasma containing runaways is the most promising method of probing the runaway phase-space distribution. For example, in contrast, the runaway current depends only on the average runaway velocity, which tends to be at the speed of light aligned with the magnetic field, and is largely insensitive to the runaway energies. Inferring the runaway distribution from the emitted radiation is complicated by the fact that only line-integrated measurements can be performed, and that different combinations of energy and pitch can often produce relatively similar emission. This can be particularly challenging when only parts of the spectrum are measured, such as when using a camera sensitive to emission in the visible range to detect synchrotron emission which tends to be the strongest in the infra-red range during runaway in tokamaks.

There are many examples in the literature of runaway distributions that have been inferred from experimental observations of radiation emitted in plasmas where runaway acceleration was believed to occur. In Refs. [90, 91] the bremsstrahlung emission of a runaway beam was observed in the DIII-D tokamak with temporal, angular and spectral resolution. From these measurements, imposing a set of simplifying assumptions, runaway energy spectra were reconstructed which were qualitatively consistent with a runaway model similar to the ones employed in this thesis. The energy reconstruction reveals an anomaly, however, where the experimentally observed runaways appear to have significantly lower maximum energies than can be understood in a spatially-homogeneous description. This finding is consistent with other reconstructions that have been made, such as in Ref. [92] where a reconstruction was performed using combined radiation diagnostics in a DIII-D post-disruption plasma. Recent analysis of camera images in the EAST tokamak, which are assumed to show the synchrotron emission of runaways due to the asymmetric pattern, has been used to infer the radial distribution of the runaway population, as well as its characteristic energy and pitch [93].

We shall now introduce a synthetic diagnostics method which predicts the emission that a detector would observe due to a runaway population in tokamaks. Formally, the spectral radiance (dimension  $W/(m^2 \text{ st Hz})$ ) reaching a detector placed at a location  $\mathbf{x}_0$ ; facing a direction  $\mathbf{n}_0$ ; along the line-of-sight described by a unit vector  $\mathbf{n}$  and parametrized by a solid angle  $\Omega_n$ ; and at a frequency  $\omega$ , can for an optically thin plasma be written in terms of the received power  $P$  as [94]

$$\frac{\partial P}{\partial A \partial \Omega_n \partial \omega} = \int d\mathbf{x} d\mathbf{p} \frac{\mathbf{n} \cdot \mathbf{n}_0}{|\mathbf{x} - \mathbf{x}_0|^2} \delta \left( \frac{\mathbf{x} - \mathbf{x}_0}{|\mathbf{x} - \mathbf{x}_0|} - \mathbf{n} \right) \frac{\partial P(\mathbf{x}, \mathbf{p}, \mathbf{n})}{\partial \Omega \partial \omega} f_e(\mathbf{x}, \mathbf{p}), \quad (3.6)$$

where  $\partial P / \partial \Omega \partial \omega$  is the differential received power due to a fast electron at the location  $(\mathbf{x}, \mathbf{p})$ .

In Paper F, the synthetic diagnostic SOFT (Synchrotron-detecting Orbit Following Toolkit) is presented which evaluates this integral with  $\partial P / \partial \Omega \partial \omega$  appropriately chosen to describe synchrotron radiation, which has later been generalized to also allow bremsstrahlung emission to be modeled (Paper P). The method is specialized to magnetized toroidal systems that vary on a time-scale much longer than the transit time scale ( $\tau \gg L/c \sim 10 \text{ ns}$  for runaways, where  $L$  indicates the system dimension). In that case, the distribution function can be fully described in terms of one spatial coordinate and two momentum coordinates. The dependence on one momentum coordinate, the gyroangle, vanishes in a magnetized plasma due to the rapid gyromotion; one spatial coordinate vanishes due to Liouville's theorem stating that for Hamiltonian motion the distribution function is constant along phase-space particle trajectories; and the final spatial coordinate, the toroidal angle, vanishes by the assumed symmetry. The resulting integral can be written

$$\frac{\partial P}{\partial A \partial \Omega_n \partial \omega} = \int dx_1 dp_1 dp_2 f_e(x_1, p_1, p_2) K(x_1, p_1, p_2; \mathbf{x}_0, \mathbf{n}_0, \mathbf{n}, \omega), \quad (3.7)$$

where  $x_1$ ,  $p_1$  and  $p_2$  are suitable guiding-center phase space coordinates describing the distribution function  $f_e$ ; the kernel function  $K$ , which SOFT calculates, provides a complete description of the emission that a detector can observe from any runaway population.

Additional insight into the observed emission from runaways can be gained by noting that for high energies, due to the relativistic-beaming effect, the emission is narrowly focused along the particle direction of

motion, and one obtains

$$\frac{\partial P}{\partial \Omega \partial \omega} \rightarrow \delta \left( \frac{\mathbf{p}}{p} + \mathbf{n} \right) \frac{\partial P}{\partial \omega}. \quad (3.8)$$

When this expression is averaged over the electron gyroangle  $\varphi$ , one obtains

$$\frac{1}{2\pi} \int_0^{2\pi} d\varphi \frac{\partial P}{\partial \Omega \partial \omega} = \delta \left( \cos \theta - \hat{V} \cdot \mathbf{n} \right) \frac{\partial P}{\partial \omega}, \quad (3.9)$$

where  $\hat{V}$  is the unit vector representing the guiding-center direction of motion. This means that emission can only be detected while the condition

$$\cos \theta = \hat{V} \cdot \mathbf{n} = \hat{V}(\mathbf{B}(\mathbf{x}), \nabla \mathbf{B}(\mathbf{x}), p, \theta) \cdot \frac{\mathbf{x} - \mathbf{x}_0}{|\mathbf{x} - \mathbf{x}_0|} \quad (3.10)$$

is satisfied, where the guiding-center velocity  $\mathbf{V}$  depends on the local magnetic field (and its gradients) and the electron momentum. Due to the conservation of magnetic moment along trajectories, the pitch-angle  $\theta = \theta(\mathbf{x})$  will also be a function of location. The solution of this equation for  $\mathbf{x}$  – given a magnetic field, detector location, particle energy and magnetic moment – represents a two-dimensional surface which we refer to as the *surface-of-visibility* (SoV); only when runaways cross this surface will they contribute observable emission, and so the SoV can explain roughly the shape of synchrotron emission spots observed by cameras in tokamaks. These synchrotron spot shapes have been previously studied in Ref. [93], using a method outlined in Ref. [95] to obtain them.

Within the observed spot, we can identify two main effects which determine the intensity variations:

- (i) The variation of the emitted intensity  $\partial P / \partial \omega$  across the plasma. For synchrotron radiation this depends strongly on the local magnetic-field strength, which is approximately inversely proportional to the major radius. This generally causes enhanced observed emission from the high-field-side of the device. For detectors which only observe the low-frequency tail of the emitted spectrum, this effect is so strong that the observed spot shape is completely altered.
- (ii) The geometrical effect, by which we mean the combination of the geometry of the magnetic field (or of the runaway trajectories), of the detector (location and shape) and of the angular distribution of

radiation. These have an effect that can be understood in terms of the *time along the runaway trajectory* that the surface-of-visibility condition is satisfied for a finite-extent camera. This can vary dramatically across the spot, and often takes a sharp maximum along the edge of the SoV (where runaways move tangentially to the surface) where orders-of-magnitude stronger detected intensities may be observed.

In particular the geometrical effect has been out of reach of previous studies of the synchrotron emission from runaways – which considered mainly spot shapes or total emission [96] – but is demonstrated to be essential in order to understand runaway images. It must, however, be stressed that the SoV is strongly dependent on the runaway momentum (especially the pitch angle, which enters explicitly into the SoV equation), and hence a complete image resulting from a distribution of runaways would be the superposition of contributions from various different surfaces-of-visibility. This reveals patterns that are often not evident from studying individual SoVs, thereby illustrating that a complete synthetic-diagnostic simulation (using e.g. SOFT) is generally required in order to predict the observed pattern.

# Chapter 4

## Runaway of positively charged species

In previous chapters of this thesis we have focused on electron runaway. In Papers C and D, however, we consider the runaway of positively charged particle species in plasmas. Although the fundamental runaway mechanism is shared with electrons, being essentially a competition between the accelerating force and collisional friction, there are differences which alter the picture.

### 4.1 Positron runaway

In Paper C we consider the runaway of positrons. These are typically generated during runaway scenarios by interactions between the thermal background plasma and the ultra-relativistic runaway electrons [97], whose energies in the 10-100 MeV range far exceed the pair-production threshold of  $2m_e c^2 \approx 1$  MeV. The defining feature of positron runaway, which sets it apart from regular electron runaway, is not their annihilation – which often occurs on time-scales longer than the runaway discharge lasts – but rather that they tend to be created moving in the direction opposite to that of their acceleration. Positrons produced in collisions of ultra-relativistic runaways will tend to be co-moving with the incident electrons, which are in turn moving predominantly antiparallel to the electric field due to their negative charge. Consequently, newly created pairs are moving antiparallel to the electric field, but the positrons will be accelerated along the field. This means that they will initially be slowed down by the electric field, and only a fraction will have

scattered to sufficiently large momenta perpendicular to the electric field that they will not thermalize before reaching the runaway region.

A common feature of many of the studies presented in this thesis is the role of large-angle collisions, and positron runaway is no exception. The creation of positrons in collisions between runaways and background ions is again given by a form of Eq. (2.5):

$$S_{\text{pos}}(\mathbf{p}) = \sum_j n_j \int d\mathbf{p}_1 v_1 f_e(\mathbf{p}_1) \frac{\partial \sigma_{\text{pos},j}(\mathbf{p}; \mathbf{p}_1)}{\partial \mathbf{p}}, \quad (4.1)$$

which describes the rate of creation of positrons at momentum  $\mathbf{p}$ , where  $\sigma_{\text{pos},j}$  is the cross-section for positron generation in the interaction between a runaway electron of momentum  $\mathbf{p}_1$  and a stationary target particle of species  $j$ . Note that the term depends only on the runaway-electron population, and not the positron distribution itself. For highly energetic electrons  $p_1 \gg m_e c$ , the cross section is sharply peaked for  $\mathbf{p}$  parallel to  $\mathbf{p}_1$ , and one may approximate

$$\frac{\partial \sigma_{\text{pos},j}(\mathbf{p}; \mathbf{p}_1)}{\partial \mathbf{p}} = \frac{\delta\left(1 - \frac{\mathbf{p}_1 \cdot \mathbf{p}}{p_1 p}\right)}{2\pi p \gamma m_e^2 c^2} \frac{\partial \sigma_{\text{pos},j}(p, p_1)}{\partial \gamma}, \quad (4.2)$$

where the problem is reduced to finding the cross-section differential in the outgoing positron energies  $\partial \sigma_{\text{pos},j}(p, p_1) / \partial \gamma$ . However, with collisional pair production being a second-order process in quantum electrodynamics, no closed-form expressions for the cross-section are available in the published literature to the author's knowledge. Instead, we have opted to use the numerical tool MadGraph 5 [98] to provide the differential cross sections. We point out that a numerically-fitted total cross-section formula given by Gryaznykh [99] – which has been used in a number of previous studies of positron runaway – disagrees with the MadGraph 5 calculation by a nearly constant factor of four. Since the MadGraph output agrees with the analytical high-energy limit given in Appendix F of Ref. [100] within 5% for all electron energies above 100 MeV, we deem it likely that there is an error in the calculation of Ref. [99]. Consequently, previous studies have overestimated the collisional pair production of positrons by approximately a factor of four.

The annihilation of positrons, on the other hand, is given by

$$S_{\text{an}}(\mathbf{p}) = -v f_{\text{pos}}(\mathbf{p}) \sigma_{\text{an}}(\mathbf{p}) \quad (4.3)$$

where  $\sigma_{\text{an}}$  is the total annihilation cross section for a positron of momentum  $\mathbf{p}$ . In a fully ionized plasma, it is given by the free-free two-quanta annihilation cross section [62]

$$\sigma(\mathbf{p}) = \frac{\pi r_0^2}{\gamma + 1} \left[ \frac{\gamma^2 + 4\gamma + 1}{\gamma^2 - 1} \ln(\gamma + \sqrt{\gamma^2 - 1}) - \frac{\gamma + 3}{\sqrt{\gamma^2 - 1}} \right]. \quad (4.4)$$

For positron energies much greater than the rest energy,  $\gamma \gg 1$ , it is a decreasing function of energy  $\sigma_{\text{an}} \sim \pi r_0^2 (\ln 2\gamma - 1)/\gamma$ , hence the mean life time  $1/(nc\sigma_{\text{an}})$  tends to be much longer than for example the avalanche time which is of the order of  $[2\pi n r_0^2 c(E/E_c - 1)]^{-1}$ .

In Paper C, we discovered that the fraction of created positrons that end up running away is highly sensitive to the electric-field strength, but relatively insensitive to the plasma charge. For example, at  $E = 2E_c$  the runaway fraction was approximately 20%, whereas at  $10E_c$  it reaches 60-80%. We also analyzed the possibility to measure the annihilation radiation that is emitted by the positrons that are slowed down instead of becoming runaway accelerated. Since this emission is strongly peaked around the distinct photon energy of 511 keV, there is hope that this annihilation radiation can be distinguished from the X-ray emission from the runaway electrons. We found that a fine energy resolution is required from a HXR spectrometer for this to be possible: if a peak in the photon-energy spectrum narrower than 1 keV can be resolved, it could be feasible to observe the runaway-created positrons in an ideal scenario. If this resolution requirement is not met, coincidence-measurement techniques may be employed to improve the signal-to-noise ratio [101].

## 4.2 Ion runaway

In Paper D we have studied the runaway of ion species present in the plasma. The defining feature here is the large mass of the runaway ions, where even strongly superthermal ions tend to be slower than the thermal electrons. The result is a dynamical friction force which does not decrease monotonically for speeds above the thermal, but instead grows as the ion speed approaches the thermal electron speed. This leads to runaway ions not actually running away; they will instead be accelerated towards some equilibrium speed. However, since the generation of these superthermal ions by strong electric fields is very similar to the electron runaway process, they are referred to as runaway ions.

The presence of a much lighter species in the plasma – the electrons – sets the ion runaway process apart from electron and positron runaway. The kinetic equation for an ion species  $i$  is given by

$$\frac{\partial f_i}{\partial t} + \frac{eZ_i}{m_i} E_{\parallel} \frac{\partial f_i}{\partial v_{\parallel}} = C_{ie} + \sum_j C_{ij}, \quad (4.5)$$

where the sum is taken over all ion species present in the plasma. The ion-electron collision operator can be written

$$C_{ie} = C_{ie}[f_i, f_e] = C_{ie}[f_i, f_{Me}] + C_{ie}[f_i, f_e - f_{Me}], \quad (4.6)$$

where we take  $f_{Me}$  to be a Maxwellian electron distribution in the rest-frame of the ion population. During near-equilibrium scenarios, i.e. when  $E \ll E_D$ , the perturbed electron population  $f_e - f_{Me}$  only contributes significantly from electron speeds much greater than the characteristic runaway ion speeds. Since the first term  $C_{ie}[f_i, f_{Me}]$  produces no net momentum transfer for the chosen  $f_{Me}$ , the operator can then be written [70]

$$C_{ie}[f_i, f_e - f_{Me}] = \frac{\mathbf{R}_{ei}}{m_i n_i} \cdot \frac{\partial f_i}{\partial \mathbf{v}}, \quad (4.7)$$

where  $\mathbf{R}_{ei} = \int d\mathbf{v} m_e \mathbf{v} C_{ei}$  is the net electron-ion friction force. The ion-electron friction  $\mathbf{R}_{ie}$  is readily calculated from the electron momentum equation,

$$\frac{\partial(n_e m_e \mathbf{V}_e)}{\partial t} = -n_e e \mathbf{E} + \sum_j \mathbf{R}_{ej}. \quad (4.8)$$

In steady state, utilizing that electron-ion collision rates scale as the ion-charge squared, we obtain

$$n_e e \mathbf{E} = \sum_j \mathbf{R}_{ej} = \frac{n_e Z_{\text{eff}}}{n_i Z_i^2} \mathbf{R}_{ei}, \quad (4.9)$$

where the effective charge is defined by  $\sum_i n_i Z_i^2 = n_e Z_{\text{eff}}$ . This allows the collisions with the perturbed electron population to be combined with the electric field to yield an ion kinetic equation

$$\begin{aligned} \frac{\partial f_i}{\partial t} + \frac{eZ_i}{m_i} E_{\parallel}^* \frac{\partial f_i}{\partial v_{\parallel}} &= C_{ie}[f_i, f_{Me}] + \sum_j C_{ij}[f_i, f_j], \\ E_{\parallel}^* &= \left(1 - \frac{Z_i}{Z_{\text{eff}}}\right) E_{\parallel}. \end{aligned} \quad (4.10)$$

In a pure plasma, where  $Z_i = Z_{\text{eff}}$ , the effective electric field  $E_{\parallel}^*$  vanishes and no ion acceleration will occur. For a high- $Z$  impurity with  $Z_i \gg Z_{\text{eff}}$ , the drag against electrons will far exceed the acceleration by the electric field, and the impurities will be accelerated in the direction of electron runaway, i.e. anti-parallel to the electric field.

For a runaway ion, the collisions with  $f_{Me}$  will describe a dynamical friction  $F_{ie} \propto v$  increasing in proportion to speed up to the electron thermal speed, whereas the collisions with other ions result in a friction force  $F_{ij} \propto 1/v^2$ , as in the standard electron runaway situation.

We developed an open source numerical tool CODION [102], based on the runaway-electron solver CODE but accounting for the additional terms of the kinetic equation specific to ion runaway, which we used to study the ion runaway dynamics in Paper D.

### **Ion friction-force estimates**

Valuable physical insight into the ion runaway process can be obtained by considering the friction force acting on a test-ion moving through the plasma. Formally, the test-particle equations of motion can be obtained by considering velocity moments of the kinetic equation for a delta distribution  $f_a = \delta(\mathbf{v} - \mathbf{u}(t))$  representing the test particle [103]. This method was pursued in Refs. [39, 42] where ion runaway in solar flares was considered, and later expanded upon in Paper D to consider general plasma compositions. The momentum moment of the ion kinetic equation yields the test-particle equation of motion

$$\frac{\partial(m_i v)}{\partial t} = Z_i e E^* \xi - \frac{m_i v_{Ti}}{\tau_{ie}} \left( \frac{Z_{\text{eff}} + \bar{n}}{v^2/v_{Ti}^2} + \frac{4}{3\sqrt{\pi}} \sqrt{\frac{m_e T_i^3}{m_i T_e^3}} \frac{v}{v_{Ti}} \right),$$

where we use the pitch-angle cosine  $\xi = v_{\parallel}/v$ , the ion-electron collision frequency  $\tau_{ie}^{-1} = n_e \ln \Lambda Z_i^2 e^4 / (4\pi \epsilon_0^2 m_i^2 v_{Ti}^3)$ , and introduced the quantity  $\bar{n} = \sum_j n_j Z_j^2 m_j / (n_e m_i)$ . Here explicit expressions for the collision operator with a Maxwellian background species [103] have been used, under the assumption that the velocities satisfy  $v_{Tj} \ll v \ll v_{Te}$  for all ion species  $j$ . The term containing the parentheses represents collisional friction, in which the first term expresses ion-ion friction which decreases with velocity and dominates for low velocities, whereas the second term describing ion-electron friction increases with velocity and dominates at high velocities.

The solutions  $\partial(m_i v)/\partial t = 0$  represent those velocities where electric-field acceleration exactly balances collisional friction. For electric fields

$$E^* > E_{\min}^* = 2 \frac{m_i v_{Ti}}{Z_i e \tau_{ie}} \frac{T_i}{T_e} \left( \frac{3}{2\pi} \frac{m_e}{m_i} (Z_{\text{eff}} + \bar{n}) \right)^{1/3},$$

two solutions  $v_{c1}$  and  $v_{c2}$  exist which describe, respectively, the runaway velocity above which an ion will be accelerated by the electric field; and the maximum velocity before electron friction overcomes the electric field, thus preventing further acceleration. Therefore, ions with velocity  $v_{c1} < v < v_{c2}$  will be accelerated, before accumulating at  $v_{c2}$ .

However, it should be noted that the above test-particle equation of motion is not unique. By considering the energy moment  $\int d\mathbf{v} m_i v^2 / 2(\dots)$  of the ion kinetic equation, one instead obtains

$$\frac{\partial(m_i v)}{\partial t} = Z_i e E^* \xi - \frac{m_i v_{Ti}}{\tau_{ie}} \left[ \bar{n} \frac{v_{Ti}^2}{v^2} + \frac{4}{3\sqrt{\pi}} \sqrt{\frac{m_e T_i^3}{m_i T_e^3}} \left( \frac{v}{v_{Ti}} - \frac{3T_e}{T_i} \frac{v_{Ti}}{v} \right) \right].$$

If we assume that  $(v/v_{Ti})^2 \gg 3T_e/T_i$ , this reduces to the momentum equation with the simple exchange  $\bar{n} \mapsto Z_{\text{eff}} + \bar{n}$ . This equation may provide more accurate estimates of the critical velocities; using the same procedure to estimate the electron runaway velocity shows that the energy-balance equation yields the well-known formula  $v_c/v_{Te} = \sqrt{E_D/2E}$ , while the momentum-balance equation gives a result which is larger by a factor  $\sqrt{2}$ . The discrepancy may be understood by the fact that pitch-angle scattering contributes to friction in the momentum-balance equation, but not in the energy-balance equation as it is an energy-conserving effect. The angular deflection will not efficiently stop a particle from running away (except sometimes indirectly), and hence the energy-balance equation provides a better estimate. The substitution  $(Z_{\text{eff}} + \bar{n}) \mapsto \bar{n}$  may thus improve the results given in Refs. [39, 42] and Paper D, although these estimates should perhaps primarily be viewed as a guide to interpret solutions of the kinetic equation, and to make qualitative predictions regarding the features of the ion runaway distribution.

Note finally the limits to the validity of the model described here. The linearization of the self-collision operator requires small runaway densities, corresponding to short times or electric fields  $E^* \sim E_{\min}^*$ ; extending far above  $E_{\min}^*$  requires the use of a non-linear self-collision operator. At the same time, the electric field must be sufficiently weak

to avoid significant runaway-electron generation which would affect  $E^*$ , therefore requiring  $E \lesssim 0.1E_D$ .



# Chapter 5

## Summary and outlook

Runaway is an important phenomenon, which occurs in both terrestrial and space plasmas. It is of particular interest in magnetic-fusion research where runaway electrons can strike the wall of the reactor after being accelerated to highly relativistic energies, at which point they can cause severe damage to plasma-facing components. Runaway is also of interest in space and astrophysical applications, where they may be responsible for observed gamma-ray emissions.

### Summary of the thesis

In this thesis, we present recent contributions to kinetic modelling of runaway in plasmas, which has been advanced by the incorporation of a full linearized Boltzmann collision model in the limit of low background temperatures. This model has been implemented into the numerical kinetic-equation solver CODE, which we have used to characterize the runaway dynamics in various scenarios. This has allowed us to assess the validity of previous collision models which have used simpler descriptions, as well as providing updated predictions for runaway generation rates. We have also demonstrated the consequences of the new model on the momentum-space distribution of runaways.

The effects of using the Boltzmann collision model is featured in Papers A, B, C and E, where it was used to describe the following processes:

**Avalanche generation** — In Paper A the Boltzmann operator was applied to Møller scattering, describing the elastic large-angle Coulomb

collisions between the runaway electrons and the thermal background electron population of the plasma. This generalized previous models for knock-on collisions, which were limited by approximating the momentum distribution of the runaway population, such as assuming zero pitch angle and infinite energy. We also presented a scheme to accordingly modify the Fokker-Planck operator when a large-angle collision operator is added to the kinetic equation, in order to avoid double counting of collisions. It was shown that in spite of the issues of previous models, they are mostly sufficient to predict the production rate of runaway electrons through the avalanche mechanism, with errors in the range of 10% or smaller.

**Bremsstrahlung energy loss** — In Paper B we applied the large-angle collision model to describe the effect of bremsstrahlung emission of the runaway dynamics for optically thin plasmas, where emitted photons are rarely absorbed by runaways. Since the average energy of the emitted photons,  $m_e c^2 \langle (\gamma - \gamma_1)^2 \rangle / \langle \gamma - \gamma_1 \rangle$ , is of the order of the incident electron energy  $m_e c^2 \gamma$  for runaways in the 10-100 MeV range, a Fokker-Planck description is inadequate. Instead, we demonstrate that a Boltzmann operator needs to be used if one wishes to understand the momentum-space dynamics of runaways when bremsstrahlung losses are important. We showed that a significant fraction of runaways can reach twice the maximum energy predicted in a Fokker-Planck description.

**Pair production during runaway** — In Paper C the large-angle collision model is used to describe the momentum-space distribution of the positrons which are generated when runaway electrons interact with the thermal background plasma. An essential feature that is captured with our model is how a created positron typically co-moves with the runaway electron responsible for its creation; since the electrons are moving antiparallel to the electric field, this means that newly created positrons are moving with high speed in the direction opposite to their acceleration in the electric field. A careful analysis of the momentum-space dynamics is carried out in order to predict the fraction of created positrons that become runaway accelerated.

**Collisions with a partially ionized medium** — Paper E describes the theory of a Fokker-Planck equation appropriate for describing collisions with partially ionized ions. The degree to which the cloud of bound

electrons will screen out the nuclear charge is sensitive to the scattering angle; generally larger scattering angles result in a stronger enhancement of the scattering rate in comparison to the completely screened situation. For this reason, we investigated to what degree a Boltzmann model of the ion collisions would differ to the Fokker-Planck model. It was found that, although some difference was observed in the momentum-space distribution of the fast runaway population, their rate of generation was captured with high accuracy within the Fokker-Planck approximation. Paper E, which presents the details of the derivation of the new electron-ion collision model as well as further exploring its consequences on the runaway dynamics, was preceded by Papers O and R which contained its first presentation, as well as a study of the threshold electric field for avalanche multiplication in a partially ionized medium.

Papers D and F are not directly concerned with the effect of large-angle collisions, but have advanced the understanding of runaway in the following ways:

**Ion runaway** — We provide new insights into the runaway acceleration of *ions* in Paper D by, for the first time, considering full numerical solutions of the 2D ion kinetic equation in runaway scenarios, allowing us to study their generation and momentum-space dynamics. An important finding is that in post-disruption tokamak plasmas – where electron runaway may become a huge issue due to the numbers in which they can be generated – we demonstrate that ion runaway generation (where the tail of a thermal Maxwellian population is accelerated) is unlikely to occur to any significant degree. An exception may be in the presence of a fast ion population existing before the disruption, for example injected for heating purposes or energetic helium nuclei created in fusion reactions, where they may be briefly sustained in the strong electric field due to their relatively lower collisionality. The numerical tool we developed for the study, CODION, is open source and freely available on Github [102].

**Radiation synthetic diagnostics** — In the final study included in the thesis, Paper F, we present a synthetic diagnostic for runaways, SOFT. The tool predicts the emission (to which the plasma is assumed to be optically thin) which would reach the aperture of a detector due to a three-dimensional runaway-electron distribution in tokamaks, which may depend arbitrarily on radius, energy and pitch angle. The tool

was originally created for predicting camera images of the synchrotron radiation emitted by a runaway beam, but has been generalized to also predict spectrometer measurements as well as those of bremsstrahlung diagnostics. The tool, which was presented in Paper F, has produced follow-up studies in Papers P, Q and S, where it was applied to model synchrotron diagnostics during runaway discharges in the Alcator C-Mod and DIII-D tokamaks. In Paper P it was also used to model the Gamma Ray Imager bremsstrahlung diagnostic at DIII-D.

## Outlook

In this thesis we present recent advancements to the modelling of collisional and radiative effects on runaways. A natural framework to quantify these processes has been to consider a slab plasma, which is the simplest system exhibiting the richness of the collisional dynamics which non-locally couples the energies and pitch angles of the runaways. Since the time of the first publication in this thesis – Paper D, carried out during 2014 – our understanding of the momentum-space dynamics of runaway electrons has significantly matured. We have developed a more confident view of which collisional and radiative processes affect the runaway dynamics, some of which were obtained through the studies presented in this thesis.

However, in comparing present-day models with experimental observations of runaways in tokamaks, it is clear that the predictive capabilities of the pure momentum-space description is often limited. This demonstrates a need to extend the model to describe also spatially varying plasmas, uniting it with the momentum space effects which the work included in this thesis has mainly focused on.

In tokamaks, three spatial effects in particular directly influence the momentum-space dynamics:

- (i) Radial transport of runaways, for example due to fluctuations of the magnetic field, where the effective rate of transport tends to be sensitive to the runaway momentum.
- (ii) Instabilities of the plasma may affect the runaways through a wave-particle interaction, which for example will tend to flatten out inverted energy gradients in a distribution. Such bump-on-tail distributions are predicted to be produced by radiation losses, as illustrated in Papers B, H and K. The anisotropy of the runaway

distribution is also known to be a potential drive of wave instabilities.

- (iii) The magnetic-mirror force acting on particles moving through an inhomogeneous magnetic field. This effect causes, among other things, particles of a sufficiently large pitch-angle to be trapped on the low-field side of a tokamak, where the orbit-averaged effect of the electric field is significantly reduced. This can be important for the rate of avalanche generation, since secondary electrons tend to have large pitch angles [104].

In addition, there are spatial effects which need to be accounted for that only indirectly influence the dynamics, but which may be no less important:

- (iv) Disruption dynamics must be better understood, since the macroscopic evolution of the magnetic topology during the early stages of the disruption sets the possibility for a runaway seed to form. The destructive potential of the final runaway beam is highly sensitive to the seed; with no seed generation one may avoid the formation of a runaway beam altogether.
- (v) The ablation of pellets and transport of impurities in cold post-disruption plasmas are essential in order to understand the distribution of the high- $Z$  ions of the plasma. This sets the generation and dissipation rates of runaways during disruption mitigation by massive material injection, which is the system currently planned for ITER [36].
- (vi) The self-consistent evolution of the electric field in the post-disruption plasma, which will set the runaway generation rate, but which in turn will also depend on the evolution of the runaway current profile.

These are six examples of significant gaps in present modelling and understanding, where I expect that advancements can help us bridge the gap between interpretive and predictive modelling. In particular points (i-iii) have seen significant progress in recent years [105, 106, 107, 108], and there are ongoing efforts in the direction of the last three points. The worldwide effort in runaway modelling will certainly lead to exciting developments in the coming years.



# Bibliography

- [1] R. D. Gill. *Generation and loss of runaway electrons following disruptions in JET*. Nucl. Fusion **33**, 1613 (1993).
- [2] A. V. Gurevich and K. P. Zybin. *Runaway breakdown and electric discharges in thunderstorms*. Phys. Usp. **44**, 1119 (2001).
- [3] G. D. Holman. *Acceleration of Runaway Electrons and Joule Heating in Solar Flares*, edited by M. R. Kundu. Springer Netherlands, Dordrecht (1985).
- [4] C. T. R. Wilson. *The electric field of a thundercloud and some of its effects*. Proc. Phys. Soc. London **37**, 32D (1924).
- [5] C. T. R. Wilson. *The Acceleration of  $\beta$ -particles in Strong Electric Fields such as those of Thunderclouds*. Math. Proc. Camb. Phil. Soc. **22**, 534 (1925).
- [6] A. S. Eddington. *The Internal Constitution of Stars*, Cambridge University Press, Cambridge (1926).
- [7] E. R. Harrison . *Runaway and suprathermal particles*, J. Nucl. Energy, Part C Plasma Phys. **1**, 105 (1960)
- [8] H. Dreicer. *Electron and ion runaway in a fully ionized gas*. Phys. Rev. **115**, 238 (1959).
- [9] B. A. Trubnikov. *Particle interactions in a fully ionized plasma*, in *Reviews of Plasma Physics 1*, edited by M. A. Leontovich. Consultants Bureau Enterprises, New York (1965).
- [10] M. D. Kruskal and I. B. Bernstein. *Runaway electrons in an ideal Lorentz plasma*. Phys. Fluids **7**, 407 (1964).

- [11] J. W. Connor and R. J. Hastie. *Relativistic limitations on runaway electrons*. Nucl. Fusion **15**, 415 (1975).
- [12] I. U. A. Sokolov. “*Multiplication*” of accelerated electrons in a tokamak. JETP Lett. **29**, 218 (1979).
- [13] M. N. Rosenbluth and S. V. Putvinski. *Theory for avalanche of runaway electrons in tokamaks*. Nucl. Fusion **37**, 1355 (1997).
- [14] R. Jayakumar, H. H. Fleischmann and S. J. Zweben. *Collisional avalanche exponentiation of runaway electrons in electrified plasmas*, Phys. Lett. A, **172**, 447 (1993)
- [15] T. C. Hender *et al.* *Progress in the ITER physics basis*, Chapter 3: MHD stability, operational limits and disruptions. Nucl. Fusion **47**, 6 (2007).
- [16] A. H. Boozer. *Pivotal issues on relativistic electrons in ITER*. Nucl. Fusion **58**, 036006 (2018).
- [17] J. Freidberg. *Plasma Physics and Fusion Energy*. Cambridge University Press, New York (2007).
- [18] J. Wesson. *Tokamaks*. Oxford University Press Inc., New York (2011).
- [19] F. C. Schüller. *Disruptions in tokamaks*. Plasma Phys. Control. Fusion **31**, A135-A162 (1995).
- [20] A. H. Boozer. *Theory of tokamak disruptions*. Phys. Plasmas **19**, 058101 (2012).
- [21] A. Gibson. *Possibility of ion runaway in Zeta*. Nature **183**, 4654 (1959).
- [22] R. W. Harvey, V. S. Chan, S. C. Chiu, T. E. Evans, M. N. Rosenbluth and D.G. Whyte. *Runaway electron production in DIII-D killer pellet experiments, calculated with the CQL3D/KPRAD model*. Phys. Plasmas **7**, 4590 (2000).
- [23] P. Helander, H. Smith, T. Fülöp and L.-G. Eriksson. *Electron kinetics in a cooling plasma*. Phys. Plasmas **11**, 5704 (2004).

- [24] H. Smith, P. Helander, L.-G. Eriksson and T. Fülöp. *Runaway electron generation in a cooling plasma*. Phys. Plasmas **12**, 122505 (2005).
- [25] H. M. Smith, T. Fehér, T. Fülöp, K. Gál and E. Verwichte. *Runaway electron generation in tokamak disruptions*. Plasma Phys. Control. Fusion **51**, 12 (2009).
- [26] P. Aleynikov and B. N. Breizman. *Generation of runaway electrons during the thermal quench in tokamaks*. Nucl. Fusion **57**, 046009 (2017).
- [27] JET, EUROfusion. <https://www.euro-fusion.org/jet/>
- [28] F. Romanelli and JET EFDA Contributors. *Overview of the JET results with the ITER-like wall*. Nucl. Fusion **53**, 104002 (2013).
- [29] ITER organization. <http://www.ITER.org/>
- [30] E. M. Hollmann *et al.* *Status of research toward the ITER disruption mitigation system*. Phys. Plasmas **22**, 021802 (2015).
- [31] A. H. Boozer. *Theory of runaway electrons in ITER: Equations, important parameters, and implications for mitigation*. Phys. Plasmas **22**, 032504 (2015).
- [32] M. Lehnhen *et al.* *Impact and mitigation of disruptions with the ITER-like wall in JET*. Nucl. Fusion **53**, 093007 (2013).
- [33] P. Helander, L-G. Eriksson and F. Andersson. *Runaway acceleration during magnetic reconnection in tokamaks*. Plasma Phys. Control. Fusion **44**, 12B (2002).
- [34] J. R. Martín-Solís, A. Loarte and M. Lehnhen. *Formation and termination of runaway beams in ITER disruptions*. Nucl. Fusion **57**, 066025 (2017).
- [35] B. N. Breizman. *Marginal stability model for the decay of runaway electron current*. Nucl. Fusion **54**, 072002 (2014).
- [36] M. Lehnhen *et al.* *Disruptions in ITER and strategies for their control and mitigation*. J. Nucl. Mater. **463**, 39 (2015).
- [37] H. P. Furth and P. H. Rutherford. *Ion runaway in tokamak discharges*. Phys. Rev. Lett. **28**, 545 (1972).

- [38] P. Helander, L.-G. Eriksson, R. J. Akers, C. Byrom, C. G. Gimblett and M. R. Tournianski. *Ion acceleration during reconnection in MAST*. Phys. Rev. Lett. **89**, 235002 (2002).
- [39] T. Fülöp, and S. Newton. *Alfvénic instabilities driven by runaways in fusion plasmas*. Phys. Plasmas **21**, 080702 (2014).
- [40] A. Sykes, the START Team, the NBI Team, the MAST Team and the Theory Team. *The spherical tokamak programme at Culham*. Nucl. Fusion **39**, 1271 (1999).
- [41] MAST, CCFE. <http://www.ccf.e.ac.uk/mast.aspx>
- [42] G. D. Holman. *DC electric field acceleration of ions in solar flares*. Astrophys. J. **452**, 451 (1995).
- [43] S. Eilerman, J. K. Anderson, J. S. Sarff, C. B. Forest, J. A. Reusch, M. D. Nornberg and J. Kim. *Runaway of energetic test ions in a toroidal plasma*. Phys. Plasmas **22**, 020702 (2015).
- [44] J. K. Anderson, J. Kim, P. J. Bonofiglo, W. Capecchi, S. Eilerman, M. D. Nornberg, J. S. Sarff and S. H. Sears. *Dynamics of reconnection-driven runaway ion tail in a reversed field pinch plasma*. Phys. Plasmas **23**, 055702 (2016).
- [45] A. A. Vlasov. *The vibrational properties of an electron gas*. Sov. Phys. Usp. **10**, 721 (1968).
- [46] R. D. Hazeltine and J. D. Meiss. *Plasma Confinement*. Dover Publications, New York (2003).
- [47] N. N. Bogolyubov. *Problems of a Dynamical Theory in Statistical Physics*. State Technical Press, Moscow, 1946. English translation available in *Studies in Statistical Mechanics*, vol. 1 by J. de Boer and G. E. Uhlenbeck, North Holland Publishing Company, Amsterdam (1962).
- [48] M. Born and H. S. Green. *A General Kinetic Theory of Liquids*. Cambridge University Press, London (1949).
- [49] H. S. Green. *The Molecular Theory of Fluids*. Interscience Publishers, Inc., New York (1952).

- [50] J. G. Kirkwood. *The statistical mechanical theory of transport processes I & II*. J. Chem. Phys. **14**, 180 (1946); **15**, 72 (1947).
- [51] J. Yvon. *La théorie des fluides et l'équation d'état: actualités scientifiques et industrielles*. Hermann & Cie, Paris (1935).
- [52] J. Liouville. *Note sur la Théorie de la Variation des constantes arbitraires*. J. Math. App. **3**, 342 (1838).
- [53] H. Goldstein, C. Poole and J. Safko. *Classical Mechanics*, third edition. Addison Wesley, San Francisco (2002).
- [54] E. A. Frieman. *On a new method in the theory of irreversible processes*. J. Math. Phys **4**, 410 (1963).
- [55] G. Sandri. *The foundations of nonequilibrium statistical mechanics, I & II*. Ann. Phys. **24**, 332 (1963).
- [56] D. C. Montgomery and D. A. Tidman. *Plasma kinetic theory*, McGraw-Hill, Inc., New York (1964).
- [57] G. Ecker. *Theory of Fully Ionized Plasmas*. Academic Press, Inc., New York (1972).
- [58] L. Landau. *The transport equation in the case of Coulomb interactions*. Phys. Z. Sowjet **10**, 154 (1936).
- [59] L. Boltzmann. *Weitere Studien über das Wärmegleichgewicht unter Gasmoleculen*. Wien Ber. **66**, 275 (1872). Translation in English can be found in L. Boltzmann, *Further studies on the thermal equilibrium of gas molecules*, in *The Kinetic Theory of Gases: An anthology of classic papers with historical commentary* by S. G. Brush. Imperial College Press, London (2003).
- [60] L. Boltzmann. *Vorlesungen über Gastheorie*. J. A. Barth, Leipzig (1896).
- [61] C. Cercignani and G. M. Kremer. *The Relativistic Boltzmann Equation: Theory and Applications*. Birkhäuser Verlag Basel, Berlin (2002).
- [62] W. Heitler. *The Quantum Theory of Radiation*. Oxford University Press, London (1954).

- [63] S. Weinberg. *The Quantum Theory of Fields, Volume 1: Foundations*. Cambridge University Press, Cambridge (2005).
- [64] C. Cercignani. *Theory and Application of the Boltzmann Equation*. Scottish Academic Press, Edinburgh (1975).
- [65] A. D. Fokker. *Die mittlere Energie rotierender elektrischer Dipole im Strahlungsfeld*. Annalen der Physik **348**, 810 (1914).
- [66] M. Planck. *Über einen Satz der Statistischen Dynamik und seine Erweiterung in der Quantentheorie*. S. B. K. Preuss. Akad. Wiss. Berlin **N**, 324 (1917).
- [67] S. T. Beliaev and G. I. Budker. *The relativistic kinetic equation*. Sov. Phys. Dokl. **1**, 218 (1956).
- [68] H. Akama. *Relativistic Boltzmann equation for plasmas*. J. Phys. Soc. Japan **28**, 478 (1970).
- [69] E. M. Lifshitz and L. P. Pitaevskii. *Physical Kinetics*, Volume 10 in *Course of Theoretical Physics*. Butterworth-Heinemann, Oxford (1981).
- [70] P. Helander and D. J. Sigmar. *Collisional Transport in Magnetized Plasmas*. Cambridge University Press, New York (2002).
- [71] H. Bethe. *Zur theorie des durchgangs schneller korpuskularstrahlen durch materie*. Annalen der Physik **397**, 325 (1930).
- [72] S. P. Sauer, J. Oddershede, J. R. Sabin. *Chapter three - the mean excitation energy of atomic ions* Concepts of Mathematical Physics in Chemistry: A Tribute to Frank E. Harris - Part A, Advances in Quantum Chemistry, **71**, 29. Academic Press (2015).
- [73] N. F. Mott and H. S. W. Massey. *The Theory of Atomic Collisions*. Clarendon Press, Oxford (1965).
- [74] A. Gulans, S. Kontur, C. Meisenbichler, D. Nabok, P. Pavone, S. Rigamonti, S. Sagmeister, U. Werner and C. Draxl. EXCITING: *a full-potential all-electron package implementing density-functional theory and many-body perturbation theory*. Journal of Physics: Condensed Matter **26**, 363202 (2014).

- [75] M. J. Frisch *et al.* *Gaussian 16 Revision B.01*. Gaussian Inc. Wallington CT (2016).
- [76] G. Papp, M. Drevlak, T. Fülöp and P. Helander. *Runaway electron drift orbits in magnetostatic perturbed fields*. Nucl. Fusion **51**, 043004 (2011).
- [77] M. N. Rosenbluth, W. M. MacDonald and D. L. Judd. *Fokker-Planck equation for an inverse-square force*. Phys. Rev. **107**, 1 (1957).
- [78] M. Landreman, A. Stahl and T. Fülöp. *Numerical calculation of the runaway electron distribution function and associated synchrotron emission*. Comp. Phys. Comm. **185**, 847 (2014).
- [79] J. Larmor. *On the theory of the magnetic influence on spectra; and on the radiation from moving ions*. Philos. Mag. Series 5 **44**, 503 (1897).
- [80] M. Abraham. *Prinzipien der Dynamik des Elektrons*. Ann. Phys. **315**, 105 (1902).
- [81] P. A. M. Dirac. *Classical theory of radiating electrons*. Proc. R. Soc. A **167**, 148 (1938).
- [82] F. Andersson, P. Helander and L.-G. Eriksson. *Damping of relativistic electron beams by synchrotron radiation*. Phys. Plasmas **8**, 5221 (2001).
- [83] J. D. Jackson. *Classical Electrodynamics*. John Wiley & Sons, Inc., Hoboken (1999).
- [84] I. H. Hutchinson. *Principles of Plasma Diagnostics*. Cambridge University Press, New York (2002).
- [85] G. Racah. *Sopra L'irradiazione nell'urto di particelle veloci*. Il Nuovo Cimento **11**, 461 (1934).
- [86] P. T. McCormick, D. G. Keiffer and G. Parzen. *Energy and angle distribution of electrons in bremsstrahlung*. Phys. Rev. **103**, 29 (1956).

- [87] I. Fernández-Gómez, J. R. Martín-Solís and R. Sánchez. *Determination of the parametric region in which runaway electron energy losses are dominated by bremsstrahlung radiation in tokamaks*. Phys. Plasmas **14**, 072503 (2007).
- [88] M. Bakhtiari, G. J. Kramer, M. Takechi, H. Tamai, Y. Miura, Y. Kusama and Y. Kamada. *Role of Bremsstrahlung Radiation in Limiting the Energy of Runaway Electrons in Tokamaks*. Phys. Rev. Lett. **94**, 215003 (2005).
- [89] M. Bakhtiari, G. J. Kramer and D. G. Whyte. *Momentum-space study of the effect of bremsstrahlung radiation on the energy of runaway electrons in tokamaks*. Phys. Plasmas **12**, 102503 (2005).
- [90] C. Paz-Soldan, C. M. Cooper, P. Aleynikov, D. C. Pace, N. W. Eidiertis, D. P. Brennan, R. S. Granetz, E. M. Hollmann, C. Liu, A. Lvovskiy, R. A. Moyer and D. Shiraki. *Spatiotemporal Evolution of Runaway Electron Momentum Distributions in Tokamaks*. Phys. Rev. Lett **118**, 255002 (2017).
- [91] C. Paz-Soldan, C. M. Cooper, P. Aleynikov, N. W. Eidiertis, A. Lvovskiy, D. C. Pace, D. P. Brennan, E. M. Hollmann, C. Liu, R. A. Moyer and D. Shiraki. *Resolving runaway electron distributions in space, time, and energy*. Phys. Plasmas **25**, 056105 (2018).
- [92] E. M. Hollmann, P. B. Parks, N. Commaux, N. W. Eidiertis, R. A. Moyer, D. Shiraki, M. E. Austin, C. J. Lasnier, C. Paz-Soldan and D. L. Rudakov. *Measurement of runaway electron energy distribution function during high-Z gas injection into runaway electron plateaus in DIII-D*. Phys. Plasmas **22**, 056108 (2015).
- [93] R. J. Zhou, I. M. Pankratov, L. Q. Hu, M. Xu and J. H. Yang. *Synchrotron radiation spectra and synchrotron radiation spot shape of runaway electrons in Experimental Advanced Superconducting Tokamak*. Physics of Plasmas **21**, 063302 (2014).
- [94] G. R. Blumenthal and R. J. Gould. *Bremsstrahlung, synchrotron radiation, and Compton scattering of high-energy electrons traversing dilute gases*. Rev. Mod. Phys. **42**, 237 (1970).
- [95] I. M. Pankratov. *Analysis of the Synchrotron Radiation Emitted by Runaway Electrons*. Plasma Physics Reports **22**, 535 (1996).

- [96] A. Stahl, M. Landreman, G. Papp, E. Hollmann and T. Fülöp. *Synchrotron radiation from a runaway electron distribution in tokamaks*. Phys. Plasmas **20**, 093302 (2013).
- [97] P. Helander and D. J. Ward. *Positron Creation and Annihilation in Tokamak Plasmas with Runaway Electrons*. Phys. Rev. Lett. **90**, 135004 (2003).
- [98] J. Alwall *et al.* *The automated computation of tree-level and next-to-leading order differential cross sections, and their matching to parton shower simulations*. Journal of High Energy Physics **7**, 79 (2014).
- [99] D. A. Gryaznykh. *Cross Section for the Production of Electron-Positron Pairs by Electrons in the Field of a Nucleus*. Phys. Atom. Nuclei **61**, 394 (1998).
- [100] V. M. Budnev, I. F. Ginzburg, G. V. Meledin and V. G. Serbo. *The two-photon particle production mechanism. Physical problems. Applications. Equivalent photon approximation*. Phys. Reports **15**, 181 (1975).
- [101] Y. Guanying, J. Liu, J. Xie and J. Li. *Detection of tokamak plasma positrons using annihilation photons*. Fusion Eng. Design **118**, 124 (2017).
- [102] CODION is an open-source tool, available for download on GitHub. <http://github.com/Embreus/CODION>
- [103] F. L. Hinton. *Collisional Transport in Plasma*, in *Basic Plasma Physics I*, edited by A. A. Galeev and R. N. Sudan. North-Holland Publishing Company, Amsterdam (1983).
- [104] E. Nilsson, J. Decker, N. J. Fisch and Y. Peysson. *Trapped-electron runaway effect*. J. Plasma Phys. **81**, 475810403 (2015).
- [105] T. Hauff and F. Jenko. *Runaway electron transport via tokamak microturbulence*. Phys. Plasmas **16**, 102308 (2009).
- [106] G. Papp, M. Drevlak, T. Fülöp, P. Helander and G. I. Pokol. *Runaway electron losses caused by resonant magnetic perturbations in ITER*. Plasma Phys. Control Fusion **53**, 095004 (2011).

- 
- [107] C. Liu, L. Shi, E. Hirvijoki, D. P. Brennan, A. Bhattacharjee, C. Paz-Soldan and M. E. Austin. *The effects of kinetic instabilities on the electron cyclotron emission from runaway electrons.* Nucl. Fusion **58**, 096030 (2018).
  - [108] C. Liu, H. Qin, E. Hirvijoki, Y. Wang and J. Liu. *Conservative magnetic moment of runaway electrons and collisionless pitch-angle scattering.* Nucl. Fusion **58**, 106018 (2018).

# Paper A

O. Embréus, A. Stahl and T. Fülöp,

*On the relativistic large-angle electron collision operator for runaway avalanches in plasmas,*

Journal of Plasma Physics **84**, 905840102 (2018).

<https://doi.org/10.1017/S002237781700099X>

arXiv:1708.08779 [physics.plasm-ph]

# On the relativistic large-angle electron collision operator for runaway avalanches in plasmas

O. Embréus<sup>1</sup>, A. Stahl<sup>1</sup> and T. Fülöp<sup>1,†</sup>

<sup>1</sup>Department of Physics, Chalmers University of Technology, Gothenburg SE-41296, Sweden

(Received 19 September 2017; revised 6 December 2017; accepted 7 December 2017)

Large-angle Coulomb collisions lead to an avalanching generation of runaway electrons in a plasma. We present the first fully conservative large-angle collision operator, derived from the relativistic Boltzmann operator. The relation to previous models for large-angle collisions is investigated, and their validity assessed. We present a form of the generalized collision operator which is suitable for implementation in a numerical kinetic equation solver, and demonstrate the effect on the runaway-electron growth rate. Finally we consider the reverse avalanche effect, where runaways are slowed down by large-angle collisions, and show that the choice of operator is important if the electric field is close to the avalanche threshold.

**Key words:** fusion plasma, runaway electrons

---

## 1. Introduction

Large-angle collisions are associated with large momentum transfers, but their influence can often be ignored in plasma physics, as the cumulative effect of many small-angle deflections are larger by a factor of the Coulomb logarithm,  $\ln \Lambda$  (Rosenbluth, MacDonald & Judd 1957; Trubnikov 1965). In many plasmas, e.g. magnetic fusion plasmas and astrophysical plasmas,  $\ln \Lambda$  is typically of the order of 10–30. This allows collisions to be accurately accounted for using a Fokker–Planck equation, originally derived for Coulomb interactions by Landau as the small-momentum-transfer limit of the Boltzmann equation (Landau 1965).

A unique situation occurs in runaway acceleration of electrons, where large-angle collisions can play a dominant role even for large  $\ln \Lambda$ , as they cause an exponential growth of the runaway density – a runaway avalanche (Sokolov 1979). Runaway is the acceleration of particles in the presence of an electric field which exceeds the critical field  $E_c = n_e \ln \Lambda e^3 (4\pi \varepsilon_0^2 m_e c^2)^{-1}$  (Connor & Hastie 1975), where  $n_e$  is the electron density,  $e$  is the elementary charge,  $\varepsilon_0$  is the vacuum permittivity,  $m_e$  is the electron rest mass and  $c$  is the speed of light. Since the collisional drag for superthermal electrons is given by  $F_c = eE_c(v/c)^{-2}$ , any electrons with speed greater than the critical speed  $v_c = c\sqrt{E_c/E}$  will be accelerated indefinitely, and are hence referred to as runaway electrons (Wilson 1925). Electron runaway occurs in a wide range of plasmas, e.g. in atmospheric discharges (Gurevich, Milikh & Roussel-Dupre 1992), in solar flares (Holman 1985) and in tokamak disruptions when the plasma current

† Email address for correspondence: [tunde@chalmers.se](mailto:tunde@chalmers.se)

changes quickly and a strong electric field is induced (Gill 1993; Jaspers 1993). Due to the large plasma current they would carry, reactor-scale tokamaks such as ITER will be particularly susceptible to the conversion of plasma current to relativistic runaway-electron current by large-angle collisions during disruptions (Rosenbluth & Putvinski 1997). The subsequent uncontrolled loss of a runaway-electron beam could damage plasma-facing components, and the runaways therefore pose a critical threat to the viability of nuclear fusion for energy production (Hollmann *et al.* 2015).

In a plasma, runaways are mainly generated by two separate mechanisms. When the electrons in the runaway region  $v > v_c$  are being accelerated, collisional velocity-space diffusion will feed thermal electrons into the runaway region at a steady rate. This primary runaway generation, or Dreicer mechanism (Dreicer 1960), generates new runaways at a rate which is exponentially sensitive to the electric field. The runaway population growth rate was derived in Connor & Hastie (1975), Cohen (1976) and is

$$\left( \frac{dn_{RE}}{dt} \right)_{\text{prim}} \approx \kappa \frac{n_e}{\tau_c} \left( \frac{E}{E_D} \right)^{-(3/16)(1+Z_{\text{eff}})h} \exp \left[ -\lambda \frac{E_D}{4E} - \sqrt{\eta \frac{(1+Z_{\text{eff}})E_D}{E}} \right], \quad (1.1)$$

where the undetermined constant factor  $\kappa$  is of order unity. Here  $n_{RE}$  is the number density of runaways,  $\tau_c = 4\pi\varepsilon_0^2 m_e^2 c^3 / (n_e e^4 \ln \Lambda)$  is the relativistic-electron collision time,  $E_D = m_e^2 c^3 / (e\tau_c T_e)$  is the so-called Dreicer field and  $Z_{\text{eff}} = \sum_i n_i Z_i^2 / \sum_i n_i Z_i$  is the effective ion charge (with the sum taken over all ion species  $i$ ). The parameters  $h$ ,  $\lambda$  and  $\eta$  (not given here) depend on  $E/E_c$  and approach unity as  $E/E_c$  becomes large (in the non-relativistic limit), and ensure that the growth rate vanishes as  $E \rightarrow E_c$ .

A secondary runaway generation mechanism is provided by large-angle collisions, whereby an electron with kinetic energy  $\epsilon = (\gamma - 1)m_e c^2 > 2\epsilon_c$  can send a stationary target electron into the runaway region in a single collision event while remaining a runaway itself, where  $\epsilon_c$  is the kinetic energy corresponding to the critical speed. Secondary generation, also referred to as avalanche generation due to the resulting exponential growth of the runaway population, generates new runaways at a rate calculated by Rosenbluth & Putvinski (1997) to be approximately

$$\left( \frac{dn_{RE}}{dt} \right)_{\text{ava}} \approx C \frac{n_{RE}}{2 \ln \Lambda \tau_c} \left( \frac{E}{E_c} - 1 \right). \quad (1.2)$$

The function  $C = C(E, Z_{\text{eff}})$  was shown to be  $C = 1$  when collisional diffusion is neglected (formally by setting  $Z_{\text{eff}} = -1$ ).

While the avalanche growth rate is formally of order  $1/\ln \Lambda$  smaller than the primary generation rate, the more favourable scaling with electric field makes it the dominant source of new runaways for sufficiently large runaway populations  $n_{RE}$  or sufficiently small  $E/E_D$ , i.e. at low temperature. In the presence of a constant electric field  $E$ , with no initial runaway population (apart from a small primary seed), the secondary generation rate will exceed the primary one after approximately one avalanche e-folding time  $t_{\text{ava}} \approx 2 \ln \Lambda m_e c / [C e(E - E_c)]$ . This corresponds to the time for an initially slow electron to be accelerated to a kinetic energy  $E_k \approx \ln \Lambda / C$  MeV (Jayakumar, Fleischmann & Zweber 1993) (neglecting the weak electric-field dependence of  $C$ ). Numerically,  $t_{\text{ava}} \approx 3.4 \ln \Lambda / [C(E - E_c)]$  ms, with  $E$  and  $E_c$  in  $\text{V m}^{-1}$ . If the electric field decreases in magnitude with time, avalanche will become important even earlier. In many practical runaway scenarios, the runaway process will last for multiple  $t_{\text{ava}}$  (Gurevich, Milikh & Roussel-Dupre 1994; Gurevich & Zybin 2001; Helander, Eriksson & Andersson 2002), and secondary generation will therefore be the dominant runaway mechanism.

In this work we derive a conservative large-angle (also known as ‘close’ or ‘knock-on’) collision model from the high-energy limit of the linearized relativistic Boltzmann collision integral. We will show how the operators used to model large-angle collisions in previous studies are obtained through various approximations of the Boltzmann collision operator, and how our more general operator resolves issues with previous models and allows the study of new physical effects. In particular, we resolve the issue of double counting of large-angle and small-angle collisions, and show that this development is essential to accurately capture the dynamics. We find that the change to the runaway growth rate due to the new operator is largest during the early stages of the runaway acceleration process, and the likelihood of a given runaway seed transforming into a serious runaway beam can thus potentially be affected. Furthermore, we consider the effect of the inverse knock-on process, where a runaway is slowed down in a single large-angle collision. This effect was recently shown by Aleynikov & Breizman (2015) to be significant for runaway in a near-threshold electric field.

The rest of the paper is organized as follows. In § 2 we introduce the theoretical models describing the large-angle collisions. After giving an overview of the existing models, we present a derivation of the new conservative operator. In § 3 we investigate the effect of the new operator on the runaway growth rate numerically, using the kinetic equation solver CODE (Landreman, Stahl & Fülöp 2014; Stahl *et al.* 2016). Finally, we summarize our conclusions in § 4.

## 2. Theoretical models for runaway generation due to large-angle collisions

One of the earliest models for avalanche runaway generation was introduced by Rosenbluth & Putvinski (1997). Due to its simple form, suitable for analytical development, it has been widely used to study the dynamics of an avalanching runaway population (Eriksson & Helander 2003; Smith *et al.* 2005; Fülöp *et al.* 2006; Nilsson *et al.* 2015). Rosenbluth and Putvinski proposed a kinetic equation for the electron distribution of the form

$$\frac{df_e}{dt} = C_{FP}(f_e) + S(f_e), \quad (2.1)$$

where  $df_e/dt$  represents the advective part of the motion,  $C_{FP}$  is the Fokker–Planck collision operator and  $S$  a source term representing ‘secondary high-energy electrons knocked out of their orbits by close collisions of a primary relativistic electron with low-energy electrons from the background plasma’ (Rosenbluth & Putvinski 1997). Assuming all existing runaways to be infinitely energetic and having zero pitch angle, they obtained (here adapting their more general result to a homogeneous plasma)

$$S_{RP}(p, \xi, \varphi) = \frac{n_{RE}}{4\pi\tau_c \ln \Lambda} \delta(\xi - \xi_0) \frac{m_e^3 c^3}{p^2} \frac{\partial}{\partial p} \left( \frac{1}{1 - \gamma} \right), \quad (2.2)$$

where  $\xi = \cos \theta = p_{\parallel}/p$  is the pitch-angle cosine,  $\gamma = \sqrt{1 + (p/m_e c)^2}$  is the Lorentz factor,  $\xi_0 = \sqrt{(\gamma - 1)/(\gamma + 1)}$  and the momentum-space volume element is  $p^2 dp d\xi d\varphi$ , with  $\varphi$  the azimuthal angle of the momentum (the gyroangle). The delta function ensures that secondary electrons are only born on the parabola  $p_{\perp}^2 = 2p_{\parallel}m_e c$  in momentum space. In the non-relativistic limit,  $p \ll m_e c$ , secondaries are born at perpendicular angles,  $p_{\parallel} \approx 0$ , and are prone to trapping in an inhomogeneous magnetic field (Rosenbluth & Putvinski 1997). Away from the magnetic axis of a tokamak,

this can lead to a strong reduction in the avalanche growth rate, as recently also demonstrated in detailed numerical simulations by Nilsson *et al.* (2015).

A more general model was later described by Chiu *et al.* (1998) (from now on referred to as the Chiu–Harvey operator), which has also been used in runaway studies (Chiu *et al.* 1998; Harvey *et al.* 2000; Stahl *et al.* 2016). Allowing runaway-electron energies to be finite but assuming the runaway pitch angle to be zero, they obtained a knock-on source term

$$S_{\text{CH}}(p, \xi, \varphi) = \frac{1}{4\pi\tau_c \ln \Lambda} \frac{p_1^2}{m_e c p \gamma \xi} F(p_1, t) \Sigma(\gamma, \gamma'_1), \quad (2.3)$$

$$\Sigma(\gamma, \gamma_1) = \frac{\gamma_1^2}{(\gamma_1^2 - 1)(\gamma - 1)^2(\gamma_1 - \gamma)^2} \left( (\gamma_1 - 1)^2 - \frac{(\gamma - 1)(\gamma_1 - \gamma)}{\gamma_1^2} \right. \\ \left. \times [2\gamma_1^2 + 2\gamma_1 - 1 - (\gamma - 1)(\gamma_1 - \gamma)] \right), \quad (2.4)$$

where  $\Sigma = (2\pi r_0^2)^{-1} d\sigma/d\gamma$  is the normalized Møller differential cross-section for free–free electron–electron scattering (Møller 1932),  $r_0 = e^2/(4\pi\epsilon_0 m_e c^2)$  is the classical electron radius and  $\gamma_1$  is connected to  $p$  and  $\xi$  by the relation

$$\xi \equiv \xi^*(\gamma, \gamma_1) = \sqrt{\frac{\gamma_1 + 1}{\gamma_1 - 1} \frac{\gamma - 1}{\gamma + 1}} \quad \Leftrightarrow \quad p_1 = \frac{2p\xi}{1 + \xi^2 - \gamma(1 - \xi^2)}, \quad (2.5)$$

where a misprint in the original paper incorrectly replaced the  $\gamma - 1$  factor with  $\gamma_1$ . Since the authors work under the assumption that the runaway pitch angles are negligible, the distribution only appears in the angle-averaged form

$$F(p_1, t) = \int d\xi_1 d\varphi_1 p_1^2 f_e(p_1, \xi_1, t). \quad (2.6)$$

Both models for large-angle collisions presented above suffer from several defects. In particular, they do not conserve particle number, energy or momentum. In addition, the Rosenbluth–Putvinski model assumes that the incoming particle momentum is infinite, which has the consequence that particles can be created with an energy higher than any of the existing runaways. This assumption is not made in the model derived by Chiu *et al.* (1998), where the electron energy distribution is properly taken into account, but all incident runaways are still assumed to have zero pitch angle. The magnitudes of both sources ( $S_{\text{RP}}$  and  $S_{\text{CH}}$ ) increase rapidly with decreasing momenta and the sources are thus sensitive to the choice of cutoff momentum (introduced to avoid double counting of small-angle collisions).

In the following we will derive a knock-on collision model from the Boltzmann collision integral. As we will show, the model takes into account the full momentum dependence of the primary distribution, and conserves particle number, momentum and energy, while also consistently distinguishing between small- and large-angle collisions, therefore avoiding double counting.

### 2.1. The Boltzmann collision integral and the Fokker–Planck limit

The Boltzmann collision operator gives the time rate of change of the distribution function due to binary collisions, described by an arbitrary differential cross-section.

It can be derived with the following heuristic argument (Montgomery & Tidman 1964; Cercignani & Kremer 2002). The collision operator can be defined as  $C_{ab}(f_a) = (dn_a)_{c,ab}/dt dp$ , where  $(dn_a)_{c,ab}$  is the differential change in the density of a species  $a$  due to collisions with species  $b$ , and is defined in terms of the differential cross-section  $d\sigma$  by Lifshitz & Pitaevski (1981) and Cercignani & Kremer (2002)

$$(dn_a)_{c,ab} = f_a(\mathbf{p}_1)f_b(\mathbf{p}_2)\bar{g}_\phi d\bar{\sigma}_{ab} d\mathbf{p}_1 d\mathbf{p}_2 dt - f_a(\mathbf{p})f_b(\mathbf{p}')g_\phi d\sigma_{ab} d\mathbf{p} d\mathbf{p}' dt. \quad (2.7)$$

The first term on the right-hand side, the gain term, describes the rate at which particles  $a$  of momentum  $\mathbf{p}_1$  will scatter to momentum  $\mathbf{p}$ . The second term, the loss term, is the rate at which particles  $a$  scatter away from momentum  $\mathbf{p}$ . Here, we introduced the Møller relative speed  $g_\phi = \sqrt{(\mathbf{v} - \mathbf{v}')^2 - (\mathbf{v} \times \mathbf{v}')^2/c^2}$  and the differential cross-section  $d\sigma_{ab}$  for scattering events  $\mathbf{p}, \mathbf{p}' \rightarrow \mathbf{p}_1, \mathbf{p}_2$ . The barred quantities are defined likewise, but with  $\mathbf{p}$  exchanged for  $\mathbf{p}_1$  and  $\mathbf{p}'$  for  $\mathbf{p}_2$ . Since the interactions are viewed as instantaneous, the time labels of the distribution functions have been suppressed for clarity of notation.

The elastic differential cross-section satisfies the symmetry property  $\bar{g}_\phi d\bar{\sigma}_{ab} d\mathbf{p}_1 d\mathbf{p}_2 = g_\phi d\sigma_{ab} d\mathbf{p} d\mathbf{p}'$  (known as the principle of detailed balance (Weinberg 2005)), allowing the collision operator to be cast in the commonly adopted symmetric form

$$C_{ab}^B = \int d\mathbf{p}' d\sigma_{ab} g_\phi [f_a(\mathbf{p}_1)f_b(\mathbf{p}_2) - f_a(\mathbf{p})f_b(\mathbf{p}')], \quad (2.8)$$

where  $\mathbf{p}_1$  and  $\mathbf{p}_2$  (six degrees of freedom) are uniquely determined in terms of  $\mathbf{p}$  and  $\mathbf{p}'$  by two scattering angles and four constraints by the conservation of momentum and energy,

$$\mathbf{p}_1 + \mathbf{p}_2 = \mathbf{p} + \mathbf{p}', \quad (2.9)$$

$$m_a \gamma_1 + m_b \gamma_2 = m_a \gamma + m_b \gamma'. \quad (2.10)$$

From this collision operator, the Fokker–Planck operator, which is often used in plasma physics, can be obtained by a Taylor expansion to second order in the momentum transfer  $\Delta\mathbf{p} = \mathbf{p}_1 - \mathbf{p}$  (Landau 1936; Akama 1970), motivated by the fact that the cross-section for Coulomb collisions is singular for small deflections. It is then seen that the contribution of small-angle collisions is larger than those of large-angle collisions by a factor of the Coulomb logarithm,

$$\ln \Lambda = \int_{\cot(\theta_{\max}/2)}^{\cot(\theta_{\min}/2)} \frac{d\lambda}{\lambda} = \ln \left( \cot \frac{\theta_{\min}}{2} \right), \quad (2.11)$$

where the maximum centre-of-mass deflection angle for self-collisions is  $\theta_{\max} = \pi/2$  (not  $\pi$  as it is for unlike-species collisions, or collisions would be double counted) and  $\theta_{\min}$  is a cutoff required to regularize the expression, typically chosen as the scattering angle corresponding to impact parameters of order the Debye length,<sup>1</sup> beyond which particles will not interact because of Debye screening.

<sup>1</sup>In the quantum mechanical treatment, it is rather the de-Broglie wavelength of the centre-of-mass momentum transfer  $\lambda = \hbar/|\mathbf{p}_1^* - \mathbf{p}^*|$  that cuts off at the Debye length.

Note that by using a total collision operator  $C_{\text{FP}} + C_{\text{Boltz}}$  as prescribed by (2.1), the Boltzmann operator has effectively been added twice, although different approximations are used to evaluate the two terms. A subset of collisions will therefore be double counted. One way to resolve this issue is to apply the Fokker–Planck operator only to collision angles smaller than some  $\theta_m$ , and the knock-on (Boltzmann) operator for  $\theta > \theta_m$ . The Coulomb logarithm used in the Fokker–Planck operator then ought to be changed from (2.11) to

$$\overline{\ln \Lambda} = \ln \Lambda - \ln \left( \cot \frac{\theta_m}{2} \right). \quad (2.12)$$

When an incident electron of momentum  $p$  knocks a stationary electron to momentum  $p_m$ , the corresponding centre-of-mass scattering angle  $\theta_m$  is given by

$$\cot \frac{\theta_m}{2} = \sqrt{\frac{\gamma - \gamma_m}{\gamma_m - 1}}. \quad (2.13)$$

By using this energy-dependent modification to the Coulomb logarithm, no collisions will be double counted. Indeed, by taking the energy moment of the test-particle collision operator (the sum of Fokker–Planck and Boltzmann), it can be verified that with this choice, the average energy loss rate experienced by a test particle becomes independent of the cutoff  $p_m$ , when  $p_m \ll m_e c$ .

The number of collisions that are double counted can often be significant when this effect is unaccounted for. Assuming  $v_m/c \sim \sqrt{E_c/E}$  to be located at a non-relativistic energy (that is, we assume  $E \gg E_c$ ), the modification to the Coulomb logarithm is approximately given by  $\ln \sqrt{2(E/E_c)(\gamma - 1)}$ . For highly energetic electrons with  $\gamma \sim 50$  and  $E/E_c \sim 100$ , this corresponds to a change of approximately 5, which – depending on plasma parameters – typically constitutes a relative change to the Coulomb logarithm of 25–50 %.

In principle, as  $\theta_m$  approaches the cutoff imposed by Debye screening (or the binding energy of atoms in the case of electrons in neutral media), the Boltzmann operator will account for all collisions and  $\overline{\ln \Lambda} = 0$ . However, this corresponds to a cutoff momentum smaller than thermal,  $p_m \ll p_{\text{Te}}$ , and the assumption of stationary targets is violated when evaluating the operator in the bulk region. In addition, to numerically resolve the Boltzmann operator in a finite-difference scheme, the grid spacing in momentum must be much smaller than  $p_m$ , and it is therefore desirable to choose  $p_m$  as large as allowed while having a well converged description of the secondary generation rate. The sensitivity of the result to the choice of  $p_m$  is investigated in the next section.

In the following we will find it more useful not to work with the symmetric form of the Boltzmann operator given by (2.8), but instead use the alternative given directly from (2.7),

$$\begin{aligned} C_{ab}\{f_a, f_b\}(\mathbf{p}) = & \int d\mathbf{p}_1 \int d\mathbf{p}_2 \frac{\partial \bar{\sigma}_{ab}}{\partial \mathbf{p}} \bar{g}_a f_a(\mathbf{p}_1) f_b(\mathbf{p}_2) \\ & - f_a(\mathbf{p}) \int d\mathbf{p}' g_a f_b(\mathbf{p}') \sigma_{ab}(\mathbf{p}, \mathbf{p}'), \end{aligned} \quad (2.14)$$

where  $\sigma_{ab}(\mathbf{p}, \mathbf{p}') = \int d\mathbf{p}_1 \partial \sigma_{ab} / \partial \mathbf{p}_1$  is the total cross-section.

## 2.2. Derivation of a conservative knock-on operator

For the avalanche problem, one is concerned with the electron-electron Boltzmann operator. We consider the scenario where a small runaway population has been accelerated by an electric field (or other mechanism), leaving a largely intact thermal bulk population. We may then write our electron distribution as  $f_e(\mathbf{p}) = f_{Me}(\mathbf{p}) + \delta f_e(\mathbf{p})$ , where the runaway distribution  $\delta f_e$  is much smaller than the bulk distribution  $f_{Me}$ ,  $\|\delta f_e\| \ll \|f_{Me}\|$  (for example in terms of number densities  $n_{RE} \ll n_e$ ). We may then linearize the bilinear Boltzmann operator by ignoring terms quadratic in  $\delta f_e$ , obtaining

$$C_{ee}^B \{f_e, f_e\} \approx C_{ee}^B \{f_e, f_{Me}\} + C_{ee}^B \{f_{Me}, f_e\} \equiv C_{\text{boltz}}(\mathbf{p}), \quad (2.15)$$

where terms  $C_{ee} \{f_{Me}, f_{Me}\}$  vanish since  $f_{Me}$  is chosen as an equilibrium distribution. The first term, the test-particle term, describes the effect of large-angle collisions on the runaway electrons as they collide with the thermal population. The second term, the field-particle term, describes the reaction of the bulk electrons as they are being struck by the runaways. Intuitively, one could expect this field-particle term to constitute the avalanche knock-on source. We shall show below that this is indeed the case.

Before giving the explicit forms of the collision operator, we will make one final approximation. We assume that both the incident and outgoing electrons in the large-angle collisions are significantly faster than the thermal speed  $v_{Te} = \sqrt{2T_e/m_e}$ , so that we may approximate the bulk population with a Dirac delta function:  $f_{Me}(\mathbf{p}) \approx n_e \delta(\mathbf{p})$ . The collision operator then takes the form

$$C_{ee}^B \{f_e, f_{Me}\} = n_e \int_{q^* > p_1 > q_0} d\mathbf{p}_1 v_1 \frac{\partial \bar{\sigma}_{ee}}{\partial \mathbf{p}} f_e(\mathbf{p}_1) - n_e v \sigma_{ee}(\mathbf{p}) f_e(\mathbf{p}), \quad (2.16)$$

$$C_{ee}^B \{f_{Me}, f_e\} = n_e \int_{p_1 > q^*} d\mathbf{p}_1 v_1 \frac{\partial \bar{\sigma}_{ee}}{\partial \mathbf{p}} f_e(\mathbf{p}_1) - n_e \delta(\mathbf{p}) \int_{p_1 > q_0} d\mathbf{p}_1 v_1 \sigma_{ee}(\mathbf{p}_1) f_e(\mathbf{p}). \quad (2.17)$$

The total cross-section  $\sigma_{ee}(\mathbf{p})$  is given in (A 9) in appendix A. The limiting momenta  $q^*$  and  $q_0$  are determined from constraints imposed by conservation laws. For the gain term, i.e. the first term in each equation, energy conservation in each collision reads  $\gamma_1 = \gamma + \gamma' - 1$ , where  $\gamma$  and  $\gamma'$  are the Lorentz factors of the two electrons after the collision. The conditions  $\gamma' > \gamma$  or  $\gamma' < \gamma$  determines whether  $\gamma$  refers to the bulk particle or runaway particle after the collision, respectively (note that the electrons are in fact indistinguishable, but an artificial distinction like this must be performed in order to avoid double counting). We therefore obtain  $q^*$  from setting  $\gamma' = \gamma$  in the conservation law, giving  $\gamma^* = 2\gamma - 1$ , which corresponds to  $q^* = m_e c \sqrt{\gamma^{*2} - 1}$ .

Similarly, we cannot account for all collisions, since we have assumed the bulk particles to be much slower than the outgoing particles. We therefore choose to account only for those collisions where incident and outgoing particles have momenta larger than some  $p = p_m \gg p_{Te}$ . Setting  $\gamma' = \gamma_m$  then yields the lower limit  $\gamma_0 = \gamma + \gamma_m - 1$ , corresponding to  $q_0 = m_e c \sqrt{\gamma_0^2 - 1}$ . Note that for the total operator  $C_{\text{Boltz}}$ , the two gain terms in (2.16) and (2.17) combine into one integral, taken over all momenta  $p_1 > q_0$ . The full expression is thus independent of the parameter  $q^*$  which distinguishes the two outgoing particles (as is expected, since the distinction is not physically relevant for scattering of identical particles).

We can now derive explicit expressions for the collision operator. Since there are only two degrees of freedom in the scattering process (for example two independent scattering angles), the differential cross-section  $\partial \bar{\sigma}_{ee} / \partial \mathbf{p}$  will invariably contain a delta function. In Møller scattering (relativistic electron-electron scattering), the

cross-section is azimuthally symmetric (assuming the electrons to be spin unpolarized) and takes the form

$$\frac{\partial \bar{\sigma}_{ee}}{\partial \mathbf{p}} = \frac{r_0^2}{(m_e c)^2 p \gamma} \delta(\cos \theta_s - \xi^*) \Sigma(\gamma, \gamma_1), \quad (2.18)$$

$$\cos \theta_s = \frac{\mathbf{p}_1 \cdot \mathbf{p}}{p_1 p} \equiv \xi_s, \quad (2.19)$$

where  $\theta_s$  is the deflection angle,  $\Sigma$  is defined in (2.4) and  $\xi^*$  is defined in (2.5). The delta function enforces the relation between scattering angle and energy transfer that follows from the conservation of 4-momentum. The gain term then takes the form

$$\begin{aligned} n_e \int d\mathbf{p}_1 v_1 \frac{\partial \bar{\sigma}_{ee}}{\partial \mathbf{p}} f_e(\mathbf{p}_1) &= \frac{1}{4\pi \tau_c \ln \Lambda} \frac{1}{p \gamma} \int dp_1 \frac{p_1^3}{\gamma_1} \Sigma(\gamma, \gamma_1) \\ &\times \int d\xi_1 d\varphi_1 \delta(\xi_s - \xi^*) f_e(\mathbf{p}_1). \end{aligned} \quad (2.20)$$

This expression (when choosing integration limits appropriate for the field-particle term) is the generalized ‘knock-on source term’  $S$ , which reduces to the expressions given by Rosenbluth & Putvinski (1997) and Chiu *et al.* (1998) – (2.2) and (2.3), respectively – using appropriate approximations, as shown in appendix B. This connection has not been acknowledged in previous studies, to the degree that Chiu *et al.* (1998) incorrectly ascribe the discrepancy between their result and that of Besedin & Pankratov (1986) by the fact that ‘The present expressions are simply a statement of the total rate at which electrons in different velocity-space elements of primary electrons knock a collection of cold bulk electrons into velocity-space elements of the secondary electrons. The expression in (Besedin & Pankratov 1986) uses a Boltzmann-like integral operator’. In fact, as we show in appendix B, the approaches are completely equivalent, and the discrepancy is the result of an error in the calculation of Besedin & Pankratov (1986).

There are multiple ways of carrying out the integration over the delta function; if we assume a distribution function independent of gyroangle,  $f_e(\mathbf{p}_1) = f_e(p_1, \cos \theta_1)$ , a few convenient expressions are given by

$$\begin{aligned} \int_{-1}^1 d\xi_1 \int_0^{2\pi} d\varphi_1 \delta(\xi_s - \xi^*) f_e(p_1, \xi_1) &= \int_0^{2\pi} d\varphi_s f_e(p_1, \xi_1) \\ &= 2 \int_{\cos(\theta+\theta^*)}^{\cos(\theta-\theta^*)} d\xi_1 \frac{f_e(p_1, \xi_1)}{\sqrt{1 - \xi^{*2} - \xi_1^2 - \xi^2 + 2\xi^* \xi_1 \xi}} \\ &= 2\pi \sum_L f_L(p_1) P_L(\xi) P_L(\xi^*), \end{aligned} \quad (2.21)$$

where we have introduced the quantities

$$\left. \begin{aligned} \cos \varphi_s &= \frac{\xi_1 - \xi^* \xi}{\sqrt{1 - \xi^{*2}} \sqrt{1 - \xi^2}}, \\ f_L(p) &= \frac{2L+1}{2} \int_{-1}^1 d\xi f_e(p, \xi) P_L(\xi). \end{aligned} \right\} \quad (2.22)$$

In particular the form involving Legendre polynomials  $P_L$  is a powerful result, as it demonstrates that the linearized Boltzmann operator is diagonal in  $L$ , in the sense that if  $C_{\text{Boltz}}(\mathbf{p}) = \sum_L C_L(p)P_L(\cos \theta)$ , then  $C_L$  depends only on  $f_L$  (and not other  $f_l$  with  $l \neq L$ ). This behaviour exhibits the spherical symmetry inherent in scattering on stationary targets. Utilizing this property leads to significant practical gains in terms of numerical computation times. Analogous expressions in terms of Legendre polynomials and the integration over  $\varphi_s$  were also found by Gurevich & Zybin (2001) for the so-called ionization integral in neutral gases. The form of the integral taken over  $\xi_1$  was obtained by Helander, Lisak & Ryutov (1993) in the analogous problem of elastic nucleon–nucleon scattering, and equivalent formulations were also recently given by Aleynikov *et al.* (2014) and Boozer (2015).

The Legendre modes of the collision operator are explicitly given by

$$C_L\{f_e, f_{Me}\} = \frac{(m_e c)^{-3}}{2\tau_c \ln \Lambda} \frac{1}{\gamma p} \int_{q_0}^{q^*} dp_1 \frac{p_1^3}{\gamma_1} f_L(p_1) P_L(\xi^*) \Sigma(\gamma, \gamma_1) - \frac{1}{4\tau_c \ln \Lambda} \frac{v}{c} f_L(p) \int_{\gamma_m}^{\gamma+1-\gamma_m} d\gamma_1 \Sigma(\gamma_1, \gamma), \quad (2.23)$$

$$C_L\{f_{Me}, f_e\} = \frac{(m_e c)^{-3}}{2\tau_c \ln \Lambda} \frac{1}{\gamma p} \int_{q^*}^{\infty} dp_1 \frac{p_1^3}{\gamma_1} f_L(p_1) P_L(\xi^*) \Sigma(\gamma, \gamma_1) - \frac{(m_e c)^{-1}}{4\tau_c \ln \Lambda} \delta_{L,0} \frac{\delta(p)}{p^2} \int_{q_0(p_m)}^{\infty} dp' \frac{p'^3}{\gamma'} f_0(p') \int_{\gamma_m}^{\gamma'+1-\gamma_m} d\gamma_1 \Sigma(\gamma_1, \gamma'). \quad (2.24)$$

Note further that since we only consider those collisions where both the incident and outgoing particles have momenta  $p > p_m$ , the gain terms must only be applied for  $\gamma > \gamma_m$ , while the test-particle loss term is applied for  $\gamma > 2\gamma_m - 1$ . In appendix A it is explicitly demonstrated that this collision operator conserves density, momentum and energy.

A qualitative illustration of the large-angle collision operators discussed here is shown in figure 1. A test runaway distribution (figure 1a) was generated by applying a constant electric field  $E = 15E_c$  for a short time  $t \approx 0.5\tau_c$  with  $Z_{\text{eff}} = 5$ , and the large-angle collision operators were evaluated in the final time step. The figures show a snapshot of where large-angle collisions between runaways and bulk particles create or remove electrons in phase space; comparing 1(c) and 1(d) shows that the Chiu–Harvey operator creates secondary runaways in a significantly smaller region in momentum space than the full field-particle operator, however the total number of secondary runaways created is equal between the models. Figure 1(b) shows the Boltzmann test-particle operator, illustrating the reaction of the already present runaways: they are removed at small pitch angles where the runaway distribution is largest, and placed at larger pitch angles and lower energy. The sum of figure 1(b,d) is the full Boltzmann operator which conserves particle number, momentum and energy.

Note finally that all of the knock-on models described in this paper share the assumption of a stationary bulk, which means that the operators can only be evaluated at speeds much larger than the thermal speed  $v_{Te}$ . Since the sources must be applied for speeds smaller than the critical speed  $v_c$  in order to accurately capture the runaway rate, the condition  $v_{Te} \ll v_c$  limits the electric-field values to  $\sqrt{E} \ll \sqrt{E_D}/2$  (effectively forming a lower limit in density and an upper limit in temperature for a given  $E$ ). As a consequence, avalanche generation in electric fields large enough for

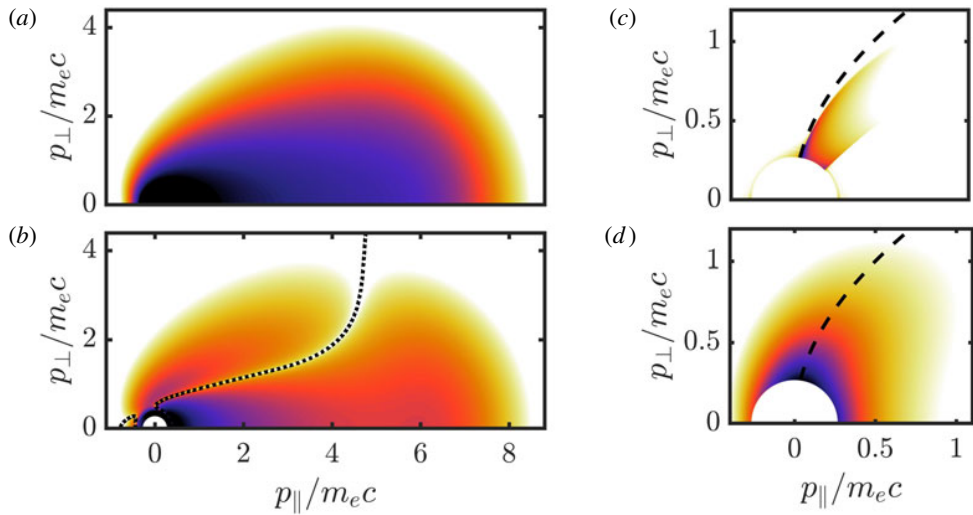


FIGURE 1. Illustration of the large-angle collision operators investigated in this study. Darker colours represent larger amplitudes (in arbitrary units), where white and black are separated by 3 orders of magnitude. (a) The distribution function  $\log f_e$  with which we evaluate the large-angle collision operator; (c) the Chiu–Harvey operator  $\log C_{\text{CH}}$ ; (d) the full field-particle operator  $\log C_{\text{boltz}}^{(\text{fp})}$  (dashed: the line  $\xi = \sqrt{(\gamma - 1)/(\gamma + 1)}$ , where the Rosenbluth–Putvinski operator creates knock-ons); (b) the magnitude of the full test-particle operator  $\log |C_{\text{boltz}}^{(\text{fp})}|$ , where the dotted line separates the region of negative contributions (to the right) from the positive contributions (to the left).

Dreicer generation to be significant is not accessible by the models used here. This limitation would be resolved by accounting for the velocity distribution of the target population in (2.7), resulting in a significantly more complicated operator. However, in many scenarios of interest this is not an issue; the critical velocity tends to be significantly larger than thermal, or is comparable only for a relatively short period of time during which a runaway seed is generated, which then proceeds to grow primarily by avalanche generation.

### 3. Numerical study of the effect of large-angle collisions

We use the kinetic equation solver CODE (Lande man *et al.* 2014; Stahl *et al.* 2016) to compare the various models for the knock-on collision operator. We use CODE to solve the relativistic 0D+2P kinetic equation for the electron distribution

$$\frac{\partial f_e}{\partial t} + \left\langle \frac{\partial}{\partial \mathbf{p}} \cdot [(\mathbf{F}_L + \mathbf{F}_S) f_e] \right\rangle = C_{\text{ei}} + C_{\text{ee}} + C_{\text{boltz}}, \quad (3.1)$$

where  $\mathbf{F}_L$  is the Lorentz force, and  $\mathbf{F}_S$  is the radiation reaction force associated with synchrotron radiation and the brackets denote averaging over the azimuthal (gyro) angle.  $C_{\text{ei}}$  and  $C_{\text{ee}}$  are the gyroaveraged Fokker–Planck collision operators for electron–ion and electron–electron collisions, respectively. The thermal bulk population is resolved in the simulations, as well as the relativistic runaway tail. The collision operator  $C_{\text{ei}} + C_{\text{ee}}$  and the numerical scheme used are described in Landre man *et al.*

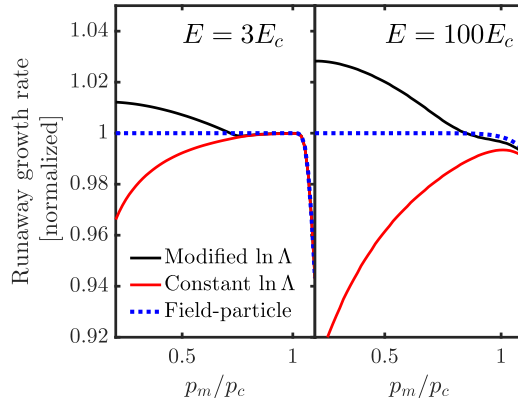


FIGURE 2. Runaway growth rate as function of momentum cutoff parameter  $p_m$  for two different electric fields, normalized to the field-particle  $p_m = 0$  value. Lines correspond to (dotted blue) the field-particle Boltzmann operator, equation (2.24) and (solid) the full operator including the test-particle operator when (red)  $\ln \Lambda$  is held fixed or (black) modified according to (2.12), which is the physically most correct model. Plasma parameters: thermal electron density  $n_e = 10^{20} \text{ m}^{-3}$ ; temperature  $T_e = 100 \text{ eV}$ .

(2014). In the numerical solutions of (3.1) a Dirichlet boundary condition  $f_e = 0$  is imposed at the upper boundary  $p_{\max}$  in momentum. The boundary is chosen large enough for the results to be insensitive to variations in  $p_{\max}$  or details of the boundary condition; the value of the distribution is naturally negligibly small near the boundary, since it asymptotically tends to decrease exponentially with energy.

First, we will study the sensitivity of the avalanche dynamics to the arbitrary cutoff parameter  $p_m$  and investigate the effects of adding the test-particle Boltzmann operator, which restores conservation laws in the knock-on collisions. We then focus on two scenarios: (i) we revisit the classical calculation of the steady-state avalanche growth rate in a constant electric field, (ii) we calculate the runaway growth rate in the near-critical field, accounting for synchrotron energy loss.

### 3.1. Sensitivity to the cutoff parameter $p_m$

We will now demonstrate that our complete knock-on model satisfies the essential property that the solutions to the kinetic equation are independent of the arbitrary cutoff momentum  $p_m$ , as long as it is chosen small enough. To determine the sensitivity of the solutions to  $p_m$ , we will consider the instantaneous runaway growth rate when the primary runaway population is described by a shifted Maxwellian runaway distribution  $f_{\text{RE}} \propto \exp[-(p - p_0)^2/q^2]$ . For this test we have chosen the momentum  $p_0 \approx 6m_e c$  in the parallel direction, with width  $q \approx 0.6m_e c$ . Two electric-field strengths are investigated, a low-field case where  $E = 3E_c$  and a high-field case  $E = 100E_c$ . The resulting growth rates are shown in figure 2, as a function of the cutoff  $p_m$  after a short time  $0.03\tau_c$ . The growth rate obtained using the field-particle operator alone is nearly independent of  $p_m$  as long as it is smaller than  $p_c$ , indicating that secondary particles created with momentum  $p < p_c$  are unlikely to run away. For the Rosenbluth–Putvinski operator, this behaviour was also observed by Nilsson *et al.* (2015).

When the test-particle operator is added, but the Coulomb logarithm  $\ln \Lambda$  is left unmodified, the growth rate is decreased. This can be understood from the fact

that the test-particle operator represents a source of energy loss for the runaways, which diverges logarithmically as  $p_m \rightarrow 0$ . When  $\ln \Lambda$  is modified (black line in figure 2, representing the most physically accurate model), the mean energy loss rate of a runaway becomes independent of  $p_m$ . The growth rate, however, is found to increase with decreasing  $p_m$ , settling to a constant value in the limit  $p_m \rightarrow 0$ . The underlying mechanism for this behaviour is that a fraction of all collisions are now accounted for with a Boltzmann operator rather than with a Fokker–Planck operator. This leads to an increase in the runaway probability for particles with  $p < p_c$ , since the Boltzmann operator fully captures the stochastic nature of the collisions; instead of continuously experiencing the average energy loss, an electron is accelerated freely until it undergoes a collision, by which point it may have gained enough energy to enter the runaway region ( $p > p_c$ ). Note that this effect only appears to modify the growth rate with a few per cent, the effect being weaker for smaller electric fields. The effect is, however, directly proportional to  $1/\ln \Lambda$ , as it depends on the relative importance of small- and large-angle collisions. This implies that for higher-density or lower-temperature plasmas, the effect can be expected to be more pronounced.

It should be remarked that the field-particle knock-on operator uses a constant Coulomb logarithm in the Fokker–Planck operator, yet is still well behaved when  $p_m$  becomes small. We have pointed out that the field-particle knock-on operators, like those used in previous runaway avalanche studies, double count collisions with the Fokker–Planck operator. However, they do so only with the field-particle Fokker–Planck operator, and not the test-particle operator which describes the friction on runaways. Therefore, only the Coulomb logarithm in the field-particle operator should be modified when using such models. The field-particle Fokker–Planck operator is essential when considering the dynamics of the bulk population, however it does not significantly affect the avalanche growth rate, thereby explaining the insensitivity to  $p_m$  for  $p_m \lesssim p_c$ .

### 3.2. Steady-state avalanche growth rate at moderate electric fields

The steady-state avalanche growth rate in a constant electric field is a classical result; Rosenbluth and Putvinski derived the growth rate formula (1.2) in 1997. After an initial transient, the distribution function tends to approach the asymptotic quasi-steady-state behaviour  $f(t, p, \xi) \sim n_{\text{RE}}(t)\bar{f}(p, \xi)$ , where  $\int \bar{f} \, d\mathbf{p} = 1$ . The kinetic equation, being linear in the runaway distribution, then prescribes that the runaway population will grow with a constant growth rate

$$\Gamma = \frac{1}{n_{\text{RE}}} \frac{dn_{\text{RE}}}{d(t/\tau_c)}. \quad (3.2)$$

In figure 3 we show the growth rate  $\Gamma$  obtained from numerical solutions of the kinetic equation using various models for the knock-on operator, for moderate electric fields ranging from  $E = 1.5E_c$  to  $E = 30E_c$  and  $Z_{\text{eff}} = 1$ . We see that using the Rosenbluth–Putvinski knock-on operator leads to a significant error compared to the more accurate models when the electric field is near the critical – of order 30% at  $1.5E_c$ . At larger electric fields the error is insignificant. Interestingly, the full Boltzmann operator (solid black line) yields a correction of only a few per cent compared to the field-particle operator alone. This means that the test-particle part of the operator does not influence the growth rate significantly. This result is robust; it is not affected by changes in thermal electron density and temperature, and only slightly modified by changes in the effective charge. Note that a significant error

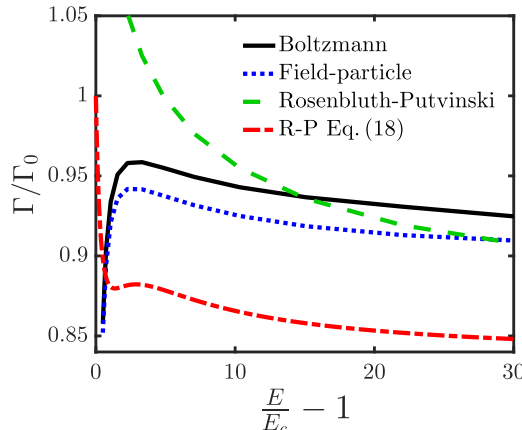


FIGURE 3. Steady-state runaway growth rate normalized to the diffusion-free result  $\Gamma_0 = (E/E_c - 1)/2 \ln \Lambda$ , equation (1.2), in the presence of a constant electric field, neglecting radiation losses. The red dot-dashed line represents the theoretical prediction, Rosenbluth & Putvinski (1997, equation (18)). Plasma parameters: thermal electron density  $n_e = 10^{20} \text{ m}^{-3}$ ; temperature  $T_e = 100 \text{ eV}$ ; effective charge  $Z_{\text{eff}} = 1$ .

is obtained if one fails to account for the double counting of small-angle collisions – the size of this error is sensitive to the cutoff  $p_m$ , diverging logarithmically as it approaches zero, and the result is included primarily for illustrative purposes.

### 3.3. Avalanche generation in a near-threshold electric field with synchrotron radiation losses

In tokamaks, the runaway dynamics in electric fields near the runaway generation threshold is of particular interest. Due to the large self-inductance of tokamaks, after a transient phase during which the ohmic current of the background is dissipated, the electric field will tend towards that value  $E_a$  – the threshold field – for which the runaway growth rate vanishes,  $\Gamma(E_a) = 0$  (Breizman 2014).

At these low electric fields, radiation losses have a large impact, and cannot be ignored in the calculation of the runaway growth rate. In this section, we will include the effect of synchrotron radiation losses and investigate runaway generation when  $E \sim E_a$ . A model for this was recently presented by Aleynikov & Breizman (2015) (referred to as A&B), using a simplified kinetic equation following a method used by Lehtinen, Bell & Inan (1999). An interesting prediction by the A&B model was that reverse knock-on can have a significant effect on the growth rate, where for electric fields  $E \lesssim E_a$ , existing runaways will be slowed down to  $v < v_c$  in single large-angle collision events. This leads to a negative avalanche growth rate, which previous large-angle collision models are incapable of describing, as this process is inherently a large-angle test-particle effect. Using the knock-on operator presented in this work, we will now assess the magnitude of the reverse knock-on effect, as well as determine the threshold field  $E_a$  and the growth rate when  $E \sim E_a$ , accounting for radiation losses.

In figure 4 we show how the quasi-steady-state growth rate  $\Gamma$  depends on the electric-field strength, similar to figure 4 of A&B. We use the same plasma parameters  $Z_{\text{eff}} = 5$  and  $\tau_r = 3m_e n_e \ln \Lambda / (2\varepsilon_0 B^2) = 70$  (corresponding to  $B \approx 1.81 \text{ T}$

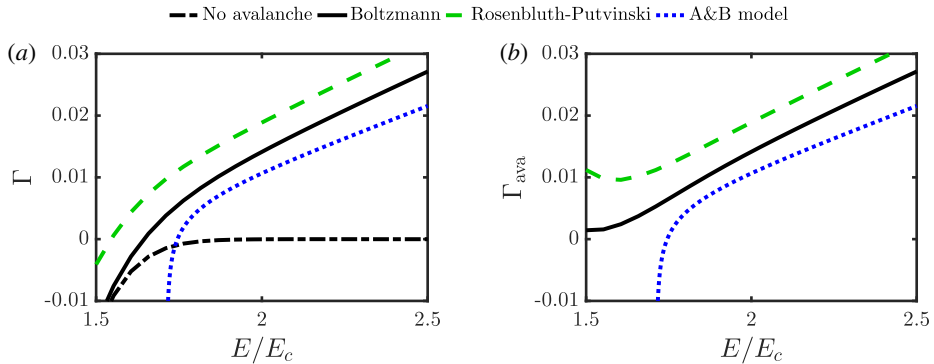


FIGURE 4. Steady-state runaway growth rate in the presence of a constant electric field, accounting for synchrotron radiation losses and using various models for the large-angle collision operator: the Rosenbluth–Putvinski operator, equation (2.2) (green, dashed); the Boltzmann operator equations (2.23)–(2.24) (black, solid) and without any large-angle collision operator (black, dash-dotted). For comparison we have included equation (11) of Aleynikov & Breizman (2015) (blue, dotted). In (b), the avalanche-free growth rate (black, dotted line in (a)) has been subtracted to yield a pure ‘avalanche growth rate’  $\Gamma_{\text{ava}}$ . Plasma parameters: thermal electron density  $n_e = 10^{20} \text{ m}^{-3}$ ; temperature  $T_e = 1 \text{ keV}$ ; effective charge  $Z_{\text{eff}} = 5$ ,  $B = 1.81 \text{ T}$ .

at  $n_e = 10^{20} \text{ m}^{-3}$ ), although a slight discrepancy occurs due to our  $\ln \Lambda = 14.9$  – consistent with the background parameters chosen – compared to their  $\ln \Lambda = 18$ . In this scenario, the A&B threshold electric field is  $E_a \approx 1.71E_c$ . Several models for the knock-on operator are included in the comparison, in addition to the no-avalanche case since we are now interested in the sub-threshold dynamics. The simulations are run for approximately 300 relativistic collision times  $\tau_c$ , upon which the growth rates have settled to the asymptotic steady-state value, corresponding to approximately 6 s with the plasma parameters given above.

It is interesting to observe that the test-particle operator, which allows runaways to be thermalized in a single large-angle collision, does not significantly modify the dynamics, in contrast to the theoretical prediction by Aleynikov & Breizman (2015). Unlike the A&B model, which predicts a significant negative growth rate due to this effect when  $E \lesssim E_a$ , we find that the large-angle collision operator always adds a positive contribution to the total growth rate compared to the no-avalanche case (see figure 4(b) where the no-avalanche growth rate has been subtracted). It can be concluded that the negative growth rates in the sub-threshold regime is a result primarily of the Fokker–Planck dynamics, rather than of large-angle collisions. The reason for this discrepancy to the A&B model can be understood by considering the behaviour of the distribution shape functions  $\bar{f} = f/n$ , defined before (3.2), which are illustrated in figures 5 and 6. A&B predicted the distribution to be a delta function in momentum, located at the point of force balance,  $p_{\text{max}}$ . When this occurs near the critical speed  $v_c$ , runaways cannot produce knock-ons with sufficient energy to become runaway. Large-angle collisions then act only to slow down the existing population. In numerical solutions of the full kinetic equation, conversely, it is found that the runaway population takes on a wide energy spectrum, and there will always be sufficiently many runaways with the energy required to produce new runaways to counter the reverse knock-on effect.

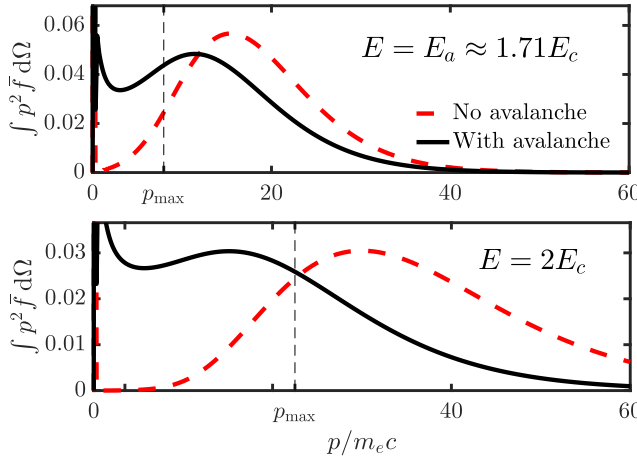


FIGURE 5. Steady-state runaway momentum distributions  $\int p^2 \bar{f} d\Omega$  (defined to have unit area under the shown curves). Included in the panels is the maximum runaway momentum  $p_{\max}$  predicted by Aleynikov & Breizman (2015). Plasma parameters: background electron density  $n_e = 10^{20} \text{ m}^{-3}$ ; temperature  $T_e = 1 \text{ keV}$ ; effective charge  $Z_{\text{eff}} = 5$ ,  $B = 1.81 \text{ T}$ .

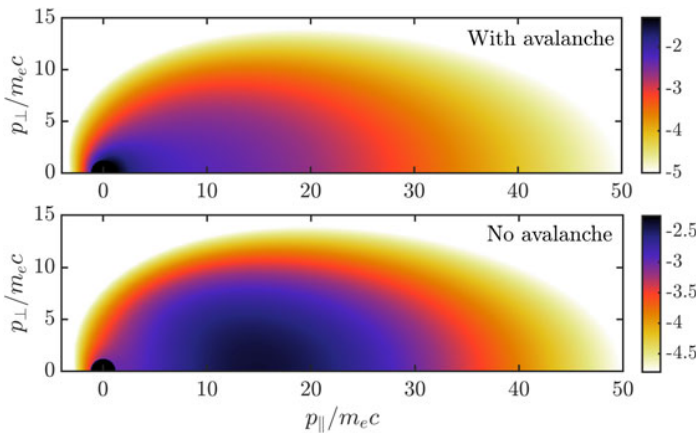


FIGURE 6. Steady-state normalized runaway momentum distributions  $\log_{10} \bar{f}$  from the  $E = E_a$  case of figure 5.

A notable difference between the A&B model and full solutions of the kinetic equation considered here, which can play an important role when considering the decay of the runaway current in tokamaks, is that the growth rate is not as sensitive to variations in electric field close to (but below) the effective critical field  $E_a$  as predicted by A&B. It is known that the decay rate is determined primarily by the value of the effective critical field  $E_a$  when the self-inductance can be considered large (roughly when the total runaway current is much larger than  $\sim 200 \text{ kA}$ ) (Breizman 2014). Since the threshold field  $E_a$  given by the A&B model is reasonably accurate in many cases, it is likely that it may be used to describe runaway current decay in large-current scenarios. However, for moderate runaway currents in the range

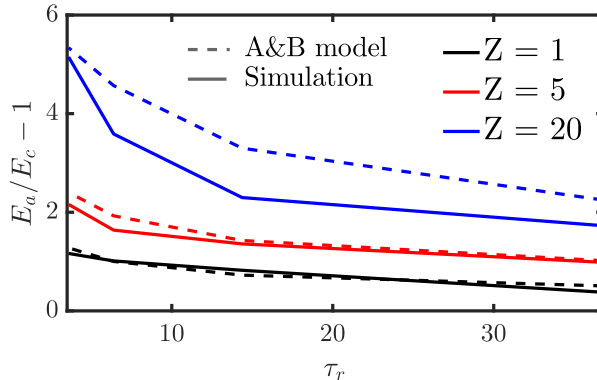


FIGURE 7. Threshold electric field determined numerically from solutions of the kinetic equation, as a function of normalized magnetic-field strength  $\tau_r$  for various values of the effective charge. Predictions by the theoretical model of Aleynikov & Breizman (2015) are included for comparison.

of hundreds of kA, the overall shape of  $\Gamma(E)$  will determine its evolution, which previous theoretical models fail to describe – particularly for electric fields  $E \lesssim E_a$ .

Finally, we show the effective critical field  $E_a$  calculated numerically by CODE for a wide range of  $Z_{\text{eff}}$  and magnetic-field strength parameters  $\tau_r = 6\pi\epsilon_0^2 m_e^2 c^3 / e^4 B^2 \tau_c$ . This is shown in figure 7, along with the values given by the A&B model by determining the roots of their equation (11). It is seen that the predictions of Aleynikov & Breizman (2015) are typically accurate unless the effective charge is very large, and are most accurate for sufficiently small or large  $B$ . The observed trend in the accuracy of their model is unexpected, since they have utilized fast pitch-angle equilibration time (large  $Z_{\text{eff}}$ ) and weak magnetic field (large  $\tau_r$ ) in order to reduce the kinetic equation to a tractable form.

#### 4. Conclusions

Predictions indicate that a major part of the initial plasma current in large tokamaks can be converted to runaway-electron current. This is partly due to the large plasma size limiting the loss of runaway-electron seeds, but more importantly, it is due to the avalanche mechanism which leads to an exponential growth of runaways. The runaway-electron growth rate due to avalanching is exponentially sensitive to the plasma current, and avalanche runaway generation is therefore expected to be a serious issue in ITER and other high-current reactor-scale tokamaks. As the plasma current in present devices cannot be increased above a few megaamperes, full experimental simulation of high-current tokamak disruptions is not possible. Therefore it is very important to develop accurate theoretical models from first principles, to test the validity of approximative models.

In this paper we have developed a fully conservative knock-on collision operator derived from the relativistic Boltzmann operator, and compared it to existing models. Close to the critical electric field, the new model leads to behaviour significantly different from that of the widely used Rosenbluth & Putvinski (1997) avalanche model. This influences the predictions for the transformation of a runaway seed to an avalanching population; fortunately the new operator predicts a lower growth rate

than Rosenbluth & Putvinski (1997) and therefore the implications for ITER should be positive, although the difference between models is marginal for high electric fields. We have also described how to resolve the issue of double counting the small- and large-angle collisions, and have illustrated the importance of this issue. The new operator includes both the test-particle and field-particle parts of the collision operator, however we have shown that the test-particle part does not influence the growth rate significantly.

Using kinetic simulations we have performed a careful study of the runaway growth rate in the presence of synchrotron radiation losses and several different avalanche operators. Again, we find a significant difference in runaway rates close to the critical field, however, the effective critical field appears to be well reproduced by simplified models unless the effective charge is very large.

### Acknowledgements

The authors would like to thank L. Hesslow, I. Pusztai, E. Hirvijoki, J. Connor, G. Papp and M. Landreman for constructive discussions. This work was supported by the Swedish Research Council (Dnr. 2014-5510) and the European Research Council (ERC-2014-CoG grant 647121). This work has been carried out within the framework of the EUROfusion Consortium and has received funding from the Euratom research and training programme 2014–2018 under grant agreement no. 633053. The views and opinions expressed herein do not necessarily reflect those of the European Commission.

### Appendix A. Density, momentum and energy conservation

The full electron–electron Boltzmann operator  $C$  is known to satisfy conservation of density, momentum and energy, expressed by the relations

$$\left. \begin{aligned} \int d\mathbf{p} C(f_e) &= 0, \\ \int d\mathbf{p} \mathbf{p} C(f_e) &= 0, \\ \int d\mathbf{p} m_e c^2 (\gamma - 1) C(f_e) &= 0, \end{aligned} \right\} \quad (A 1)$$

or in our case of a cylindrically symmetric plasma, in terms of the Legendre modes of the collision operator,

$$\left. \begin{aligned} \int dp p^2 C_0(p) &= 0, \\ \int dp p^3 C_1(p) &= 0, \\ \int dp p^2 (\gamma - 1) C_0(p) &= 0. \end{aligned} \right\} \quad (A 2)$$

We will show that our explicit form of the knock-on operator, accounting only for collisions involving electrons with momenta  $p > p_m$ , satisfies the same conservation laws. Taking the full operator  $C_L = C_L\{f_e, f_{Me}\} + C_L\{f_{Me}, f_e\}$  from (2.23)–(2.24), noting that the gain term only applies for  $\gamma > \gamma_m$  and the loss term for  $\gamma > 2\gamma_m - 1$ , we find upon integration (changing momentum integrals to energy integrals by  $v dp = m_e c^2 d\gamma$ )

$$\begin{aligned} \Gamma_L\{h\} &= \int_0^\infty dp p^2 h(p) C_L(p) \\ &= \frac{m_e c}{2\tau_c \ln \Lambda} \int_{\gamma_m}^\infty d\gamma h(p) \int_{\gamma+\gamma_m-1}^\infty d\gamma_1 p_1^2 \Sigma(\gamma, \gamma_1) P_L(\xi^*) f_L(p_1) \\ &\quad - \frac{m_e c}{4\tau_c \ln \Lambda} \int_{2\gamma_m-1}^\infty d\gamma p^2 h(p) f_L(p) \int_{\gamma_m}^{\gamma+1-\gamma_m} d\gamma_1 \Sigma(\gamma_1, \gamma) \\ &\quad - \frac{m_e c h(0)}{4\tau_c \ln \Lambda} \delta_{L,0} \int_{2\gamma_m-1}^\infty d\gamma p^2 f_0(p) \int_{\gamma_m}^{\gamma+1-\gamma_m} d\gamma_1 \Sigma(\gamma_1, \gamma). \end{aligned} \quad (\text{A } 3)$$

In the first term, the integration order can be interchanged by using

$$\int_{\gamma_m}^\infty d\gamma \int_{\gamma+\gamma_m-1}^\infty d\gamma_1 = \int_{2\gamma_m-1}^\infty d\gamma_1 \int_{\gamma_m}^{\gamma_1+1-\gamma_m} d\gamma. \quad (\text{A } 4)$$

Exchanging the names of the dummy variables  $\gamma_1$  and  $\gamma$  in this term then yields

$$\begin{aligned} \frac{2\tau_c \ln \Lambda}{m_e c} \Gamma_L\{h\} &= \int_{2\gamma_m-1}^\infty d\gamma p^2 f_L(p) \\ &\times \int_{\gamma_m}^{\gamma+1-\gamma_m} d\gamma_1 \left[ h(p_1) P_L \left( \frac{\gamma+1}{\gamma_1+1} \frac{p_1}{p} \right) - \frac{h(p) + \delta_{L,0} h(0)}{2} \right] \Sigma(\gamma_1, \gamma). \end{aligned} \quad (\text{A } 5)$$

The conservation of density, momentum and energy correspond to the conditions  $0 = \Gamma_0\{1\} = \Gamma_1\{p\} = \Gamma_0\{\gamma - 1\}$ , respectively. With  $L = 0$  and  $h = 1$ , the bracket term in the  $\gamma_1$ -integral vanishes identically; therefore the knock-on operator will conserve density independently of the differential cross-section  $\Sigma(\gamma_1, \gamma) = (2\pi r_0^2)^{-1} \partial\sigma/\partial\gamma$ . For the other two conditions, one finds

$$\begin{aligned} 2\tau_c \ln \Lambda \Gamma_1\{p\} &= (m_e c)^2 \int_{2\gamma_m-1}^\infty d\gamma p(\gamma+1) f_1(p) \\ &\times \int_{\gamma_m}^{\gamma+1-\gamma_m} d\gamma_1 \left[ \gamma_1 - 1 - \frac{\gamma-1}{2} \right] \Sigma(\gamma_1, \gamma), \end{aligned} \quad (\text{A } 6)$$

$$\begin{aligned} 2\tau_c \ln \Lambda \Gamma_0\{\gamma - 1\} &= m_e c \int_{2\gamma_m-1}^\infty d\gamma p^2 f_0(p) \\ &\times \int_{\gamma_m}^{\gamma+1-\gamma_m} d\gamma_1 \left[ \gamma_1 - 1 - \frac{\gamma-1}{2} \right] \Sigma(\gamma_1, \gamma). \end{aligned} \quad (\text{A } 7)$$

The integrals over  $\gamma_1$  will vanish for all cross-sections that respect the indistinguishability of the electrons, i.e. for which  $\Sigma(\gamma_1, \gamma) = \Sigma(\gamma_2, \gamma)$  where  $\gamma_2 = \gamma + 1 - \gamma_1$ . This follows directly from the observation that

$$\left[ \gamma_1 - 1 - \frac{\gamma-1}{2} \right] = - \left[ \gamma_2 - 1 - \frac{\gamma-1}{2} \right], \quad (\text{A } 8)$$

confirming that our operator indeed satisfies the conservation laws.

### A.1. Total cross-section

For our case of the Møller cross-section, the differential cross-section of (2.4) can be integrated analytically to produce the total cross-section. One obtains

$$\begin{aligned}\sigma(p) &= \int_{\gamma_m}^{\gamma+1-\gamma_m} d\gamma_1 2\pi r_0^2 \Sigma(\gamma_1, \gamma) \\ &= \frac{2\pi r_0^2}{\gamma^2 - 1} \left[ \left( \frac{\gamma + 1}{2} - \gamma_m \right) \left( 1 + \frac{2\gamma^2}{(\gamma - \gamma_m)(\gamma_m - 1)} \right) - \frac{2\gamma - 1}{\gamma - 1} \ln \frac{\gamma - \gamma_m}{\gamma_m - 1} \right].\end{aligned}\quad (\text{A } 9)$$

## Appendix B. The Chiu–Harvey and Rosenbluth–Putvinski models

We derive the Chiu–Harvey source by assuming runaways to have a negligible perpendicular velocity component, i.e. that  $f_e$  is well described by a delta function in pitch angle,  $f_e(p_1, \cos \theta_1) = F(p_1) \delta(\cos \theta_1 - 1) / (2\pi p_1^2)$  with  $F(p_1) = 2\pi \int_{-1}^1 d\cos \theta_1 p_1^2 f_e(p_1, \cos \theta_1)$ . From (2.20) we then find

$$\begin{aligned}S_{\text{CH}} &= \frac{1}{4\pi \tau_c \ln \Lambda} \frac{1}{p\gamma} \int_{q^*}^{\infty} dp_1 \frac{p_1}{\gamma_1} F(p_1) \Sigma(\gamma, \gamma_1) \int_{-1}^1 d\xi_1 \delta(\xi_s - \xi^*) \delta(\xi_1 - 1) \\ &= \frac{1}{4\pi \tau_c \ln \Lambda} \frac{1}{p\gamma} \int_{q^*}^{\infty} dp_1 \frac{p_1}{\gamma_1} F(p_1) \Sigma(\gamma, \gamma_1) \delta(\xi - \xi^*) \\ &= \frac{1}{4\pi \tau_c \ln \Lambda} \frac{p_1^2}{p\gamma\xi} F(p_1) \Sigma(\gamma, \gamma_1) H(p_1 - q^*),\end{aligned}\quad (\text{B } 1)$$

where  $H(x)$  denotes the Heaviside step function, and we used

$$\left. \frac{dp_1}{d\xi^*} \right|_{\xi^*=\xi} = \frac{\gamma_1 p_1}{\xi}.\quad (\text{B } 2)$$

We also utilized  $\cos \theta_s = \cos \theta$  when  $\cos \theta_1 = 1$ , and kinematics constrain the incident momentum  $p_1$  according to (2.5). This result agrees exactly with the Chiu–Harvey source  $S_{\text{CH}}$  of (2.3). In terms of an expansion in Legendre polynomials, the Chiu–Harvey avalanche source is obtained from the general field-particle operator in (2.24) simply by replacing  $f_L(p)$  by  $(2L + 1)f_0(p)$ , corresponding to the delta function approximation. In this representation, however, the approximation holds limited appeal as it does not provide a significant simplification of the collision operator; indeed, compared to the full operator it requires a larger number of Legendre polynomials to be retained since the true  $f_L$  decreases rapidly with  $L$  for sufficiently large  $L$ .

By the addition of the sink terms in (2.23) and (2.24), and extending the integration limit down from  $q^*$  to  $q_0$ , the Chiu–Harvey operator can be made conservative. However, the delta function assumption in pitch angle causes incorrect momentum dynamics, and the total momentum of the distribution will not be conserved in this treatment. This can be corrected by treating the  $L = 1$  mode exactly, corresponding to a total conservative knock-on operator in the Chiu–Harvey approximation of the form

$$\begin{aligned}
C_{\text{CH}}^{(\text{cons})} = & \bar{S}_{\text{CH}} - \frac{1}{4\tau_c \ln \Lambda} v f_e(\mathbf{p}) \sigma(p) - \frac{\delta(\mathbf{p})}{4\tau_c \ln \Lambda} \int_{p' > q_0(p_m)} d\mathbf{p}' v' f_e(\mathbf{p}') \sigma(p') \\
& - \frac{3(m_e c)^{-3}}{8\pi \tau_c \ln \Lambda} \frac{\xi}{\gamma(\gamma+1)} \int_{p_1 > q_0} d\mathbf{p}_1 \frac{\gamma_1 + 1}{\gamma_1} \Sigma(\gamma, \gamma_1) (1 - \xi_1) f_e(\mathbf{p}_1) \\
& + \frac{3}{8\tau_c \ln \Lambda} \xi v \sigma(p) \int_{-1}^1 d\xi_1 (1 - \xi_1) f_e(p, \xi_1),
\end{aligned} \tag{B 3}$$

where  $\bar{S}_{\text{CH}}$  equals (B 1) with  $q^*$  changed to  $q_0$ , and the last two momentum-correcting terms are small when the runaway population consists predominantly of electrons with small pitch-angle,  $1 - \xi_1 \ll 1$ . Unlike the Chiu–Harvey model, this operator depends not only on the angle-averaged distribution  $\int f_e d\xi$ , but also on  $\int (1 - \xi) f_e d\xi$ .

Note that the issue of double counting is important only in the test-particle part of the operator. In the Chiu–Harvey approach, when the test-particle part is neglected, only field-particle collisions would be double counted, and for those the small-angle collisions have negligible impact on runaway generation.

The Rosenbluth–Putvinski result is obtained under the assumptions that the primary electrons not only have small pitch angle, but also large energy. Therefore, in the second line of (B 1),  $(p_1/\gamma_1)\Sigma(\gamma, \gamma_1)\delta(\xi - \xi^*)$  can be replaced by  $m_e c \Sigma(\gamma, \infty)\delta(\xi - \xi_0)$  with an error of order  $1/\gamma_1$ , where  $\xi_0 = \lim_{\gamma_1 \rightarrow \infty} \xi^* = \sqrt{(\gamma - 1)/(\gamma + 1)}$ . Under this assumption, the source term reduces to

$$S_{\text{RP}} = \frac{m_e c}{4\pi \tau_c \ln \Lambda} \frac{\delta(\xi - \xi_0)}{p\gamma} \Sigma(\gamma, \infty) \int_{q^*}^{\infty} dp_1 F(p_1) + O(1/\gamma_1) \tag{B 4}$$

$$\approx \frac{n_{\text{RE}}}{4\pi \tau_c \ln \Lambda} \delta(\xi - \xi_0) \frac{m_e^3 c^3}{p^2} \frac{d}{dp} \frac{1}{1 - \gamma}, \tag{B 5}$$

where the last step follows by replacing the integral over  $F$  by the runaway number density  $n_{\text{RE}}$ , valid when  $\gamma^* = \sqrt{(q^*/m_e c)^2 + 1} = 2\gamma - 1$  is small compared to typical runaway energies. This result agrees exactly with  $S_{\text{RP}}$  in (2.2). Note that this final approximation allows secondary electrons to be created with momentum and energy larger than that of any present primary electron. In fact, when integrated over all momenta the Rosenbluth–Putvinski source term is found to create energy and momentum at an infinite rate.

## REFERENCES

- AKAMA, H. 1970 Relativistic Boltzmann equation for plasmas. *J. Phys. Soc. Japan* **28**, 478.
- ALEYNIKOV, P., ALEYNIKOVA, K., BREIZMAN, B., HUIJSMANS, G., KONOVALOV, S., PUTVINSKI, S. & ZHOGOLEV, V. 2014 Kinetic modelling of runaway electrons and their mitigation in iter. In *International Atomic Energy Agency 25th Fusion Energy Conference, Saint Petersburg, Russia*, pp. 13–18.
- ALEYNIKOV, P. & BREIZMAN, B. N. 2015 Theory of two threshold fields for relativistic runaway electrons. *Phys. Rev. Lett.* **114**, 155001.
- BESEDIN, N. & PANKRATOV, I. 1986 Stability of a runaway electron beam. *Nucl. Fusion* **26**, 807.
- BOOZER, A. H. 2015 Theory of runaway electrons in iter: equations, important parameters, and implications for mitigation. *Phys. Plasmas* **22** (3), 032504.
- BREIZMAN, B. N. 2014 Marginal stability model for the decay of runaway electron current. *Nucl. Fusion* **54** (7), 072002.

- CERCIGNANI, C. & KREMER, G. 2002 *The Relativistic Boltzmann Equation: Theory and Applications*. Springer.
- CHIU, S., ROSENBLUTH, M., HARVEY, R. & CHAN, V. 1998 Fokker-Planck simulations mylb of knock-on electron runaway avalanche and bursts in tokamaks. *Nucl. Fusion* **38** (11), 1711–1721.
- COHEN, R. 1976 Runaway electrons in an impure plasma. *Phys. Fluids* **19**, 239.
- CONNOR, J. & HASTIE, R. 1975 Relativistic limitations on runaway electrons. *Nucl. Fusion* **15** (3), 415–424.
- DREICER, H. 1960 Electron and ion runaway in a fully ionized gas ii. *Phys. Rev.* **117**, 329–342.
- ERIKSSON, L.-G. & HELANDER, P. 2003 Simulation of runaway electrons during tokamak disruptions. *Comput. Phys. Commun.* **154** (3), 175–196.
- FÜLÖP, T., POKOL, G., HELANDER, P. & LISAK, M. 2006 Destabilization of magnetosonic-whistler waves by a relativistic runaway beam. *Phys. Plasmas* **13**, 062506.
- GILL, R. 1993 Generation and loss of runaway electrons following disruptions in jet. *Nucl. Fusion* **33**, 1613.
- GUREVICH, A., MILIKH, G. & ROUSSEL-DUPRE, R. 1992 Runaway electron mechanism of air breakdown and preconditioning during a thunderstorm. *Phys. Lett. A* **165** (5–6), 463–468.
- GUREVICH, A., MILIKH, G. & ROUSSEL-DUPRE, R. 1994 Nonuniform runaway air-breakdown. *Phys. Lett. A* **187** (2), 197–203.
- GUREVICH, A. V. & ZYBIN, K. P. 2001 Runaway breakdown and electric discharges in thunderstorms. *Phys.-Usp.* **44** (11), 1119.
- HARVEY, R. W., CHAN, V. S., CHIU, S. C., EVANS, T. E. & ROSENBLUTH, M. N. 2000 Runaway electron production in diii-d killer pellet experiments, calculated with the cql3d/kprad model. *Phys. Plasmas* **7**, 4590.
- HELANDER, P., ERIKSSON, L.-G. & ANDERSSON, F. 2002 Runaway acceleration during magnetic reconnection in tokamaks. *Plasma Phys. Control. Fusion* **44**, B247–62.
- HELANDER, P., LISAK, M. & RYUTOV, D. 1993 Formation of hot ion populations in fusion plasmas by close collisions with fast particles. *Plasma Phys. Control. Fusion* **35** (3), 363.
- HOLLMANN, E. M., ALEYNIKOV, P., FÜLÖP, T., HUMPHREYS, D., IZZO, V., LEHNEN, M., LOARTE, A., LUKASH, V. E., PAPP, G., PARKS, P. et al. 2015 Status of research toward the iter disruption mitigation system. *Phys. Plasmas* **22** (2), 021802.
- HOLMAN, G. D. 1985 Acceleration of runaway electrons and joule heating in solar flares. *Astrophys. J.* **293**, 584–594.
- JASPERS, R. 1993 Experimental investigation of runaway electron generation in textor. *Nucl. Fusion* **33**, 1775.
- JAYAKUMAR, R., FLEISCHMANN, H. & ZWEBEN, S. 1993 Collisional avalanche exponentiation of runaway electrons in electrified plasmas. *Phys. Lett. A* **172**, 447–451.
- LANDAU, L. 1936 Kinetic equation for the coulomb effect. *Physikalische Zeitschrift der Sowjetunion* **10**, 154.
- LANDAU, L. D. 1965 The transport equation in the case of coulomb interactions. In *Collected Papers of L. D. Landau* (ed. D. Ter Haar), p. 163. Pergamon.
- LANDREMAN, M., STAHL, A. & FÜLÖP, T. 2014 Numerical calculation of the runaway electron distribution function and associated synchrotron emission. *Comput. Phys. Commun.* **185** (3), 847–855.
- LEHTINEN, N. G., BELL, T. F. & INAN, U. S. 1999 Monte Carlo simulation of runaway mev electron breakdown with application to red sprites and terrestrial gamma ray flashes. *J. Geophys. Res.* **104** (A11), 24699–24712.
- LIFSHITZ, E. & PITAEVSKI, L. 1981 *Physical Kinetics*. Butterworth-Heinemann.
- MØLLER, C. 1932 Zur theorie des durchgangs schneller elektronen durch materie. *Ann. Phys.* **406** (5), 531.
- MONTGOMERY, D. & TIDMAN, D. 1964 *Plasma Kinetic Theory*. McGraw-Hill.
- NILSSON, E., DECKER, J., PEYSSON, Y., GRANETZ, R., SAINT-LAURENT, F. & VLAINIC, M. 2015 Kinetic modelling of runaway electron avalanches in tokamak plasmas. *Plasma Phys. Control. Fusion* **57**, 095006.

- ROSENBLUTH, M. N., MACDONALD, W. M. & JUDD, D. L. 1957 Fokker–Planck equation for an inverse-square force. *Phys. Rev.* **107**, 1–6.
- ROSENBLUTH, M. & PUTVINSKI, S. 1997 Theory for avalanche of runaway electrons in tokamaks. *Nucl. Fusion* **37**, 1355–1362.
- SMITH, H., HELANDER, P., ERIKSSON, L.-G. & FÜLÖP, T. 2005 Runaway electron generation in a cooling plasma. *Phys. Plasmas* **12** (12), 122505.
- SOKOLOV, Y. 1979 ‘Multiplication’ of accelerated electrons in a tokamak. *JETP Lett.* **29**, 218–221.
- STAHL, A., EMBRÉUS, O., PAPP, G., LANDREMAN, M. & FÜLÖP, T. 2016 Kinetic modelling of runaway electrons in dynamic scenarios. *Nucl. Fusion* **56** (11), 112009.
- TRUBNIKOV, B. 1965 *Reviews of Plasma Physics*, vol. 1. Consultants Bureau.
- WEINBERG, S. 2005 *The Quantum Theory of Fields, Volume 1: Foundations*. Cambridge University Press.
- WILSON, C. T. R. 1925 The acceleration of  $\beta$ -particles in strong electric fields such as those of thunderclouds. *Math. Proc. Camb. Phil. Soc.* **22**, 534.



# Paper B

O. Embréus, A. Stahl and T. Fülöp,

*Effect of bremsstrahlung radiation emission on fast electrons in plasmas*,  
New Journal of Physics **18**, 093023 (2016).

<https://doi.org/10.1088/1367-2630/18/9/093023>  
arXiv:1604.03331 [physics.plasm-ph]

# New Journal of Physics

The open access journal at the forefront of physics

Deutsche Physikalische Gesellschaft  DPG

IOP Institute of Physics

Published in partnership  
with: Deutsche Physikalische  
Gesellschaft and the Institute  
of Physics



## PAPER

### OPEN ACCESS

RECEIVED  
24 March 2016

REVISED  
21 June 2016

ACCEPTED FOR PUBLICATION  
29 July 2016

PUBLISHED  
9 September 2016

# Effect of bremsstrahlung radiation emission on fast electrons in plasmas

O Embréus<sup>1</sup>, A Stahl and T Fülöp

Department of Physics, Chalmers University of Technology, Gothenburg, Sweden

<sup>1</sup> Author to whom any correspondence should be addressed.

E-mail: [embreus@chalmers.se](mailto:embreus@chalmers.se)

**Keywords:** runaway electrons, bremsstrahlung, Boltzmann equation, Fokker–Planck equation

Original content from this work may be used under the terms of the [Creative Commons Attribution 3.0 licence](#).

Any further distribution of this work must maintain attribution to the author(s) and the title of the work, journal citation and DOI.



## Abstract

Bremsstrahlung radiation emission is an important energy loss mechanism for energetic electrons in plasmas. In this paper we investigate the effect of spontaneous bremsstrahlung emission on the momentum–space structure of the electron distribution, fully accounting for the emission of finite–energy photons by modeling the bremsstrahlung interactions with a Boltzmann collision operator. We find that electrons accelerated by electric fields can reach significantly higher energies than predicted by the commonly used radiative stopping–power model. Furthermore, we show that the emission of soft photons can contribute significantly to the dynamics of electrons with an anisotropic distribution by causing pitch–angle scattering at a rate that increases with energy.

Energetic electrons are ubiquitous in plasmas, and bremsstrahlung radiation is one of their most important energy loss mechanisms [1, 2]. At sufficiently high electron energy, around a few hundred megaelectronvolts in hydrogen plasmas, the energy loss associated with the emission of bremsstrahlung radiation dominates the energy loss by collisions. Bremsstrahlung emission can also strongly affect electrons at lower energies, particularly in plasmas containing highly charged ion species.

An important electron acceleration process, producing energetic electrons in both space and laboratory plasmas, is the runaway mechanism [3]. In the presence of an electric field which exceeds the minimum to overcome collisional friction [4], a fraction of the charged particles can detach from the bulk population and be accelerated to high energies, where radiative losses become important. Previous studies of laboratory plasmas [5, 6] and lightning discharges [7] have shown that the energy carried away by bremsstrahlung radiation is important in limiting the energy of runaway electrons. The effect of bremsstrahlung radiation loss on energetic-electron transport has also been considered in astrophysical plasmas, for example in the context of solar flares [8]. However, only the average bremsstrahlung friction force on test particles has been considered in these studies. In this paper, we present the first quantitative kinetic study of how bremsstrahlung emission affects the runaway-electron distribution function.

Starting from the Boltzmann electron transport equation, we derive a collision operator representing bremsstrahlung radiation reaction, fully accounting for the finite energies and emission angles of the emitted photons. We implement the operator in a continuum kinetic-equation solver [9], and use it to study the effect of bremsstrahlung on the distribution of electrons in 2D momentum space. We find significant differences in the distribution function when bremsstrahlung losses are modeled with a Boltzmann equation (referred to as the ‘Boltzmann’ or ‘full’ bremsstrahlung model), compared to the model where only the average friction force is accounted for (the ‘mean-force’ model). In the former model, the maximum energy reached by the energetic electrons is significantly higher than is predicted by the latter. In previous treatments which considered average energy loss [5–7] or isotropic plasmas [2], the emission of soft (low-energy) photons did not influence the electron motion. We show that in the general case, emission of soft photons contributes significantly to angular deflection of the electron trajectories.

## Kinetic description of bremsstrahlung losses

We will treat bremsstrahlung as a binary interaction ('collision') between two charged particles, resulting in the emission of a photon [1]. We shall describe the effect of such collisions on the rate of change of the distribution function  $f_a(t, \mathbf{x}, \mathbf{p})$  of some particle species  $a$  at time  $t$ , position  $\mathbf{x}$  and momentum  $\mathbf{p}$ , defined such that  $n_a(t, \mathbf{x}) = \int d\mathbf{p} f_a(t, \mathbf{x}, \mathbf{p})$  is the number density of species  $a$  at  $\mathbf{x}$ . In what follows we suppress the time- and space dependence of all functions, as the collisions will be assumed local in space-time, and we shall consider only spatially homogeneous plasmas.

The collision operator  $C_{ab}^B \{f_a, f_b\}$  describing the rate of change of the distribution function due to bremsstrahlung interactions between species  $a$  and  $b$  is given by  $C_{ab}^B = (\partial f_a / \partial t)_{c,ab} = \int (dn_a)_{c,ab} / dt d\mathbf{p}$ . The integration is to be carried out over target-particle momenta and scattering angles, and the differential change  $(dn_a)_{c,ab}$  in the phase-space density due to collisions in a time interval  $dt$  is given by [10, 11]

$$(dn_a)_{c,ab} = f_a(\mathbf{p}_1) f_b(\mathbf{p}_2) \bar{g}_o d\bar{\sigma}_{ab} d\mathbf{p}_1 d\mathbf{p}_2 dt - f_a(\mathbf{p}) f_b(\mathbf{p}') g_o d\sigma_{ab} d\mathbf{p} d\mathbf{p}' dt. \quad (1)$$

Here,  $d\sigma_{ab} = d\sigma_{ab}(\mathbf{p}_1, \mathbf{p}_2, \mathbf{k}; \mathbf{p}, \mathbf{p}')$  is the differential cross-section for a particle  $a$  of momentum  $\mathbf{p}$  and a particle  $b$  of momentum  $\mathbf{p}'$  to be taken to momentum  $\mathbf{p}_1$  and  $\mathbf{p}_2$ , respectively, while emitting a photon of momentum  $\mathbf{k}/c$ . We have also introduced the Møller relative speed [10]  $g_o = \sqrt{(\mathbf{v} - \mathbf{v}')^2 - (\mathbf{v} \times \mathbf{v}')^2/c^2}$ . The barred quantities  $d\bar{\sigma}$  and  $\bar{g}_o$  are defined likewise, but with  $(\mathbf{p}, \mathbf{p}')$  and  $(\mathbf{p}_1, \mathbf{p}_2)$  exchanged. Equation (1) accounts only for the effect on the distribution of the spontaneous emission of photons; interactions with existing photons by absorption and stimulated bremsstrahlung emission will be neglected here. The correction to the collision operator by these processes is described in [12]; the effect is negligible when  $\phi(t, \mathbf{x}, \mathbf{p}) \ll 2/h^3$ , where  $h$  is Planck's constant and  $\phi$  is the distribution function of photons. An estimate of the photon distribution function shows that the corrections are important for sufficiently dense, or large, plasmas; however, for the special case of electron runaway during tokamak disruptions, which is of particular concern, the corrections may be safely neglected. In other scenarios it is primarily bremsstrahlung processes involving low-energy photons that may be affected.

The collision operator then takes the form

$$C_{ab}^B(\mathbf{p}) = \int d\mathbf{p}_1 f_a(\mathbf{p}_1) \int d\mathbf{p}_2 \bar{g}_o f_b(\mathbf{p}_2) \frac{\partial \bar{\sigma}_{ab}}{\partial \mathbf{p}} - f_a(\mathbf{p}) \int d\mathbf{p}' g_o f_b(\mathbf{p}') \sigma_{ab}, \quad (2)$$

where  $\sigma_{ab} = \int d\mathbf{p}_1 (\partial \sigma_{ab} / \partial \mathbf{p}_1)$  is the total bremsstrahlung cross-section. A significant simplification to (2) occurs if (i) target particles can be assumed stationary,  $f_b(\mathbf{p}) = n_b \delta(\mathbf{p})$ ; and (ii) the plasma is cylindrically symmetric (and spin unpolarized),  $f_a(\mathbf{p}) = f_a(p, \cos \theta)$ , where  $\cos \theta = p_{\parallel}/p$  and  $p_{\parallel}$  is the Cartesian component of  $\mathbf{p}$  along the symmetry axis. Then the differential cross-section  $\partial \bar{\sigma}_{ab} / \partial \mathbf{p}$ , for an electron to scatter from momentum  $\mathbf{p}$  into  $\mathbf{p}_1$  with the emission of a photon, depends only on  $p$ ,  $p_1$  and  $\cos \theta_s = \mathbf{p}_1 \cdot \mathbf{p} / p_1 p$ . The resulting operator can be conveniently expressed in terms of an expansion in Legendre polynomials  $P_L$ . We write

$f_a(\mathbf{p}) = \sum_L f_L(p) P_L(\cos \theta)$  and  $C_{ab}^B(\mathbf{p}) = \sum_L C_L^B(p) P_L(\cos \theta)$ , and obtain

$$C_L^B(p) = n_b \int d\mathbf{p}_1 \left[ p_1^2 v_1 f_L(p_1) 2\pi \int_{-1}^1 d\cos \theta_s P_L(\cos \theta_s) \frac{\partial \bar{\sigma}_{ab}}{\partial \mathbf{p}} \right] - n_b v f_L(p) \sigma_{ab}(p). \quad (3)$$

The integration limits in  $p_1$  are determined by the conservation of energy, giving  $m_e c \sqrt{(\gamma + k/m_e c^2)^2 - 1} < p_1 < \infty$ . In this work we use the differential cross-section  $\partial \bar{\sigma} / \partial \mathbf{p}$  for scattering in a static Coulomb field in the Born approximation, integrated over photon emission angles. This expression was first derived by Racah [13], with a misprint later corrected in [14]. For the Boltzmann model this full cross-section is employed, while for the mean-force model we use the high-energy limit as in [5–7].

A useful approximation to the collision operator (3) is obtained by noting that the radiation emitted by runaway electrons will be strongly focused in the forward direction by relativistic beaming ('the headlight effect'), and the dominant contribution to the integral then originates from scattering angles  $\theta_s \lesssim 1/\gamma$ . For small angles, the Legendre polynomials take the asymptotic form  $P_L(\cos \theta_s) \sim 1 - L(L+1)\theta_s^2/4$ . Consequently, when  $L \ll 2\gamma$  the angular integral in (3) can be replaced with

$$\int d\cos \theta_s P_L(\cos \theta_s) \partial \bar{\sigma}_{ab} / \partial \mathbf{p} \approx \int d\cos \theta_s \partial \bar{\sigma}_{ab} / \partial \mathbf{p} \equiv 1/(2\pi p^2) \partial \bar{\sigma} / \partial p.$$

This approximation leads to a bremsstrahlung collision operator of the form

$$C_{ab}^B(\mathbf{p}) \approx n_b \int d\mathbf{p}_1 v_1 f_a(p_1, \cos \theta) \frac{\partial \bar{\sigma}}{\partial p}(p; p_1) - n_b v f_a(p, \cos \theta) \sigma(p). \quad (4)$$

This is a one-dimensional integral operator acting only on the energy variable, and involves the integrated cross-section which is well known (it is related to the cross-section in photon energy by  $\partial \bar{\sigma} / \partial p = (p/\gamma) \partial \bar{\sigma} / \partial k$ ) and is given analytically for example in equation (14) of [1].

*Low-energy photon contribution*—The bremsstrahlung cross-section has an infrared divergence; for low photon energies  $k$ , it diverges logarithmically as  $d\sigma \propto 1/k$ . The total energy loss rate is however finite, indicating that a large number of photons carrying negligible net energy are emitted. A consequence of this behavior is that the two terms in the Boltzmann operator (2) are individually infinitely large, necessitating the introduction of a photon cut-off energy  $k_0$ , below which the bremsstrahlung interactions are ignored in (3) and (4). We can however proceed analytically to evaluate the effect of the low-energy photons. While they carry little energy, they may contribute to angular deflection, analogously to the small-angle collisions associated with elastic scattering. Taylor expanding (3) in small photon energy  $k = \gamma_1 - \gamma$  yields to leading order

$$C_L^{\text{small-}k} = -n_b v f_L(p) \int_{k_c}^{k_0} dk \int_{-1}^1 d\cos\theta_s [1 - P_L(\cos\theta_s)] \frac{\partial\bar{\sigma}}{\partial k \partial\cos\theta_s}. \quad (5)$$

Since  $P_0(\cos\theta_s) \equiv 1$ , the angle-averaged electron distribution (represented by the  $L = 0$  term) is not directly affected by the low-energy photons, reflecting the fact that the photons carry negligible energy, consistent with the description by Blumenthal and Gould [2] for the isotropic case. Due to the logarithmic divergence of the cross-section, however, a significant contribution to angular deflection (represented by the  $L \neq 0$  terms) is possible. Inspection of the integrand in (5) further reveals that significant contributions originate from large-angle scatterings, indicating that a Fokker–Planck approximation is inappropriate. Indeed the bremsstrahlung cross-section  $\partial\sigma^{\text{low-}k}/\partial\cos\theta_s = \int_{k_c}^{k_0} dk \partial\bar{\sigma}/\partial k \partial\cos\theta_s$ , integrated over small photon energies, behaves for small angles ( $\theta_s^2 \ll k_0^2/\gamma^4$ ) as  $1/\theta_s^2$ , which can be compared to the elastic Coulomb cross-section proportional to  $1/\theta_s^4$ . This weaker singularity of the bremsstrahlung cross-section means that the contribution from small-angle collisions will be negligible compared to those from the large-angle deflections, and therefore a Boltzmann model must be used to account for these events. While it may seem counter-intuitive that low-energy photon emissions contribute to large-angle collisions, note that due to the large mass ratio between electron and ion, large momentum transfers to the nucleus are allowed even without any energy transfer. For very energetic electrons, however, when the kinetic energy exceeds the ion rest energy, ion recoil effects would need to be accounted for in deriving (5).

We can quantify the importance of the low-energy photons by calculating the  $L = 1$  term of (5)—giving the loss rate of parallel momentum—and comparing it to the corresponding term of the elastic-scattering collision operator given in [9]. Carrying out the integration, one obtains the ratio

$$\frac{C_1^{\text{small-}k}}{C_1^{\text{elastic}}} = \alpha \frac{2}{\pi} \frac{\ln \Lambda_B}{\ln \Lambda} \left[ \left( \ln \frac{2p}{m_e c} - 1 \right)^2 + 1 \right], \quad (6)$$

with a relative error of magnitude  $O(m_e^2 c^2/p^2) + O(k_0/pc)$ , and where  $\alpha = e^2/4\pi\epsilon_0\hbar c \simeq 1/137$  is the fine-structure constant. Here, we have introduced a bremsstrahlung logarithm  $\ln \Lambda_B = \ln(k_0/k_c)$ , which arises in a way similar to the Coulomb logarithm  $\ln \Lambda$  for elastic collisions, and is due to cutting off the logarithmically diverging integral at some lowest photon energy  $k_c$ .

Various mechanisms may suppress the bremsstrahlung interactions at low photon energy, such as multiple scattering, photon interactions with the medium, pair production and more [15]. Most important in dilute ionized gases, in the energy range we are interested in, is the photon interaction with the medium; the effect may be viewed as coherent forward Compton scattering on the target, causing destructive interference in the emitted radiation due to the induced phase shift in the emission. The analysis, originally due to Ter-Mikaelian [16], shows that the suppression can be accounted for by multiplying the cross-section with a suppression factor  $S$ , given by the ratio of in-medium to vacuum formation lengths  $l_B = \hbar/(p_{\parallel} - p_{1\parallel} - \sqrt{\epsilon/\epsilon_0} k_{\parallel}/c)$ , with  $\epsilon$  the dielectric constant of the medium. The formation length is approximately the distance over which the interaction amplitudes add coherently, and  $\parallel$  here denotes the direction of the incident electron. Evaluating the ratio yields the suppression factor  $S = k^2/(k^2 + k_p^2)$  where  $k_p \sim \hbar\omega_p$  is the photon energy corresponding to radiation at the plasma frequency, suggesting an effective lower cut-off  $k_c = k_p$  of our collision operator.

This gives a bremsstrahlung logarithm  $\ln \Lambda_B \approx 21 + \ln(k_0/(m_e c^2 \sqrt{n_{20}}))$ , where  $n_{20}$  is the electron density in units of  $10^{20} \text{ m}^{-3}$ . Assuming a plasma with  $\ln \Lambda = 15$ ,  $n_{20} = 1$  and choosing  $k_0 = 0.01p$ , the ratio (6) is of order 10% at 30 MeV, 50% at 2 GeV and 100% at 30 GeV, demonstrating that angular deflection caused by the emission of low-energy photons can contribute significantly to the motion of highly energetic electrons.

The bremsstrahlung collision operator has been implemented in the initial-value continuum kinetic-equation solver CODE (COllisional Distribution of Electrons) [9]. For this study we use CODE to solve the equation

$$\frac{\partial f_e}{\partial t} - eE_{\parallel} \frac{\partial f_e}{\partial p_{\parallel}} = C^{\text{FP}} \{f_e\} + C^{\text{B}} \{f_e\}, \quad (7)$$

which in a magnetized plasma represents the gyro-averaged kinetic equation, with the parallel direction given by the magnetic field  $\mathbf{B}$ . The equation is also valid for an unmagnetized plasma which is cylindrically symmetric

around the electric field  $\mathbf{E}$ . Elastic collisions are accounted for by the linearized relativistic Fokker–Planck operator for Coulomb collisions  $C^{\text{FP}}$ , and  $C^{\text{B}}$  is the bremsstrahlung operator  $C_{eb}^{\text{B}}$  summed over all particle species  $b$  in the plasma. Both thermal and fast electrons are resolved simultaneously, allowing runaway generation as well as the slowing-down of the fast population to be accurately modeled.

We will compare the effect of bremsstrahlung radiation losses on the momentum-space distribution of fast electrons using several models. The contribution from the emission of large-energy photons (with  $k > k_0$ ) are accounted for by either the Boltzmann operator in (3) or its approximation without angular deflection (4), while the low-energy photon contribution ( $k < k_0$ ) is described by (5). For the numerical solutions we choose an energy-dependent cut-off  $k_0 = m_e c^2 (\gamma - 1) / 1000$ . We have found that this is sufficiently small that the results are not sensitive to the choice of this cut-off parameter. The cut-off, which determines when the emitted photons will be counted as ‘low energy’, and when the interaction is treated as elastic using the operator in (5), generally produces a relative error in the solution of order  $k_0 / [m_e c^2 (\gamma - 1)]$ .

The Boltzmann models will be compared to the mean-force model where the bremsstrahlung losses are accounted for by an isotropic force term in the kinetic equation, defined as  $\mathbf{F}_B = -\hat{\mathbf{p}} \sum_b n_b \int_0^{m_e c^2 (\gamma - 1)} dk k \partial \sigma_{eb} / \partial k$ , which is chosen to produce the correct average energy-loss rate [1].

## Numerical results

To characterize the effect of bremsstrahlung on the electron distribution, we investigate quasi-steady-state numerical solutions of the kinetic equation (7). These are obtained by evolving the distribution function in time until an equilibrium is reached, typically after a few seconds at density  $n_{20} = 1$  if an initial seed of fast electrons is provided (this equilibration time is directly proportional to  $n_e$ ). This means that if, in reality, the duration of near-constant acceleration is shorter than this equilibration time scale, the amplitude of the runaway tail will be smaller than reported here. The qualitative features of the runaway distribution are however set up on a shorter time scale of a few hundred milliseconds at  $n_{20} = 1$ , and can be representative of a wider range of realistic scenarios.

We investigate a range of electric-field values near the minimum electric field  $E_c = 4\pi \ln \Lambda n_e r_0^2 m_e c^2 / e$  to overcome collisional friction [4], using plasma parameters characteristic of tokamak-disruption experiments with massive gas injection. We assume accumulated impurity densities to be of order  $n_Z \sim 10^{20} \text{ m}^{-3}$  and that, for the ultrarelativistic electrons in the far tail of the distribution, the binding energy of the bound electrons is negligible. The electron density  $n_e$  then denotes the full electron density  $n_e \sim n_{\text{free}} + n_{\text{bound}}$ .

Figure 1 shows the electron distribution function in momentum space, calculated using CODE, with full Boltzmann bremsstrahlung effects included (black, solid); neglecting angular deflections in the large- $k$  contribution (yellow, dash-dotted); also neglecting the small- $k$  contribution (blue, dashed); and finally using the mean-force model (red, solid). Non-monotonic features form in the mean-force as well as the Boltzmann models, but their characteristics are significantly different. With the Boltzmann models, an extended tail forms in the electron distribution. In contrast, the mean-force model produces a sharp feature, located where the energy gain due to the electric-field acceleration balances friction and bremsstrahlung losses. The addition of low- $k$  scatterings (5), which lead to large-angle deflections, causes a subpopulation of fast electrons with significant perpendicular momentum to form. Furthermore, (3) and (4) appear to generally produce the same qualitative features, indicating that scatterings involving large-energy photons are well approximated by neglecting the angular deflection of the electron.

Inclusion of synchrotron radiation losses associated with the gyromotion of electrons in a straight magnetic field has been shown to be an important energy-loss mechanism [17–21]. Figure 1(b) shows that, in conjunction with bremsstrahlung losses, synchrotron losses (modeled as in [17]) shift the distribution towards lower energies but does not change its qualitative features. The difference between the Boltzmann and mean-force models is reduced in such cases, as the extent of the distribution when full bremsstrahlung effects are included is reduced by the synchrotron effect. When bremsstrahlung losses are ignored, and synchrotron emission alone is responsible for the energy loss by radiation, a non-monotonic runaway tail can also form (solutions to this problem have been characterized in [17, 20]). However, for the present values of density, magnetic and electric fields this occurs at the significantly higher momentum [6, 20]

$$p \sim \frac{3n_e \ln \Lambda m_e^2 c}{2\epsilon_0 B^2 (Z + 1)} \frac{E}{E_c} \left( \frac{E}{E_c} - 1 \right) \approx 300 m_e c,$$

corresponding approximately to an energy of 150 MeV.

Angle-averages of the electron distribution functions in figure 1 are shown in figure 2 as a function of electron kinetic energy  $W = m_e c^2 (\gamma - 1)$ . The bulk population ( $W < 1 \text{ MeV}$ ) has been excluded from the figure in order to highlight the differences in the shape of the tail of the runaway distribution, which is where the

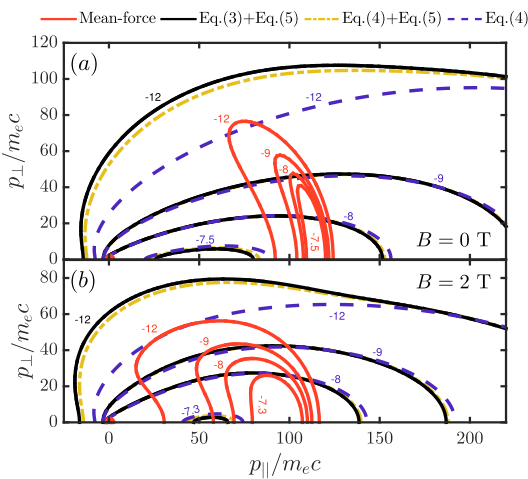


**Figure 1.** Steady-state electron 2D distribution functions; (a) with no magnetic field, (b) with  $B = 2$  T. Electric field  $E = 2E_c$ , plasma parameters  $Z_{\text{eff}} = 10$ ,  $n_{20} = 30$  and  $T_e = 10$  keV. Contours show  $\log_{10} F$ , where  $F = (2\pi m_e T_e)^{3/2} f_e / n_e$ .

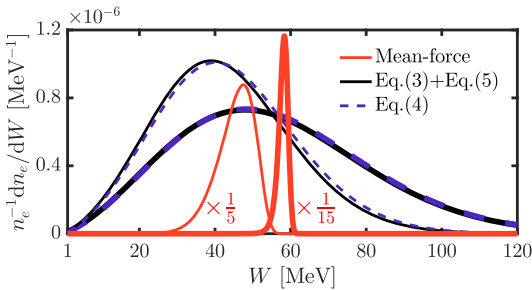


**Figure 2.** Angle-averaged tail of the electron distributions in figure 1, with  $B = 0$  (thick lines) and  $B = 2$  T (thin lines).

greatest variation between the different radiation-loss models can be seen. When there are no synchrotron losses present, the difference between the two Boltzmann models for bremsstrahlung losses is seen to be insignificant when considering the angle-averaged distribution. In the presence of effects which are sensitive to the angular distribution of electrons, such as synchrotron radiation losses (which are proportional to  $p_{\perp}^2$ ), the difference is somewhat enhanced as angular deflection amplifies the dissipation.

To quantify the width in energy of the fast-electron tail, figure 3 shows the fraction of total plasma kinetic energy carried by electrons with energy greater than  $W$ , for a range of plasma compositions and electric fields, neglecting synchrotron losses. Again, the steady-state solutions are considered, and the energy ratio is calculated as  $\int_W^{\infty} dW W (dn_e/dW) / W_{\text{tot}}$ . When normalized to the energy  $W_0$  which solves the energy-balance equation  $eE_{\parallel} - eE_c + F_B = 0$  (accounting for collisional and bremsstrahlung energy loss), the behavior is seen to be insensitive to electric field and effective charge. The Boltzmann model consistently predicts that a fraction of the electron population reaches significantly higher energies than in the mean-force model, where all electrons have energy near  $W_0$ . For instance, in the Boltzmann model 5% of the plasma energy is carried by electrons with energy more than  $2W_0$ .

## Summary

We have developed a kinetic description of the effect of spontaneous bremsstrahlung emission on energetic electrons in plasmas. By treating bremsstrahlung emission as a discrete process, we have shown that electrons

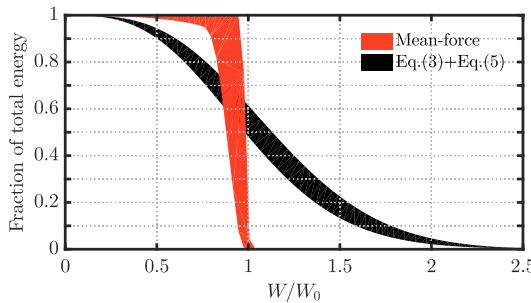


**Figure 3.** Fraction of plasma kinetic energy carried by electrons of energy greater than  $W$ . The values are calculated from numerical solutions of the kinetic equation, and are shown as a function of normalized electron kinetic energy. Filled regions indicate the values spanned when  $Z_{\text{eff}}$  and the normalized electric field  $(E/E_c - 1)/(Z_{\text{eff}} + 1)$  are varied between 1 and 35, and 0.05 and 0.25, respectively.

may be accelerated to significantly higher energies than would be predicted by energy balance alone, with a significant fraction of particles reaching at least twice the expected energy. This effect has important implications for the interpretation of experimental observation of fast electron beams in plasmas where bremsstrahlung losses are important, such as those in magnetic-confinement fusion. Since we have furthermore demonstrated that the features of the bremsstrahlung-loss dominated distribution function are insensitive to plasma composition and electric field, our findings may also be important in the study of other scenarios where runaway occurs, such as in lightning discharges and solar flares. The explanation for the increased maximum energy can be intuitively understood in the single-particle picture, where the new model allows some electrons to suddenly lose a large fraction of their energy in one emission, whereas other electrons may be accelerated for a long time before a bremsstrahlung reaction occurs, thereby allowing higher maximum energies to be reached.

Furthermore, new effects are revealed in our treatment, as the emission of soft photons is found to contribute to angular deflection of the electron trajectory at a rate that increases with electron energy. This effect shifts part of the momentum-space distribution function towards higher perpendicular momenta, which in turn has implications for e.g. the destabilization of kinetic instabilities or the level of synchrotron radiation loss in magnetized plasmas.

In order to resolve the logarithmically divergent contribution from low-energy photons, the bremsstrahlung collision operator is split into two contributions by introducing a cut-off photon energy  $k_0 \ll m_e c^2 (\gamma - 1)$ . In the contribution from photons with energy  $k < k_0$ , the energy carried by the photons may be neglected, and the corresponding term in the kinetic equation is given by the elastic collision operator given in (5). However, both contributions must be treated with a Boltzmann collision operator in order to accurately capture the dynamics of the fast electrons. For the  $k < k_0$  contribution, it is required as those interactions are dominated by large-angle deflections of the electron orbit, while the  $k > k_0$  part requires it as the emitted photon causes a large change of the electron energy in each emission.

A computationally efficient representation of the bremsstrahlung collision operator has been obtained using an expansion in Legendre polynomials, with which the operator is reduced to a set of one-dimensional energy integrals. This allows for rapid evaluation of the self-consistent electron distribution function in the presence of bremsstrahlung losses derived from the full Boltzmann operator.

## Acknowledgments

The authors are grateful to G Papp for fruitful discussions. This work has been carried out within the framework of the EUROfusion Consortium and has received funding from the Euratom research and training programme 2014-2018 under grant agreement number 633053. The views and opinions expressed herein do not necessarily reflect those of the European Commission. This work was supported by the Swedish Research Council (Dnr. 2014-5510), the Knut and Alice Wallenberg Foundation (PLIONA project) and the European Research Council (ERC-2014-CoG grant 647121).

## References

- [1] Bethe H and Heitler W 1934 *Proc. Roy. Soc. A* **146** 83
- [2] Blumenthal G R and Gould R J 1970 *Rev. Mod. Phys.* **42** 237
- [3] Dreicer H 1959 *Phys. Rev.* **115** 2
- [4] Connor J W and Hastie R J 1975 *Nucl. Fusion* **15** 415
- [5] Bakhtiari M, Kramer G J, Takechi M, Tamai H, Miura Y, Kusama Y and Kamada Y 2005 *Phys. Rev. Lett.* **94** 215003
- [6] Fernández-Gómez I, Martín-Solís J and Sánchez R 2007 *Phys. Plasmas* **14** 072503
- [7] Gurevich A V and Zybin K P 2001 *Sov. Phys. Usp.* **44** 1119
- [8] Miller J A and Ramaty R 1989 *Astrophys. J.* **344** 973
- [9] Landreman M, Stahl A and Fülöp T 2014 *Comp. Phys. Comm.* **185** 847
- [10] Cercignani C and Kremer G M 2002 *The Relativistic Boltzmann equation: Theory and Applications* (Springer Series in Progress in Mathematical Physics vol 22) ed A Boudet de Monvel and G Kaiser (Berlin: Springer)
- [11] Akama H 1970 *J. Phys. Soc. Japan* **28** 478
- [12] Oxenius J 1986 *Kinetic Theory of Particles and Photons: Theoretical Foundations of Non-LTE Plasma Spectroscopy* ((Springer Series in Electrophysics vol 20)) ed G Ecker (Berlin: Springer)
- [13] Racah G 1934 *Il Nuovo Cimento* **11** 461
- [14] McCormick P T, Keiffer D G and Parzen G 1956 *Phys. Rev.* **103** 29
- [15] Klein S 1999 *Rev. Mod. Phys.* **71** 1501
- [16] Ter-Mikaelian M L 1953 *Zh. Eksp. Teor. Fiz.* **25** 296
- [17] Hirvijoki E, Pusztai I, Decker J, Embréus O, Stahl A and Fülöp T 2015 *J. Plasma Phys.* **81** 475810502
- [18] Andersson F, Helander P and Eriksson L-G 2001 *Phys. Plasmas* **8** 5221
- [19] Stahl A, Hirvijoki E, Decker J, Embréus O and Fülöp T 2015 *Phys. Rev. Lett.* **114** 115002
- [20] Decker J, Hirvijoki E, Embréus O, Peysson Y, Stahl A, Pusztai I and Fülöp T 2016 *Plasma Phys. Control. Fusion* **58** 025016
- [21] Aleynikov P and Breizman B N 2015 *Phys. Rev. Lett.* **114** 155001

# Paper C

O. Embréus, L. Hesslow, M. Hoppe, G. Papp, K. Richards and T. Fülöp,  
*Dynamics of positrons during relativistic electron runaway*,  
Journal of Plasma Physics **84**, 905840506 (2018).  
<https://doi.org/10.1017/S0022377818001010>  
arXiv:1807.04460 [physics.plasm-ph]

# Dynamics of positrons during relativistic electron runaway

O. Embréus<sup>1,†</sup>, L. Hesslow<sup>1</sup>, M. Hoppe<sup>1</sup>, G. Papp<sup>2</sup>, K. Richards<sup>1</sup>  
and T. Fülöp<sup>1</sup>

<sup>1</sup>Department of Physics, Chalmers University of Technology, SE-41296 Göteborg, Sweden

<sup>2</sup>Max-Planck-Institute for Plasma Physics, D-85748 Garching, Garching, Germany

(Received 28 May 2018; revised 27 August 2018; accepted 28 August 2018)

Sufficiently strong electric fields in plasmas can accelerate charged particles to relativistic energies. In this paper we describe the dynamics of positrons accelerated in such electric fields, and calculate the fraction of created positrons that become runaway accelerated, along with the amount of radiation that they emit. We derive an analytical formula that shows the relative importance of the different positron production processes, and show that, above a certain threshold electric field, the pair production by photons is lower than that by collisions. We furthermore present analytical and numerical solutions to the positron kinetic equation; these are applied to calculate the fraction of positrons that become accelerated or thermalized, which enters into rate equations that describe the evolution of the density of the slow and fast positron populations. Finally, to indicate operational parameters required for positron detection during runaway in tokamak discharges, we give expressions for the parameter dependencies of detected annihilation radiation compared to bremsstrahlung detected at an angle perpendicular to the direction of runaway acceleration. Using the full leading-order pair-production cross-section, we demonstrate that previous related work has overestimated the collisional pair production by at least a factor of four.

**Key words:** runaway electrons

---

## 1. Introduction

The production of positrons has been investigated extensively both theoretically and experimentally since their first identification (Anderson 1932). Low-energy positrons are used in many areas of science and technology, ranging from positron emission tomography (Raichle 1985) and surface science (Hunt *et al.* 1999) to fundamental studies of antimatter (Gabrielse *et al.* 2002; Surko & Greaves 2004). High-energy positrons can also be routinely produced in particle accelerators and intense laser–solid interactions (Chen *et al.* 2009; Sarri 2015). Positrons are present in a wide range of atmospheric and astrophysical plasmas, e.g. lightning discharges (Dwyer & Uman 2014), solar flares (Murphy *et al.* 2005), pulsars and black-hole physics (Prantzos *et al.* 2011). Also in post-disruption plasmas in large tokamaks, where the energy of

†Email address for correspondence: [embreus@chalmers.se](mailto:embreus@chalmers.se)

the runaway electrons is in the tens of MeV range, high-energy positrons should be present (Helander & Ward 2003; Fülöp & Papp 2012), but they have not yet been experimentally observed.

Plasmas with strong electric fields are particularly interesting for positron generation, as particles accelerated by the field often reach energies larger than the pair-production threshold. For example, the electric field in solar flares is believed to be the result of magnetic reconnection (Priest & Forbes 2002; Liu & Wang 2009). In thunderstorms strong electric fields are produced by the charged regions, sometimes lasting tens of minutes (Tsuchiya *et al.* 2011). In intense laser-matter interaction, the positrons experience the sheath field that is set-up by the relativistic electrons leaving the target (Wilks *et al.* 2001). In disruptive tokamak plasmas, the resistivity increase due to the sudden cooling of the plasma leads to a high electric field that is induced to maintain the plasma current (Helander, Eriksson & Andersson 2002). Regardless of the cause, the electric field will strongly affect the dynamics of the positrons.

If the electric field exceeds a certain critical field, the accelerating force on the charged particles overcomes the friction, and they are accelerated to high energies and run away (Wilson 1925; Dreicer 1959). Existing runaway electrons may create new (secondary) runaways in close collisions with thermal electrons, and this can lead to an exponential growth of the runaway population, i.e. an avalanche (Sokolov 1979; Rosenbluth & Putvinski 1997). The runaways are accelerated to energies that are well above the pair-production threshold (Hollmann *et al.* 2015; Paz-Soldan *et al.* 2017) and create positrons in collisions with electrons and ions. The created positrons are also accelerated by the electric field, in the opposite direction with respect to the electrons, and if the electric field is sufficiently strong, a substantial fraction of them will run away (Fülöp & Papp 2012). Eventually they will annihilate, either directly with electrons or through the formation of positronium (Charlton & Humberston 2001). Due to their drift motion, for runaway positrons in tokamaks this will typically occur after they have escaped the plasma and struck the first wall (Liu *et al.* 2014).

The direct annihilation of an electron-positron pair at rest will result in the creation of two gamma-ray photons, each of energy 511 keV. Positron annihilation is often invoked to explain the observed emission features in the vicinity of 500 keV in the radiation spectrum of gamma-ray bursts, pulsars, solar flares (Murphy *et al.* 2005), terrestrial lightning (Briggs *et al.* 2011) and the galactic centre (Prantzos *et al.* 2011). In laboratory plasmas, the bremsstrahlung of the energetic electrons may overwhelm the annihilation radiation from the positrons, as the positron/electron fraction is usually low (Fülöp & Papp 2012). However, due to the directionality of the bremsstrahlung radiation, the isotropic annihilation radiation may still be detectable.

In this paper, we analyse the dynamics of high-energy positrons produced in collisions between charged particles in a strong electric field, where both electrons and positrons may run away. We use MadGraph 5 simulations (Alwall *et al.* 2014) to obtain the cross-section for pair production in collisions between electrons and ions, which reveals that the high-energy limit (Landau & Lifshitz 1983) and the formula given in Gryaznykh (1998) significantly overestimate the cross-section. We consider the relative importance of pair production by collisions and photons, which has previously been considered in the context of lightning discharges (Vodopiyanov *et al.* 2015). We derive a critical pair-production electric field above which collisional pair production dominates in avalanching runaway scenarios.

In the case when pair production by photons is negligible, we solve the kinetic equation for positrons. We derive an analytical expression for the positron distribution function in the presence of an avalanching runaway-electron population. The analytical

results for the distribution function and critical electric field are corroborated with numerical simulations using the kinetic equation solver CODE (Landreman, Stahl & Fülöp 2014; Stahl *et al.* 2016) modified to include the positron source and annihilation terms. Furthermore, we consider the radiation emitted by positrons and find the parameter dependencies of the annihilation to bremsstrahlung radiation ratio. This allows determination of the parameter regions where the annihilation radiation could be detectable in these plasmas.

The structure of the paper is the following. In § 2 we describe the kinetic equation of the positrons including details of the positron production source term. We present both analytical and numerical solutions of the kinetic equation, showing excellent agreement in the relevant limit. Following this, in § 3 we describe rate equations for runaway positrons, which are useful to predict the parametric dependencies of the fraction of positrons without extensive kinetic simulations. In § 4 we calculate the expected annihilation radiation from positrons in tokamak plasmas. Finally we summarize our conclusions in § 5.

## 2. Kinetic equation for positrons

In this paper we consider the dynamics of positrons during a relativistic electron runaway avalanche (Jayakumar, Fleischmann & Zweben 1993). Due to the non-monotonic dynamical friction acting on a charged test particle in a plasma, in an electric field larger than a critical value  $E_c$  fast electrons may experience a net force that can rapidly accelerate them to energies in the range of tens of MeV. In a fully ionized plasma, the critical field is  $E_c = \ln \Lambda n_e e^3 / (4\pi \epsilon_0^2 m_e c^2)$  (Connor & Hastie 1975), where  $\ln \Lambda \approx 14.6 + 0.5 \ln(T[\text{eV}]/n_e[10^{20} \text{ m}^{-3}])$  is the Coulomb logarithm (Solodov & Betti 2008). We neglect a logarithmic energy dependence in  $\ln \Lambda$ , and use the value for relativistic electrons at 1 MeV for simplicity. Here,  $n_e$  is the electron density,  $e$  the elementary charge,  $\epsilon_0$  the vacuum permittivity,  $m_e$  the electron rest mass and  $c$  the speed of light. The background plasma is assumed to be nearly Maxwellian for all species with the same temperature  $T$ . In a neutral gas,  $\ln \Lambda$  depends on the mean excitation energy of the medium instead of the temperature, and corresponds to  $\ln \Lambda \approx 11$  in air (Gurevich & Zybin 2001). In this case the electron density refers to the density of bound electrons.

A sufficiently energetic electron can produce new runaway electrons through elastic large-angle collisions. The result is an exponentially growing number of runaway electrons, a so-called runaway avalanche. Each  $e$ -folding of the number density takes a time  $t_{\text{ava}} = c_Z / [4\pi n_e r_0^2 c (E/E_c - 1)]$  where  $c_Z$  is only weakly dependent on electric field, and can be approximated by  $c_Z \approx \sqrt{5 + Z_{\text{eff}}}$  in a fully ionized plasma (Rosenbluth & Putvinski 1997), where the effective charge is  $Z_{\text{eff}} = \sum n_i Z_i^2 / \sum n_i Z_i$  with the sum taken over all ion species  $i$ . We shall find that several results in the paper are insensitive to the details of  $c_Z$ , assuming only that it is independent of  $E$ . As such, more accurate models of the avalanche process can in principle be implemented by inserting for  $c_Z$  the value characterizing any particular scenario of interest.

Since the electrons are ultra-relativistic, they will create positrons which are predominantly co-moving; these are created either directly in collisions or indirectly through the hard X-rays emitted in collisions (Heitler 1954), which can produce a pair in a subsequent interaction. Since the positrons experience an acceleration by the electric field in the direction opposite to the runaway-electron motion, they will immediately start decelerating. A fraction of these positrons will slow down to thermal

speeds where they eventually annihilate, whereas the remainder obtain sufficiently large momenta perpendicular to the acceleration direction that they become runaway accelerated along the electric field, moving anti-parallel to the runaway electrons. Annihilation – which occurs at a rate that decreases with positron energy – does not have a significant effect on the dynamics of the energetic positrons since the avalanche rate is typically much faster, which is demonstrated in § 2.2.

Throughout this paper, we shall assume that the plasma is fully ionized. In a partially ionized plasma or a neutral gas, screening effects due to the bound electrons would enter into all binary interactions. In the 10 MeV energy range, these are however largely negligible for the pair-production mechanisms as well as for the emission of bremsstrahlung, meaning that they are to be calculated using the full nuclear charge of the target. The screening effects become significant when  $p/m_e c \gtrsim 137/Z^{1/3}$  (Heitler 1954). Elastic Coulomb collisions are to a greater extent affected by screening effects, where the pitch-angle scattering rates may be reduced by approximately up to two thirds and energy loss rates by one third (Hesslow *et al.* 2017) in the energy range of interest, compared to the results obtained treating the medium as fully ionized. This would modify primarily two important quantities that affect our results: the avalanche growth rate factor  $c_Z$ , as well as the critical field  $E_c$  (Hesslow *et al.* 2018), which can here be assumed to be accurate only up to an order-of-unity factor in partially ionized plasmas. While the results we present are strictly valid for a fully ionized plasma, we expect to capture the correct order of magnitude also in a partially ionized plasma or neutral gas, if the effective charge and electron densities appearing in the formulas are always evaluated using the fully ionized values. We denote these by

$$n_{\text{tot}} = \sum_i Z_i n_i, \quad (2.1)$$

$$Z_{\text{tot}} = \frac{1}{n_{\text{tot}}} \sum_i n_i Z_i^2, \quad (2.2)$$

where  $Z_i$  is the atomic number of species  $i$ . Thus, the density is always to be taken as the total density of free plus bound electrons, and in a single-component gas or plasma  $Z_{\text{tot}}$  is the atomic number of the ion species regardless of ionization degree.

The dynamics described above can be most lucidly captured in a two-dimensional model. The distribution function of positrons with momentum  $\mathbf{p} = m_e \mathbf{v} / \sqrt{1 - \mathbf{v}^2/c^2}$ , where the positron velocity is denoted  $\mathbf{v}$ , at a time  $t$  is denoted  $f_{\text{pos}}(t, \mathbf{p})$ . In a homogeneous cylindrically symmetric plasma in the presence of an electric field  $\mathbf{E}$  it satisfies the kinetic equation

$$\frac{\partial f_{\text{pos}}}{\partial t} + eE \left[ \xi \frac{\partial}{\partial p} + \frac{1 - \xi^2}{p} \frac{\partial}{\partial \xi} \right] f_{\text{pos}} = C_{\text{pos}} + S_{\text{pos}} + S_{\text{an}}, \quad (2.3)$$

where  $E = |\mathbf{E}|$ ,  $p = |\mathbf{p}|$ ,  $\xi \equiv \cos \theta = \mathbf{p} \cdot \mathbf{E} / pE$  is the pitch-angle cosine,  $C_{\text{pos}}$  is the positron collision operator,  $S_{\text{pos}}$  denotes the source term of positrons generated in collisions between relativistic runaway electrons and field particles of the plasma, as well as positron production by highly energetic photons, and  $S_{\text{an}}$  denotes the annihilation term. In a magnetized plasma, the equation is valid for an axisymmetric positron distribution if  $E$  is replaced by the component of the electric field parallel to the magnetic field, and the pitch angle is instead defined relative to the magnetic field.

In the limit of small-energy transfers, the elastic positron–electron and positron–ion differential scattering cross-sections coincide with the electron–electron and electron–ion cross-sections, respectively (Landau & Lifshitz 1983). Consequently, the positron collision operator  $C_{\text{pos}}$  equals the electron collision operator  $C_e$  up to terms small in the Coulomb logarithm  $\ln \Lambda$ . Large-angle collisions, which are primarily important for avalanche generation when  $\ln \Lambda$  is large, can be neglected since the thermal positron population will always be small in number. The positron distribution therefore satisfies the same kinetic equation as the electron distribution, except for the electric field accelerating them in the opposite direction (with these definitions positrons are accelerated towards  $\xi = 1$ , and electrons towards  $\xi = -1$ ), and the presence of the terms  $S_{\text{pos}}$  and  $S_{\text{an}}$  describing their creation and annihilation, respectively.

The number of positrons created with momentum  $\mathbf{p}$  in time  $dt$  has two main contributions: (i) the collisions between stationary ions of species  $i$  with density  $n_i$  and the number  $dn_{\text{RE}}$  of runaways at momentum  $\mathbf{p}_1$  and speed  $v_1$ , and (ii) the pair production of  $dn_\gamma$  photons in the field of ions  $i$ :

$$dn_{\text{pos}} = \sum_i [n_i v_1 d\sigma_{ci}^+ dn_{\text{RE}} dt + n_i c d\sigma_{\gamma i}^+ dn_\gamma dt]. \quad (2.4)$$

Here,  $d\sigma_{ci}^+$  is the differential cross-section for producing a positron in a collision between an electron and a stationary ion, and similarly  $d\sigma_{\gamma i}^+$  for a photon interacting with stationary ions, and are given in appendix A. We use the Madgraph 5 tool (Alwall *et al.* 2014) for obtaining the pair-production cross-sections throughout this paper. In appendix A, figure 6, we compare the total cross-section as a function of electron energy with a previously published formula by Gryaznykh (1998). The latter is shown to be approximately a constant factor of four times as large as the cross-section that we have obtained.

Using  $dn_{\text{RE}}(\mathbf{p}_1) = f_{\text{RE}}(\mathbf{p}_1) d\mathbf{p}_1$ , where  $f_{\text{RE}}$  is the distribution function of runaway electrons, and similarly for the positron distribution  $f_{\text{pos}}(\mathbf{p}) = dn_{\text{pos}}/d\mathbf{p}$  and photons  $\phi_\gamma(\mathbf{k}) = dn_\gamma/d\mathbf{k}$  where  $\mathbf{k}/c$  is the photon momentum, we find the following form for the positron source  $S_{\text{pos}}$ :

$$S_{\text{pos}} \equiv \left( \frac{\partial f_{\text{pos}}}{\partial t} \right)_{\text{pp}} = \sum_i n_i c \left[ \int d\mathbf{p}_1 \frac{v_1}{c} \frac{\partial \sigma_{ci}^+}{\partial \mathbf{p}} f_{\text{RE}}(\mathbf{p}_1) + \int d\mathbf{k} \frac{\partial \sigma_{\gamma i}^+}{\partial \mathbf{p}} \phi_\gamma(\mathbf{k}) \right]. \quad (2.5)$$

In an avalanching runaway scenario, the photon distribution can be eliminated in favour of an expression involving only the runaway distribution because of the relatively slow evolution of the photon energy spectrum. The runaway-electron population grows exponentially in time on the time scale (Rosenbluth & Putvinski 1997)

$$t_{\text{ava}} = \frac{c_Z}{4\pi n_{\text{tot}} r_0^2 c (E/E_c - 1)}. \quad (2.6)$$

The photons on the other hand evolve on the Compton-scattering time scale (Heitler 1954)

$$t_{\text{Co}} = \frac{k}{\pi n_{\text{tot}} r_0^2 c m_e c^2 \ln[2k/(m_e c^2)]}, \quad (2.7)$$

where the photon energies  $k = |\mathbf{k}|$  are larger than the pair-production threshold  $2m_e c^2$ , and  $r_0 = e^2/(4\pi\epsilon_0 m_e c^2) \approx 2.82 \times 10^{-15}$  m is the classical electron radius.

Comparing the two time scales shows that the photons do not have time to change significantly from the distribution in which they are created whenever

$$\frac{k/m_e c^2}{\ln(2k/m_e c^2)} \gg \frac{c_Z}{4(E/E_c - 1)}. \quad (2.8)$$

Since the right-hand side is typically smaller than unity, this is generally well satisfied in an avalanching runaway scenario. The photon distribution is then given by

$$\phi(\mathbf{k}) = t_{\text{ava}} \sum_i n_i \int d\mathbf{p}_1 v_1 \frac{\partial \sigma_{\text{br},i}}{\partial \mathbf{k}}(\mathbf{k}, \mathbf{p}_1) f_{\text{RE}}(\mathbf{p}_1), \quad (2.9)$$

where  $d\sigma_{\text{br},i}$  is the differential bremsstrahlung cross-section for interactions between electrons and particle species  $i$ .

Since the cross-sections appearing in these formulas depend on target species only through  $Z_i^2$ , the target charge squared (Heitler 1954), these may be factored out when screening effects are neglected, yielding a factor of the effective plasma charge  $Z_{\text{tot}}$  when summed over  $i$ . We shall therefore suppress the indices  $i$  of the cross-sections by writing  $\sum_i n_i \sigma_{ci}^+ = n_{\text{tot}} Z_{\text{tot}} \sigma_c^+$  for collisional pair production, and  $\sum_i n_i \sigma_{\text{br},i} = n_{\text{tot}} (Z_{\text{tot}} + 1) \sigma_{\text{br}}$  (and likewise for  $\sigma_\gamma^+$ ) for the photon pair-production cross-sections. Here we have added the contribution from electron-electron bremsstrahlung in the approximation that the electron-electron and electron-proton bremsstrahlung cross-sections are the same, which has satisfactory accuracy since the majority of interactions occur with negligible momentum transfer to the target particle (Haug 1975). Conversely, for collisional pair production the electron-electron interactions are negligible, which was verified with MadGraph 5 simulations (Alwall *et al.* 2014) which indicated that the  $e$ - $e$  cross-section is 10%–20% of the  $e$ - $i$  cross-section when the incident electron laboratory-frame energy ranges over 10–20 MeV and  $Z_i = 1$ .

The positron source can then be written

$$S_{\text{pos}} = Z_{\text{tot}} n_{\text{tot}} \int d\mathbf{p}_1 v_1 \frac{\partial \sigma^+}{\partial \mathbf{p}} f_{\text{RE}}(\mathbf{p}_1), \quad (2.10)$$

where the effective pair-production cross-section  $d\sigma^+$ , accounting for both direct pair production in collisions as well as by X-rays, is given by

$$\frac{\partial \sigma^+}{\partial \mathbf{p}} = \frac{\partial \sigma_c^+}{\partial \mathbf{p}} + \frac{(Z_{\text{tot}} + 1)^2}{Z_{\text{tot}}} t_{\text{ava}} n_{\text{tot}} c \int d\mathbf{k} \frac{\partial \sigma_\gamma^+}{\partial \mathbf{p}}(\mathbf{p}, \mathbf{k}) \frac{\partial \sigma_{\text{br}}}{\partial \mathbf{k}}(\mathbf{k}, \mathbf{p}_1). \quad (2.11)$$

Positrons are created with a significant fraction of the energy of the incident electron that created them, but with a momentum perpendicular to the direction of the incident electron of order (Heitler 1954; Landau & Lifshitz 1983)  $p_\perp \approx m_e c$ . This means that the differential cross-section for their production is strongly peaked in the direction of the incident electron; throughout this work we assume that it is delta distributed in the scattering angles, and write

$$\left. \begin{aligned} \frac{\partial \sigma_c^+}{\partial \mathbf{p}} &= \frac{\delta(\cos \theta - \cos \theta_1)}{2\pi(m_e c)^2 p \gamma} \frac{\partial \sigma_c^+}{\partial \gamma}(p, p_1), \\ \frac{\partial \sigma_\gamma^+}{\partial \mathbf{p}} &= \frac{\delta(\cos \theta - \cos \theta_k)}{2\pi(m_e c)^2 p \gamma} \frac{\partial \sigma_\gamma^+}{\partial \gamma}(p, k), \\ \frac{\partial \sigma_{\text{br}}}{\partial \mathbf{k}} &= \frac{\delta(\cos \theta_k - \cos \theta_1)}{2\pi k^2} \frac{\partial \sigma_{\text{br}}}{\partial k}(k, p_1), \end{aligned} \right\} \quad (2.12)$$

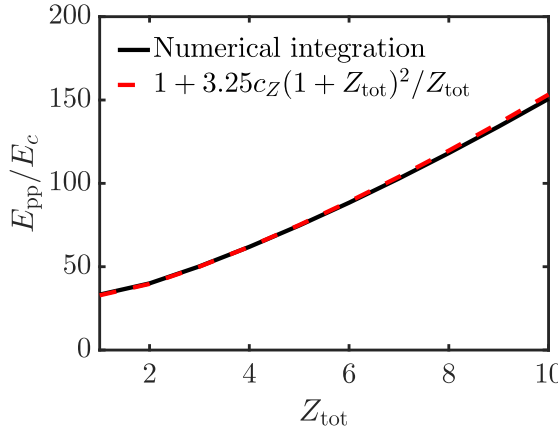


FIGURE 1. Critical field  $E_{\text{pp}}$  above which collisional positron production is the dominant pair-production mechanism in a uniform plasma, normalized to the avalanche threshold field  $E_c$ , calculated from the two expressions given in (2.23) with  $c_Z = \sqrt{5 + Z_{\text{tot}}}$ .

where  $\gamma = \sqrt{1 + (p/m_e c)^2}$  is the Lorentz factor. The angles  $\theta$ ,  $\theta_1$  and  $\theta_k$  are the angles between the accelerating electric field  $\mathbf{E}$  (or in a magnetized plasma the magnetic field  $\mathbf{B}$ ) and  $\mathbf{p}$ ,  $\mathbf{p}_1$  and  $\mathbf{k}$ , respectively. With an axisymmetric runaway distribution  $f_{\text{RE}}(\mathbf{p}_1) = f_{\text{RE}}(p_1, \cos \theta_1)$ , we then obtain the approximated positron source term

$$S_{\text{pos}}(\gamma, \cos \theta) = \frac{n_{\text{tot}} Z_{\text{tot}} m_e c^2}{p \gamma} \int_{\gamma+2}^{\infty} d\gamma_1 (\gamma_1^2 - 1) \frac{\partial \sigma^+}{\partial \gamma} f_{\text{RE}}(\gamma_1, \cos \theta), \quad (2.13)$$

where the effective cross-section now takes the form

$$\frac{\partial \sigma^+}{\partial \gamma}(\gamma, \gamma_1) = \frac{\partial \sigma_c^+}{\partial \gamma}(\gamma, \gamma_1) + \frac{(Z_{\text{tot}} + 1)^2}{Z_{\text{tot}}} t_{\text{ava}} n_{\text{tot}} c \int_{\gamma+1}^{\gamma_1-1} dk \frac{\partial \sigma_\gamma^+}{\partial \gamma}(\gamma, k) \frac{\partial \sigma_{\text{br}}^+}{\partial k}(k, \gamma_1), \quad (2.14)$$

depending only on the simpler integrated cross-sections that are only differential in the energy of the outgoing particle of interest. In (2.13) it is explicit that positrons are only generated in the direction of the incident energetic electrons – the electron distribution is sampled at the same pitch angle as the source. Further details of the positron source term in the presence of an avalanching electron distribution are given in appendix A, where we present the differential cross-sections used as well as illustrate typical shapes of the source term in (2.13).

The annihilation source takes the simpler form

$$S_{\text{an}}(\mathbf{p}) = -n_{\text{tot}} v \sigma_{\text{an}}(p) f_{\text{pos}}(\mathbf{p}), \quad (2.15)$$

where  $\sigma_{\text{an}}$  is the cross-section for free positron–electron two-quanta annihilation against stationary target electrons (Heitler 1954)

$$\sigma_{\text{an}} = \frac{\pi r_0^2}{(p/m_e c)(\gamma + 1)} \left[ \frac{\gamma^2 + 4\gamma + 1}{p/m_e c} \ln \left( \gamma + \frac{p}{m_e c} \right) - \gamma - 3 \right]. \quad (2.16)$$

### 2.1. Relative importance of pair production by collisions and by photons

A peculiar phenomenon occurs when considering pair production in the presence of a strong electric field, where the number of energetic electrons grows exponentially in time. Because there is a delay between the emission of photons and their subsequent pair production, if the electron population has time to grow by a significant amount during one such photon pair-production time, the direct positron generation in collisions may contribute with a relatively larger production of pairs. We will now proceed to derive the threshold electric field above which pair production in collisions is dominant due to this effect.

In order to evaluate the pair-production source terms we need an expression for the runaway-electron distribution. In a spatially uniform fully ionized plasma with constant electric field, when the runaway generation is dominated by the avalanche mechanism – i.e. by multiplication through large-angle collisions – it is given by (Fülöp *et al.* 2006)

$$\left. \begin{aligned} f_{\text{RE}}(p, \xi, t) &= \frac{n_{\text{RE}}(t)A(p)}{2\pi m_e c \gamma_0 p^2} \frac{\exp \left[ -\frac{\gamma}{\gamma_0} - A(p)(1 + \xi) \right]}{1 - e^{-2A}}, \\ A(p) &= \frac{E/E_c + 1}{Z_{\text{tot}} + 1} \gamma, \\ n_{\text{RE}}(t) &= n_{\text{RE}}(0) e^{t/t_{\text{ava}}}, \\ \gamma_0 &= c_Z \ln \Lambda. \end{aligned} \right\} \quad (2.17)$$

Our choice for  $A$  differs slightly from that in Fülöp *et al.* (2006), however agrees in the limit  $E \gg E_c$ ,  $p \gg m_e c$  and  $1 + \xi \ll 1$  where the solution is expected to be valid, but is here generalized to also capture the near-threshold limit  $E \rightarrow E_c$  (Lehtinen, Bell & Inan 1999; Hesslow *et al.* 2018). When pitch-angle averaged, the electron distribution is given by

$$\mathcal{F}_{\text{RE}}(p, t) = 2\pi \int_{-1}^1 d\xi f_{\text{RE}}(p, \xi, t) = \frac{n_{\text{RE}}(t)}{m_e c \gamma_0} e^{-\gamma/\gamma_0}, \quad (2.18)$$

where the average runaway energy is given by  $\gamma_0 m_e c^2 \approx (c_Z \ln \Lambda / 2)$  MeV, which is typically of the order of 10–30 MeV in most scenarios of interest. Runaway-electron populations with energies in this range have been observed in avalanching scenarios in tokamaks (Paz-Soldan *et al.* 2017). In our results we will indicate the dependence on average runaway energy through the parameters  $\gamma_0$  or  $c_Z$ .

The total number of pairs created per unit time and volume is obtained by integrating the positron source function (2.13) over all momenta, yielding

$$\frac{dn_{\text{pair}}}{dt} = n_e Z_{\text{tot}} m_e c^2 \int_3^\infty d\gamma_1 \sigma^+(\gamma_1) \mathcal{F}_{\text{RE}}(\gamma_1) \equiv n_e n_{\text{RE}} Z_{\text{tot}} \langle v \sigma^+ \rangle_{\text{RE}}, \quad (2.19)$$

$$\left. \begin{aligned} \sigma^+(\gamma_1) &= \int_1^{\gamma_1-2} \frac{\partial \sigma^+}{\partial \gamma}(\gamma, \gamma_1) d\gamma, \\ \langle v \sigma^+ \rangle_{\text{RE}} &= \frac{1}{n_{\text{RE}}} \int_{\sqrt{8}}^\infty dp_1 v_1 \sigma^+(\gamma_1) \mathcal{F}_{\text{RE}}(\gamma_1). \end{aligned} \right\} \quad (2.20)$$

With the analytic form of (2.18) for the electron distribution, the pair-production rate defined by the above equations is characterized by the two integrals

$$\left. \begin{aligned} \langle v\sigma_c^+ \rangle_{\text{RE}} &= \frac{m_e c^2}{n_{\text{RE}}} \int_3^\infty d\gamma_1 \sigma_c^+(\gamma_1) \mathcal{F}_{\text{RE}}(\gamma_1) \approx \alpha^2 r_0^2 c \frac{\gamma_0 - 6.7}{15}, \\ \langle v\sigma_\gamma^+ \rangle_{\text{RE}} &= \frac{m_e c^2}{n_{\text{RE}}} \int_3^\infty d\gamma_1 \mathcal{F}_{\text{RE}}(\gamma_1) \int_2^{\gamma_1-1} dk \sigma_\gamma^+(k) \frac{\partial \sigma_{\text{br}}}{\partial k}(k, \gamma_1) \approx \alpha^2 r_0^4 c (2.6\gamma_0 - 14.8), \end{aligned} \right\} \quad (2.21)$$

where  $\sigma_\gamma^+ = \int_1^{k-1} (\partial \sigma_\gamma^+ / \partial \gamma) d\gamma$ , and the approximate formulas are least-square fits on the interval of  $\gamma_0$  between 20 and 80, giving a maximum error of 2.5 %. Within an error of less than 3 %, the second expression differs from the first by a constant factor 40.75  $r_0^2$ , allowing the total pair-production rate to be written

$$\frac{dn_{\text{pair}}}{dt} \approx Z_{\text{tot}} \alpha^2 n_e r_0^2 c \frac{\gamma_0 - 6.7}{15} \left( 1 + 40.75 \frac{(Z_{\text{tot}} + 1)^2}{Z_{\text{tot}}} t_{\text{ava}} n_e c r_0^2 \right). \quad (2.22)$$

With  $t_{\text{ava}} n_e c r_0^2 = c_Z / [4\pi(E/E_c - 1)]$ , it is clear that there is a threshold field  $E = E_{\text{pp}}(Z_{\text{tot}})$  above which the collisional pair production (described by the first term within the parentheses) will be dominant. When  $c_Z$  is independent of  $E$ , this threshold field is given by

$$\begin{aligned} \frac{E_{\text{pp}}}{E_c} - 1 &= \frac{(1 + Z_{\text{tot}})^2}{Z_{\text{tot}}} \frac{c_Z}{4\pi r_0^2} \frac{\int_3^\infty d\gamma_1 e^{-\gamma_1/\gamma_0} \int_2^{\gamma_1-1} dk \sigma_\gamma^+(k) \frac{\partial \sigma_{\text{br}}}{\partial k}(k, \gamma_1)}{\int_3^\infty d\gamma_1 e^{-\gamma_1/\gamma_0} \sigma_c^+(\gamma_1)} \\ &\approx 3.25 c_Z \frac{(1 + Z_{\text{tot}})^2}{Z_{\text{tot}}}. \end{aligned} \quad (2.23)$$

When  $Z_{\text{tot}} = 1$ , the threshold field is  $E_{\text{pp}} \approx 33E_c$ , but grows rapidly with  $Z_{\text{tot}}$ . With an air-like value of  $Z_{\text{tot}} = 14.5$ , one obtains  $E_{\text{pp}} \approx 240E_c$ .

The role of direct pair production in lightning has been investigated by Vodopiyanov *et al.* (2015) using comprehensive Monte Carlo simulations of the runaway dynamics to investigate the degree to which positrons contribute to the relativistic feedback mechanism (Dwyer 2012). Their numerical study revealed a similar qualitative dependence on the electric field when comparing the contributions from photon-produced and directly produced positrons; direct production becomes relatively more important for larger electric fields. Their study, however, uses the Gryaznykh (1998) cross-section for pair production as well as a simplified description of the energy spectrum of newly created positrons, and they find a significantly lower threshold field than predicted here. Spatial dynamics along the discharge may also play a role in determining the feedback gain, which prevents a simple direct comparison between our results.

In the above we assumed an infinitely large homogeneous system. When runaway acceleration occurs only over a finite distance of length  $L$  of constant background parameters, the threshold field calculated above is valid when  $L \gg L_{\text{ava}} = ct_{\text{ava}}$ , that is, when the system is significantly longer than one avalanche mean-free path. When this

is not satisfied, i.e. when  $L \lesssim L_{\text{ava}}$ , a threshold condition for the length of the system is obtained instead, taking the form

$$L_{\text{pp}} \approx \frac{Z_{\text{tot}}}{(1 + Z_{\text{tot}})^2} \frac{3 \times 10^7 \text{ m}}{n_e [10^{20} \text{ m}^{-3}]} \quad (2.24)$$

When  $L_{\text{pp}} \lesssim L \lesssim L_{\text{ava}}$ , photon pair production will be the dominant positron-generation mechanism.

In the remainder of this work, we will focus on scenarios where either  $E \gtrsim E_{\text{pp}}$  or  $L \lesssim L_{\text{pp}}$ , so that pair production by photons is negligible. This is typical of runaway scenarios in tokamaks, where  $L/L_{\text{pp}} \ll 10^{-5}$  due to the small size of the device.

## 2.2. Distribution function of fast positrons

Equipped with the kinetic equation for positrons in a runaway scenario, we can now characterize its solutions. When the electric field is sufficiently large for the average pitch angle to be small, typically well satisfied when  $A = (E/E_c + 1)\gamma/(Z_{\text{tot}} + 1) \gtrsim 1$ , the distribution function of fast positrons can be readily calculated analytically. The kinetics are then essentially one-dimensional, with the pitch-angle dynamics playing a peripheral role in the evolution of the energy spectrum.

We introduce a half-plane pitch-angle-averaged positron distribution function  $\mathcal{F}$  as

$$\mathcal{F}(p) = 2\pi p^2 \times \begin{cases} \int_0^1 d\xi f_{\text{pos}}(p, \xi), & p \geq 0 \\ \int_{-1}^0 d\xi f_{\text{pos}}(|p|, \xi), & p < 0, \end{cases} \quad (2.25)$$

where the coordinate  $p$  now ranges from  $-\infty$  to  $\infty$ . This distribution is defined so that  $\int_{p_c}^{\infty} \mathcal{F} dp = n_{\text{RP}}$  equals the total runaway-positron density, with  $p_c$  a superthermal threshold in momentum distinguishing thermal positrons from runaways. In the same way, the thermal number density of positrons is  $n_{\text{TP}} = \int_{-p_c}^{p_c} \mathcal{F} dp$ .

In appendix B we solve the positron kinetic equation (2.3) in the limit  $(p/m_e c)^2 \gg 1$  assuming small pitch angles  $1 - |\xi| \ll 1$ . The resulting positron distribution is given by

$$\mathcal{F}(p) = \frac{Z_{\text{tot}}}{4\pi \ln \Lambda r_0^2} \frac{n_{\text{RE}}(t)}{\gamma_0 m_e c} e^{\rho\gamma/\gamma_0} \int_{\gamma}^{\infty} dy' \int_{\gamma'+2}^{\infty} dy_1 \frac{\partial \sigma^+}{\partial \gamma'}(\gamma', \gamma_1) \exp\left(-\frac{\rho\gamma' + \gamma_1}{\gamma_0}\right) \quad (2.26)$$

for  $p < 0$ , which describes the slowing-down distribution of the newly created positrons, where  $\rho = (E/E_c - 1)/(E/E_c + 1)$ , and

$$\left. \begin{aligned} \mathcal{F}(p, t) &= \frac{n_{\text{RP}}(t)}{m_e c \gamma_0} e^{-\gamma/\gamma_0}, \\ n_{\text{RP}}(t) &= n_{\text{RP}}(0) e^{t/t_{\text{ava}}} \end{aligned} \right\} \quad (2.27)$$

for  $p > 0$ , describing the runaway-positron population that is undergoing acceleration in the electric field. Note that the prefactor, including the runaway-positron density evaluated at  $t = 0$ , is not determined in this derivation, but must instead be calculated in a more comprehensive kinetic equation accounting for the dynamics near  $p \lesssim m_e c$ .

We see that when  $p > 0$ , the runaway-positron distribution satisfies  $\mathcal{F}(p) = (n_{\text{RP}}/n_{\text{RE}})\mathcal{F}_{\text{RE}}(-p)$ . Indeed, for the full positron distribution, since the kinetic equation

(2.3) is identical to the runaway-electron equation for  $\xi > 0$  where the pair-production source vanishes, we would expect

$$f_{\text{RP}}(p, \xi, t) \approx \frac{n_{\text{RP}}(t)}{n_{\text{RE}}(t)} f_{\text{RE}}(p, -\xi, t). \quad (2.28)$$

The expressions given above are valid for collisional as well as for photon pair production during runaway scenarios.

We can now accurately evaluate the annihilation rate of runaway positrons, obtaining in the ultra-relativistic limit,

$$\begin{aligned} \frac{1}{\tau_{\text{aR}}} &= \frac{n_e}{n_{\text{RP}}} \int_{p_c}^{\infty} dp v \mathcal{F}(p) \sigma_{\text{an}}(p) \approx \frac{1}{4 \ln \Lambda(E/E_c - 1) t_{\text{ava}}} \int_1^{\infty} d\gamma \frac{\ln 2\gamma - 1}{\gamma} e^{-\gamma/\gamma_0} \\ &\approx \frac{\ln^2(\gamma_0/2.42) + 1.55}{8 \ln \Lambda(E/E_c - 1) t_{\text{ava}}}, \end{aligned} \quad (2.29)$$

the final approximation having an error less than 2% for  $\gamma_0 > 20$ , and where the annihilation cross-section  $\sigma_{\text{an}}$  was given in (2.16). We find that typically  $t_{\text{ava}}/\tau_{\text{aR}} \lesssim 0.1/(E/E_c - 1)$ , showing that annihilation has negligible impact on the avalanche time scale dynamics except for very close to the threshold field  $E_c$ . At that point, however, most of the created positrons will become thermalized, and only a negligible fraction will have time to annihilate before reaching thermal energies.

For  $v \ll c$  the annihilation cross-section takes the simple form  $\sigma_{\text{an}} \sim \pi r_0^2 c/v$ , so that the thermal annihilation time  $\tau_{\text{aT}}$  for a thermal positron population of temperature  $T \ll 511$  keV is given simply by

$$\frac{1}{\tau_{\text{aT}}} = \pi n_e r_0^2 c = \frac{1}{4t_{\text{ava}}} \frac{c_Z}{E/E_c - 1}. \quad (2.30)$$

In the presence of partially ionized or neutral gases, however, the cold positrons may annihilate also through the formation of positronium, which has significantly shorter, sub- $\mu$ s lifetime. The annihilation time of thermal positrons is then rather set by the positronium formation rate, which is of the order of  $n_i v a_0^2$ , with  $a_0$  the Bohr radius (Charlton & Humberston 2001).

### 2.3. Numerical distribution function

The positron Fokker–Planck equation, equation (2.3), can be solved as an initial value problem to give the evolution of the positron distribution function in the presence of an accelerating electric field. By adding the source and annihilation terms to the CODE (Landreman *et al.* 2014; Stahl *et al.* 2016) numerical kinetic solver, we calculate the distribution function for various electric fields and effective ion charges. CODE uses a continuum-spectral discretization scheme and has been used extensively to calculate runaway-electron distributions including partial screening effects (Hesslow *et al.* 2017), synchrotron radiation (Hirvijoki *et al.* 2015; Stahl *et al.* 2015), bremsstrahlung (Embréus, Stahl & Fülöp 2016) and close collisions (Embréus, Stahl & Fülöp 2018).

Figure 2 illustrates the angle-averaged positron distribution for two cases: (i) with  $E = 2E_c$  and  $Z_{\text{tot}} = 10$ , and (ii)  $E = 10E_c$  and  $Z_{\text{tot}} = 1$ . The analytic solution, equations (2.26) and (2.27), is nearly indistinguishable from the numerical solution for  $p < 0$  for both cases, and for  $p > 0$  in case (ii) with the higher electric field

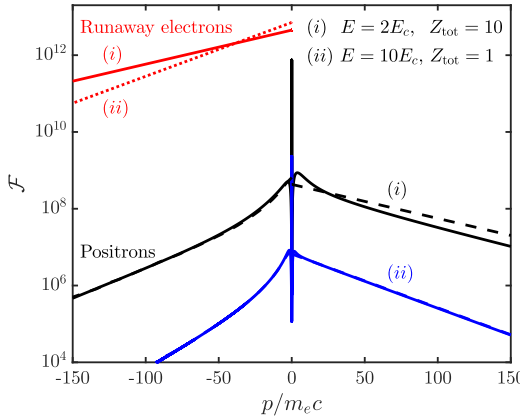


FIGURE 2. Pitch-angle-averaged distribution functions  $\mathcal{F}$  after 10 avalanche times  $t_{\text{ava}}$ , with an initial runaway-electron density  $n_{\text{RE},0} = 10^{10} \text{ m}^{-3}$ ,  $n_e = 5 \times 10^{19} \text{ m}^{-3}$  and  $T = 100 \text{ eV}$ . Runaway electrons in red and positrons in black and blue. Dashed lines denote the theoretical predictions of (2.26) and (2.27); in the (ii)  $E = 10E_c$ ,  $Z_{\text{tot}} = 1$  case it fully overlaps with the numerical solution.

(shown in blue). The analytic solution fails to fully capture the low energy behaviour in case (i) with low electric field and high plasma charge (black), where pitch-angle dynamics becomes important. The accuracy of the analytic solution at high electric field further motivates the neglect of annihilation in the dynamics of fast positrons. The sharp peaks at  $p = 0$  in the numerical positron energy spectra contain the thermalized positron populations, which we do not consider the detailed dynamics of here.

### 3. Rate equations for runaway positrons

From the kinetic description of §2 we can find a reduced set of fluid equations which govern the evolution of the number densities of runaway positrons as well as thermal positrons. We introduce the runaway-positron density  $n_{\text{RP}}$  and thermal positron density  $n_{\text{TP}}$  in the same way as in the previous section. These then satisfy the equations

$$\frac{\partial n_{\text{RP}}}{\partial t} = Z_{\text{tot}} n_e n_{\text{RE}} \kappa(E, Z_{\text{tot}}) \langle v \sigma_c^+ \rangle_{\text{RE}} - n_{\text{RP}} / \tau_{\text{aR}} \quad (3.1)$$

$$\frac{\partial n_{\text{TP}}}{\partial t} = Z_{\text{tot}} n_e n_{\text{RE}} \eta(E, Z_{\text{tot}}) \langle v \sigma_c^+ \rangle_{\text{RE}} - n_{\text{TP}} / \tau_{\text{aT}} \quad (3.2)$$

$$\frac{\partial n_{\text{RE}}}{\partial t} = n_{\text{RE}} \Gamma_{\text{ava}}(E, Z_{\text{tot}}), \quad (3.3)$$

where  $\kappa$  denotes the fraction of created positrons that are accelerated as runaways,  $\eta$  the fraction that is thermalized and  $\Gamma_{\text{ava}} = 1/t_{\text{ava}}$  is the avalanche growth rate of runaway electrons.

Kinetic simulations must be used to determine the runaway fraction  $\kappa$  and thermalization fraction  $\eta$  (note that they will not sum to unity, since the population of fast newly born positrons with  $\xi < 0$  also grows in time). Results from numerical simulations for a variety of electric fields and plasma charges are shown in figure 3,

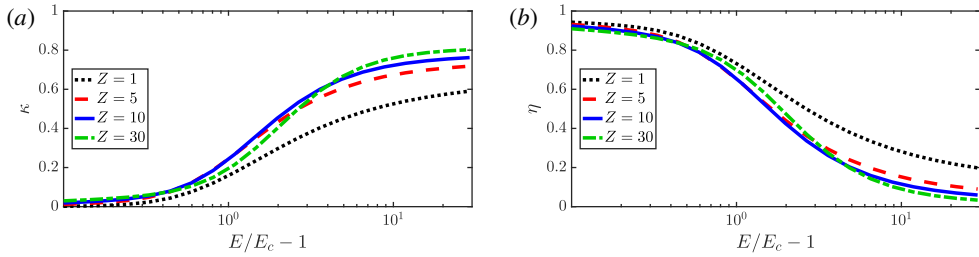


FIGURE 3. (a) Positron runaway fraction  $\kappa$  defined by (3.1), for various electric-field strengths and plasma effective charge  $Z_{\text{tot}}$ . (b) Positron thermalization fraction  $\eta$  defined by (3.2), for various electric-field strengths and plasma effective charge  $Z_{\text{tot}}$ .

obtained for constant electric fields and plasma charge. These are applicable to scenarios where  $E$  and  $Z_{\text{tot}}$  vary slowly in time compared to the avalanche time. When  $E \gg E_c$ , the runaway fraction is near unity, but decreases exponentially in magnitude when the electric field approaches the threshold value  $E_c$ . As only a small fraction of positrons are annihilated before slowing down (or entering the runaway region) (Heitler 1954), the effect of annihilation on the positron runaway-generation dynamics can be ignored, and we can assume that positrons are only annihilated after being either thermalized or runaway accelerated.

In the presence of a constant electric field, background density and charge, the rate equations have a simple analytic solution given by (after a short transient phase on the scale of  $t_{\text{ava}}$ )

$$\left. \begin{aligned} n_{\text{RE}}(t) &= n_0 \exp(\Gamma_{\text{ava}} t), \\ n_{\text{RP}}(t) &= n_{\text{RE}}(t) \frac{Z_{\text{tot}} \kappa n_e \langle v \sigma_c^+ \rangle}{\Gamma_{\text{ava}} + \tau_{\text{aR}}^{-1}}, \\ n_{\text{TP}}(t) &= n_{\text{RE}}(t) \frac{Z_{\text{tot}} \eta n_e \langle v \sigma_c^+ \rangle}{\Gamma_{\text{ava}} + \tau_{\text{aT}}^{-1}}. \end{aligned} \right\} \quad (3.4)$$

Note that the positron populations grow in time despite annihilation; this occurs due to the ever-increasing amplitude of the positron source, since the runaway electrons are avalanching.

When the electric field is significantly above threshold one finds that  $\Gamma_{\text{ava}} \gg \tau_{\text{aR}}^{-1}$  meaning that annihilation is negligible, so that

$$\frac{n_{\text{RP}}}{n_{\text{RE}}} \approx \frac{\kappa(E, Z_{\text{tot}})}{E/E_c - 1} \frac{Z_{\text{tot}} \langle v \sigma_c^+ \rangle}{4\pi c r_0^2 / c_Z} \approx \alpha^2 c_Z Z_{\text{tot}} \frac{\kappa(E, Z_{\text{tot}})}{E/E_c - 1} \frac{\gamma_0 - 6.7}{60\pi}, \quad (3.5)$$

where again  $\gamma_0 = c_Z \ln \Lambda$ . The electric-field dependence is fully captured in the factor  $\kappa/(E/E_c - 1)$ , which takes its maximal value  $\approx 0.2$  near  $E \approx 2E_c$ , only weakly dependent on the charge  $Z_{\text{tot}}$ . With  $\ln \Lambda = 15$ , we then find that the maximal ratio of runaway positrons to electrons is  $n_{\text{RP}}/n_{\text{RE}} \lesssim 8.5 \cdot 10^{-7} Z_{\text{tot}} c_Z (c_Z - 0.45)$ , which for a low- $Z$  plasma with  $Z_{\text{tot}} = 1$  is approximately  $4 \times 10^{-6}$ , and for a high- $Z$  plasma with  $Z_{\text{tot}} = 20$  of the order of  $4 \times 10^{-4}$ . This means that the runaway-positron synchrotron and hard X-ray (HXR) emission may be challenging to distinguish from the radiation emitted by the runaway electrons in a tokamak, since even a small fraction of reflected or scattered radiation from electrons or noise from other sources could drown out the positron signal.

#### 4. Radiation from positrons in tokamak plasmas

In the previous section we found that runaway positrons are less numerous than the runaway electrons by a factor smaller than approximately  $10^{-4}$ . This causes a direct measurement of runaway positrons in a laboratory plasma to be challenging, and an appealing option is instead to detect the annihilation radiation of the positrons that have slowed down, which is distinctly peaked around photon energies of 511 keV. The annihilation radiation from slow positrons is emitted approximately isotropically, whereas runaway electrons emit radiation primarily along their direction of motion, which when the electric field is large is along the electric field, or along the magnetic field in a magnetized plasma. This means that when measuring perpendicularly to the direction of runaway acceleration, even though the positrons are much fewer, their annihilation radiation may be detected through the X-ray background of runaway electrons for which only a small fraction is emitted at a  $\pi/2$  angle and near<sup>1</sup> 511 keV. Furthermore, coincidence measurement techniques can be employed to carry out measurements in poor signal-to-noise ratio cases (Guanying *et al.* 2017).

We can make the heuristic discussion above stricter by the following arguments. The number density of bremsstrahlung photons emitted per unit solid angle, time and photon energy is given by

$$\frac{\partial n_{\text{HXR}}}{\partial t \partial \Omega \partial k} = n_e Z_{\text{tot}} \int_{\gamma > k+1} v \frac{\partial \sigma_{\text{br}}}{\partial k \partial \Omega} f_{\text{RE}}(\mathbf{p}) d\mathbf{p}. \quad (4.1)$$

This can be compared to the number density of annihilation photons emitted per unit time and solid angle due to the thermal positrons  $n_{\text{TP}}$  annihilating against the cold background,

$$\frac{\partial n_{\text{an}}}{\partial t \partial \Omega} = \frac{n_{\text{TP}}}{4\pi \tau_{\text{aT}}} \approx Z_{\text{tot}} \frac{n_{\text{RE}} n_e \eta \langle v \sigma_c^+ \rangle_{\text{RE}}}{4\pi}, \quad (4.2)$$

where we have assumed the thermal positron-annihilation rate to be much larger than the avalanche growth rate,  $\Gamma_{\text{ava}} \tau_{\text{aT}} \ll 1$ .

The annihilation radiation will have a line profile in photon energy with a characteristic width comparable to the background temperature. We consider the case where the profile is not resolved in the measurement, and the full line is captured in one channel. In this case, since the hard X-rays have a broad spectrum, we find it useful to characterize the visibility of the annihilation line with the parameter

$$\Delta k = \frac{\partial n_{\text{an}} / \partial t \partial \Omega}{\partial n_{\text{HXR}} / \partial t \partial \Omega \partial k}, \quad (4.3)$$

which (when  $\Delta k \ll k$ ) can be interpreted as the photon-energy interval  $\Delta k$  around  $k = m_e c^2$  within which the total HXR emission equals the annihilation photon flux. From a detection point of view,  $\Delta k$  would approximate the energy resolution required for the annihilation peak to appear with twice the amplitude of the continuous X-ray background. The finite line width of the annihilation peak would need to be accounted for when the plasma temperature satisfies  $T \gtrsim \Delta k$ .

In figure 4 we show  $\Delta k$  for detection at a  $\pi/2$  angle relative to the direction of runaway acceleration, using the analytic runaway distribution of (2.17). We observe

<sup>1</sup>More precisely, the ratio of perpendicular to tangential bremsstrahlung emission is given by approximately  $3/(8\gamma^4)$  at  $k = 511$  keV.

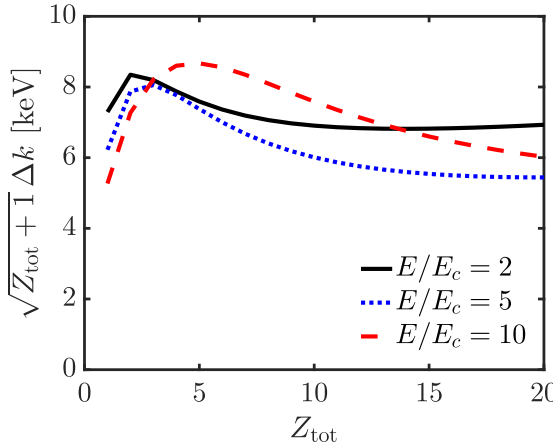


FIGURE 4. The photon-energy resolution parameter  $\Delta k = (\partial n_{\text{an}}/\partial t\partial\Omega)/(\partial n_{\text{HXR}}/\partial t\partial\Omega\partial k)$  for perpendicular detection of annihilation radiation from thermalized positrons and hard X-rays from runaway electrons.

a relatively weak dependence on electric field where the main trend is approximately captured, within approximately 25 %, by

$$\Delta k \approx \frac{7 \text{ keV}}{\sqrt{Z_{\text{tot}} + 1}}. \quad (4.4)$$

This means that in order for the annihilation peak to be clearly distinguishable from the X-ray background due to runaway electrons, an energy resolution better than or comparable to  $(7/\sqrt{Z_{\text{tot}} + 1})$  keV is desirable. The contrast of X-rays to annihilation radiation, quantified through  $\Delta k$ , is largely insensitive to other parameters of the scenario, since the cross-sections for the two processes scale in the same way with the background parameters. Commercial high purity germanium (HPGe) radiation detectors are available with energy resolutions near 1 keV. Therefore, our calculations indicate that sufficient signal-to-noise ratios can be achieved in the presence of most magnetic-fusion relevant plasma compositions.

There are two main competing effects which are sensitive to  $E$  and  $Z_{\text{tot}}$  that determine the observed behaviour in  $\Delta k$ . When  $E$  increases, the thermalization fraction  $\eta$  of positrons rapidly decreases, as illustrated in figure 3(b), which reduces the amount of 511 keV annihilation radiation. At the same time the runaway-electron population becomes more anisotropic, which sharply reduces the amount of bremsstrahlung emitted at a perpendicular angle. In the parameter range shown in the figure, these effects are found to approximately cancel, leaving only a weak  $E$  dependence. On the other hand, an increase in charge  $Z_{\text{tot}}$  causes the electron population to become more isotropic, increasing the amount of bremsstrahlung emitted at a perpendicular angle, however, it also increases the average runaway-electron energy which increases the number of positrons created per electron. The former effect is significantly stronger, which causes a net  $1/\sqrt{Z_{\text{tot}} + 1}$  dependence.

Finally we note that, in the post-disruption runaway plateau where the runaway current slowly dissipates on the inductive time scale of the device, the analytical avalanche runaway distribution that we have used here is not valid, as it tends

to significantly overestimate the average energy of the distribution. Due to its experimental accessibility, we consider this scenario separately for a singly ionized argon-dominated plasma (Pautasso *et al.* 2016). For the runaway electron distribution we use the self-consistent slowing-down distribution of Hesslow *et al.* (2018) obtained from a numerical solution of the kinetic equation with an inductive electric field and accurate modelling of screening effects on collisions, at a plasma temperature  $T = 10$  eV. Using such a numerical distribution function in evaluating the rate of pair production  $\langle v\sigma_c^+ \rangle_{\text{RE}}$  and the bremsstrahlung photon flux yields  $\Delta k = 0.31$  keV, which is approximately 20 % of the value predicted by the rule-of-thumb given in (4.4) evaluated with  $Z_{\text{tot}} = 18$ . One may therefore expect that during the runaway plateau following a disruption, the positron radiation is overwhelmed by X-rays more easily than during the transient avalanche phase.

As well as being distinguishable from the runaway X-rays, it is required that the total number of annihilation photons reaching a detector is sufficiently large. While this is highly sensitive to the details of the set-up, we can provide a rough estimate in the following way. The total number of annihilation photons per unit time reaching a detector with area  $A_{\text{det}}$  placed a distance  $R$  from the plasma detecting emission within an opening angle  $\Delta\theta$ , is given approximately by

$$\begin{aligned} \frac{\partial N_{\text{an}}}{\partial t} &\approx \Delta\theta \frac{A}{R} A_{\text{det}} \frac{\partial n_{\text{an}}}{\partial t \partial \Omega} \approx \Delta\theta A_{\text{det}} A Z_{\text{tot}} \frac{n_{\text{RE}} n_e \eta \langle v\sigma_c^+ \rangle_{\text{RE}}}{4\pi R} \\ &\approx \Delta\theta A_{\text{det}} \frac{A n_{\text{RE}} e c}{e} Z_{\text{tot}} \frac{n_e r_0^2}{4\pi 137^2 R} \eta \frac{\gamma_0 - 6.7}{15} \\ &\approx (1.4 \times 10^6 \text{ s}^{-1}) n_{20} I_{\text{RE}} [100 \text{ kA}] \Delta\theta \frac{A_{\text{det}} [\text{dm}^2]}{R [\text{m}]} Z_{\text{tot}} (\gamma_0 - 6.7) \eta. \end{aligned} \quad (4.5)$$

Here, the cross-sectional area  $A$  of the plasma is assumed to be completely within the detector field-of-view. Then, discharges with higher plasma charge, background density and runaway current are seen to yield higher total annihilation photon fluxes. Note that a strong decrease in total photon flux is found when the electric field increases above the threshold value  $E_c$ , due to the change in the thermalization fraction  $\eta$ . As an example, inserting values typical of a disruption in a medium-sized tokamak with  $R = 1.5$  m,  $Z_{\text{tot}} = 10$ ,  $n_{\text{tot}} = 10^{20} \text{ m}^{-3}$ ,  $I_{\text{RE}} = 400$  kA,  $E = 2E_c$ ,  $A_{\text{det}} = 1 \text{ dm}^2$ ,  $\Delta\theta = 0.5$  rad and with  $\ln A = 15$ , one obtains a detected 511 keV annihilation photon count of  $\partial N_{\text{an}} / \partial t \approx 7 \times 10^8 \text{ s}^{-1}$ .

In poor signal-to-noise cases coincidence measurements can be employed, where only positrons annihilated between two detectors are counted. This can be approximately accounted for in the previous formula by using an opening angle  $\Delta\theta = \sqrt{A_{\text{det}}}/R$  if two identical detectors are placed on either side of the plasma, which reduces the number of counts by another factor  $0.1 \sqrt{A_{\text{det}} [\text{dm}]/R [\text{m}]}$ .

## 5. Conclusions

Fast electrons can produce electron–positron pairs, primarily via either a two-step process based on the emission of a bremsstrahlung photon and a subsequent photon–particle interaction, or the direct process where pairs are produced in collisions between fast electrons and nuclei. Using MadGraph 5 (Alwall *et al.* 2014) to calculate the differential cross-section for collisional pair production, it is shown that the cross-section given by Gryaznykh (1998), used in previous studies of runaway-positron

generation, overestimates the pair production approximately by a constant factor of four. A comparison of the cross-sections is presented in appendix A.

We show that collisional pair production is dominant when the electric field exceeds a certain threshold value, which is given in (2.23) and illustrated in figure 1. This has recently been investigated in the context of lightning discharges (Vodopiyanov *et al.* 2015), using the Gryaznykh (1998) cross-section for pair production. Our results, applied to an air-like plasma, show an elevated threshold. The collisional process is, however, always dominant when the fast electrons are confined to a region in space which is smaller than the photon mean-free path, e.g. in magnetic-fusion plasmas.

In strong electric fields electrons and positrons are accelerated and may run away. The kinetic equations for electrons and positrons are similar, except for the opposite directions of acceleration in an electric field, and the source and annihilation terms present in the positron kinetic equation. We show that when the electric field is sufficiently large the positron distribution function can be calculated analytically, with explicit solutions given in (2.26) and (2.27). The analytical solution shows remarkable agreement with numerical solutions of the kinetic equation in the relevant limit (high electric field and moderate charge number), as illustrated in figure 2.

Since the characteristic initial energy of the newly born positrons is large, a fluid description for the positron population can be used. Kinetic simulations are then only needed to determine the fraction of created positrons that are thermalized or runaway accelerated as a function of the background parameters. The evolution of the number density of thermal and runaway positrons can then be calculated from simple rate equations, given in (3.1)–(3.3). These equations admit analytical solutions in the presence of a constant electric field, and can be used to determine the ratio of the runaway-positron and -electron populations. The runaway and thermalized positron fractions determined from numerical kinetic simulations are given for a variety of electric fields and charge numbers in figure 3.

Finally we calculate the radiation emitted by a runaway-positron population, and evaluate the annihilation to HXR ratio of photon fluxes emitted at a perpendicular angle to the system. Our model implies that in tokamaks, the positron population produced during electron runaway may plausibly be measured using the isotropic annihilation radiation that the thermalized positrons emit. Sufficient signal-to-noise is obtainable with a single gamma-ray detector having a photon-energy resolution of  $\Delta k \lesssim 1$  keV at the distinct annihilation peak at 511 keV. If the energy-resolution requirement is not met, the annihilation peak may not be distinguishable from the background X-ray emission of the runaway electrons, and two detectors set-up for a coincidence measurement would need to be employed.

## Acknowledgements

The authors would like to thank G. Ferretti and I. Pusztai for fruitful discussions. This work was supported by the European Research Council (ERC-2014-CoG grant 647121) and the Swedish Research Council (Dnr. 2014-5510).

## Appendix A. Positron source term

The differential cross-sections appearing in (2.14) are given in the Born approximation by (Heitler 1954)

$$\frac{\partial\sigma_{\gamma}^{+}}{\partial\gamma}=\alpha r_0^2\frac{pp_{-}}{k^3}\left\{ -\frac{4}{3}-2\gamma_{-}\gamma\frac{p_{-}^2+p^2}{p_{-}^2p^2}+\frac{\gamma}{p_{-}^3}\epsilon_{-}\right. \\ \left.+\frac{\gamma_{-}}{p^3}\epsilon-\frac{\epsilon_{-}\epsilon}{p_{-}p}+L_{-}\left[k^2\frac{\gamma^2\gamma^2+p_{-}^2p^2}{p_{-}^3p^3}-\frac{8}{3}\frac{\gamma_{-}\gamma}{p_{-}p}\right.\right. \\ \left.\left.-\frac{k}{2p_{-}p}\left(\frac{\gamma_{-}\gamma-p_{-}^2}{p_{-}^3}\epsilon_{-}+\frac{\gamma_{-}\gamma-p^2}{p^3}\epsilon+\frac{2k\gamma_{-}\gamma}{p_{-}^2p^2}\right)\right]\right\}, \quad (\text{A } 1)$$

$$\frac{\partial\sigma_{\text{br}}}{\partial k}=\alpha r_0^2\frac{p}{kp_1}\left\{ \frac{4}{3}-2\gamma_1\gamma\frac{p_1^2+p^2}{p_1^2p^2}+\epsilon_1\frac{\gamma}{p_1^3}+\epsilon\frac{\gamma_1}{p^3}-\frac{\epsilon_1\epsilon}{p_1p}\right. \\ \left.+L_1\left[\frac{8}{3}\frac{\gamma_1\gamma}{p_1p}+k^2\frac{\gamma_1^2\gamma^2+p_1^2p^2}{p_1^3p^3}\right.\right. \\ \left.\left.+\frac{k}{2p_1p}\left(\epsilon_1\frac{\gamma_1\gamma+p_1^2}{p_1^3}-\epsilon\frac{\gamma_1\gamma+p^2}{p^3}+2k\frac{\gamma_1\gamma}{p_1^2p^2}\right)\right]\right\}, \quad (\text{A } 2)$$

$$\left. \begin{aligned} \epsilon &= 2\ln(\gamma+p) \\ \epsilon_1 &= 2\ln(\gamma_1+p_1) \\ \epsilon_{-} &= 2\ln(\gamma_{-}+p_{-}) \\ L_1 &= 2\ln\frac{\gamma_1\gamma+p_1p-1}{k}, \\ L_{-} &= 2\ln\frac{\gamma_{-}\gamma+p_{-}p-1}{k}, \end{aligned} \right\}$$

and  $1/\alpha = 4\pi\varepsilon_0\hbar c/e^2 \approx 137$  denotes the inverse fine-structure constant. In the expression for  $\partial\sigma_{\gamma}^{+}/\partial\gamma$ , energy conservation constrains  $\gamma_{-} = k - \gamma$  where  $p_{-} = \sqrt{\gamma_{-}^2 - 1}$  denotes the momentum of the electron created in the pair, whereas in the expression for  $\partial\sigma_{\text{br}}/\partial k$  one has  $\gamma = \gamma_1 - k$  and  $p = \sqrt{\gamma^2 - 1}$  is the momentum of the outgoing positron. Here, momenta are expressed in units of  $m_e c$  and  $k$  is the photon energy in units of  $m_e c^2$ .

The cross-section  $\partial\sigma_c^{+}/\partial\gamma$  for pair production in collisions by electrons and ions is evaluated in the Born approximation by the MadGraph 5 tool (Alwall *et al.* 2014), where 1 300 000 events were generated for each incident electron energy  $\gamma_1$ , for which 140 values between 3.13 and 587 were sampled (corresponding to a range from 1.6 MeV to 300 MeV). In figure 5 we compare  $\partial\sigma_c^{+}/\partial\gamma$  as calculated by MadGraph 5 with the corresponding differential cross-section evaluated in the main logarithmic approximation neglecting contributions of order  $1/\ln\gamma_1$  (Landau & Lifshitz 1983),

$$\frac{\partial\sigma_{c,\text{LL}}^{+}}{\partial\gamma}=\frac{56\alpha^2r_0^2}{9\pi}\frac{\ln\gamma}{\gamma}\ln\frac{\gamma_1}{\gamma}. \quad (\text{A } 3)$$

We observe that the shape of the Landau–Lifshitz cross-section  $d\sigma_{c,\text{LL}}^{+}$  is qualitatively similar to the MadGraph 5 results, although the values deviate significantly from the more accurate calculation. At moderate-to-low electron energies, the Landau–Lifshitz formula also significantly overestimates the average positron energy. The disagreement between the Landau–Lifshitz formula and the corresponding Born approximation result is expected, since the logarithmic approximation is only valid at significantly higher energies than those relevant to runaway scenarios.

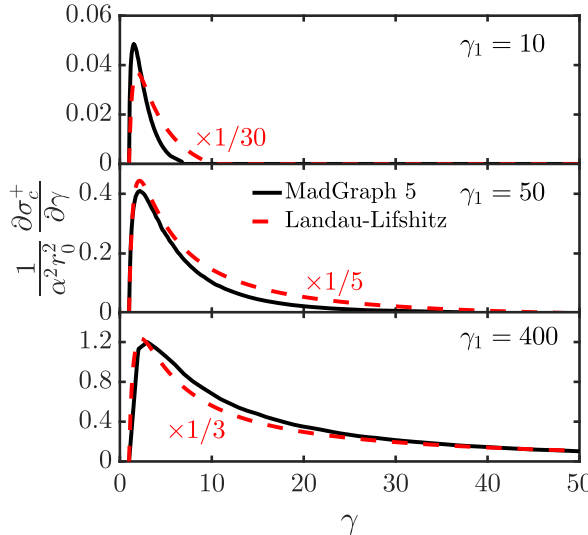


FIGURE 5. Differential cross-section for pair production in collisions, by MadGraph 5 (solid black line, employed for results in this paper) and for comparison the Landau-Lifshitz formula (dashed red).  $\gamma_1$  and  $\gamma$  are the incident electron and outgoing positron Lorentz factors, respectively. The Landau-Lifshitz formula has been multiplied by 1/30, 1/5 and 1/3 in the three subplots, respectively, in order to illustrate better the shapes of the curves. The MadGraph 5 results are significantly overestimated by the approximate formula.

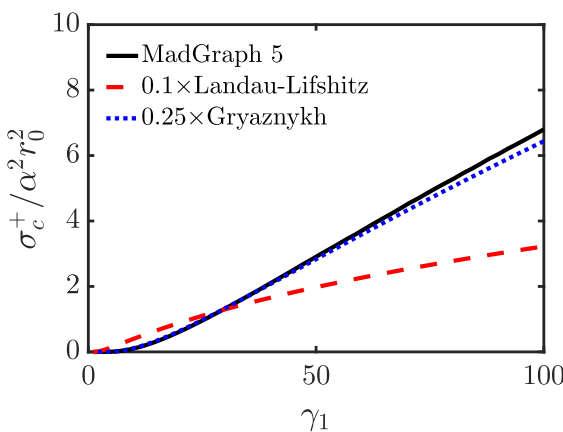


FIGURE 6. Total cross-sections  $\sigma_c^+$  by MadGraph 5 (solid, black), the Landau-Lifshitz formula (dashed, red) and the Gryaznykh formula (dotted, blue) as function of the incident electron Lorentz factor  $\gamma_1$ . The Landau-Lifshitz and Gryaznykh formulas have been rescaled for better visibility; they both significantly overestimate the positron production compared to the full MadGraph 5 computation in the energy range of interest for electron runaway.

In figure 6 we compare the total pair-production cross-section  $\sigma_c^+$  between MadGraph 5, the Landau-Lifshitz formula as well as with the formula given by

Gryaznykh (1998),

$$\sigma_{c,\text{Gr}}^+ = (5.11 \mu\text{b}) \ln^3 \frac{\gamma_1 + 3.6}{6.6}, \quad (\text{A } 4)$$

that has been employed in previous runaway-positron studies. Although Gryaznykh's formula is a numerical fit to the full Born approximation result, it appears that the prefactor is too large by a factor of 4.

It is furthermore insightful to consider the energy spectrum of created positrons by integrating the positron source  $S_{\text{pos}}$  of (2.13) over angles,

$$S_{\text{pos}}(p) = p^2 \int S_{\text{pos}}(\mathbf{p}) d\Omega_{\mathbf{p}} = S_c(p) + S_{\gamma}(p), \quad (\text{A } 5)$$

where we have split the source into the contribution  $S_c$  from collisional pair production and  $S_{\gamma}$  from pair production via X-rays. These are defined so that  $\int S_{\text{pos}} dp$  is the total rate at which positrons are produced, and are given explicitly by

$$S_c = n_e Z_{\text{tot}} v \int_{\gamma+2}^{\infty} d\gamma_1 \frac{\partial \sigma_c^+}{\partial \gamma} \mathcal{F}_{\text{RE}}(\gamma_1), \quad (\text{A } 6)$$

$$S_{\gamma} = n_e^2 Z_{\text{tot}} t_{\text{ava}} v c \int_{\gamma+2}^{\infty} d\gamma_1 \int_{\gamma+1}^{\gamma_1-1} dk \frac{\partial \sigma_{\gamma}^+}{\partial \gamma} \frac{\partial \sigma_{\text{br}}}{\partial k} \mathcal{F}_{\text{RE}}(\gamma_1). \quad (\text{A } 7)$$

Figure 7 shows  $S_c$  and  $S_{\gamma}$  for two different systems, characterized by  $\gamma_0 \equiv c_Z \ln \Lambda = 20$  and  $\gamma_0 = 50$ . It illustrates the dependence on the positron momentum  $p$  of the two pair-production mechanisms, when averaged over the electron (and photon) distribution. It is clear that the two main pair-production channels due to runaway electrons – in collisions and via X-rays – produce very similar positron-energy spectra.

We find that the average positron energy is not particularly sensitive to the average electron energy  $\gamma_0$ : by evaluating  $\langle \gamma \rangle = \int_0^{\infty} \gamma S dp / \int_0^{\infty} S dp$ , we obtain  $\langle \gamma \rangle_c \approx 8$  and 11 when  $\gamma_0 = 20$  and 50, respectively, for the collision term  $S_c$ . For the X-ray term  $S_{\gamma}$ , we find  $\langle \gamma \rangle_{\gamma} \approx 9$  and 13 for the corresponding cases. Energies of newly created positrons during runaway are therefore typically always in the 5 MeV range on average.

## Appendix B. Derivation of positron distribution function

We here present the derivation of the positron distributions (2.26) and (2.27) in the high-energy, small pitch-angle limit. The positron distribution varies over energies much larger than the rest energy, and thus satisfies the ultra-relativistic, one-dimensional kinetic equation

$$\frac{\partial \mathcal{F}(p, t)}{\partial t} + eE_c \left( \frac{E}{E_c} - \text{sgn}(p) \right) \frac{\partial \mathcal{F}(p, t)}{\partial p} = n_e c Z_{\text{tot}} \int_{\gamma+2}^{\infty} d\gamma_1 \frac{\partial \sigma^+}{\partial \gamma} (\gamma, \gamma_1) \mathcal{F}_{\text{RE}}(p_1, t), \quad (\text{B } 1)$$

where  $p_1 = \text{sgn}(p) \sqrt{\gamma_1^2 - 1}$ . Here we have ignored the effect of annihilation on the evolution of the distribution, since this process occurs on a significantly longer time scale than the acceleration time in a strong electric field, and neglected the weak logarithmic energy dependence in the collisional friction force, taken to be constantly of magnitude  $eE_c = m_e c / \tau_c$  with  $\tau_c^{-1} = 4\pi \ln \Lambda n_e r_0^2 c$ , opposing the direction of motion. We furthermore neglect radiation losses through synchrotron emission and bremsstrahlung; for high  $Z$  and low  $E$ , this assumption may be violated in the far tail of the energy distribution.

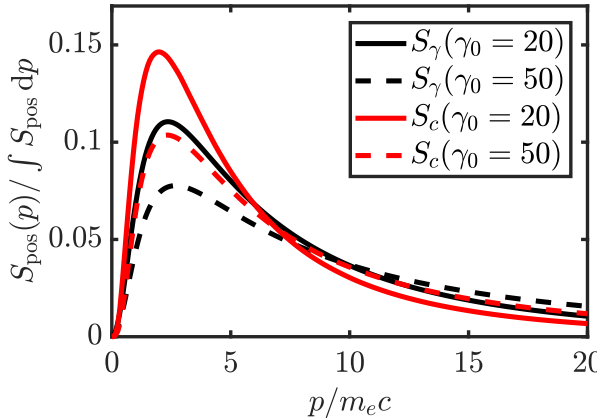


FIGURE 7. Positron source terms  $S_c$  (red), due to collisional pair production, and  $S_\gamma$  (black), due to pair production via X-ray emission, normalized to unity production rate, evaluated at different values of the average runaway energy  $\gamma_0 = c_Z \ln \Lambda$ . (solid,  $\gamma_0 = 20$ ; dashed  $\gamma_0 = 50$ ).

Since the electron population – which drives the generation of positrons through the pair-production source term – grows exponentially in time we expect the positron kinetic equation to have a quasi-steady-state solution of the form  $\mathcal{F}(p, t) = e^{t/t_{ava}} \mathcal{F}(p, 0)$ , growing at the same rate as the energetic electrons. For  $p < 0$ , the positron distribution then satisfies the first-order linear ordinary differential equation

$$\left[ \frac{E/E_c - 1}{\gamma_0} - \left( \frac{E}{E_c} + 1 \right) \frac{\partial}{\partial \gamma} \right] \mathcal{F} = \frac{Z_{\text{tot}}}{4\pi \ln \Lambda r_0^2} \frac{n_{\text{RE}}}{\gamma_0 m_e c} \int_{\gamma}^{\infty} d\gamma_1 \frac{\partial \sigma^+}{\partial \gamma} e^{-\gamma_1/\gamma_0}, \quad (\text{B } 2)$$

where  $\gamma_0 = c_Z \ln \Lambda$  is the average runaway-electron energy. Imposing the boundary condition  $\mathcal{F}(-\infty, t) = 0$ , thus constraining the solutions to a finite total positron number, it is solved by

$$\mathcal{F} = \frac{Z_{\text{tot}}}{4\pi \ln \Lambda r_0^2} \frac{n_{\text{RE}}}{\gamma_0 m_e c} e^{\rho \gamma/\gamma_0} \times \int_{\gamma}^{\infty} d\gamma' \int_{\gamma'+2}^{\infty} d\gamma_1 \left[ \frac{\partial \sigma^+}{\partial \gamma'}(\gamma', \gamma_1) \exp \left\{ -\frac{\rho \gamma' + \gamma_1}{\gamma_0} \right\} \right], \quad (\text{B } 3)$$

where  $\rho = (E/E_c - 1)/(E/E_c + 1)$ .

Conversely, for  $p > 0$ , the pair-production source vanishes, and the positron distribution satisfies the same equation as the high-energy runaway electrons except for the opposite charge,

$$\frac{\partial \mathcal{F}}{\partial t} + eE_c \left( \frac{E}{E_c} - 1 \right) \frac{\partial \mathcal{F}}{\partial p} = 0, \quad (\text{B } 4)$$

which is solved by

$$\mathcal{F}(p, t) = \mathcal{F} \left( 0, t - \frac{p}{e(E - E_c)} \right). \quad (\text{B } 5)$$

Using as boundary condition at  $p = 0$  that the positron population grows in time in the same way as the  $p < 0$  population:

$$\frac{\mathcal{F}(0^+, t)}{\mathcal{F}(0^+, 0)} = \frac{\mathcal{F}(0^-, t)}{\mathcal{F}(0^-, 0)} = e^{t/t_{ava}}, \quad (\text{B } 6)$$

which then immediately yields

$$\mathcal{F}(p, t) = \frac{n_{\text{RP}}(0)}{m_e c \gamma_0} e^{t/t_{\text{ava}}} e^{-\gamma/\gamma_0}. \quad (\text{B } 7)$$

## REFERENCES

- ALWALL, J., FREDERIX, R., FRIXIONE, S., HIRSCHI, V., MALTONI, F., MATTELAER, O., SHAO, H.-S., STELZER, T., TORIELLI, P. & ZARO, M. 2014 The automated computation of tree-level and next-to-leading order differential cross sections, and their matching to parton shower simulations. *J. High Energy Phys.* **7**, 79.
- ANDERSON, C. D. 1932 The apparent existence of easily deflectable positives. *Science* **76** (1967), 238–239.
- BRIGGS, M. S., CONNAUGHTON, V., WILSON-HODGE, C., PREECE, R. D., FISHMAN, G. J., KIPPEN, R. M., BHAT, P. N., PACIESAS, W. S., CHAPLIN, V. L., MEEGAN, C. A. *et al.* 2011 Electron–positron beams from terrestrial lightning observed with Fermi GBM. *Geophys. Res. Lett.* **38** (2), 102808.
- CHARLTON, M. & HUMBERSTON, J. 2001 *Positron Physics*. Cambridge University Press.
- CHEN, H., WILKS, S. C., BONLIE, J. D., LIANG, E. P., MYATT, J., PRICE, D. F., MEYERHOFER, D. D. & BEIERSDORFER, P. 2009 Relativistic positron creation using ultraintense short pulse lasers. *Phys. Rev. Lett.* **102**, 105001.
- CONNOR, J. & HASTIE, R. 1975 Relativistic limitations on runaway electrons. *Nucl. Fusion* **15**, 415.
- DREICER, H. 1959 Electron and ion runaway in a fully ionized gas I. *Phys. Rev.* **115**, 238–249.
- DWYER, J. R. 2012 The relativistic feedback discharge model of terrestrial gamma ray flashes. *J. Geophys. Res.* **117** (A2), a02308.
- DWYER, J. R. & UMAN, M. A. 2014 The physics of lightning. *Phys. Rep.* **534** (4), 147–241.
- EMBRÉUS, O., STAHL, A. & FÜLÖP, T. 2016 Effect of bremsstrahlung radiation emission on fast electrons in plasmas. *New J. Phys.* **18** (9), 093023.
- EMBRÉUS, O., STAHL, A. & FÜLÖP, T. 2018 On the relativistic large-angle electron collision operator for runaway avalanches in plasmas. *J. Plasma Phys.* **84** (1), 905840102.
- FÜLÖP, T. & PAPP, G. 2012 Runaway positrons in fusion plasmas. *Phys. Rev. Lett.* **108**, 225003.
- FÜLÖP, T., POKOL, G., HELANDER, P. & LISAK, M. 2006 Destabilization of magnetosonic-whistler waves by a relativistic runaway beam. *Phys. Plasmas* **13** (6), 062506.
- GABRIELSE, G., BOWDEN, N. S., OXLEY, P., SPECK, A., STORRY, C. H., TAN, J. N., WESSELS, M., GRZONKA, D., OELERT, W., SCHEPERS, G. *et al.* 2002 Background-free observation of cold antihydrogen with field-ionization analysis of its states. *Phys. Rev. Lett.* **89**, 213401.
- GRYAZNYKH, D. 1998 Cross section for the production of electron–positron pairs by electrons in the field of a nucleus. *Phys. Atom. Nucl.* **61** (3), 394–399.
- GUANYING, Y., LIU, J., XIE, J. & LI, J. 2017 Detection of tokamak plasma positrons using annihilation photons. *Fusion Engng Des.* **118**, 124–128.
- GUREVICH, A. V. & ZYBIN, K. P. 2001 Runaway breakdown and electric discharges in thunderstorms. *Phys.-Usp.* **44** (11), 1119–1140.
- HAUG, E. 1975 Bremsstrahlung and pair production in the field of free electrons. *Zeitsch. für Natur. A* **30** (9), 1099–1113.
- HEITLER, W. 1954 *The Quantum Theory of Radiation*, vol. 86. Courier Corporation.
- HELANDER, P., ERIKSSON, L.-G. & ANDERSSON, F. 2002 Runaway acceleration during magnetic reconnection in tokamaks. *Plasma Phys. Control. Fusion* **44**, B247–B262.
- HELANDER, P. & WARD, D. J. 2003 Positron creation and annihilation in tokamak plasmas with runaway electrons. *Phys. Rev. Lett.* **90**, 135004.
- HESSLOW, L., EMBRÉUS, O., STAHL, A., DUBOIS, T. C., PAPP, G., NEWTON, S. L. & FÜLÖP, T. 2017 Effect of partially screened nuclei on fast-electron dynamics. *Phys. Rev. Lett.* **118**, 255001.

- HESSLOW, L., EMBRÉUS, O., WILKIE, G. J., PAPP, G. & FÜLÖP, T. 2018 Effect of partially ionized impurities and radiation on the effective critical electric field for runaway generation. *Plasma Phys. Control. Fusion* **60**, 074010.
- HIRVIJOKI, E., PUSZTAI, I., DECKER, J., EMBRÉUS, O., STAHL, A. & FÜLÖP, T. 2015 Radiation reaction induced non-monotonic features in runaway electron distributions. *J. Plasma Phys.* **81** (5), 475810502.
- HOLLMANN, E. M., PARKS, P. B., COMMAUX, N., EIDETIS, N. W., MOYER, R. A., SHIRAKI, D., AUSTIN, M. E., LASNIER, C. J., PAZ-SOLDAN, C. & RUDAKOV, D. L. 2015 Measurement of runaway electron energy distribution function during high-z gas injection into runaway electron plateaus in DIII-D. *Phys. Plasmas* **22** (5), 056108.
- HUNT, A. W., CASSIDY, D. B., SELIM, F. A., HAAKENAASEN, R., COWAN, T. E., HOWELL, R. H., LYNN, K. G. & GOLOVCHENKO, J. A. 1999 Spatial sampling of crystal electrons by in-flight annihilation of fast positrons. *Nature* **402**, 157.
- JAYAKUMAR, R., FLEISCHMANN, H. & ZWEBEN, S. 1993 Collisional avalanche exponentiation of runaway electrons in electrified plasmas. *Phys. Lett. A* **172**, 447–451.
- LANDAU, L. & LIFSHITZ, E. 1983 *Quantum Electrodynamics*. Pergamon.
- LANDREMAN, M., STAHL, A. & FÜLÖP, T. 2014 Numerical calculation of the runaway electron distribution function and associated synchrotron emission. *Comput. Phys. Commun.* **185** (3), 847–855.
- LEHTINEN, N. G., BELL, T. F. & INAN, U. S. 1999 Monte Carlo simulation of runaway MeV electron breakdown with application to red sprites and terrestrial gamma ray flashes. *J. Geophys. Res.* **104** (A11), 24699.
- LIU, C. & WANG, H. 2009 Reconnection electric field and hardness of X-Ray emission of solar flares. *Astrophys. J.* **696**, L27–L31.
- LIU, J., QIN, H., FISCH, N. J., TENG, Q. & WANG, X. 2014 What is the fate of runaway positrons in tokamaks?. *Phys. Plasmas* **21** (6), 064503. doi:10.1063/1.4882435.
- MURPHY, R. J., SHARE, G. H., SKIBO, J. G. & KOZLOVSKY, B. 2005 The physics of positron annihilation in the solar atmosphere. *Astrophys. J. Suppl. Ser.* **161** (2), 495.
- PAUTASSO, G., BERNERT, M., DIBON, M., DUVAL, B., DUX, R., FABLE, E., FUCHS, J., CONWAY, G., GIANNONE, L., GUDE, A. *et al.* 2016 Disruption mitigation by injection of small quantities of noble gas in ASDEX Upgrade. *Plasma Phys. Control. Fusion* **59** (1), 014046.
- PAZ-SOLDAN, C., COOPER, C. M., ALEYNIKOV, P., PACE, D. C., EIDETIS, N. W., BRENNAN, D. P., GRANETZ, R. S., HOLLMANN, E. M., LIU, C., LVOVSKIY, A. *et al.* 2017 Spatiotemporal evolution of runaway electron momentum distributions in tokamaks. *Phys. Rev. Lett.* **118**, 255002.
- PRANTZOS, N., BOEHM, C., BYKOV, A. M., DIEHL, R., FERRIÈRE, K., GUESSOUM, N., JEAN, P., KNOEDLEDER, J., MARCOWITH, A., MOSKALENKO, I. V. *et al.* 2011 The 511 keV emission from positron annihilation in the galaxy. *Rev. Mod. Phys.* **83**, 1001–1056.
- PRIEST, E. & FORBES, T. 2002 The magnetic nature of solar flares. *Astron. Astrophys. Rev.* **10** (4), 313–377.
- RAICHLE, M. E. 1985 Positron emission tomography: progress in brain imaging. *Nature* **317**, 574.
- ROSENBLUTH, M. & PUTVINSKI, S. 1997 Theory for avalanche of runaway electrons in tokamaks. *Nucl. Fusion* **37**, 1355–1362.
- SARRI, G. 2015 Laser-driven generation of high-quality ultra-relativistic positron beams. *J. Plasma Phys.* **81** (2), 415810202.
- SOKOLOV, Y. 1979 ‘Multiplication’ of accelerated electrons in a tokamak. *JETP Lett.* **29**, 218–221.
- SOLODOV, A. & BETTI, R. 2008 Stopping power and range of energetic electrons in dense plasmas of fast-ignition fusion targets. *Phys. Plasmas* **15** (4), 042707.
- STAHL, A., EMBRÉUS, O., PAPP, G., LANDREMAN, M. & FÜLÖP, T. 2016 Kinetic modelling of runaway electrons in dynamic scenarios. *Nucl. Fusion* **56** (11), 112009.
- STAHL, A., HIRVIJOKI, E., DECKER, J., EMBRÉUS, O. & FÜLÖP, T. 2015 Effective critical electric field for runaway electron generation. *Phys. Rev. Lett.* **114**, 115002.
- SURKO, C. M. & GREAVES, R. G. 2004 Emerging science and technology of antimatter plasmas and trap-based beams. *Phys. Plasmas* **11** (5), 2333–2348.

- TSUCHIYA, H., ENOTO, T., YAMADA, S., YUASA, T., NAKAZAWA, K., KITAGUCHI, T., KAWAHARADA, M., KOKUBUN, M., KATO, H., OKANO, M. *et al.* 2011 Long-duration  $\gamma$  ray emissions from 2007 and 2008 winter thunderstorms. *J. Geophys. Res.* **116** (D9), d09113.
- VODOPIYANOV, I., DWYER, J. R., CRAMER, E. S., LUCIA, R. & RASSOUL, H. K. 2015 The effect of direct electron–positron pair production on relativistic feedback rates. *J. Geophys. Res.* **120** (1), 800–806.
- WILKS, S. C., LANGDON, A. B., COWAN, T. E., ROTH, M., SINGH, M., HATCHETT, S., KEY, M. H., PENNINGTON, D., MACKINNON, A. & SNAVELY, R. A. 2001 Energetic proton generation in ultra-intense laser–solid interactions. *Phys. Plasmas* **8** (2), 542–549.
- WILSON, C. T. R. 1925 The acceleration of  $\beta$ -particles in strong electric fields such as those of thunderclouds. *Math. Proc. Cambridge Philos. Soc.* **22**, 534.



# Paper D

O. Embréus, S. Newton, A. Stahl, E. Hirvijoki and T. Fülöp,  
*Numerical calculation of ion runaway distributions*,  
Physics of Plasmas **22**, 052122 (2015).  
<http://doi.org/10.1063/1.4921661>  
arXiv:1502.06739 [physics.plasm-ph]

## Numerical calculation of ion runaway distributions

O. Embréus,<sup>1</sup> S. Newton,<sup>2</sup> A. Stahl,<sup>1</sup> E. Hirvijoki,<sup>1</sup> and T. Fülöp<sup>1</sup>

<sup>1</sup>Department of Applied Physics, Chalmers University of Technology, SE-412 96 Göteborg, Sweden

<sup>2</sup>CCFE, Culham Science Centre, Abingdon, Oxon OX14 3DB, United Kingdom

(Received 24 February 2015; accepted 11 May 2015; published online 26 May 2015)

Ions accelerated by electric fields (so-called runaway ions) in plasmas may explain observations in solar flares and fusion experiments; however, limitations of previous analytic work have prevented definite conclusions. In this work, we describe a numerical solver of the 2D non-relativistic linearized Fokker-Planck equation for ions. It solves the initial value problem in velocity space with a spectral-Eulerian discretization scheme, allowing arbitrary plasma composition and time-varying electric fields and background plasma parameters. The numerical ion distribution function is then used to consider the conditions for runaway ion acceleration in solar flares and tokamak plasmas. Typical time scales and electric fields required for ion acceleration are determined for various plasma compositions, ion species, and temperatures, and the potential for excitation of toroidal Alfvén eigenmodes during tokamak disruptions is considered. © 2015 AIP Publishing LLC.

[<http://dx.doi.org/10.1063/1.4921661>]

### I. INTRODUCTION

The phenomenon of particle runaway in a plasma is well known, occurring in both space and laboratory plasmas.<sup>1,2</sup> It arises because the friction force experienced by a charged particle decreases with particle energy, so that the presence of a sufficiently strong induced electric field can allow the particle to be accelerated—or *run away*—to high energy.

Electron runaway<sup>3</sup> has been extensively studied in the context of magnetic confinement fusion in tokamaks, where it can lead to the formation of localized high-energy beams which must be carefully controlled.<sup>4</sup> The standard analytic method used to determine the initial evolution of the electron distribution function in a fully ionized plasma was introduced by Kruskal and Bernstein<sup>5</sup> and later generalized by Connor and Hastie.<sup>6</sup> It takes the form of an asymptotic expansion of the electron kinetic equation in the electric field strength. Once a fast electron population—known as the primary distribution—is established, it can rapidly produce further fast electrons through large-angle, or *knock-on*, collisions.<sup>7</sup> This avalanche process leads to the so-called secondary runaway-electron generation, which is often dominant.

Ion runaway has long been of interest in the astrophysical community, where it is thought to contribute to the observed abundance of high energy ions in solar flares.<sup>1</sup> It has also been used to study the behavior of lightning channels<sup>8</sup> and was observed in laboratory plasmas, e.g., in the Mega Ampere Spherical Tokamak (MAST)<sup>9</sup> and in the Madison Symmetric Torus.<sup>10</sup> The detailed mechanism of ion runaway differs from that of electron runaway. Friction with the electrons, which are also drifting in the electric field, acts to cancel a portion of the accelerating field. In the ion rest frame, the electrons have net motion anti-parallel to the electric field, and a test ion will experience two main forces beyond friction against the background of charged particles: acceleration in the electric field and friction due to the electron drift. These forces scale differently with ion charge, and the dominant force is either electron friction—with the

consequence that the ions are dragged along with the electrons—or acceleration by the electric field. In a pure plasma, the cancellation of electric field acceleration and electron friction is complete, but the presence of impurities, neutrals, or effects such as particle trapping in a non-uniform confining magnetic field allow a finite effective field to remain.<sup>11,12</sup>

Farth and Rutherford<sup>12</sup> generalized earlier treatments by adopting a similar expansion procedure to that used to study electron runaway. They determined the steady state ion distribution function in conditions typical of operational fusion plasmas. Helander *et al.*<sup>9</sup> then considered the initial value problem resulting from the onset of an accelerating electric field, produced, for example, by a plasma instability. An analytic solution for the initial time evolution of the accelerated ion distribution function was developed, but it was noted that its application was limited due to the low electric fields required for it to be valid. Both of these ion runaway studies considered only the presence of a trace impurity population, consistent with typical operating conditions in fusion plasmas.

Plasmas with significant impurity content are also common, however. Astrophysical plasmas often consist of a mixture of dominant species, as well as containing trace elements.<sup>1,13</sup> Disruptions,<sup>2</sup> which are a common cause of electron runaway in tokamaks, are also typically associated with an increase in impurity content, either due to deliberate gas injection for mitigation purposes or due to plasma-wall interaction. Therefore, in Ref. 14, the initial value formulation of the problem posed in Ref. 9 was extended to account for arbitrary plasma composition. The potential for ions accelerated during a disruption to excite low frequency plasma instabilities was considered analytically. The results were inconclusive since the asymptotic expansion used to develop the analytic solution was not strictly valid for disruption-type parameters. The limitations of the analytic solutions available in previous work motivate the development of a numerical tool to allow detailed study of the time evolution of an ion runaway distribution.

Here, we describe the formulation and implementation of an efficient finite-difference-spectral-method tool, CODION (COlisional Distribution of IONs), that solves the two-dimensional momentum space ion kinetic equation in a homogeneous plasma. CODION solves the ion Fokker-Planck equation as an initial value problem and allows for time-variation of the electric field and bulk distribution parameters (temperature, density, charge, and mass) of each plasma species independently. Due to its speed, it is highly suitable for coupling within more expensive calculations, e.g., studies of instabilities driven by the fast ions or comprehensive modeling of ion acceleration with self-consistent coupling to solvers of Maxwell's equations. Using CODION, we obtain illustrative two-dimensional ion velocity space distributions, which demonstrate the typical behaviour of runaway ions in a variety of physical scenarios. We show that during typical tokamak disruptions, ions are unlikely to be accelerated to velocities high enough for resonant interaction with toroidal Alfvén eigenmodes (TAEs). Therefore, the experimentally observed TAE activity cannot be explained by the ion runaway mechanism alone.

The rest of the paper is organized as follows. In Sec. II, we describe the ion Fokker-Planck equation, and in Sec. III we outline its numerical implementation in CODION. In Sec. IV, we explore the numerical solution, including the effect of various approximations to the collision operator. In Sec. V, the model is applied to a variety of physical scenarios, illustrating typical acceleration time scales in laboratory and space plasmas. Finally, we close with concluding remarks in Sec. VI.

## II. RUNAWAY ION DISTRIBUTION

We consider the problem of ion acceleration by induced electric fields with a component parallel to the background magnetic field in a plasma. We restrict ourselves to straight field line geometry and assume a homogeneous background plasma. The time evolution of the ion distribution is then given by the Fokker-Planck equation, and particle acceleration will be opposed by various friction forces. The effect of friction with neutral particles can be significant in various physical situations, for example, giving rise to charge exchange losses, which was studied in the context of lightning discharges in Ref. 8. Here, we will focus on fully ionized quasi-neutral plasmas, in which case the friction is the result of inter-species Coulomb collisions only.

We are interested in the initial value problem where an electric field appears in what was previously an equilibrium state. Therefore, we assume that the initial particle distribution functions are stationary Maxwellians  $f_M$ —possibly at different temperatures—and consider their distortion from this state by the electric field. We linearize the collision operator about this background Maxwellian, and neglect the non-linear contribution to the evolution. This restricts the study to situations where only a small fraction of the ion population is accelerated, or to the initial stages of ion runaway. Once a high energy population forms, the runaway ions have the potential to excite instabilities,<sup>14</sup> which will have a strong impact on the further evolution of the

distribution. Note that the non-linear terms of the kinetic equation are sometimes required to account for the transfer of energy from the electric field into heating the distribution. These aspects of the longer term evolution of the distribution are beyond the scope of the work presented here.

The linearized collision operator for self-collisions is given by  $C_{ii}^l\{f_i\} = C_{ii}\{f_i, f_M\} + C_{ii}\{f_M, f_i\}$  as described in Ref. 9, where the first term, the test-particle operator, describes collisions of the perturbed distribution with the bulk, while the second term, the field-particle operator, describes the response of the bulk to the perturbation. We will follow the approach described in Ref. 15 and approximate the field-particle operator with restoring terms such that the collision operator satisfies momentum and energy conservation, non-negative entropy production, and vanishes for a perturbed Maxwellian—properties which are known to be satisfied by the exact operator.

Collisions with the other ion species could be treated similarly, however this would require the simultaneous evolution of the distribution functions of multiple species. Therefore, we consider only the evolution of the ion species with the highest runaway rate, so that the other ion species remain approximately stationary and only the test-particle piece of the unlike ion collision operator needs to be retained. While it is difficult to verify *a priori* that this condition is satisfied, it can be determined by numerical simulation of each ion species individually, assuming the others to remain stationary. Due to the sensitivity of the acceleration rate to ion charge and mass (as demonstrated in Sec. V), the condition can typically be well satisfied as the acceleration rate of different species is often separated by several orders of magnitude.

The velocity-dependent friction on a test particle resulting from collisions with a Maxwellian background species has a peak near the thermal velocity of the background due to the form of the Coulomb interaction between charged particles. In the case of electrons, the friction force will be a monotonically decreasing function for velocities above the electron thermal velocity, allowing an electron to run away to large energy (where relativistic<sup>6</sup> and synchrotron effects<sup>16</sup> become dominant). We focus on situations where the ion,  $i$ , and electron,  $e$ , thermal velocities satisfy  $v_{Te} \gg v_{Ti}$ , meaning that their temperatures are sufficiently similar that  $T_e/T_i \gg \sqrt{m_e/m_i}$ . Then, if an ion is accelerated away from the bulk, friction against the electron population will increase with velocity. This has the consequence that the ion acceleration will be naturally balanced by the electron friction for some  $v < v_{Te}$ , if the electric field is below a threshold value similar to the Dreicer field<sup>17</sup> for electrons.

Since an electron reacts to the electric field on a time-scale  $m_e/m_i$  times shorter than the ions, we assume the electron population to be in a quasi-steady state on all time-scales of interest for ion acceleration. Parallel force balance for the electron distribution then requires that the total electron-ion friction cancels the acceleration by the electric field,  $n_e e E_{\parallel} = \sum_j R_{ej\parallel} = \sum_j \int dv m_e v_{\parallel} C_{ej}$ , where the sum is taken over all ion species  $j$  in the plasma. Due to the small mass ratio, the electron-ion interaction is dominated by pitch-angle scattering, so that  $C_{ej} = C_{ei} n_j Z_j^2 / n_i Z_i^2$ , and we

can solve for the friction between electrons and the ion species of interest,  $R_{ei\parallel} = (n_i Z_i^2 / Z_{\text{eff}}) e E_{\parallel}$ , where the effective charge is  $Z_{\text{eff}} = \sum_j n_j Z_j^2 / n_e$ .

The electron distribution can be written as  $f_e = f_{Me} + f_{e1}$ , with  $f_{Me}$  a Maxwellian distribution drifting with the bulk ion velocity  $\mathbf{V}_i$ , and a correction  $f_{e1}$  varying over velocities of order  $v_{Te}$ , accounting for the electron drift behavior in the electric field. Then, the linearized ion-electron collision operator, neglecting terms quadratic in  $f_{e1}$ , can be simplified,<sup>1,18</sup> noting that momentum conservation in binary collisions requires that  $\mathbf{R}_{ie} = -\mathbf{R}_{ei}$ ,

$$C_{ie}\{f_i, f_e\} = \frac{\mathbf{R}_{ei}}{m_i n_i} \cdot \frac{\partial f_i}{\partial \mathbf{v}} + C_{ie}\{f_i, f_{Me}(\mathbf{v} - \mathbf{V}_i)\}. \quad (1)$$

The first term, which describes the friction arising from the drifting electron distribution and was calculated above, readily combines with that describing acceleration by an electric field, giving rise to the effective electric field  $E^* = E_{\parallel} - R_{ei\parallel} / n_i Z_i e = (1 - Z_i / Z_{\text{eff}}) E_{\parallel}$ . Thus, as noted in the Introduction, in a pure plasma where  $Z_i = Z_{\text{eff}}$ , net ion acceleration will not occur. Light ions with  $Z_i < Z_{\text{eff}}$  can be accelerated in the direction of the electric field. Heavy impurities with  $Z_i > Z_{\text{eff}}$  will be accelerated in the opposite direction, which is in the direction of electron runaway (the latter case was studied by Gurevich<sup>11</sup>). The second term in Eq. (1) describes the slowing down of the fast ions on the electrons, as well as the slow energy exchange between the bulk species. Note that the ion flow velocity correction is time dependent and formally small in the runaway density. This term will become more significant in the ion-electron momentum exchange as the runaway distribution builds up.

Finally then, the kinetic equation we consider for the evolution of the ion distribution function in the presence of an accelerating electric field and arbitrary plasma composition is the following:

$$\frac{\partial f_i}{\partial t} + \frac{Z_i e}{m_i} E^* \left( \xi \frac{\partial}{\partial v} + \frac{1 - \xi^2}{v} \frac{\partial}{\partial \xi} \right) f_i = \sum_s C_{is}\{f_i\}, \quad (2)$$

where  $\xi = v_{\parallel}/v$ , and the effect of collisions with the background Maxwellian populations is described by the sum over all particle species  $s$  in the plasma

$$\begin{aligned} \sum_s C_{is}\{f_i\} = & \frac{1}{\tau_{ie}} \sum_s \frac{n_s Z_s^2}{n_e} \left\{ \frac{\phi(x_s) - G(x_s)}{2x_i^3} \frac{\partial}{\partial \xi} \left[ (1 - \xi^2) \frac{\partial f_i}{\partial \xi} \right] \right. \\ & + \frac{1}{x_i^2} \frac{\partial}{\partial x_i} \left[ 2 \frac{T_i}{T_s} x_i^2 G(x_s) f_i + x_i G(x_s) \frac{\partial f_i}{\partial x_i} \right] \left. \right\} \\ & + \frac{1}{\tau_{ii}} \left[ 2\nu_s(v) x_i \xi u_{\parallel} + \nu_E(v) x_i^2 Q \right] f_{Mi}, \end{aligned} \quad (3)$$

where  $\tau_{is}^{-1} = n_s e^4 Z_i^2 Z_s^2 \ln \Lambda / 4\pi c_0^2 m_i^2 v_{Ts}^3$ ,  $x_s = v/v_{Ts} = \sqrt{m_s v^2 / 2T_s}$  and the usual error function  $\phi(x) = (2/\sqrt{\pi}) \int_0^x dy e^{-y^2}$  and Chandrasekhar function  $G(x) = [\phi(x) - x\phi'(x)] / 2x^2$  appear. The dimensionless moments  $u_{\parallel}$  and  $Q$  of the distribution function appearing in the momentum and energy restoring terms of the self-collision operator are

$$u_{\parallel}\{f_i\} = \frac{3}{2} v_{Ti} \int \frac{d^3 v \nu_s(v) v_{\parallel} f_i}{d^3 v \nu_s(v) v^2 f_{Mi}}, \quad Q\{f_i\} = v_{Ti}^2 \int \frac{d^3 v \nu_E(v) v^2 f_i}{d^3 v \nu_E(v) v^4 f_{Mi}}, \quad (4)$$

with the scattering frequencies given by

$$\nu_s(v) = 4 \frac{G(x_i)}{x_i}, \quad \nu_E(v) = 2 \left( 4 \frac{G(x_i)}{x_i} - \frac{\phi(x_i)}{x_i^3} \right). \quad (5)$$

The runaway behavior of interest can be demonstrated by considering the simpler dynamics of an ion test particle<sup>8,19</sup> in the presence of the electric field. The ion equation of motion takes the form  $m_i dv_{\parallel} / dt = Z_i e E^* + F_i^{\text{test}}$ , where the collisional friction on a test particle is given by

$$F_i^{\text{test}}(v) = -Z_i^2 e E_D \sum_s \frac{n_s Z_s^2}{n_e} \frac{T_e}{T_s} \left( 1 + \frac{m_s}{m_i} \right) G(x_s), \quad (6)$$

and  $E_D = n_e e^3 \ln \Lambda / 4\pi c_0^2 T_e$  is the Dreicer field. Thus, ion acceleration can occur when  $E/E_D > F_i^{\text{test}} / [Z_i e E_D |1 - Z_i / Z_{\text{eff}}|]$ . The required electric field values are illustrated in Fig. 1, for low and high effective charge. The figures illustrate the non-monotonic ion friction force, with one maximum near the thermal velocities of the ion species, and another near the electron thermal velocity. Therefore, as first described by Furth and Rutherford,<sup>12</sup> for a sufficiently strong electric field we may expect ions to be accelerated from their initial velocity to a higher velocity at which friction on the electrons dominates, giving rise to a suprathermal population in the plasma. We will compare the characteristics of the test-particle behavior, governed by the friction force illustrated in Fig. 1, to the numerical solution of Eq. (2) in Sec. III.

Figure 1 also illustrates that the electric fields needed to accelerate ions are highly sensitive to ion charge and plasma composition, due to their effect on the effective electric field  $E^* = (1 - Z_i / Z_{\text{eff}}) E$ . Note that the electric fields needed to accelerate ions beyond the electron thermal velocity are significantly larger than the minimum electric field necessary for acceleration. Such strong fields will not be considered here, since the validity of the linearization typically breaks down before the ions reach a significant fraction of the electron thermal velocity.

### III. CODION

In this section, we outline the implementation of Eq. (2) in the numerical tool CODION, which solves the ion Fokker-Planck equation numerically as an initial value problem to give the evolution of the ion distribution function in the presence of an accelerating electric field. It uses a continuum-spectral discretization scheme based on that used in CODE.<sup>20</sup> Illustrative solutions for a tokamak-like plasma are presented, and a comparison of the obtained distribution function is made with the behavior predicted by test-particle equations, demonstrating the importance of collisional diffusion for the runaway of ions. In addition, we investigate the

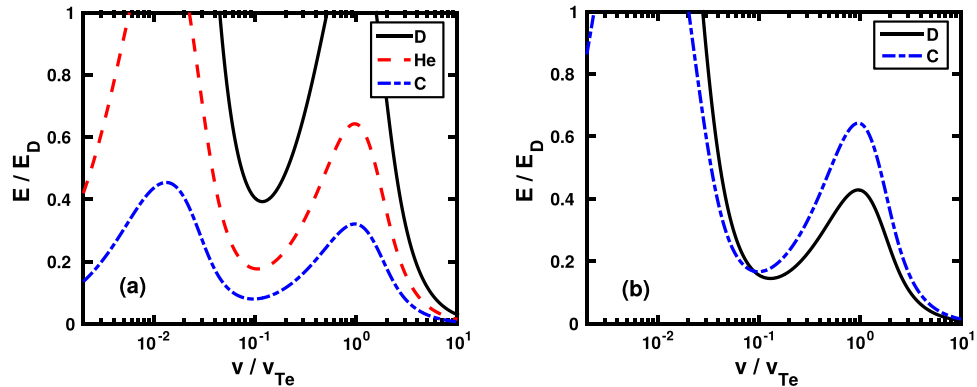


FIG. 1. Electric field needed to accelerate fully ionized test particles of various ion species in an impure deuterium plasma, as a function of velocity. (a)  $n_C/n_D = 0.4\%$ ,  $n_{He}/n_D = 5\%$ ,  $Z_{eff} = 1.2$  and (b)  $n_C/n_D = 4\%$ ,  $n_{He}/n_D = 5\%$ ,  $Z_{eff} = 2$ , and all particle species are taken to be at the same temperature. Since  $Z_{eff} = Z_{He}$  in (b), no electric field for which the model is valid will accelerate helium ions. The quantities shown are independent of the density and temperature of the plasma.

effect of different choices for the self-collision field-particle operator.

The pitch-angle dependence of the distribution function is represented by a truncated Legendre polynomial expansion, while velocity is discretized on a uniform grid  $v = v_n = n\Delta v$ ,  $n = 0, 1, \dots, N - 1$ :

$$f_l(v_n, \xi, t) = \sum_{l=0}^{l_{max}} f_l(v_n, t) P_l(\xi), \quad (7)$$

where the Legendre polynomials  $P_l$  obey the orthogonality relation  $\int_{-1}^1 d\xi P_l(\xi) P_p(\xi) = \delta_{lp} 2/(2l+1)$ , and

$$f_l(v_n, t) = \frac{2l+1}{2} \int_{-1}^1 d\xi P_l(\xi) f_l(v_n, \xi, t). \quad (8)$$

The integral operation  $(L+1/2) \int_{-1}^1 d\xi P_L(\xi) \dots$  is applied to the kinetic equation in Eq. (2) for each  $L$ , producing a linear set of equations for the quantities  $f_L(v, t)$ , using the boundary condition  $f_{l_{max}}(v, t) = 0$  for all  $v$ . Well-known recurrence relations for the Legendre polynomials are used to obtain analytic expressions for all the terms appearing in the equation. For example, the Legendre polynomials are eigenfunctions of the linearized collision operator, while the electric field-term will produce a coupling between  $f_L$  and  $f_{L\pm 1}$  modes. This procedure exactly captures number conservation for any choice of  $l_{max} > 1$ . The velocity derivatives appearing in the kinetic equation are represented with five-point stencils

$$\frac{\partial f_l}{\partial v} \Big|_{v_n} = \frac{1}{12\Delta v} \sum_{m=0}^{N-1} (-\delta_{n,m-2} + 8\delta_{n,m-1} - 8\delta_{n,m+1} + \delta_{n,m+2}) f_l(v_m), \quad (9)$$

$$\frac{\partial^2 f_l}{\partial v^2} \Big|_{v_n} = \frac{1}{12\Delta v^2} \sum_{m=0}^{N-1} (-\delta_{n,m-2} + 16\delta_{n,m-1} - 30\delta_{n,m} + 16\delta_{n,m+1} - \delta_{n,m+2}) f_l(v_m), \quad (10)$$

formally introducing an error of order  $\mathcal{O}(\Delta v^4)$ . The integral moments of the ion distribution appearing in the self-collision model operator are discretized with a quadrature of the form  $\int dv A(v) = \sum_m w_m A(v_m)$ , where the quadrature weights  $w_m$  are chosen according to Simpson's rule, also with error of order  $\mathcal{O}(\Delta v^4)$ .

For the distribution function to be single-valued and smooth at the origin, we enforce the boundary condition  $f_l(0) = 0$  for all  $l > 0$  and  $df_l/dv|_{v=0} = 0$ . Since we restrict ourselves to cases where electron friction will dominate the electric field at sufficiently high velocities, the maximum resolved velocity can always be chosen so that only insignificant numbers of particles are near the edge of the grid, minimizing the effect of the choice of boundary condition. We use the Dirichlet boundary condition  $f_l(v_N) = 0$  for all  $l$  at the maximum velocity. A detailed investigation of the convergence properties of solutions with respect to discretization parameters is described in Ref. 21.

The discretization procedure outlined above casts the kinetic equation, Eq. (2), into the form

$$\frac{\partial F}{\partial t} + MF = 0, \quad (11)$$

where  $M$  is a sparse matrix and  $F$  is a vector representing the discretized distribution function. Time integration is performed with the first order implicit scheme

$$F(t_{n+1}) = [I + \Delta t M(t_{n+1})]^{-1} F(t_n), \quad (12)$$

where any time-dependence of the operator  $M$  is due to time-variation of electric fields and background plasma parameters. An arbitrary plasma composition is determined by a set of input vectors containing particle masses  $m_s$ , corresponding charge states  $Z_s$ , charge densities  $\rho_s = n_s Z_s$  and temperatures  $T_s$ .

Figure 2(a) shows a typical example of the evolution of the ion distribution for a case where the electric field is above the minimum required for runaway acceleration. The plasma parameters used are characteristic for tokamaks with

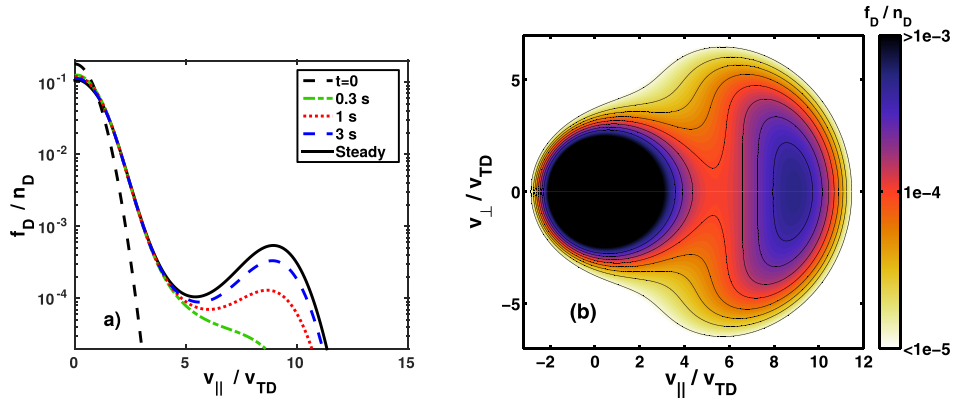


FIG. 2. Deuterium distribution function in a hot plasma characterized by  $T = 1$  keV for all particle species,  $n_e = 3 \times 10^{19} \text{ m}^{-3}$  and effective charge  $Z_{\text{eff}} = 2$  due to fully ionized carbon impurities with  $n_C/n_D = 4\%$ . The electric field  $E = 1.64 \text{ V/m}$  corresponds to  $E/E_D = 0.13$ . (a) Time evolution of the  $\xi = 1$  cut of the distribution and (b) contour plot of the steady state distribution, established after 20 s.

a hot bulk deuterium plasma at 1 keV and fully ionized native carbon impurities. Note that the loop voltage is typically  $\lesssim 1$  V in normal tokamak operation, corresponding to  $E \lesssim 0.2 \text{ V/m}$ .<sup>29</sup> A contour plot of the distribution in velocity space when steady state is reached is shown in Fig. 2(b). For the parameters used here, approximately 5% of the ion population has been accelerated and the linearization used to derive Eq. (2) is well satisfied.

The steady state distribution is typically established in 10–20 s at this temperature and density, and the time-scale varies with plasma parameters as the collision time defined in connection with Eq. (3),  $\tau_{ie} \propto T_i^{3/2}/n_e$ . For stronger electric fields, the initial evolution of the distribution can be followed, but the linearization breaks down before the steady state can be reached. Numerical simulations indicate that the entire ion distribution will eventually run away when  $E \gtrsim 0.2E_D$  for the  $Z_{\text{eff}} = 2$  case considered here (this will vary with species and composition as indicated in Fig. 1), and the linearization breaks down within  $\sim 30$  ms with such an electric field.

As discussed in the Introduction, approximate analytic solutions of the ion kinetic equation can be found in the literature. However, their potential for use in benchmarking is severely limited. The initial-value problem was considered in Refs. 9 and 14, but as noted in the derivations the solutions were restricted to very short timescales—in the case presented in Fig. 2, this corresponds to 20 ms, by which time only a negligible fast-ion population has formed. Furthermore, the derivations neglect the limiting fast-ion friction against electrons, which is essential for the long time evolution of the runaway ion distribution. The steady-state solution considered analytically in Ref. 12 provides the magnitude of the distribution in the runaway region, as a function of electric field; however, it is given in closed form only in the case of a strong field. A direct comparison is therefore not possible in the case of Fig. 2, where the long-time evolution of the distribution due to realistic electric fields, near the critical value needed to produce runaway, was considered. A

further discussion of the comparison to the analytic solutions may be found in Ref. 21, but it is not pursued further here.

#### IV. RESULTS

Expansions of the collision operators appearing in Eq. (2) have previously been used to consider ion runaway analytically. Here, we compare the effect of various approximations to the collision operator on the numerical solution of the distribution function. The plasma parameters of Fig. 2 are used as a basis in the comparisons, but the behavior illustrated is characteristic of a wide range of parameters. We first consider the effect of neglecting the conservative field-particle terms in the self-collision operator. Figure 3 shows the  $\xi = 1$  cut of the distribution of the bulk deuterium population for two cases, with effective charge  $Z_{\text{eff}} = 1.5$  and  $Z_{\text{eff}} = 2$ , respectively. It can be seen that, using only the test-particle operator, the dominant behavior of the fast-ion population as given by the fully conserving case is reproduced. This is expected, since the conserving field-particle terms are proportional to  $f_{Mi} \propto \exp(-x_i^2)$ , and therefore act mainly on the thermal bulk of the distribution. The main difference is that the conservative operators typically lead to a runaway rate which is at least twice as large, due to the parallel momentum they inject back into the low-energy part of the distribution.

Figure 3(a) shows a case with  $Z_{\text{eff}} = 1.5$ . With a lower amount of impurities to which momentum and energy can be transferred, the fully conserving linearized collision operator for self-collisions will exhibit unphysical behavior before a significant runaway population has time to form, which is clearly illustrated by the distortion near  $v = 0$ . The reason is that when the conserving terms are kept in the kinetic equation, the distribution is heated by the electric field, causing the linearized equation to break down after some time. This is also observed in the solution obtained using only the energy conserving term, albeit less pronounced. The distribution functions obtained with the momentum conserving self-collision operator tend to stay regular for longer. Figure 3(b)

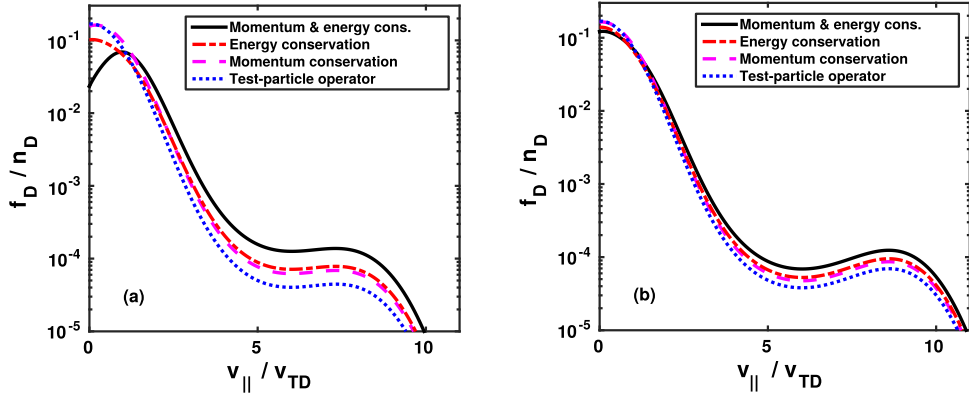


FIG. 3. Comparison of the  $\xi = 1$  cut of deuterium distributions calculated using CODION, retaining all (solid) or individual (dashed, dashed-dotted, and dotted) conservative terms in the ion self-collision operator. Here,  $T = 1$  keV for all species, and  $n_{D^+} = 3 \times 10^{19} \text{ m}^{-3}$ . The only impurity is fully ionized carbon, of density such that the specified effective charge is obtained, and electric fields and times are chosen to produce a significant runaway population. (a)  $Z_{\text{eff}} = 1.5$ ,  $E = 2.5 \text{ V/m}$  at  $t = 0.9 \text{ s}$ , and (b)  $Z_{\text{eff}} = 2$ ,  $E = 2 \text{ V/m}$  at  $t = 0.8 \text{ s}$ .

shows a similar case but with higher impurity content,  $Z_{\text{eff}} = 2$ , for which all operators yield well-behaving results. An additional consequence of the low effective charge was demonstrated in Fig. 1(a), where impurity ions were shown to be more easily accelerated by an electric field than the bulk species, implying that for low  $Z_{\text{eff}}$  the assumption of stationary impurity ions may be violated.

In conclusion, the high-energy part of the ion distribution obtained using only the test-particle operator is in qualitative agreement with the result obtained with conservative operators, but the runaway rate is expected to be lower in the test-particle case. A quantitative investigation of runaway rates for impurity species is presented in Sec. V.

It is instructive to compare the behavior of the numerical solution to the characteristic behavior indicated by the test particle friction given in Eq. (6). Noting that the runaway ion velocity satisfies  $v_{Ti} \ll v \ll v_{Te}$ , we can expand the contributions to Eq. (6) using the known low and high-velocity limits of the Chandrasekhar function. The test particle friction in this limit reduces to

$$F_i^{\text{test}} \approx -\frac{m_i v_{Ti}}{\tau_{ie}} \left[ \frac{Z_{\text{eff}} + \bar{n}}{x_i} + \frac{4}{3\sqrt{\pi}} \left( \frac{T_i}{T_e} \right)^{3/2} \sqrt{\frac{m_e}{m_i}} x_i \right], \quad (13)$$

where  $\bar{n} = \sum_j n_j Z_j^2 m_i / n_e m_j$  allows for arbitrary impurity content. Consider first the minimum value of the magnitude of the collisional friction force; this will determine the minimum electric field which can accelerate a fast test ion. Minimizing Eq. (13) yields

$$v_{\min} = v_{Te} \left[ \frac{3\sqrt{\pi} m_e}{2 m_i} (Z_{\text{eff}} + \bar{n}) \right]^{1/3}, \quad (14)$$

$$F_i^{\text{test}}(v_{\min}) = -2 \frac{m_i v_{Ti}}{\tau_{ie}} \frac{T_i}{T_e} \left[ \frac{3}{2\pi} \frac{m_e}{m_i} (Z_{\text{eff}} + \bar{n}) \right]^{1/3}. \quad (15)$$

From this it follows that the minimum, “critical,” value  $E_{ci}$  of the electric field above which a test ion can be accelerated is given by

$$\frac{E_{ci}}{E_D} = \frac{Z_i (Z_{\text{eff}} + \bar{n})^{1/3}}{|1 - Z_i/Z_{\text{eff}}|} \left( \frac{3 m_e}{2\pi m_i} \right)^{1/3}. \quad (16)$$

By taking  $Z_i e E^* + F_i^{\text{test}} = 0$ , we can find the range of test ion velocities,  $v_{c1} < v < v_{c2}$ , for which acceleration in a given electric field occurs, as discussed in Refs. 1 and 12. Using the expression for the friction given in Eq. (13) results in a third order equation, however simpler approximate formulae can be obtained by noting that  $v_{c1}$  will fall near to the region dominated by ion friction, and  $v_{c2}$  in the region dominated by electron friction. Retaining only the corresponding terms in Eq. (13) yields, for arbitrary impurity content,

$$v_{c1} = v_{Ti} \sqrt{\frac{Z_i T_e}{2 T_i} \left( \frac{E}{E_D} \right)^{-1} \frac{Z_{\text{eff}} + \bar{n}}{|1 - Z_i/Z_{\text{eff}}|}}, \quad (17)$$

$$v_{c2} = v_{Te} \frac{3\sqrt{\pi}}{2} \frac{E}{E_D} \frac{|1 - Z_i/Z_{\text{eff}}|}{Z_i}. \quad (18)$$

These equations generalize the corresponding expressions in Ref. 1 to arbitrary plasma composition. Note that these formulae are only valid when  $E$  is sufficiently large compared to  $E_{ci}$ , since at  $E = E_{ci}$  ion and electron friction contribute equally. We may expect that in steady-state, the position of the high-velocity maximum of the distribution function, denoted  $v_m$ , is close to  $v_{c2}$ , which scales linearly with  $E$  in the approximate form given by Eq. (18). This is confirmed numerically and illustrated in Fig. 4, where we show the variation with electric field of  $v_m$  obtained from steady-state CODION solutions of Eq. (2). Also shown are the boundary velocities of the acceleration region, resulting from numerical solution of the force balance using the full test particle friction, Eq. (6), as well as their approximate forms Eqs. (17) and (18). The values converge when the system is strongly driven by a large  $E$ . The linear dependence of  $v_m$  is clearly visible at large  $E$ , where it approaches the value given by the test particle approximation. The analytic approximation for  $E_{ci}$ , Eq. (16), is only accurate to  $\sim 20\%$ , however, indicating

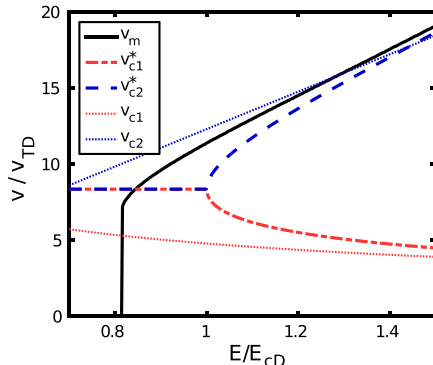


FIG. 4. Electric field dependence of the location  $v_m$  of the maximum in the runaway tail, obtained using CODION, for a fully ionized impure deuterium plasma with  $n_c/n_D = 4\%$ ,  $Z_{\text{eff}} = 2.5$  and equal temperature for all particle species. The boundary velocities  $v_{c1}^*$  and  $v_{c2}^*$  of the acceleration region obtained numerically from Eq. (6) (using the velocity which minimizes the friction when  $E < E_{ci}$ ), and their approximate values  $v_{c1}$  and  $v_{c2}$  given by Eqs. (17) and (18), are also shown. The quantities shown are independent of electron density and temperature. For electric fields  $E \lesssim 0.8E_{ci}$ , no maximum forms in the runaway ion distribution.

that collisional diffusion contributes significantly to the evolution at lower electric fields. Since the linearization breaks down more rapidly at larger electric fields, it is mainly at fields near the threshold for runaway generation that the model can consistently be applied to study the long-term evolution of the ion runaway tail, making a full kinetic simulation essential for capturing the important physics. For the more massive impurities, the features of the test-particle model become increasingly accurate since the runaway ion population is further separated in velocity space from the thermal bulk.

It is important to point out that neither the diffusion terms nor the field-particle self-collisions have been accounted for in the derivations of the above estimates, which are meant to give simple expressions that show how the essential quantities scale with the plasma parameters, and to provide a useful physical picture for illustrating the ion runaway phenomenon. A complete description will be provided only by numerical solution of the kinetic equation.

## V. APPLICATIONS

In this section, CODION is applied to calculate runaway ion distributions for typical solar flare and fusion plasmas. The time it takes for a fast ion population to form due to the runaway mechanism is determined, and it is investigated whether the difference in acceleration rate between different ion species can explain the enhanced abundance of heavy ions in the solar wind. We also consider the possibility of Alfvénic instabilities being driven by runaway ions during tokamak disruptions.

Throughout this section, time-scales are chosen so that significant fast ion populations have time to form, which typically takes between a few hundred to a few thousand ion-electron collision times. We define the runaway density,

$n_r = (1/n_i) \int_{v > v_{ci}^*} d^3v f_i$ , as the fraction of ions with velocity larger than the low-velocity numerical solution of  $Z_i e E^* + F_i^{\text{test}} = 0$ , denoted  $v_{ci}^*$ , which if  $E < E_{ci}$  is taken as the velocity  $v_{\min}$  minimizing the friction  $F_i^{\text{test}}$ .

### A. Ion acceleration in solar flares

Solar flares are thought to be initiated by reconnection in the corona,<sup>22</sup> but the origin of the observed fast ion populations in flares is still not completely understood.<sup>23</sup> Both stochastic acceleration by waves and the direct acceleration of the particles by the electric field have been considered, and it appears likely that a combination of the two can be at work.<sup>1,24,25</sup>

The effective accelerating field experienced by a given species varies with its charge and the effective charge of the plasma, as discussed in Sec. II. This can give rise to preferential acceleration of heavier elements under certain circumstances, and this effect was considered in Ref. 1, where estimates of the runaway rate were given based on the approximate formula of Ref. 11. With CODION we can determine the time evolution of the ion distribution function numerically, and evaluate the dependence of the runaway population on various ion parameters.

The composition of the solar plasma, particularly the metallic elements, has been studied extensively in recent years, however much uncertainty remains. We will choose parameters consistent with the choices made by Holman.<sup>1</sup> We use the plasma temperature  $T = 700$  eV for all particle species, and hydrogen density  $n_H = 3 \times 10^{17} \text{ m}^{-3}$ . Elements with atomic number  $Z \leq 6$  can readily be assumed to be fully ionized at this temperature. The plasma composition is based on the ion abundance recommended by Schmelz *et al.*<sup>13</sup> We use a helium population of density  $n_{\text{He}}/n_H = 6\%$ , and represent all heavier impurities by a carbon population of density  $n_C/n_H = 0.1\%$ , corresponding to an effective charge  $Z_{\text{eff}} = 1.13$ . Electric field strengths in solar flares are not well constrained by experimental observation, and we will investigate the rate of acceleration at a range of values. The Dreicer field is  $E_D = 224$  mV/m for this set of plasma parameters.

The critical electric fields  $E_{ci}$  for the ion species in such a plasma are  $E_{c,H} = 154$  mV/m for hydrogen,  $E_{c,He} = 40$  mV/m for helium, and  $E_{c,C} = 20$  mV/m for carbon. Note that the acceleration rate depends strongly not only on  $E/E_{ci}$  but also on  $v_{ci}/v_{Te}$ .

Figure 5 shows the  $v_{\perp} = 0$  cut of the distribution functions of hydrogen ( ${}^1\text{H}$ ), helium ( ${}^4\text{He}$ ), and carbon ( ${}^{12}\text{C}$ ) after 30 s of acceleration from initial Maxwellians, with the plasma parameters specified above and an electric field  $E = 50$  mV/m. At this electric field, the critical velocities are given by  $v_{c1}^*/v_{Te} = v_{c2}^*/v_{Te} = 0.15$  for hydrogen (coinciding since  $E < E_{cH}$ ),  $v_{c1}^*/v_{Te} = 0.08$  and  $v_{c2}^*/v_{Te} = 0.21$  for helium, and  $v_{c1}^*/v_{Te} = 0.04$  and  $v_{c2}^*/v_{Te} = 0.48$  for carbon. The electric field is significantly below the hydrogen critical field, and no hydrogen runaway population forms. Runaway ion populations of both helium and carbon do form however, with runaway densities  $n_{r,He} = 0.037\%$  and  $n_{r,C} = 18\%$ , respectively.

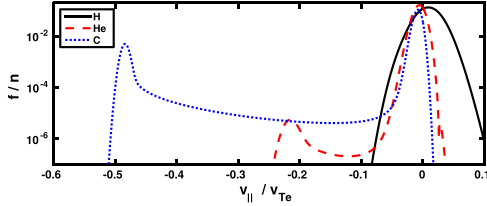


FIG. 5. Distribution functions of hydrogen, helium, and carbon after 30 s of acceleration in a solar flare-like plasma, with  $E = 50$  mV/m. All distribution functions are normalized to their respective densities. The temperature is  $T = 700$  eV for all species,  $n_{\text{H}} = 3 \times 10^{17} \text{ m}^{-3}$ ,  $n_{\text{He}}/n_{\text{H}} = 6\%$ , and all other impurities are represented by a carbon population with  $n_{\text{C}}/n_{\text{H}} = 0.1\%$ , yielding  $Z_{\text{eff}} = 1.13$ . The runaway densities are  $n_{r,\text{H}} \approx 0$ ,  $n_{r,\text{He}} = 3.7 \times 10^{-4}$ , and  $n_{r,\text{C}} = 0.18$ .

Positive values of  $v_{\parallel}$  represent the direction of the electric field. Therefore, Fig. 5 also illustrates how heavier ions (charge  $Z > Z_{\text{eff}}$ ) are accelerated in the direction opposite to the electric field, dragged by electron friction. The corresponding 2D carbon distribution function is shown in Fig. 6, displaying a strong directional anisotropy (compare to Fig. 2(b)). This can be understood by the observation that the accumulation velocity  $v_{c2}$  is located at a higher value of  $x_i = v/v_{Ti}$  for heavier ions. Since pitch angle scattering of the energetic heavy ions scales with velocity like  $Z_{\text{eff}}/x_i^3$ , the mechanism will be less effective than for light bulk ion species in increasing the perpendicular energy of the distribution.

We will now investigate how the runaway population varies with electric field strength for different ion species. To

determine the runaway density of heavier ions, we have introduced trace amounts of each ion species with charge between 2 (helium) and 18 (argon), assumed to be fully ionized. In practice, ions of charge  $Z_i > 8$  will typically not be fully ionized at the temperature considered due to their high ionization energy, meaning that the results shown here will overestimate the acceleration rate of the heavier ions. The ion masses have been set to that of the most common isotope, i.e.,  $^7\text{Li}$ ,  $^9\text{Be}$ ,  $^{20}\text{Ne}$ , etc. Both  $^3\text{He}$  and  $^4\text{He}$  are shown, with  $^3\text{He}$  showing significantly enhanced runaway compared to  $^4\text{He}$ , for all values of  $E$ .

Figure 7(a) shows how the runaway density  $n_r$  depends on electric field after 1 s of acceleration for various ion species present in the solar flare plasma. The figure illustrates how the average runaway rate is sensitive to ion parameters; at low electric fields, the heavier ions tend to be accelerated more slowly than light ions, while at higher fields they are the most readily accelerated. Note that above the critical electric field,  $E_{ci} \approx 40$  mV/m for helium, the runaway population increases significantly faster than for  $E < E_{ci}$ . The average runaway rate of  $^3\text{He}$  is seen to be orders of magnitude higher than that of  $^4\text{He}$  for all electric fields considered.

Finally, we illustrate the dependence of the average acceleration rate on ion charge and mass. Figure 7(b) shows the runaway density  $n_r$  after 1 s of acceleration as a function of ion charge  $Z_i$  for various electric fields. Ions of charge between  $Z_i = 4$  ( $^9\text{Be}$ ) and  $Z_i = 8$  ( $^{16}\text{O}$ ) are seen to be preferentially accelerated over lighter or heavier elements for low electric fields. For  $Z_i > 8$ , the trend depends on electric field. For low electric fields, the runaway population decreases

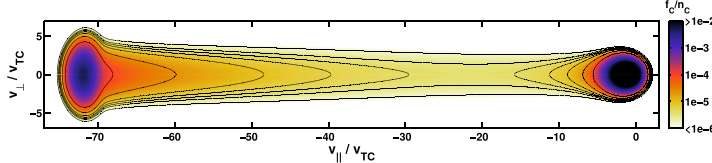


FIG. 6. Distribution function  $f_C$  of carbon, accelerated from an initial Maxwellian with zero flow velocity for 30 s by an electric field  $E = 50$  mV/m. The parameters represent a fully ionized solar flare-type plasma, with  $n_{\text{H}} = 3 \times 10^{17} \text{ m}^{-3}$ ,  $n_{\text{He}}/n_{\text{H}} = 6\%$ , and  $n_{\text{C}}/n_{\text{H}} = 0.1\%$ , and temperature  $T = 700$  eV for all species.

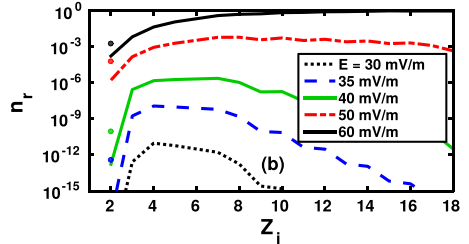
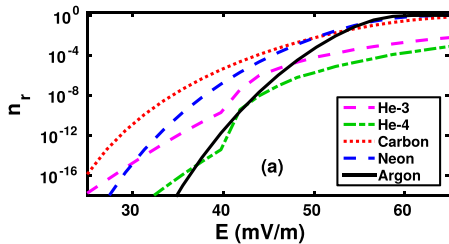


FIG. 7. Solar flare-like plasma with all particle species at the same temperature  $T = 700$  eV. The composition is mainly hydrogen,  $n_{\text{H}} = 3 \times 10^{17} \text{ m}^{-3}$ , and helium-4,  $n_{\text{He}}/n_{\text{H}} = 6\%$ , with carbon of density  $n_{\text{C}}/n_{\text{H}} = 0.1\%$  representing all other impurities, each appearing in trace amounts. Ions are accelerated for 1 s from initial Maxwellians. Due to the low effective charge  $Z_{\text{eff}} = 1.13$ , the hydrogen background remains stationary ( $E$  is small). Since heavier elements are assumed to be present only in trace amounts, self-collisions are negligible and they can be followed to large runaway fraction. (a) Runaway density  $n_r$  as a function of electric field strength  $E$  for various ion species. (b) Runaway density as a function of atomic number  $Z_i$ . For each atomic number, the most common isotope is used, except for helium ( $Z_i = 2$ ) where both  $^3\text{He}$  and  $^4\text{He}$  are shown, with the  $^3\text{He}$  runaway density indicated by dots.

with charge, while for larger electric fields (in this case above approximately 50 mV/m), heavier ion species may be accelerated more readily than the lighter species. Further studies are required to determine the full effects of variation in background composition, temperature, density, and charge states on the relative rates of acceleration between different ion species. The results presented here demonstrate the utility of CODION for the problem.

As previously noted, acceleration by quasi-static electric fields is not the only mechanism for ion acceleration in a flare plasma. Interaction with Alfvén waves can accelerate ions which have velocities above the Alfvén velocity. As this is usually well above the thermal ion velocity, an initial acceleration by electric fields may be required before the process becomes significant.<sup>1,26</sup> CODION provides the means for more accurate modeling of the effects of such interactions.

## B. Tokamak disruptions

During tokamak disruptions the plasma temperature drops from the typical operating regime of around several keV to a few eV in a couple of milliseconds. A large electric field is initially induced parallel to the magnetic field to maintain the plasma current of several MA, potentially leading to the formation of a beam of energetic electrons through the runaway mechanism. The potential for damage by such a focused high-energy beam on contact with the vessel wall is large, and runaway generation must as far as possible be suppressed. To study the physics and mitigation of runaway electrons, disruptions can be induced by the injection of large quantities of noble gas, often in amounts comparable to the initial plasma inventory or larger.<sup>2</sup>

The large induced electric field will usually decay rapidly on a timescale of a few ms in response to the formation of a narrow runaway electron (RE) beam. With runaway electrons reaching energies of order tens of MeV, they can carry a significant fraction of the pre-disruption plasma current and can drive high frequency electromagnetic instabilities through resonant interactions.<sup>27–30</sup> Recently, low-frequency magnetic fluctuations in the range of  $f \approx 60 - 260$  kHz have been observed in the TEXTOR tokamak during induced-disruption studies with argon massive gas injection (MGI). These fluctuations take the form of either a strong signal at a distinct frequency<sup>31</sup> or accompanied by broadband activity.<sup>32</sup> The fluctuations appear to limit the RE beam formation in these cases, as the magnetic perturbations may scatter the runaway electrons and provide passive mitigation. Aside from the potential consequences for mitigation, observed instabilities offer a non-intrusive diagnostic for both bulk plasma and fast-particle properties, through the extensively applied technique of MHD spectroscopy.<sup>33</sup>

Fast ions resulting, for example, from certain heating schemes are well known to resonantly drive low frequency Alfvénic instabilities in typical operational scenarios.<sup>34,35</sup> Runaway ions may thus also provide a potential drive for the fluctuations observed. Interestingly, TAEs<sup>36</sup> can have frequencies and mode numbers in the same range as the post-disruption magnetic activity. Therefore, the excitation of

TAEs by runaway ions was recently considered in Ref. 14 using an analytical approximation for the runaway distribution function. As the validity of the approximate distribution was limited, definite conclusions could not be drawn. With CODION we can extend the study using the numerically calculated ion distribution. The cold post-disruption plasma is highly collisional, motivating the use of a homogeneous background plasma and the neglect of magnetic trapping when evaluating the effective electric field.

The TAE perturbation is typically dominated by two neighboring toroidally coupled harmonics at large aspect ratio, with poloidal mode numbers  $m$  and  $m+1$ . The mode is localized about the minor radius  $r = r_0$  at which the magnetic safety factor is  $q_0 = (2m+1)/2n$ , where  $R_0$  is the radius of the magnetic axis and  $n$  is the toroidal mode number. The TAE frequency is  $\omega = v_A/(2q_0R_0)$ , where  $v_A = B/\sqrt{\mu_0\rho_m}$  is the Alfvén speed and  $\rho_m$  the mass density. The two component harmonics allow resonant interaction with particles whose parallel velocity  $v_{\parallel}$  satisfies  $|v_{\parallel}| \simeq v_A/3$  or  $|v_{\parallel}| \simeq v_A$ . It was argued in Ref. 14 that as the runaway ions accelerate, the inverted region of their energy distribution,  $\partial f/\partial \mathcal{E} > 0$  where  $\mathcal{E} = m_i v^2/2$  is the particle energy, can reach the lower Alfvén resonance,  $v_{\parallel} = v_A/3$  and may drive the TAE. If the radial runaway ion profile peaks on axis, the spatial gradient  $\partial f/\partial r$  will give an additional positive contribution to the growth rate. Taking parameters characteristic of argon MGI-induced disruptions,  $n_D = 3 \times 10^{19} \text{ m}^{-3}$ ,  $n_{\text{Ar}} = 0.1n_D$ ,  $Z_{\text{Ar}} = 2$ , and anticipating a native background carbon impurity with  $n_C = 0.08n_D$  and  $Z_C = 2$ , so that  $Z_{\text{eff}} = 1.26$ , a background ion temperature of  $T_i = 10 \text{ eV}$ , toroidal magnetic field  $B = 2 \text{ T}$  and major radius  $R_0 = 1.75 \text{ m}$  means that the resonance condition  $v_{\parallel} = v_A/3$  requires deuterium ions with velocities  $v \simeq 35v_{TD}$ .

The electric field required to accelerate bulk ions to the resonant velocity at these low temperatures is substantial, varying in response to changes in  $Z_{\text{eff}}$  but is typically  $\gtrsim 0.3E_D \sim 100 \text{ V/m}$ . Such field strengths are unlikely to occur during a disruption, and they would be short-lived if they did.<sup>37</sup> Therefore, we conclude that whilst ion runaway may be of interest in hot fusion plasmas, runaway ions are unlikely to provide the drive for the observed fluctuations during disruptions.

To quantify the electric field needed for significant ion runaway, we show in Fig. 8 how the deuterium distribution evaluated after 2 ms of acceleration from an initial Maxwellian—a typical time scale for the induced electric field—varies with (a constant) electric field. The parameters are  $n_D = 3 \times 10^{19} \text{ m}^{-3}$ ,  $T = 10 \text{ eV}$ , and the same plasma composition as before with  $Z_{\text{eff}} = 1.26$ . It is seen that for electric fields below  $\sim 200 \text{ V/m}$ , no runaway tail tends to form, and even with  $E = 260 \text{ V/m}$  the fast ions are far from the resonant velocity near  $35v_{TD}$ . The behavior is sensitive to which temperature is chosen for the plasma: increased temperature decreases the electric fields needed to accelerate ions, but makes the acceleration timescale longer.

Note that a higher amount of assimilated argon, or a weaker magnetic field, would lead to a lower Alfvén velocity and TAE frequency, and therefore the runaway ions would reach the resonance condition more easily. The higher

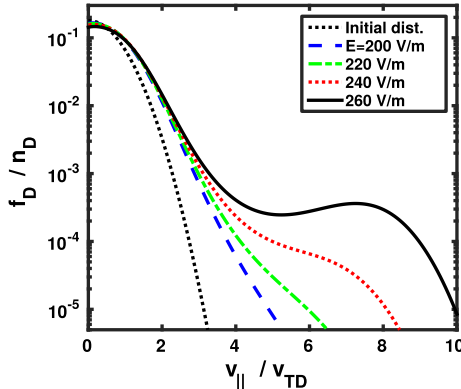


FIG. 8. Deuterium distribution function resulting from various electric fields after  $t = 2$  ms of acceleration from an initial Maxwellian in a TEXTOR MG1 post-disruption-like plasma, with  $n_D = 3 \times 10^{19} \text{ m}^{-3}$ ,  $n_C = 0.08n_D$ ,  $n_{Ar} = 0.1n_D$ , and  $T = 10 \text{ eV}$  for all species, with  $Z_C = Z_{Ar} = 2$ . The critical field for deuterium is  $E_{cD} = 295 \text{ V/m}$ , and the Dreicer field is  $E_D = 962 \text{ V/m}$ . For this scenario,  $v_{c1}^* = 7.0v_{TD}$ .

electron density leads to an increased collision frequency, however, so that the runaway ion distribution requires a longer time to form. The level of argon absorption during mitigation varies between machines<sup>2</sup> and the absorption appears to decrease for bigger machines. Therefore, although we may expect a higher electric field in large tokamaks such as ITER, the higher bulk plasma density and likely lower absorption suggests no ion runaway will occur. Note that as the ITER magnetic field is so high, even if the assimilated argon was equal to the initial deuterium inventory, the ions would need to reach  $\sim 40v_{Ti}$  (at 10 eV) to reach the typical  $v_A/3$  resonance, assuming  $B = 5 \text{ T}$ ,  $R_0 = 6 \text{ m}$ , and  $n_D = 1 \times 10^{20} \text{ m}^{-3}$ .

Finally, we note that the model presented in this paper assumes the initial ion distribution to be a stationary Maxwellian. Fast ion populations present due to heating schemes in use before the disruption may not be completely expelled, and it is not certain that the initial distribution is accurately described by a Maxwellian. The dynamics of ion acceleration starting from these non-Maxwellian distributions may yield a fast-ion population more readily. Furthermore, since plasma conditions change on a time scale of a few collision times during the sudden cooling associated with instabilities or disruptions, so-called “hot-tail” runaway generation may occur. This has been shown to be an important effect for runaway of electrons, where a seed of runaway electrons is provided by fast electrons present before cooling.<sup>38</sup> These fast electrons are cooled at a slower rate than the low-energy electrons, and may find themselves in the runaway region when the plasma has reached its final temperature. However, using CODION to investigate the effect of hot-tail ions, it has been concluded that the effect is small for realistic fields. The reason is that, if the electric field is not high enough for the ions to overcome the friction and become runaways in the first place, all hot-tail ions will necessarily also be slowed down. A low-velocity inverted ion

population may however form as a result of the cooling process even for such low electric fields, with its peak near the velocity which minimizes the collisional friction at the final temperature (typically around 6–8 thermal velocities). This is still significantly lower than that needed for resonant interaction with Alfvén waves.

One refinement to the model would be the inclusion of “knock-ons,” i.e., large-angle collisions, which have been neglected in the Fokker-Planck equation. It is well known that single collisions can change the momenta of the interacting particles significantly, and a runaway ion interacting with a bulk ion could cause both to end up in the runaway region. In a situation where the electric field is low enough that runaway ions are produced at a low rate through the standard acceleration mechanism, knock-on collisions could possibly contribute significantly to the runaway generation rate. This has been demonstrated to be the case for electron runaway, where this effect drastically affects the rate at which runaways are produced. A simplified runaway ion knock-on operator could potentially be constructed from the Boltzmann collision integral under the assumption that fast ions accumulate near  $v_{c2}$  and collide mainly with the bulk distribution, since the fast ion distribution is assumed to be a small perturbation in our linearized model. However, there are differences between ion runaway and electron runaway that suggest that knock-on runaway generation is a less significant effect for ions than for electrons. Since our linearized model restricts the study to cases where  $E \sim E_{ci}$  (which is also the regime where knock-on generation would be expected to be significant), the accumulation velocity near  $v_{c2}$  will not be significantly larger than the runaway velocity  $v_{c1}$ . Therefore, collision events where both particles end up in the runaway region will be less frequent. This is in contrast to electron runaway, where the electrons have unbounded energy (neglecting radiation effects).

There are applications for knock-on operators other than avalanche generation. It has been suggested that fast ion populations due to other sources—for example, hot alpha particles created in fusion reactions or ions heated by external sources such as neutral beam injection (NBI) or radio frequency (RF)-heating—could accelerate bulk impurity ions, which could in turn be used for diagnostics.<sup>39,40</sup> The suggested collision operator could be implemented in CODION, and the time-evolution of bulk impurities solved for in the vicinity of an assumed or numerically obtained background of fast ions, however this is outside the scope of the present paper.

## VI. CONCLUSIONS

Electron runaway resulting from the occurrence of a strong electric field in a plasma has been the subject of extensive study, and numerical tools exist to simulate the electron dynamics. The analytic description of the associated ion acceleration was developed at the same time, but its application has been much more limited and is restricted by the various approximations to the collision operator which were required.

We have developed an efficient open-source numerical tool, CODION,<sup>41</sup> which solves the ion Fokker-Planck equation as an initial value problem in a fully ionized plasma. A uniform background magnetic field is assumed, along with initially stationary Maxwellian distributions, however arbitrary impurity densities and temperatures may be specified. A model operator for ion self-collisions based on that used in the gyrokinetic code GS2 (Ref. 42) has been employed, satisfying momentum and energy conservation, non-negative entropy production, and self-adjointness. A simplified analytical model based on the large mass ratio is used for ion-electron collisions, allowing a description of ion-electron friction caused by the perturbation of the electron distribution due to the electric field. However, we wish to note that our model will break down for strong electric fields, as the electrons—which are assumed to be in force balance with the electric field and ion friction—will be rapidly accelerated by electric fields approaching the Dreicer field. A full description of such scenarios would require the simultaneous evolution of the ion and electron distributions, for example, by coupling the CODION and CODE<sup>20</sup> codes.

The effect of various approximations to the collision operator commonly used in the literature has been studied numerically. It has been demonstrated that the addition of momentum and energy conservation in self-collisions mainly acts to increase the rate at which the fast ion population builds up, while the qualitative behavior is largely unaffected. For strong electric fields, the test particle description is seen to reproduce well the characteristic velocity achieved by the runaway population, and the predicted critical electric field for ion acceleration is accurate to  $\sim 20\%$ . Using the test particle approximation, we derived concise analytic expressions for the critical electric field for ion runaway, Eq. (16), and the typical runaway energy, Eqs. (17) and (18), and tested these expressions against direct numerical simulation with CODION.

The output of CODION is the evolution of the 2D velocity space ion distribution. The utility of this has been demonstrated for calculating acceleration rates of ions in solar flare plasmas. The average rate at which ions are accelerated has been evaluated for a range of ion masses and charges for a solar flare scenario based on that considered by Holman,<sup>1</sup> and an exponential dependence of the buildup of a runaway population with charge for  $Z > 8$  has been illustrated for this scenario.

Low-frequency instabilities, in the range characteristic of TAE modes, have been observed in post-disruption tokamak plasmas, where the disruption was induced by massive gas injection. Using CODION, we have considered the potential for ions accelerated in the disruption-induced electric field to drive such modes resonantly. The post-disruption discharge parameters are not well constrained experimentally and simulations of a range of values indicate that ion acceleration is possible. The typical maximum ion velocity achieved is too low for resonant interaction to occur, however, and the rate of runaway generation is too slow for a significant runaway density to be reached in the short-lived electric fields of a typical disruption.

## ACKNOWLEDGMENTS

The authors are grateful to Gergely Papp, Matt Landreman, István Pusztai, and Joan Decker for fruitful discussions. This project has received funding from the Knut and Alice Wallenberg Foundation and the RCUK Energy Programme [Grant No. EP/I501045].

- <sup>1</sup>G. D. Holman, *Astrophys. J.* **452**, 451 (1995).
- <sup>2</sup>E. M. Hollmann, M. E. Austin, J. A. Boedo, N. H. Brooks, N. Commaux, N. W. Eideits, D. A. Humphreys, V. A. Izzo, A. N. James, T. C. Jernigan, A. Loarte, J. Martin-Solis, R. A. Moyer, J. M. Muñoz-Burgos, P. B. Parks, D. L. Rudakov, E. J. Strait, C. Tsui, M. A. Van Zeeland, J. C. Wesley, and J. H. Yu, *Nucl. Fusion* **53**, 083004 (2013).
- <sup>3</sup>R. M. Kulsrud, Y.-C. Sun, N. K. Winsor, and H. A. Fallon, *Phys. Rev. Lett.* **31**, 690 (1973).
- <sup>4</sup>M. Lehnert, A. Alonso, G. Arnoux, N. Baumgarten, S. A. Bozhenkov, S. Brezinsek, M. Brix, T. Eich, S. N. Gerasimov, A. Huber, S. Jachmich, U. Kruezi, P. D. Morgan, V. V. Plyusnin, C. Reux, V. Riccardo, G. Sergienko, M. F. Stamp, and JET EFDA Contributors, *Nucl. Fusion* **51**, 123010 (2011).
- <sup>5</sup>M. D. Kruskal and I. B. Bernstein, Princeton Plasma Physics Laboratory Report No. MATT-Q-20, 1962 (unpublished).
- <sup>6</sup>J. W. Connor and R. J. Hastie, *Nucl. Fusion* **15**, 415 (1975).
- <sup>7</sup>M. N. Rosenbluth and S. V. Putivinskii, *Nucl. Fusion* **37**, 1355 (1997).
- <sup>8</sup>T. Fülöp and M. Landreman, *Phys. Rev. Lett.* **111**, 015006 (2013).
- <sup>9</sup>P. Helander, L.-G. Eriksson, R. J. Akers, C. Byrom, C. G. Gimblett, and M. R. Tournianski, *Phys. Rev. Lett.* **89**, 235002 (2002).
- <sup>10</sup>S. Eilerman, J. K. Anderson, J. S. Sarff, C. B. Forest, J. A. Reusch, M. D. Nornberg, and J. Kim, *Phys. Plasmas* **22**, 020702 (2015).
- <sup>11</sup>A. V. Gurevich, Sov. Phys. JETP **13**, 1282 (1961), available at: [http://www.jetp.ac.ru/cgi-bin/dn/e\\_013\\_06\\_1282.pdf](http://www.jetp.ac.ru/cgi-bin/dn/e_013_06_1282.pdf).
- <sup>12</sup>H. P. Furth and P. H. Rutherford, *Phys. Rev. Lett.* **28**, 545 (1972).
- <sup>13</sup>J. T. Schmelz, D. V. Reames, R. von Steiger, and S. Basu, *Astrophys. J.* **755**, 33 (2012).
- <sup>14</sup>T. Fülöp and S. Newton, *Phys. Plasmas* **21**, 080702 (2014).
- <sup>15</sup>I. G. Abel, M. Barnes, S. C. Cowley, W. Dorland, and A. A. Schekochihin, *Phys. Plasmas* **15**, 122509 (2008).
- <sup>16</sup>A. Stahl, E. Hirvijoki, J. Decker, O. Embréus, and T. Fülöp, *Phys. Rev. Lett.* **114**, 115002 (2015).
- <sup>17</sup>H. Dreicer, *Phys. Rev.* **115**, 238 (1959).
- <sup>18</sup>P. Helander and D. J. Sigmar, *Collisional Transport in Magnetized Plasmas* (Cambridge University Press, Cambridge, 2002).
- <sup>19</sup>F. L. Hinton, *Collisional Transport in Plasma* in *Handbook of Plasma Physics* (North-Holland Publishing Company, 1983), Vol. 1.
- <sup>20</sup>M. Landreman, A. Stahl, and T. Fülöp, *Comput. Phys. Commun.* **185**, 847 (2014).
- <sup>21</sup>O. Embréus, Master's thesis, Chalmers University of Technology, 2014. See <http://publications.lib.chalmers.se/records/fulltext/210276/210276.pdf>.
- <sup>22</sup>C. Liu and H. Wang, *Astrophys. J.* **696**, 121 (2009).
- <sup>23</sup>T. L. Garrard and E. C. Stone, *Adv. Space Res.* **14**, 589 (1994).
- <sup>24</sup>D. Braddy, J. Chan, and P. B. Price, *Phys. Rev. Lett.* **30**, 669 (1973).
- <sup>25</sup>B. Sylwester, J. Sylwester, K. J. H. Phillips, A. Kępa, and T. Mrozek, *Astrophys. J.* **787**, 122 (2014).
- <sup>26</sup>E. R. Harrison, *J. Nucl. Energy, Part C* **1**, 105 (1960).
- <sup>27</sup>T. Fülöp, G. Pokol, P. Helander, and M. Lisak, *Phys. Plasmas* **13**, 062506 (2006).
- <sup>28</sup>G. Pokol, T. Fülöp, and M. Lisak, *Plasma Phys. Controlled Fusion* **50**, 045003 (2008).
- <sup>29</sup>A. Kómar, G. I. Pokol, and T. Fülöp, *Phys. Plasmas* **20**, 012117 (2013).
- <sup>30</sup>G. I. Pokol, A. Kómar, A. Budai, A. Stahl, and T. Fülöp, *Phys. Plasmas* **21**, 102503 (2014).
- <sup>31</sup>G. Papp, Ph. W. Lauber, M. Schneller, S. Braun, H. R. Koslowski, and TEXTOR Team, in *41st EPS Conference on Plasma Physics* (2014), Vol. 38F, see [http://ocs.ciemat.es/EPS2014PAP/pdf/P2\\_032.pdf](http://ocs.ciemat.es/EPS2014PAP/pdf/P2_032.pdf).
- <sup>32</sup>L. Zeng *et al.*, *Phys. Rev. Lett.* **110**, 235003 (2013).
- <sup>33</sup>H. A. Holties, A. Fasoli, J. P. Goedbloed, G. T. A. Huysmans, and W. Kerner, *Phys. Plasmas* **4**, 709 (1997).
- <sup>34</sup>W. W. Heidbrink, *Phys. Plasmas* **15**, 055501 (2008).
- <sup>35</sup>F. Zonca *et al.*, *Nucl. Fusion* **47**, 1588 (2007).
- <sup>36</sup>C. Z. Cheng and M. S. Chance, *Phys. Fluids* **29**, 3695 (1986).

<sup>37</sup>H. Smith, P. Helander, L.-G. Eriksson, D. Anderson, M. Lisak, and F. Andersson, *Phys. Plasmas* **13**, 102502 (2006).

<sup>38</sup>P. Helander, H. Smith, T. Fülöp, and L.-G. Eriksson, *Phys. Plasmas* **11**, 5704 (2004).

<sup>39</sup>V. G. Nesenevich *et al.*, *Plasma Phys. Controlled Fusion* **56**, 125002 (2014).

<sup>40</sup>P. Helander, M. Lisak, and D. D. Ryutov, *Plasma Phys. Controlled Fusion* **35**, 363 (1993).

<sup>41</sup>CODION is available at <https://github.com/Embreus/CODION>.

<sup>42</sup>M. Kotschenreuther, G. Rewoldt, and W. M. Tang, *Comput. Phys. Commun.* **88**, 128 (1995).



# Paper E

L. Hesslow, O. Embréus, M. Hoppe, T. C. DuBois, G. Papp, M. Rahm and T. Fülöp,

*Generalized collision operator for fast electrons interacting with partially ionized impurities,*

Journal of Plasma Physics **84**, 905840605 (2018).

<https://doi.org/10.1017/S0022377818001113>

arXiv:1807.05036 [physics.plasm-ph]

# Generalized collision operator for fast electrons interacting with partially ionized impurities

L. Hesslow<sup>1,†</sup>, O. Embréus<sup>1</sup>, M. Hoppe<sup>1</sup>, T. C. DuBois<sup>1</sup>, G. Papp<sup>2</sup>,  
M. Rahm<sup>3</sup> and T. Fülöp<sup>1</sup>

<sup>1</sup>Department of Physics, Chalmers University of Technology, SE-41296 Göteborg, Sweden

<sup>2</sup>Max Planck Institute for Plasma Physics, D-85748 Garching, Germany

<sup>3</sup>Department of Chemistry and Chemical Engineering, Chalmers University of Technology,  
SE-41296 Gothenburg, Sweden

(Received 7 June 2018; revised 15 October 2018; accepted 16 October 2018)

Accurate modelling of the interaction between fast electrons and partially ionized atoms is important for evaluating tokamak disruption mitigation schemes based on material injection. This requires accounting for the effect of screening of the impurity nuclei by the cloud of bound electrons. In this paper, we generalize the Fokker–Planck operator in a fully ionized plasma by accounting for the effect of screening. We detail the derivation of this generalized operator, and calculate the effective ion length scales, needed in the components of the collision operator, for a number of ion species commonly appearing in fusion experiments. We show that for high electric fields, the secondary runaway growth rate can be substantially larger than in a fully ionized plasma with the same effective charge, although the growth rate is significantly reduced at near-critical electric fields. Furthermore, by comparison with the Boltzmann collision operator, we show that the Fokker–Planck formalism is accurate even for large impurity content.

**Key words:** fusion plasma, runaway electrons

---

## 1. Introduction

Runaway acceleration of an electron in a plasma occurs if the electric field exceeds a critical value, above which the friction force on the electron from collisions with other plasma particles becomes smaller than the force from the electric field (Wilson 1925). Electrons can enter the runaway region in velocity space as a result of a random walk caused by long-range Coulomb collisions (primary or Dreicer generation) (Dreicer 1959). If there is an initial population of fast electrons in the plasma, they may produce secondary runaway electrons via close collisions – leading to an exponential multiplication of the fast-electron population – an avalanche (Sokolov 1979). Secondary generation of runaway electrons is expected to be substantial in future high-current tokamak disruptions (Jayakumar, Fleischmann & Zweber 1993;

† Email address for correspondence: [hesslow@chalmers.se](mailto:hesslow@chalmers.se)

Rosenbluth & Putvinski 1997), and successful mitigation is required to prevent unacceptable wall damage if a runaway population is formed (Boozer 2015; Reux *et al.* 2015).

The most promising runaway-mitigation method is to inject impurities which dissipate the runaway beam by collisional scattering (Hollmann *et al.* 2015). Due to the low temperatures of the post-disruption plasma, the impurities will only be partially ionized. Since the collision frequencies scale strongly with charge, the runaway dissipation rate will be heavily influenced by the extent to which fast electrons can penetrate the bound electron cloud around the impurity ion, i.e. the effect of partial screening.

Partial screening has a strong effect on collision frequencies (Kirillov, Trubnikov & Trushin 1975; Mosher 1975; Lehtinen, Bell & Inan 1999; Dwyer 2007; Zhogolev & Konovalov 2014; Hesslow *et al.* 2017), which calls for accurate models of the collisional processes. Such a model requires a quantum-mechanical treatment of both elastic and inelastic collisions, as well as knowledge of the electronic charge density of the impurity ion. Previous treatments of partially screened elastic electron-ion collisions are limited to either a semi-classical treatment (Mosher 1975; Martín-Solís, Loarte & Lehnen 2015), or employ the Thomas-Fermi theory for the electron charge density (Kirillov *et al.* 1975; Zhogolev & Konovalov 2014), which is limited to intermediate distances from the nucleus, and does not capture the shell structure of the ion (Landau & Lifshitz 1958). Therefore, in a recent paper we presented a collision operator based on a quantum-mechanical treatment of both elastic and inelastic collisions, and used density functional theory (DFT) to obtain the electron-density distribution of the impurity ions (Hesslow *et al.* 2017). This generalization of the Fokker-Planck operator to a partially ionized plasma was expressed as modifications to the deflection and slowing-down frequencies, and it was shown that both frequencies increased significantly compared to the case of complete screening, already at subrelativistic energies. This generalized operator was used by Hesslow *et al.* (2018) to derive an analytical expression including the effect of screening and radiation on the effective critical field for runaway formation and runaway current decay.

The present paper details the theoretical basis of the collision operator in Hesslow *et al.* (2017) and applies it to investigate the effects of partial screening on runaway electron dynamics. We compare these results with the predictions from the approximate Thomas-Fermi theory. Using the generalized collision operator, we present a detailed analysis of the steady-state runaway avalanche growth rate in the presence of partially ionized atoms. The increased collisional rates with partially ionized impurities lead to a substantially increased critical electric field for runaway generation (Hesslow *et al.* 2018). However, when the electric field is significantly larger than the critical field, the runaway avalanche growth rate is considerably higher than in the complete-screening case – corresponding to a fully ionized plasma with the same net ion charge. This behaviour, which contradicts previous predictions (Putvinski *et al.* 1997), produces an additional layer of complexity when evaluating the effect of partially ionized impurities on the number of runaway electrons.

The presence of partially ionized impurities enhances the relative frequency of large-angle collisions, which are beyond the Fokker-Planck formalism. We therefore investigate the validity of the Fokker-Planck operator by comparing it to the more general Boltzmann operator. The results show that the Fokker-Planck operator accurately captures the key quantities, such as the runaway density and current, only the synchrotron emission spectrum at large electric fields is slightly less accurate.

This demonstrates that the generalized collision operator derived here is adequate for most runaway studies.

The structure of the paper is as follows. Section 2 details the derivation of the generalized collision operator for fast electrons in the presence of partially ionized impurities. In §3, we investigate the effects of screening on the avalanche growth rate. Section 4 compares the results obtained using the Fokker–Planck operator to the corresponding ones using the Boltzmann operator. Finally, §5 summarizes our conclusions.

## 2. Generalized collision operator for fast electrons in a plasma with partially ionized impurities

There are two types of collisions between fast electrons and partially ionized atoms: elastic collisions, where the state of the ion remains unchanged during the collision and the incident electron is only deflected with a negligible energy transfer; and inelastic collisions, where the ion is excited or further ionized, causing the incident electron to impart a fraction of its kinetic energy to the bound electrons. For fast electrons, both types of collisions can be treated using the Born approximation. In the case of elastic collisions, this requires knowledge of the electronic charge density of the impurity ion, which we obtain from DFT calculations. In contrast, the inelastic collisions with bound electrons primarily lead to collisional friction; the rate of pitch-angle scattering against bound electrons is smaller than the rate against ions by approximately a factor of the charge number (the full nuclear charge)  $Z \gg 1$ . This allows us to model collisions with bound electrons with Bethe’s theory for the collisional stopping power (Bethe 1930) without the need for detailed differential cross-sections for these processes.

In both processes, the target particle can be treated as stationary since we consider incident suprathermal electrons. The average momentum of the bound electrons must be below the thermal electron momentum at a given temperature if the ionization state is roughly equilibrated with the electron temperature. Moreover, the ion thermal speed fulfills  $v_{Ti} \ll v_{Te}$  due to the small electron-to-ion mass ratio. Consequently, the collision operator presented here is valid for electron speeds  $v$  fulfilling

- (i)  $v/c \gg Z\alpha$  (the Born approximation), with  $\alpha \approx 1/137$  the fine-structure constant. The Born approximation may be accurate even at lower energies, as it has been experimentally verified for incident electron energies from 1 keV and above for argon and neon, which are particularly relevant for fusion experiments (Mott *et al.* 1965).
- (ii)  $\gamma - 1 \gg I_j/(m_e c^2)$  (Bethe’s stopping power formula), where  $\gamma$  is the Lorentz factor and  $I_j/(m_e c^2)$  is the mean excitation energy of the ion normalized to the electron rest energy, which is of the order  $10^{-4}$ – $10^{-3}$  for argon and neon, increasing with ionization degree (Sauer, Oddershede & Sabin 2015).
- (iii)  $v \gg v_{Ti}$  (ions at rest).

By matching the high-energy expressions describing the effects of partial screening to the completely screened low-energy limit, where the electron only interacts with the ion through the net ion charge number  $Z_0$ , we obtain a collision operator which can be applied at all energies, although it is known to be correct only when the conditions above are fulfilled.

### 2.1. The Fokker–Planck operator

The Fokker–Planck collision operator between species  $a$  and  $b$  is given by

$$C^{ab} = -\nabla_k(f_a \langle \Delta p^k \rangle_{ab}) + \frac{1}{2} \nabla_k \nabla_l(f_a \langle \Delta p^k \Delta p^l \rangle_{ab}), \quad (2.1)$$

where the term  $\langle \Delta p^k \rangle_{ab}$  represents the average change in the  $k$ th component of the momentum of the incoming electron during a collision, while  $\langle \Delta p^k \Delta p^l \rangle_{ab}$  describes the change in the tensor  $p^k p^l$ . Moreover,  $p = \gamma v/c$ , and  $\nabla_k$  refers to the momentum-space gradient operator. These moments are given by

$$\langle \Delta p^k \rangle_{ab} = \int d\mathbf{p}' f_b(\mathbf{p}') \int \frac{d\sigma_{ab}}{d\Omega} g_\phi \Delta p^k d\Omega, \quad (2.2)$$

$$\langle \Delta p^k \Delta p^l \rangle_{ab} = \int d\mathbf{p}' f_b(\mathbf{p}') \int \frac{d\sigma_{ab}}{d\Omega} g_\phi \Delta p^k \Delta p^l d\Omega, \quad (2.3)$$

where  $g_\phi = \sqrt{(\mathbf{v} - \mathbf{v}')^2 - (\mathbf{v} \times \mathbf{v}')^2/c^2}$  is the Møller relative speed and  $d\sigma_{ab}/d\Omega$  is the differential scattering cross-section between species  $a$  and  $b$ . Here, the angular integral is taken over

$$\int d\Omega = \int_{\theta_{\min}}^{\pi} \sin \theta d\theta \int_0^{2\pi} d\phi, \quad (2.4)$$

where the Coulomb logarithm, a large factor which will be described in more detail in § 2.2, enters through  $\ln \Lambda = \ln(2/\theta_{\min})$ . The Fokker–Planck operator can formally be seen as an expansion of the Boltzmann operator in small momentum transfers, which is motivated by the rapid decay of the Coulomb collision differential cross-section with momentum transfer;  $d\sigma_{ab}/d\Omega \sim \sin^{-4}(\theta/2)$ . This grazing collision nature of Coulomb interaction translates to a prefactor of  $\ln \Lambda$  when the collision operator is evaluated explicitly. Consequently, the Fokker–Planck operator only retains the terms of order  $\ln \Lambda$  in (2.1).

When species  $b$  has a Maxwellian distribution, the resulting collision operator is parametrized by the three collision frequencies  $v_D^{ab}$ ,  $v_S^{ab}$  and  $v_{\parallel}^{ab}$ , describing deflection at constant energy (pitch-angle scattering), collisional friction and parallel (energy) diffusion (Helander & Sigmar 2005):

$$C^{ab} = v_D^{ab} \mathcal{L}(f_a) + \frac{1}{p^2} \frac{\partial}{\partial p} \left[ p^3 \left( v_S^{ab} f_a + \frac{1}{2} v_{\parallel}^{ab} p \frac{\partial f_a}{\partial p} \right) \right]. \quad (2.5)$$

The pitch-angle scattering operator

$$\mathcal{L} = \frac{1}{2} \frac{\partial}{\partial \xi} (1 - \xi^2) \frac{\partial}{\partial \xi}, \quad (2.6)$$

represents scattering at constant energy, and is proportional to the angular part of the Laplace operator. Here it is specialized to azimuthally symmetric systems, and  $\xi = \mathbf{p} \cdot \mathbf{B}/(pB)$  is the cosine of the pitch angle with respect to a preferred direction, set here by an applied magnetic field  $\mathbf{B}$ .

## 2.2. The Coulomb logarithm

The Coulomb logarithm  $\ln \Lambda$  determines a minimum scattering angle below which Debye shielding screens out long-range interaction. Furthermore, it quantifies the dominance of small-angle collisions compared to large-angle collisions, and therefore provides a measure of the validity of the Fokker–Planck operator, which only captures small-angle collisions accurately. For electrons,  $\ln \Lambda$  is the logarithm of the Debye length divided by the de Broglie wavelength, which depends on the electron energy (Solodov & Betti 2008). At thermal speeds, the Coulomb logarithm is given by (Wesson 2011)

$$\ln \Lambda_0 \approx 14.9 - 0.5 \ln n_{e20} + \ln T_{\text{keV}}, \quad (2.7)$$

where  $T_{\text{keV}}$  is the temperature in keV and  $n_{e20}$  is the free-electron density in units of  $10^{20} \text{ m}^{-3}$ . The suprathermal expressions take the following form (Solodov & Betti 2008):

$$\left. \begin{aligned} \ln \Lambda^{\text{ee}} &= \ln \Lambda_c + \ln \sqrt{\gamma - 1}, \\ \ln \Lambda^{\text{ei}} &= \ln \Lambda_c + \ln(\sqrt{2}p), \end{aligned} \right\} \quad (2.8)$$

where we introduced a Coulomb logarithm evaluated at relativistic electron energies:

$$\ln \Lambda_c = \ln \Lambda_0 + \frac{1}{2} \ln \frac{m_e c^2}{T} \approx 14.6 + 0.5 \ln(T_{\text{eV}}/n_{e20}). \quad (2.9)$$

Note that the temperature dependence of  $\ln \Lambda_c$  is reduced compared to  $\ln \Lambda_0$ , since it describes collisions between thermal particles and relativistic electrons as opposed to collisions among thermal electrons. Although the energy dependence of the Coulomb logarithm can be neglected in many scenarios, it can be significant for relativistic electrons at post-disruption temperatures. In such cases, the thermal Coulomb logarithm is often of the order of  $\ln \Lambda_0 \approx 10$  while  $(1/2) \ln(m_e c^2/T) \approx 5$  at  $T = 10 \text{ eV}$ . It is then appropriate to use  $\ln \Lambda_c$  in the relativistic collision time:  $\tau_c = (4\pi n_e c r_0^2 \ln \Lambda_c)^{-1}$ , where  $r_0$  is the classical electron radius.

An accurate treatment of the Coulomb logarithm that can be used in the collision operator however requires a formula that is valid from thermal to relativistic energies. We therefore match the thermal Coulomb logarithm (2.7) with the suprathermal Coulomb logarithms (2.8) according to

$$\left. \begin{aligned} \ln \Lambda^{\text{ee}} &= \ln \Lambda_0 + \frac{1}{k} \ln \{1 + [2(\gamma - 1)/p_{Te}^2]^{k/2}\}, \\ \ln \Lambda^{\text{ei}} &= \ln \Lambda_0 + \frac{1}{k} \ln [1 + (2p/p_{Te})^k], \end{aligned} \right\} \quad (2.10)$$

where  $p_{Te} = \sqrt{2T/(m_e c^2)}$  is the thermal momentum, and the parameter  $k = 5$  is chosen to give a smooth transition between  $\ln \Lambda_0$  and  $\ln \Lambda^{\text{ee(ei)}}$ . The precise value of  $k$  does not significantly impact the resulting runaway dynamics, but a differentiable function facilitates implementation in numerical kinetic solvers.

## 2.3. Elastic electron–ion collisions

In this section, we follow the recipe of Rosenbluth, MacDonald & Judd (1957) and Akama (1970) to derive a generalized collision operator that takes partial screening into account by including a more general differential cross-section in (2.1). We model elastic electron–ion collisions quantum mechanically in the Born approximation. With

the ions as infinitely heavy stationary target particles initially at rest, the differential scattering cross-section takes the following form (Mott *et al.* 1965):

$$\frac{d\sigma_{ej}}{d\Omega} = \frac{r_0^2}{4p^4} \left( \frac{\cos^2(\theta/2)p^2 + 1}{\sin^4(\theta/2)} \right) |Z_j - F_j(q)|^2, \quad (2.11)$$

where the form factor for ion species  $j$  is defined as

$$F_j(\mathbf{q}) = \int \rho_{ej}(r) e^{-i\mathbf{q}\cdot\mathbf{r}/a_0} d\mathbf{r}. \quad (2.12)$$

Here,  $\mathbf{q} = 2\mathbf{p} \sin(\theta/2)/\alpha$ , and  $a_0 = \hbar/(m_e c \alpha)$  is the Bohr radius. The high- and low-energy behaviour of the form factor represent the limits of complete and no screening: at low  $q$ , the exponential approaches unity and thus the form factor is to lowest order given by the number of bound electrons  $N_{ej}$ , whereas at high  $q$  the fast oscillations in the exponential instead cause the form factor to vanish. Consequently, the factor  $|Z_j - F_j|^2$  varies between the net charge number squared  $Z_{0j}^2$  and the atomic number squared  $Z_j^2$  of ion species  $j$ . The ratio between these limits is typically of order  $10^2$  for weakly ionized high- $Z$  impurities, which motivates an accurate description of the effect of partial screening in the intermediate region.

We define a local centre of mass frame  $\{e_L^i\}$  with  $e_L^0$  time-like,  $e_L^1 = \mathbf{p}/p$  parallel to the initial momentum, while  $e_L^2$  and  $e_L^3$  are orthogonal to  $e_L^1$ . The momentum transfers can then be written in terms of the deflection angle  $\theta$  as follows:

$$\left. \begin{array}{l} \Delta p_L^0 = 0, \\ \Delta p_L^1 = p(\cos \theta - 1), \\ \Delta p_L^2 = p \sin \theta \cos \phi, \\ \Delta p_L^3 = p \sin \theta \sin \phi. \end{array} \right\} \quad (2.13)$$

Inserting the cross-section in (2.11) and  $\Delta p^k$  from (2.13) into the moments in (2.2)–(2.3), we evaluate the integral over the azimuthal angle  $\phi$ . There are three non-vanishing moments:  $\int_0^{2\pi} d\phi = 2\pi$  and  $\int_0^{2\pi} \sin^2 \phi d\phi = \int_0^{2\pi} \cos^2 \phi d\phi = \pi$ , respectively corresponding to  $\langle \Delta p_L^1 \rangle$ ,  $\langle \Delta p_L^1 \Delta p_L^1 \rangle$  and  $\langle \Delta p_L^2 \Delta p_L^2 \rangle = \langle \Delta p_L^3 \Delta p_L^3 \rangle$ . With species  $a$  denoting electrons and the target particles  $b$  denoting stationary ions of species  $j$ , so that  $f_j(\mathbf{p}) = n_j \delta(\mathbf{p})$ , the moments are given by

$$\left. \begin{array}{l} \langle \Delta p_L^1 \rangle_{ej} = -4\pi n_j p v \int_{1/A}^1 4 \frac{d\sigma_{ej}}{d\Omega} x^3 dx, \\ \langle \Delta p_L^1 \Delta p_L^1 \rangle_{ej} = 8\pi n_j p^2 v \int_{1/A}^1 4 \frac{d\sigma_{ej}}{d\Omega} x^5 dx, \\ \langle \Delta p_L^2 \Delta p_L^2 \rangle_{ej} = 4\pi n_j p^2 v \int_{1/A}^1 4 \frac{d\sigma_{ej}}{d\Omega} x^3 (1-x^2) dx = \langle \Delta p_L^3 \Delta p_L^3 \rangle, \end{array} \right\} \quad (2.14)$$

where  $x = \sin(\theta/2)$ . Inserting the differential cross-section from (2.11) yields

$$\left. \begin{aligned} \langle \Delta p_L^1 \rangle_{ej} &= -4n_j \pi r_0^2 \frac{v}{p^3} \int_{1/\Lambda}^1 \frac{1}{x} [(1-x^2)p^2 + 1] |Z_j - F_j(q)|^2 dx, \\ \langle \Delta p_L^1 \Delta p_L^1 \rangle_{ej} &= 8n_j \pi r_0^2 \frac{v}{p^2} \int_{1/\Lambda}^1 x [(1-x^2)p^2 + 1] |Z_j - F_j(q)|^2 dx, \\ \langle \Delta p_L^2 \Delta p_L^2 \rangle_{ej} &= 4n_j \pi r_0^2 \frac{v}{p^2} \int_{1/\Lambda}^1 \frac{1-x^2}{x} [(1-x^2)p^2 + 1] |Z_j - F_j(q)|^2 dx = \langle \Delta p_L^3 \Delta p_L^3 \rangle. \end{aligned} \right\} \quad (2.15)$$

Unlike the non-relativistic case, the relativistic Fokker–Planck operator does not capture the correct interspecies energy transfer of the corresponding Boltzmann operator. In the case considered here, of collisions with stationary heavy targets, an unphysical non-zero energy transfer occurs. This can be avoided by expanding the integrands of (2.15) to leading order in the scattering-angle parameter  $x$ , but at the same time allowing the momentum transfer  $q = 2px/\alpha$  to be non-negligible as it contains the large factor  $p/\alpha$ . The resulting form of the operator is validated against the Boltzmann operator in § 4: it is shown that with this choice the loss rates of parallel momentum of the Fokker–Planck and Boltzmann operators are equal at non-relativistic energies, and differ by a term of order  $1/\ln \Lambda$  in the ultra-relativistic limit.

For the moments, we thus obtain

$$\left. \begin{aligned} \langle \Delta p_L^1 \rangle_{ej} &= -4\pi n_j c r_0^2 \frac{\gamma}{p^2} [Z_0^2 \ln \Lambda^{ei} + g_j(p)], \\ \langle \Delta p_L^1 \Delta p_L^1 \rangle_{ej} &= 0, \\ \langle \Delta p_L^2 \Delta p_L^2 \rangle_{ej} &= 4\pi n_j c r_0^2 \frac{\gamma}{p} [Z_0^2 \ln \Lambda^{ei} + g_j(p)], \end{aligned} \right\} \quad (2.16)$$

where

$$g_j(p) \equiv \int_{1/\Lambda}^1 \frac{1}{x} [|Z_j - F_j(q)|^2 - Z_{0,j}^2] dx. \quad (2.17)$$

To obtain an explicit form of the collision operator in spherical coordinates  $\{p, \theta, \phi\}$ , where  $\mathbf{p} = (p, 0, 0)$ , we transform the expressions in (2.16) into an arbitrary coordinate system  $\{\mathbf{e}^\mu\}$  and then evaluate the collision operator using covariant notation. For details of this calculation, we refer the reader to appendix A. The collision operator then becomes

$$C^{ej} = \frac{1}{p^2 \sin \theta} \partial_\mu (p^2 \sin \theta V^\mu), \quad (2.18)$$

where

$$V^\mu = \begin{pmatrix} - \left[ \langle \Delta p_L^1 \rangle_{ej} + \frac{1}{p} \langle \Delta p_L^2 \Delta p_L^2 \rangle_{ej} \right] f_e \\ (2p^2)^{-1} \langle \Delta p_L^2 \Delta p_L^2 \rangle_{ej} \partial_\theta f_e \\ (2p^2 \sin^2 \theta)^{-1} \langle \Delta p_L^2 \Delta p_L^2 \rangle_{ej} \partial_\phi f_e \end{pmatrix}. \quad (2.19)$$

From the first component of (2.19), it is clear that the contributions to the energy loss vanish identically only if higher-order terms in the Fokker–Planck operator

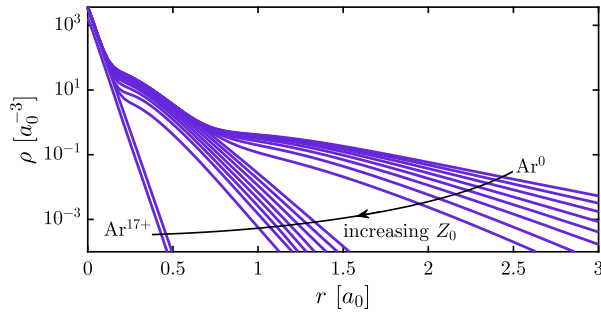


FIGURE 1. Number density of bound electrons averaged over solid angle as a function of radius for all ionization states of argon. The length scale is given in units of the Bohr radius  $a_0$ .

are neglected so that  $\langle \Delta p_L^1 \rangle_{ej} = -p^{-1} \langle \Delta p_L^2 \Delta p_L^2 \rangle_{ej}$ . Finally, evaluating (2.18) for an axisymmetric plasma yields, after summation over ion species  $j$ , the electron-ion collision operator

$$C^{ei} = \sum_j \frac{1}{p^2} \langle \Delta p_L^2 \Delta p_L^2 \rangle_{ej} \frac{1}{2} \frac{\partial}{\partial \xi} (1 - \xi^2) \frac{\partial}{\partial \xi} f_e \quad (2.20)$$

$$= \sum_j 4\pi n_j c r_0^2 \frac{\gamma}{p^3} [Z_0^2 \ln \Lambda^{ei} + g_j(p)] \mathcal{L}\{f_e\}, \quad (2.21)$$

and we can identify the deflection frequency

$$\nu_D^{ei} = 4\pi c r_0^2 \frac{\gamma}{p^3} \left( n_e Z_{\text{eff}} \ln \Lambda^{ei} + \sum_j n_j g_j(p) \right), \quad (2.22)$$

where the first term is the completely screened collision frequency with the effective charge defined as  $Z_{\text{eff}} = \sum_j n_j Z_{0,j}^2 / n_e$ . Note that the properties of the form factor ensure that the completely screened limit is reached if either  $p \rightarrow 0$ , or if the ion is fully ionized so that  $Z = Z_0$ .

What remains is to find the screening function  $g_j(p)$  for all ion species  $j$ . This requires the electronic charge distribution of the ion, which we determine from density functional theory (DFT), using the programs EXCITING (Gulans *et al.* 2014) and GAUSSIAN (Frisch *et al.* 2016). The GAUSSIAN calculations were performed using the hybrid-exchange correlation functional PBE0 (Adamo & Barone 1999), a Douglas–Kroll–Hess second-order scalar relativistic Hamiltonian (Douglas & Kroll 1974; Hess 1986; Barysz & Sadlej 2001), and the atomic natural orbital-relativistic correlation consistent basis set, ANO-RCC (Widmark, Malmqvist & Roos 1990; Roos *et al.* 2004, 2005). As an example, figure 1 shows the density of bound electrons as a function of radius for all argon ionization states. Note that the density decay can be approximately parametrized with piecewise exponentials having different slopes for each of the atomic shells.

When calculating the form factor, the electronic density was first spherically averaged, in which case the form factor in (2.12) simplifies to

$$F_j(q) = 4\pi \int_0^\infty \rho_{ej}(r) \frac{ra_0}{q} \sin(qr/a_0) dr, \quad (2.23)$$

where again  $q = 2px/\alpha$  and the total number of bound electrons is given by  $N_e = 4\pi \int r^2 \rho_{e,j}(r) dr$ .

Numerically, we find that the form factor is well described by a generalized version of the form factor obtained from the Thomas–Fermi model by Kirillov *et al.* (1975):

$$F_{j,\text{TF-DFT}}(q) = \frac{N_{e,j}}{1 + (qa_j)^{3/2}}. \quad (2.24)$$

Note that we can extend the lower integration limit to zero in the definition of  $g_j(p)$  (2.17) since the integrand is finite as  $p \rightarrow 0$  (the logarithmically diverging terms cancel as shown in appendix B). In the form factor in (2.23), this extension of the integral amounts to neglecting terms of order  $\Lambda^{-3/2} \ll 1$  and  $(p\bar{a}_j/\Lambda)^{3/2} \ll 1$  which describe the transition from partial screening to no screening. However, since  $\Lambda^{\text{ei}} = \exp(\ln \Lambda^{\text{ei}}) \propto p$  at high energies from (2.8), we obtain  $(p\bar{a}_j/\Lambda)^{3/2} \sim 137/\Lambda_c$ ; therefore, this approximation is always valid and the no-screening limit will never be reached. Equation (2.24) then gives

$$g_j(p) = \frac{2}{3}(Z_j^2 - Z_{0,j}^2) \ln[(p\bar{a}_j)^{3/2} + 1] - \frac{2}{3} \frac{N_{e,j}^2 (p\bar{a}_j)^{3/2}}{(p\bar{a}_j)^{3/2} + 1}. \quad (2.25)$$

This model, which we denote the Thomas–Fermi–DFT (TF-DFT) model, includes one free parameter: the effective ion length scale  $a_j$  in units of the Bohr radius  $a_0$ , with  $\bar{a}_j = 2a_j/\alpha$ . This parameter is determined from the density of bound electrons obtained from the DFT calculations.

The general properties of the screening function  $g_j(p)$  allow us to determine  $a_j$  so that the deflection frequency exactly matches the high-energy asymptote of the DFT results. As shown in appendix B,  $g_j(p)$  always takes the form

$$g_j(p) = (Z_j^2 - Z_{0,j}^2) \ln(2p/\alpha) + C, \quad 2p/\alpha \gg 1, \quad (2.26)$$

where only the constant  $C$  depends on the specific ionic distribution. Since the additive constant can be absorbed into the effective length scale, the high-energy behaviour of the screening function is reduced to a one-parameter problem. This indicates that (2.25) should be well suited as an analytic model of the screening problem, if it approximates the transition from the low-momentum behaviour to the high-momentum behaviour. Accordingly, we determine  $a_j$  for an arbitrary charge distribution  $\rho_{e,j}(r)$  by matching the  $g_j(p)$  in (2.26) to the general high-energy asymptote of  $g_j(p)$ ,

$$g_j(p) \sim (Z_j^2 - Z_{0,j}^2) \ln(p\bar{a}_j) - \frac{2}{3} N_{e,j}^2, \quad p\bar{a}_j \gg 1. \quad (2.27)$$

The resulting closed form of the effective length scale  $\bar{a}_j$  is given in (B 11) in appendix B, and tabulated for many of the fusion-relevant ion species in table 1. The constants for argon and neon are illustrated in figure 2 as a function of  $Z_0$  in solid line. Curiously, the shell structure observed in the charge density of figure 1 can be discerned as discontinuities in  $\partial\bar{a}_j/\partial Z_{0,j}$ .

Since the obtained values are  $\bar{a}_j \sim 10^2$  for several weakly ionized species such as neon and argon, the deflection frequency will be significantly enhanced compared to complete screening already at  $p \sim 10^{-2}$ . This is confirmed in figure 3, which also shows that the most accurate model for the deflection frequency – the DFT model (solid, green line) – is well approximated by the TF-DFT model in dash-dotted blue over the entire energy interval from non-relativistic to ultra-relativistic energies.

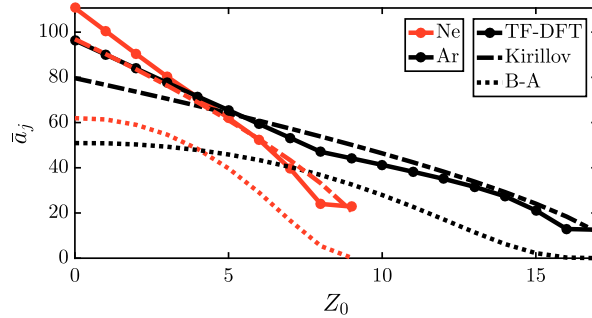


FIGURE 2. Length scale  $\bar{a}_j$  for Ne and Ar, compared to both the Thomas–Fermi model with the Kirillov solution from (2.28), and the Breizman–Aleynikov (B–A) model from (2.29). Note that by definition,  $\bar{a}_j = \bar{a}_{\text{TF-DFT}} \equiv \bar{a}_{\text{DFT}}$ .

Ion	$\bar{a}_j$	Ion	$\bar{a}_j$	Ion	$\bar{a}_j$	Ion	$\bar{a}_j$
$\text{He}^0$	173	$\text{N}^0$	135	$\text{Ar}^0$	96	$\text{Xe}^{1+}$	65
$\text{He}^{1+}$	123	$\text{N}^{1+}$	115	$\text{Ar}^{1+}$	90	$\text{Xe}^{2+}$	63
$\text{Be}^0$	159	$\text{N}^{2+}$	97	$\text{Ar}^{2+}$	84	$\text{Xe}^{3+}$	61
$\text{Be}^{1+}$	114	$\text{N}^{3+}$	79	$\text{Ar}^{3+}$	78	$\text{W}^0$	59
$\text{Be}^{2+}$	67	$\text{N}^{4+}$	59	$\text{Ar}^{4+}$	72	$\text{W}^{30+}$	33
$\text{Be}^{3+}$	59	$\text{N}^{5+}$	35	$\text{Ar}^{5+}$	65	$\text{W}^{40+}$	25
$\text{C}^0$	144	$\text{N}^{6+}$	33	$\text{Ar}^{6+}$	59	$\text{W}^{50+}$	18
$\text{C}^{1+}$	118	$\text{Ne}^0$	111	$\text{Ar}^{7+}$	53	$\text{W}^{60+}$	13
$\text{C}^{2+}$	95	$\text{Ne}^{1+}$	100	$\text{Ar}^{8+}$	47		
$\text{C}^{3+}$	70	$\text{Ne}^{2+}$	90	$\text{Ar}^{9+}$	44		
$\text{C}^{4+}$	42	$\text{Ne}^{3+}$	80	$\text{Ar}^{10+}$	41		
$\text{C}^{5+}$	39	$\text{Ne}^{4+}$	71	$\text{Ar}^{11+}$	38		
		$\text{Ne}^{5+}$	62	$\text{Ar}^{12+}$	35		
		$\text{Ne}^{6+}$	52	$\text{Ar}^{13+}$	32		
		$\text{Ne}^{7+}$	40	$\text{Ar}^{14+}$	27		
		$\text{Ne}^{8+}$	24	$\text{Ar}^{15+}$	21		
		$\text{Ne}^{9+}$	23	$\text{Ar}^{16+}$	13		
				$\text{Ar}^{17+}$	13		

TABLE 1. Values of the normalized effective length scale  $\bar{a}_j = 2a_j/\alpha$  for different ion species. These values were obtained with (B11) using electronic charge densities from DFT calculations.

The length parameter  $\bar{a}_j$  is well suited to compare our result with previous work since it completely characterizes the behaviour of the deflection frequency at high energy, which is the most important region for fast-electron dynamics. A comparison at low energies, where the screening function cannot in general be described by a single parameter, should be approached with caution as the Born approximation is only valid in the regime  $\beta \gtrsim Z\alpha \Leftrightarrow p \gtrsim [(Z\alpha)^{-2} - 1]^{-1/2} \sim 10^{-1}$ . The behaviour at lower momenta is approximate, and should merely be regarded as an interpolation between the low-energy limit of complete screening (which is reproduced by the TF-DFT model) and the behaviour at higher energies. Therefore, we primarily focus on

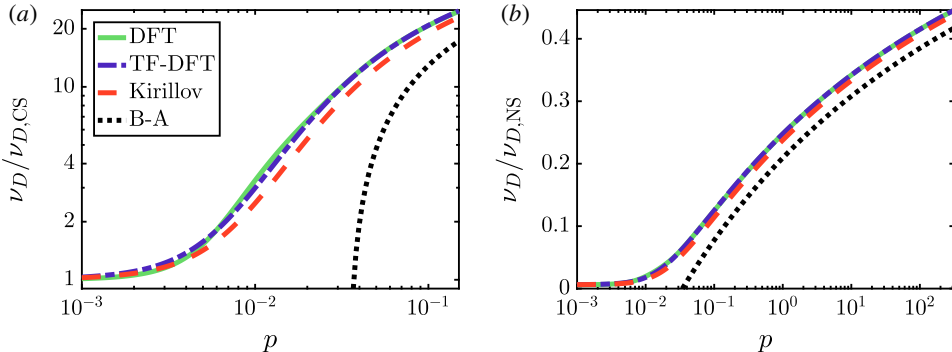


FIGURE 3. Comparison between the DFT and TF-DFT models for the enhancement of the deflection frequency. (a) Shows the low-energy behaviour, and is normalized to the completely screened (CS), low-energy limit. (b) Shows the behaviour up to higher energies, and is normalized to the no-screening (NS) limit. The deflection frequency is significantly lower than the no-screening limit even at ultrarelativistic speeds. The figure is for  $\text{Ar}^{1+}$ , and the Coulomb logarithm was determined by setting  $T = 10$  eV and  $n_e = 10^{20} \text{ m}^{-3}$ .

the length scale  $\bar{a}_j$  when comparing with previous work. For example, the result of Kirillov *et al.* (1975) corresponds to

$$\bar{a}_{\text{Kirillov}} = \frac{2}{\alpha} \frac{(9\pi)^{1/3}}{4} \frac{N_e^{2/3}}{Z} \approx \frac{2}{\alpha} \frac{3}{4} \frac{N_e^{2/3}}{Z}. \quad (2.28)$$

The Kirillov model captures the approximate scaling of  $\bar{a}_j$  with  $Z$  and  $Z_0$ , however it differs significantly from the DFT results at low ionization degrees (maximum relative error 20 %, obtained for  $\text{C}^0$ ) and for  $N_e = 2$  (maximum 43 %,  $\text{Ar}^{16+}$ ). As shown in figure 2, this is because the Kirillov model does not capture the shell structure of the ion, which is an inherent characteristic of the Thomas–Fermi theory employed by Kirillov *et al.* (1975). Although these relative errors are significant, the final error in the deflection frequency is modest at high energies, since the deflection frequency is only sensitive to  $\ln \bar{a}_j$ . At  $p = 0.1$ , the relative error of  $\bar{a}_j$  between the TF-DFT model and the Thomas–Fermi model is at most 14 %.

We find a significantly larger difference between our model for the deflection frequency and the model used by Breizman & Aleynikov (2017). In this model, which we refer to as the B–A model, the deflection frequency always increases logarithmically. The deflection frequency therefore diverges as  $p \rightarrow 0$  and the complete-screening limit is consequently not reproduced, which is illustrated in figure 3(a). This means that the B–A model is only applicable at relativistic energies and is unable to describe phenomena involving mildly relativistic electrons, such as hot-tail, primary runaway generation and the avalanche mechanism at high electric fields. In the B–A model, the logarithmic increase of the deflection frequency corresponds to the length constant

$$\bar{a}_{\text{B-A}} = \frac{2}{\alpha} Z_j^{-1/3} \exp \left( \frac{2}{3} \frac{N_{e,j}^2 - 6 \ln 2(Z_j Z_{0,j} - Z_j^2 - Z_{0,j}^2)}{Z_j^2 - Z_{0,j}^2} \right). \quad (2.29)$$

As shown in figure 2,  $\bar{a}_{\text{B-A}}$  differs significantly from both  $\bar{a}_{\text{Kirillov}}$  and our more accurate DFT-based values of  $\bar{a}_j$ .

We conclude that the Kirillov formula suffices for an accurate description of screening in most situations, although the constants derived from DFT have a higher level of accuracy, especially at low momenta.

#### 2.4. Inelastic collisions with bound electrons

Unlike for elastic collisions with partially screened nuclei, there is no analytic expression for the differential cross-section for inelastic collisions between fast and bound electrons, but the energy loss is described by the Bethe stopping-power formula (Bethe 1930; Jackson 1999). Accordingly, we modify the slowing-down frequency  $\nu_S^{ee}$  in (2.5), which describes collisional drag, whereas we neglect the modification of the electron-electron deflection frequency  $\nu_D^{ee}$ , since it does not follow from the stopping-power calculation. The error introduced through this approximation, i.e.  $\nu_D \approx \nu_D^{ei} + \nu_{D,CS}^{ee}$ , can be estimated by considering the limits of no screening and complete screening of  $\nu_D^{ee}$ . For suprathermal electrons,  $\nu_{D,CS}^{ee} = 4\pi c r_0^2 (\gamma/p^3) n_e \ln \Lambda^{ee}$ , while  $\nu_{D,NS}^{ee}$  is enhanced by a factor of  $n_e^{\text{tot}}/n_e = 1 + \sum_j N_{e,j} n_j/n_e$ . Comparing to the electron-ion deflection frequency (2.22), we find that our approximation is valid if either  $\sum_j Z_j^2 n_j \gg \sum_j N_{e,j} n_j$ , or if  $1 + Z_{\text{eff}} \gg \nu_D^{ee}/\nu_{D,CS}^{ee}$  due to either significant ionization levels or low electron momentum. In other words, our model is accurate both when screening effects are small and in the presence of high-Z impurities.

The Bethe stopping-power formula modifies the slowing-down frequency  $\nu_S^{ee}$  describing collisional drag according to Bethe (1930) and Jackson (1999)

$$\nu_S^{ee} = 4\pi c r_0^2 \frac{\gamma^2}{p^3} \left[ n_e \ln \Lambda^{ee} + \sum_j n_j N_{e,j} (\ln h_j - \beta^2) \right], \quad (2.30)$$

where  $h_j = p \sqrt{\gamma - 1} (m_e c^2 / I_j)$ , and  $I_j$  is the mean excitation energy of the ion. In this work, the numerical values of  $I_j$  for different ion species were obtained from Sauer *et al.* (2015). In addition, several sources list the mean excitation energy for neutral atoms, for instance Berger *et al.* (1984), which is used in ESTAR (Berger *et al.* 2005). Equation (2.30) is valid for  $m_e c^2 (\gamma - 1) \gg I_j$ , which is typically of the order of hundreds to thousands of eV. In order to find an expression that is applicable over the entire energy range from thermal to ultrarelativistic energies, we match (2.30) to the low-energy asymptote corresponding to complete screening. The resulting interpolation formula, which we refer to as the Bethe-like model, is given by

$$\nu_S^{ee} = 4\pi c r_0^2 \frac{\gamma^2}{p^3} \left\{ n_e \ln \Lambda^{ee} + \sum_j n_j N_{e,j} \left[ \frac{1}{k} \ln(1 + h_j^k) - \beta^2 \right] \right\}, \quad (2.31)$$

where we set  $k = 5$ . This is plotted as a function of momentum in figure 4, and compared to the completely screened limit on the left y-axis, and the limit of no screening on the right y-axis. Unlike the deflection frequency, equation (2.31) will exceed the limit of no screening in the limit of infinite momentum, since it increases by a power of  $p^{3/2}$  compared to a power of  $p^{1/2}$  for  $\ln \Lambda^{ee}$  in (2.8). For fusion-like densities, this will however happen around  $p \sim 10^4$  ( $\sim 10$  GeV), which is well above realistic runaway energies. At these ultra-large momentum scales, the so-called density effect (Jackson 1999; Solodov & Betti 2008) would ensure that the logarithmic term smoothly approaches the Coulomb logarithm.

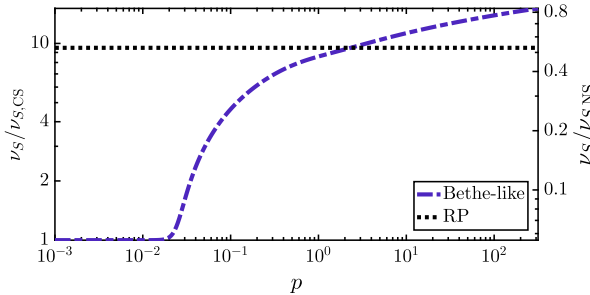


FIGURE 4. The partially screened slowing-down frequency for the Bethe-like model in (2.31) and the RP model from (2.32), for singly ionized argon. The collision frequency is normalized to the completely screened (CS), low-energy limit on the left y-axis, and to the limit of no screening (NS) on the right y-axis. The figure is for  $\text{Ar}^{1+}$ , and the Coulomb logarithm was determined by setting  $T = 10$  eV and  $n_e = 10^{20} \text{ m}^{-3}$ .

We also compare the Bethe-like model to the Rosenbluth–Putvinski (RP) model (Rosenbluth & Putvinski 1997), which includes half of the bound electron density  $n_b = \sum_j n_j N_{e,j}$ :

$$v_S^{\text{ee}} \approx 4\pi c r_0^2 \frac{\gamma^2}{p^3} \ln \Lambda \left( n_e + \frac{n_b}{2} \right). \quad (2.32)$$

Figure 4 shows that this estimate coincides with the Bethe-like model at  $p \approx 1$ , but results in a notable overestimation at mildly relativistic momenta and a significant underestimation at ultra-relativistic momenta.

Note that (2.31) ensures that the enhancement of  $v_S^{\text{ee}}$  does not extend into the bulk electron population, which means that the first term  $4\pi c r_0^2 (\gamma^2/p^3) n_e \ln \Lambda^{\text{ee}}$  can be replaced by the complete expression for  $v_{S,CS}^{\text{ee}}$  accounting for a finite bulk temperature (Braams & Karney 1989). This is because  $I_j$  is greater than the temperature  $T$  at which a certain ion species  $j$  would be present in equilibrium. Since the ions can always be treated as stationary (at rest), the same issue does not arise for  $v_D^{\text{ei}}$ . This means that the generalization of the Fokker–Planck operator to a partially ionized plasma can be expressed as modifications to  $v_D^{\text{ei}}$  and  $v_S^{\text{ee}}$  in the collision operator (2.5), according to (2.22), with  $g_j(p)$  defined in (2.25) and  $\bar{a}_j$  given in table 1, as well as (2.31), with  $I_j$  from Sauer *et al.* (2015).

### 3. Effect on avalanche growth rate and runaway distribution

The presence of partially ionized atoms has a peculiar effect on the avalanche growth rate at high electric fields: as will be shown in the present section, the partial-screening effect can increase the avalanche growth rate despite the increased collisional damping and in contrast to previous predictions (Putvinski *et al.* 1997). Moreover, the quasi-steady-state runaway distribution acquires an electric field-dependent average energy since the growth rate no longer depends linearly on the electric field.

The avalanche growth rate is defined as

$$\Gamma = \frac{1}{n_{\text{RE}}} \frac{dn_{\text{RE}}}{dt}. \quad (3.1)$$

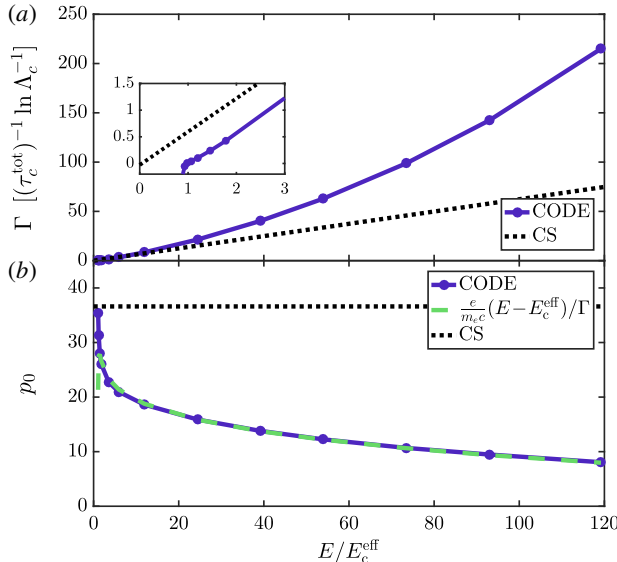


FIGURE 5. (a) Steady-state runaway growth rate as a function of normalized electric field. The partially screened growth rate (solid line) exceeds the completely screened limit (dotted line) at high electric fields, but is significantly lower in the near-critical electric-field region, which is shown in the inset. (b) With partial screening (solid line), the average momentum  $p_0$  decreases with electric field, as predicted by the green dashed line, and is lower than in the completely screened limit (dotted line). The simulation was done at  $T = 10$  eV with a plasma composition of D and  $\text{Ar}^{1+}$ , where  $n_{\text{D}} = 10^{20} \text{ m}^{-3}$  and  $n_{\text{Ar}} = 4n_{\text{D}}$ .

With constant background parameters, the runaway distribution reaches a quasi-steady state and the avalanche growth rate approaches a constant value. This quasi-steady-state growth rate is shown in the presence of singly ionized argon impurities in figure 5(a). Here, the growth rate is plotted against  $E/E_c^{\text{eff}}$ , where the effective critical electric field  $E_c^{\text{eff}} \gtrsim E_c^{\text{tot}} = E_c n_e^{\text{tot}}/n_e$  is given in Hesslow *et al.* (2018). These results were obtained by solving the kinetic equation using the numerical solver CODE (Landreman, Stahl & Fülöp 2014; Stahl *et al.* 2016), including avalanche generation using the field particle Boltzmann operator given in equation (2.17) of Embréus, Stahl & Fülöp (2018), which was also studied by Chiu *et al.* (1998). Since we here focus on electric fields well above the critical electric field, which are associated with low critical momenta, synchrotron and bremsstrahlung radiation losses are neglected as they are important only at highly relativistic energies; Hesslow *et al.* (2018) demonstrated that radiation losses only have an appreciable effect near the effective critical electric field. The parameters are characteristic of a post-disruption tokamak plasma: temperature  $T = 10$  eV, and density of singly ionized argon  $n_{\text{Ar}} = 4n_{\text{D}}$  with  $n_{\text{D}} = 10^{20} \text{ m}^{-3}$ .

As shown in figure 5(a), the partially screened avalanche growth rate is nonlinear in the electric field. We attribute this nonlinearity to the energy-dependent enhancement of the collision frequencies. At weak electric fields, the critical momentum is large, and therefore also the enhancement of the collision frequencies; however, at larger electric fields, the critical momentum is reduced and the collision frequencies approach

the completely screened value. This leads to an avalanche growth which increases faster than  $\Gamma \propto E - E_c^{\text{eff}}$ .

Interestingly, this nonlinearity of the growth rate causes the partially screened avalanche growth rate to exceed the completely screened limit at large electric fields. For the completely screened limit, we use the Rosenbluth–Putvinski growth-rate formula (Rosenbluth & Putvinski 1997), which has been shown to be accurate to around 10 % in the fully ionized case (Embréus *et al.* 2018) and is given by

$$\Gamma_{\text{RP,CS}} = \frac{1}{\tau_c \ln \Lambda_c} \sqrt{\frac{\pi}{3(Z_{\text{eff}} + 5)}} \left( \frac{E}{E_c} - 1 \right) \left( 1 - \frac{E_c}{E} + \frac{4\pi(Z_{\text{eff}} + 1)^2}{3(Z_{\text{eff}} + 5)(E^2/E_c^2 + 3)} \right)^{-1/2} \quad (3.2)$$

$$\approx \frac{1}{\tau_c \ln \Lambda_c} \sqrt{\frac{\pi}{3(Z_{\text{eff}} + 5)}} \left( \frac{E}{E_c} - 1 \right), \quad E/E_c \gg 2\sqrt{Z_{\text{eff}} + 1}. \quad (3.3)$$

In figure 5(a), it is shown that the partially ionized growth rate is considerably higher than the completely screened value at large electric fields, even though it is significantly lower close to the critical electric field which is illustrated in the zoomed inset.

The enhancement of the avalanche growth rate in the presence of partially ionized atoms originates from the increased number of possible runaway electrons: since the binding energy is negligible compared to the critical runaway energy, the free and the bound electrons have equal probability of becoming runaways through close collisions. At high electric fields, this large enhancement by a factor of  $n_e^{\text{tot}}/n_e$  dominates over the increased rate of collisional losses, which sets the threshold energy for an electron to become a runaway.

The fact that partially screened impurities can lead to a reduction of the avalanche growth at low electric fields, but an enhancement at larger electric fields, is not captured by the partially screened Rosenbluth–Putvinski formula (Putvinski *et al.* 1997; Rosenbluth & Putvinski 1997)

$$\Gamma_{\text{RP}} = \frac{1}{\tau_c \ln \Lambda_c} \frac{n_e^{\text{tot}}}{n_e} \sqrt{\frac{\pi}{3(Z_{\text{eff}}^{\text{RP}} + 5)}} \left( \frac{E}{E_c^{\text{RP}}} - 1 \right), \quad (3.4)$$

where the effective field includes half of the bound electron density  $n_b$ , originating from the same factor in  $v_S^{\text{ee}}$  from (2.32):

$$E_c^{\text{RP}} = \left( 1 + \frac{n_b}{2n_e} \right) E_c, \quad (3.5)$$

and the partially ionized effective charge  $Z_{\text{eff}}^{\text{RP}}$  is taken from Parks–Rosenbluth–Putvinski (Parks, Rosenbluth & Putvinski 1999):

$$Z_{\text{eff}}^{\text{RP}} = \sum_{j \text{ part.}} \frac{n_j}{n_e} \frac{Z_j^2}{2} + \sum_{j \text{ fully ionized}} \frac{n_j}{n_e} Z_j^2. \quad (3.6)$$

For large electric fields,  $E \gg E_c^{\text{RP}}$ , and if the plasma is dominated by a weakly ionized, high-Z impurity such as  $\text{Ar}^{1+}$ , one obtains

$$\frac{\Gamma_{\text{RP}}}{\Gamma_{\text{RP,CS}}} \approx \frac{n_e + n_b}{n_e + \frac{1}{2}n_b} \sqrt{\frac{Z_{\text{eff}} + 5}{Z_{\text{eff}}^{\text{RP}} + 5}} < 1. \quad (3.7)$$

In this case, partially ionized impurities decrease the avalanche growth rate significantly, although we find the opposite behaviour with our more accurate kinetic model:

$$\Gamma > \Gamma_{\text{RP,CS}} > \Gamma_{\text{RP}}, \quad E \gg E_c^{\text{eff}}. \quad (3.8)$$

Finally, we note that the avalanche growth rate in figure 5(a) may be approximated by a second-order polynomial. This behaviour is somewhat similar to the quadratic behaviour of the full Rosenbluth–Putvinski formula (3.2) in the limit  $2\sqrt{Z_{\text{eff}} + 1} \gg E/E_c \gg 1$ . However, evaluating this criterion with  $Z_{\text{eff}}^{\text{RP}}$  and  $E_c^{\text{RP}}$  predicts that this quadratic regime should only occur if  $E \lesssim 9E_c^{\text{eff}}$  for the range of parameters in figure 5. Consequently, the Rosenbluth–Putvinski formula cannot easily be modified to accurately capture the effect of screening on the avalanche growth rate.

The increased growth rate has direct implications for the avalanche multiplication factor, which determines the maximum amplification of a small seed due to avalanche multiplication. To estimate this effect we consider the example of a tokamak disruption, where a part of the initial current is converted to runaways via avalanching. We follow the calculation of Helander, Eriksson & Andersson (2002) under the approximation  $\Gamma \approx \Gamma_0 E/E_c^{\text{eff}}$  where  $\Gamma_0$  is independent of the electric field. Neglecting electric-field diffusion – which may however significantly affect the final runaway current profile (Eriksson *et al.* 2004; Smith *et al.* 2006) – the zero-dimensional induction equation is

$$E = -\frac{L}{2\pi R} \frac{dI}{dt}, \quad (3.9)$$

where  $L \sim \mu_0 R$  is the self-inductance and  $R$  is the major radius of the tokamak. Then, equation (3.1) can be written

$$\frac{d}{dt} \ln n_{\text{RE}} \approx -\frac{d}{dt} \frac{IL\Gamma_0}{2\pi RE_c^{\text{eff}}}, \quad (3.10)$$

and therefore an initial seed  $n_0$  can be multiplied by up to a factor of

$$\frac{n_{\text{RE}}}{n_0} = \exp \left( \frac{I_0 L \Gamma_0}{2\pi R E_c^{\text{eff}}} \right). \quad (3.11)$$

The exponent can be large in high-current devices (Rosenbluth & Putvinski 1997). Consequently, if the induced electric field is much larger than  $E_c^{\text{eff}}$ , heavy-impurity injection can increase the avalanche multiplication factor significantly. However, to fully understand runaway beam formation in the presence of partially ionized impurities, the combined effect of avalanche multiplication and seed generation must be accounted for, as the seed formation is also sensitive to the injected impurities (Aleynikov & Breizman 2017).

The nonlinear avalanche growth rate also manifests itself in the quasi-steady-state avalanche distribution, which can be seen by following the derivation of the avalanching distribution in the limit  $E \gg E_c$  by Fülöp *et al.* (2006), which we detail in appendix C. Analogously to Fülöp *et al.* (2006), the resulting energy dependence of the distribution function  $F(p, t) \approx 2\pi p^2 \int_{-p}^1 f d\xi$  is given by

$$F(p, t) = n_{\text{RE}}(t) \frac{1}{p_0} e^{-p/p_0}, \quad (3.12)$$

where the average momentum is given by

$$p_0 = \frac{e}{m_e c} \frac{E - E_c^{\text{eff}}}{\Gamma(E)}. \quad (3.13)$$

In contrast to the fully ionized result  $p_0 = \sqrt{Z+5} \ln \Lambda_c$ , the average momentum acquires a significant electric-field dependence in the presence of partially screened ions. This momentum dependence is shown in figure 5(b), where we find  $p_0$  from fitting the high-energy part of the electron distribution to an exponential decay. This average energy obtained in the CODE simulation agrees well with the prediction in (3.12) in the region where it is valid, i.e.  $E \gg E_c^{\text{eff}}$ . Note that the average energy is well below the complete-screening limit shown in dotted line, where  $p_0 \approx \sqrt{6} \ln \Lambda_c$ .

#### 4. Effect of partial screening on the validity of the Fokker–Planck operator

Scenarios where small-angle collisions dominate can be accurately modelled by the Fokker–Planck collision operator, whereas the more complicated Boltzmann operator must be used if large-angle collisions are significant. Partial screening enhances the elastic electron–ion scattering cross-section for large momentum transfers while leaving it unaltered for small momentum transfers (see figure 6). Thus, large-angle collisions are expected to be relatively more important in the partially screened collision operator than in the limit of complete screening. In this section we will show that even though the two collision operators produce slightly different distribution functions, this difference has a negligible effect on the key runaway quantities, such as the runaway density and current.

Here, we consider the full Boltzmann operator for collisions between runaway electrons and the background plasma. For electron–ion collisions, we use the full operator, whereas for electron–electron collisions, we follow the method developed by Embréus *et al.* (2018) and only consider collisions with a momentum transfer larger than a cutoff  $p_m$ . Note that in modelling collisions with the bound electrons, for which the full differential cross-section is unknown, the Møller cross-section can still be used since the energy transfer corresponding to the cutoff is typically chosen to be significantly larger than the binding energy.

The general form of the Boltzmann operator is (Cercignani & Kremer 2002)

$$C^{\text{B},ab} = \int d\mathbf{p}' d\sigma_{ab} g_\theta [f_a(\mathbf{p}_1) f_b(\mathbf{p}_2) - f_a(\mathbf{p}) f_b(\mathbf{p}')], \quad (4.1)$$

where  $g_\theta = \sqrt{(\mathbf{v} - \mathbf{v}')^2 - (\mathbf{v} \times \mathbf{v}')^2/c^2}$  is the Møller relative speed and  $d\sigma_{ab}$  is the differential cross-section for collisions in which the momentum of species  $a$  changes from  $\mathbf{p}$  to  $\mathbf{p}_1$ , while  $\mathbf{p}' \rightarrow \mathbf{p}_2$  for species  $b$ . The collision operator can be understood as the rate at which species  $a$  scatters from  $\mathbf{p}_1$  into  $\mathbf{p}$ , minus the rate of the opposite scattering process. Elastic electron–ion collisions are particularly convenient to model with the Boltzmann operator, since the ions can be modelled as stationary, infinitely heavy target particles and the cross-section only depends on  $p$ ,  $p_1$  and  $\theta$ . When expanded in Legendre polynomials,

$$C^{\text{B},\text{ei}} = \sum_j \sum_L C_L^{\text{B},\text{ej}} P_L(\xi) \quad (4.2)$$

$$f_e(p, \theta, t) = \sum_L f_L(p, t) P_L(\xi), \quad (4.3)$$

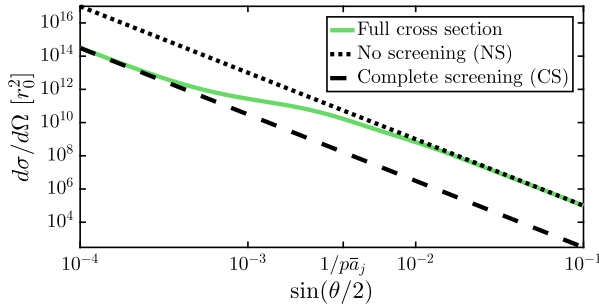


FIGURE 6. The differential cross-section for elastic electron–ion collisions as a function of deflection angle using the full DFT density to calculate the form factor (solid green), which exhibits a smooth transition from complete screening (dashed black line) to the larger cross-section with no screening (dotted black line). The cross-section falls off as  $\sin^4(\theta/2)$ ; however the curve is flatter in the transition region around  $\sin(\theta/2)p\bar{a}_j \sim 1$ . The cross-section was evaluated for singly ionized argon at  $p = 3$ .

the Boltzmann operator takes the following form:

$$C_L^{B,ej} = -n_j v f_L \int_{\theta_{\min}}^{\pi} [1 - P_L(\cos \theta)] \frac{\partial \sigma_{ej}}{\partial \Omega} d\Omega \quad (4.4)$$

$$= -2\pi n_j c r_0^2 f_L \frac{\gamma}{p^3} \int_{1/\Lambda}^1 \frac{|Z_j - F_j(q)|^2}{x} \frac{1 - P_L(1 - 2x^2)}{x^2} \frac{(1 - x^2)p^2 + 1}{p^2 + 1} dx, \quad (4.5)$$

where we again introduced  $x = \sin(\theta/2)$  and inserted the differential cross-section in (2.11). Using  $\mathcal{L}\{f_e\} = -(1/2) \sum_L L(L+1)P_L(\xi)f_L$ , we arrive at the following ratio between the Boltzmann operator and the Fokker–Planck electron–ion collision operator in (2.21):

$$\frac{C_L^{B,ej}}{C_L^{FP,ej}} = \left( \int_{1/\Lambda}^1 \frac{|Z_j - F_j(q)|^2}{x} dx \right)^{-1} \int_{1/\Lambda}^1 \frac{|Z_j - F_j(q)|^2}{x} \frac{1 - P_L(1 - 2x^2)}{L(L+1)x^2} \frac{(1 - x^2)p^2 + 1}{p^2 + 1} dx. \quad (4.6)$$

Since  $P_1(x) = x$ , equation (4.6) evaluates to unity for  $L = 1$  and  $p = 0$ . Note that the same is true for the integrand when  $x \ll 1 \forall L, p$ .

Like the Fokker–Planck operator, the Boltzmann operator drives the distribution towards spherical symmetry, which can be seen by noting that  $C_L^{B,ej}$  is negative and proportional to  $f_L$ , while  $C_0^{B,ej} = 0$ . Effectively, the Boltzmann operator takes the form of a generalized  $v_D^{ei}$  which depends on the Legendre mode number  $L$ . The ratios of the Legendre modes of the Boltzmann and Fokker–Planck operators are shown in figure 7 for four different values of  $L$ . As expected from (4.6), the Boltzmann operator produces the same result as the Fokker–Planck operator for  $L = 1$  and  $p \ll 1$ , and only differs by a factor of order  $1/\ln \Lambda$  at higher energies. In contrast, the ratio between the Boltzmann operator and the Fokker–Planck operator decreases rapidly with  $L$ , and the diffusion rates are significantly reduced for  $L \geq 10$  for a large range of momenta. High- $L$ -structure will therefore be suppressed too quickly by the Fokker–Planck operator compared to the more accurate Boltzmann operator. This means that the two operators can be expected to produce different pitch-angle distributions in scenarios where the average pitch angle is small.

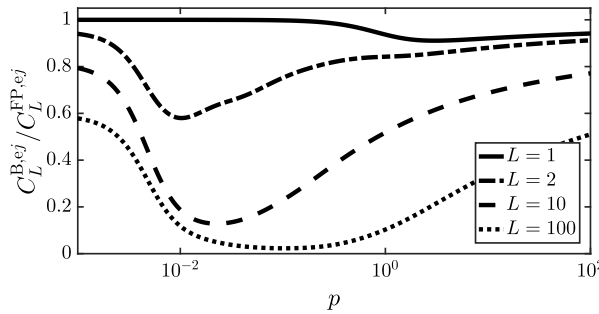


FIGURE 7. Ratio of the Legendre modes of the Boltzmann and Fokker–Planck operators for singly ionized argon. The full DFT model was used in the figure, but the results are similar if the TF-DFT model is used instead.

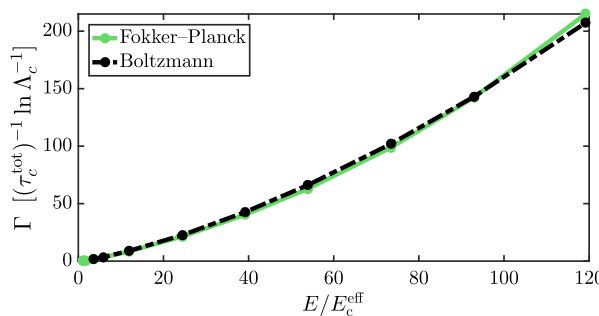


FIGURE 8. Steady-state avalanche growth rate as a function of normalized electric field. The Fokker–Planck and Boltzmann operators give almost identical results. The simulation was done at  $T = 10$  eV with a plasma composition of D and  $\text{Ar}^{1+}$ , where  $n_{\text{D}} = 10^{20} \text{ m}^{-3}$  and  $n_{\text{Ar}} = 4n_{\text{D}}$ .

A suitable scenario to study the effect of the Boltzmann operator is the avalanche growth rate at high electric fields, which gives a narrow distribution function and thus requires a large number of Legendre modes to describe the distribution. Figure 8 shows the steady-state runaway growth rate as a function of  $E/E_c^{\text{eff}}$  where  $E_c^{\text{eff}}$  is the effective critical field given by Hesslow *et al.* (2018). These growth rates were obtained by solving the kinetic equation using CODE with the same parameters as in figure 5, with both the Fokker–Planck operator and the Boltzmann operator. As we show in figure 8, the difference in the runaway growth rate between the Fokker–Planck operator and the Boltzmann operator is relatively small. This result may appear surprising, since the avalanche growth rate formula (3.3) depends on  $Z$ , indicating a sensitivity to the pitch-angle dynamics. We speculate that the similarity can be attributed to the agreement in the zeroth and first Legendre modes of the Fokker–Planck and Boltzmann operators as shown in figure 7. This may be sufficient since the essential runaway quantities are most sensitive to the behaviour of these modes, with the runaway density and energy fully contained in  $f_0$ , and the current in  $f_1$ .

Figure 9 shows contour plots of the runaway electron distribution function using the Fokker–Planck and Boltzmann operators respectively. While the overall shape and

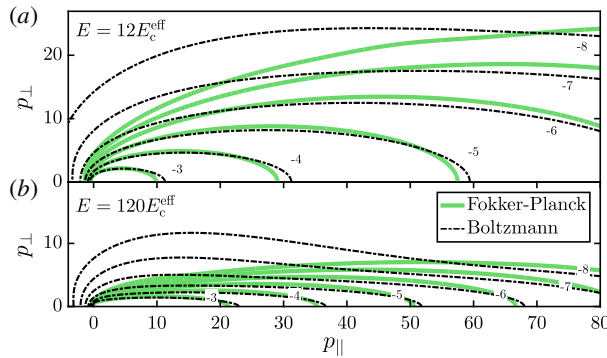


FIGURE 9. Contour plots of the quasi-steady-state runaway electron distribution function obtained using the Fokker–Planck operator (solid green) and the Boltzmann operator (dash-dotted, thin black), respectively. The contours show  $\log_{10}(F) = (-8, -7, \dots, -3)$  as indicated in the figure, where  $F = m_e^3 c^3 f_e / n_{RE}$ , so that  $\int 2\pi p_\perp F dp_\perp dp_\parallel = 1$  when integrated over the runaway population. The distributions are taken from the data points (a)  $E = 12E_c^{\text{eff}}$  and (b)  $E = 120E_c^{\text{eff}}$  in figure 8.

energy of the distributions are similar, the Boltzmann operator leads to a pitch-angle distribution which develops ‘wings’ consisting of a small runaway population with significantly enhanced perpendicular momentum. This effect is particularly pronounced at high electric fields where the average pitch angle is small and at moderate energies, which is consistent with our expectation based on figure 7. This indicates that using the Boltzmann operator could affect quantities that are particularly sensitive to the angular distribution, such as the emitted synchrotron radiation (Finken *et al.* 1990; Hoppe *et al.* 2018a,b). In order to quantify the differences we used the SYRUP code (Stahl *et al.* 2013) to calculate synchrotron spectra from the runaway electron distributions using the Fokker–Planck and Boltzmann operators, respectively, with a 5 T magnetic field. Figure 10 shows that in comparison with the Fokker–Planck operator, the Boltzmann collision operator leads to a spectrum with peak at a shorter wavelength. Again, we see that the difference is more pronounced at larger electric fields.

Another quantity which is highly sensitive to input parameters is the primary (Dreicer) growth rate, which in a fully ionized plasma varies exponentially with both the electric field normalized to the Dreicer field  $E_D$  and the effective charge (Connor & Hastie 1975). One may therefore expect that the differences between the Fokker–Planck and the Boltzmann operator are amplified in the Dreicer growth rate, which is verified in figure 11. Most notably, the partially screened collision operator reduces the Dreicer growth rate by several orders of magnitude compared to the completely screened case. In contrast, the Fokker–Planck and the Boltzmann operator exhibit a similar qualitative behaviour, with differences around tens of per cent in most of the interval. Although significant, this growth rate difference between the two collision operators is small compared to uncertainties in both experimental parameters and the collision operator. As discussed in § 2, the latter is because the validity of the Born approximation breaks down at the low critical momenta obtained with the electric fields in figure 11. Consequently, the differences between the Fokker–Planck and the Boltzmann operator cannot be regarded as practically relevant.

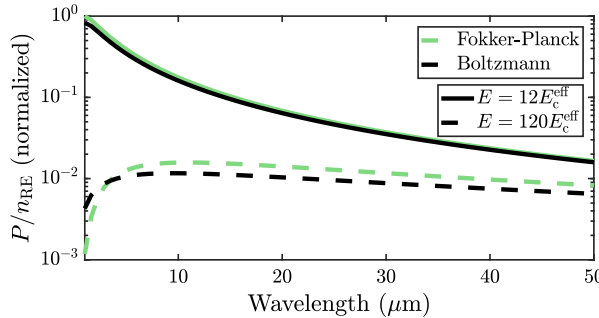


FIGURE 10. Synchrotron radiation spectra from the runaway electron distribution function, comparing the Boltzmann collision operator with the Fokker–Planck collision operator, in a magnetic field with strength  $B = 5$  T. Both are normalized to the maximum value of the Fokker–Planck spectrum in the chosen wavelength interval. As in figure 9, the distributions are taken from  $E = 12E_c^{\text{eff}}$  and  $E = 120E_c^{\text{eff}}$  in figure 8. The Boltzmann collision operator causes significantly stronger synchrotron emission than the Fokker–Planck operator, although the shape of the spectra are similar.

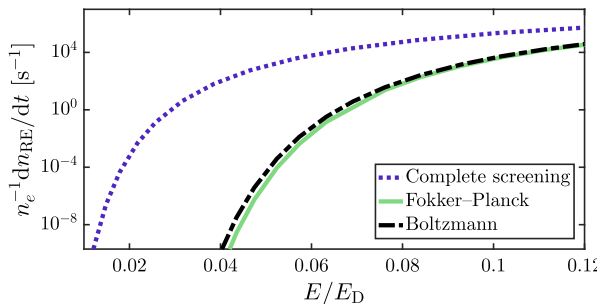


FIGURE 11. Steady-state primary growth rate as a function of the electric field normalized to the Dreicer field (calculated with the free electron density). Screening effects lead to significantly lower growth rates than the completely screened dotted blue line, but the Fokker–Planck operator (solid green) and Boltzmann operator (dash-dotted black) show a qualitatively similar behaviour. The simulation was done at  $T = 10$  eV with a plasma composed of D and  $\text{Ar}^{1+}$ , where  $n_{\text{D}} = 10^{20} \text{ m}^{-3}$  and  $n_{\text{Ar}} = 4n_{\text{D}}$ .

## 5. Conclusions

Collisions between fast electrons and partially ionized atoms are sensitive to the effect of screening. In this paper, we derived a collision operator accounting for the effect of partial screening. This generalization of the Fokker–Planck operator in a fully ionized plasma can be expressed as modifications to the deflection and slowing-down frequencies. To obtain these collision frequencies, we treated the interaction between fast electrons and partially ionized impurities quantum mechanically in the Born approximation. We used DFT calculations to obtain the electron-density distribution of the impurity ions, which determined the differential cross-sections for elastic scattering. This allowed us to define an effective ion length scale, and we display these results in table 1 for the ion species that are most common in fusion experiments: helium, beryllium, carbon, nitrogen, neon, argon, xenon and tungsten. The results showed that a formula for this length scale based on the Thomas–Fermi model usually suffices for

an accurate description of screening effects. However, the length scales derived from DFT give higher accuracy, especially for low electron momenta. Combined with a stopping-power description of inelastic scattering, this forms the generalized collision operator for fast electrons interacting with partially ionized impurities.

Using the generalized collision operator, the runaway growth rate and energy spectrum were calculated. Unlike the completely screened description, screening effects lead to a stronger-than-linear electric-field dependence causing a significantly enhanced avalanche growth rate at high electric fields. This behaviour contrasts previous results (Putvinski *et al.* 1997), which predicted the growth rate to always be reduced compared to the completely screened limit. At weak electric fields, partial screening however reduces the avalanche growth rate by significantly enhancing the threshold field. In addition, we found that the exponentially decaying avalanche-dominated energy spectrum has an average energy that depends on the electric field. This energy is significantly lower than with complete screening, which is equivalent to a fully ionized plasma having the same effective charge.

Finally, we showed that the validity of the Fokker–Planck equation is less clearly satisfied for partially screened collisions than in the pure Coulomb case, due to the enhancement of large momentum transfers. Despite this, we found that the runaway energy and growth rate are well captured by a treatment based on the Fokker–Planck operator. The overall shape of the fast-electron distribution is somewhat different in the more precise Boltzmann approach, but this has negligible effect on the integrated quantities such as the energy spectrum and runaway current. However, quantities which are highly sensitive to the angular distribution, such as synchrotron radiation, can be moderately affected in high-electric-field cases.

### Acknowledgements

The authors are grateful to S. Newton, G. Wilkie and I. Pusztai for fruitful discussions. This work was supported by the Swedish Research Council (Dnr. 2014-5510), the Knut and Alice Wallenberg Foundation and the European Research Council (ERC-2014-CoG grant 647121). The work has been carried out within the framework of the EUROfusion Consortium and has received funding from the Euratom research and training programme 2014–2018 under grant agreement no. 633053. The views and opinions expressed herein do not necessarily reflect those of the European Commission.

### Appendix A. Evaluating the terms in the collision operator with covariant notation

To obtain an explicit form of the collision operator in spherical coordinates  $\{p, \theta, \phi\}$  where  $\mathbf{p} = (p, 0, 0)$ , we transform the expressions in (2.16) into an arbitrary coordinate system  $\{\mathbf{e}^\mu\}$ , where the moments are

$$\left. \begin{aligned} \langle \Delta p^\mu \rangle_{ej} &= (\mathbf{e}^\mu \cdot \mathbf{e}_{L,j}) \Delta p_L^\nu \\ &= \frac{p^\mu}{p} \langle \Delta p_L^1 \rangle, \\ \langle \Delta p^\mu \Delta p^\nu \rangle_{ej} &= (\mathbf{e}^\mu \cdot \mathbf{e}_{L,\rho}) (\mathbf{e}^\nu \cdot \mathbf{e}_{L,\sigma}) \Delta u_L^\rho \Delta u_L^\sigma \end{aligned} \right\} \quad (A\,1)$$

$$= \left[ \delta^{\mu\nu} - \frac{p^\mu p^\nu}{p^2} \right] \langle \Delta p_L^2 \Delta p_L^2 \rangle.$$

We now wish to convert the expressions (A 1) into the coordinate basis  $\{p, \theta, \phi\}$ . In this system, the three-dimensional metric is

$$g_{\mu\nu} = \begin{pmatrix} 1 & 0 & 0 \\ 0 & p^2 & 0 \\ 0 & 0 & p^2 \sin^2 \theta \end{pmatrix}. \quad (\text{A } 2)$$

Note that to convert the expressions in (A 1) from a normalized basis into a coordinate basis, any contravector  $V^\mu$  must be multiplied by a factor of the square root of the inverse metric:  $\sqrt{g^{\mu\mu}} = [1, 1/p, 1/(p \sin \theta)]^\mu$  and similarly for tensors. In covariant notation, the divergence can be written elegantly as

$$\nabla_\mu V^\mu = \frac{1}{\sqrt{g}} \partial_\mu (\sqrt{g} V^\mu), \quad (\text{A } 3)$$

where  $\sqrt{g} = \sqrt{|\det(g_{\mu\nu})|} = p^2 \sin \theta$ , while the second-order differential operator in the Fokker–Planck terms requires Christoffel symbols  $\Gamma_{\mu\nu}^\rho = (1/2)g^{\rho\sigma}(\partial_\nu g_{\sigma\mu} + \partial_\mu g_{\sigma\nu} - \partial_\sigma g_{\mu\nu})$ , according to

$$\nabla_\nu T^{\mu\nu} = \partial_\nu T^{\mu\nu} + \Gamma_{\nu\rho}^\mu T^{\rho\nu} + \Gamma_{\nu\rho}^\nu T^{\mu\rho}. \quad (\text{A } 4)$$

Thus,

$$C^{ej} = \frac{1}{\sqrt{g}} \partial_\mu (\sqrt{g} V^\mu), \quad (\text{A } 5)$$

$$V^\mu = -f_e \langle \Delta p^\mu \rangle_{ej} + \frac{1}{2} [\partial_\nu (f_e \langle \Delta p^\mu \Delta p^\nu \rangle_{ej}) + \Gamma_{\nu\rho}^\mu (f_e \langle \Delta p^\rho \Delta p^\nu \rangle_{ej}) + \Gamma_{\nu\rho}^\nu f_e \langle \Delta p^\mu \Delta p^\rho \rangle_{ej}], \quad (\text{A } 6)$$

and  $\Gamma_{\mu\nu}^\rho$  has the following non-zero components:

$$\Gamma_{22}^1 = -p, \quad \Gamma_{33}^1 = -p \sin^2 \theta, \quad (\text{A } 7a,b)$$

$$\Gamma_{21}^2 = 1/p, \quad \Gamma_{33}^2 = -\cos \theta \sin \theta, \quad (\text{A } 8a,b)$$

$$\Gamma_{31}^3 = 1/p, \quad \Gamma_{32}^3 = \cot \theta. \quad (\text{A } 9a,b)$$

This yields

$$V^1 = - \left[ \langle \Delta p_L^1 \rangle_{ej} + \frac{1}{p} \langle \Delta p_L^2 \Delta p_L^2 \rangle_{ej} \right] f_e = 0, \quad (\text{A } 10)$$

$$V^2 = \frac{1}{2p^2} \langle \Delta p_L^2 \Delta p_L^2 \rangle_{ej} \partial_\theta f_e, \quad (\text{A } 11)$$

$$V^3 = \frac{1}{2p^2 \sin^2 \theta} \langle \Delta p_L^2 \Delta p_L^2 \rangle_{ej} \partial_\phi f_e. \quad (\text{A } 12)$$

## Appendix B. General properties of the screening function: high-energy behaviour

Utilizing the fact that  $F_j(q) \rightarrow 0$  for  $q \gg 1$  and  $F_j(q) \rightarrow N_{e,j}$  for  $q \ll 1$ , we can find a closed expression for  $g_j(p)$  in the limit of large  $y = 2p/\alpha = q/x$  which is then valid from mildly relativistic energies (if the transition from complete screening to full screening in the form factor is located around  $y \sim 1 \Leftrightarrow p \sim 10^{-2}$ ). The screening function is defined as

$$\begin{aligned} g_j(p) &= \int_{1/\Lambda}^1 [|Z_j - F_j(q)|^2 - Z_{0,j}^2] \frac{dx}{x} \\ &\approx \lim_{\Lambda \rightarrow \infty} \int_{y/\Lambda}^y \{2Z_j[N_{e,j} - F_j(q)] + F_j^2(q) - N_{e,j}^2\} \frac{dq}{q}. \end{aligned} \quad (\text{B } 1)$$

For simplicity, we normalize the radial coordinate to the Bohr radius  $a_0$  and the density such that  $N_{e,j} = 4\pi \int r^2 \rho_{e,j}(r) dr$ . The form factor (for a spherically averaged charge distribution) is then determined by

$$F_j(q) = 4\pi \int_0^\infty \rho_{e,j}(r) \frac{r}{q} \sin(qr) dr. \quad (\text{B } 2)$$

The first term of (B 1) can be simplified using partial integration, and extending the remaining integral to infinity:

$$\begin{aligned} I_{1,j} &\equiv 2Z_j \int_{y/\Lambda}^y [N_{e,j} - F_j(q)] \frac{dq}{q} \\ &= 2Z_j \left( [\ln q[N_{e,j} - F_j(q)]]_{y/\Lambda}^y - \int_0^\infty \ln q F'_j(q) dq \right). \end{aligned} \quad (\text{B } 3)$$

Note that if the atom has a spherically symmetric potential, the mean dipole moment ( $\propto \int d^3r \mathbf{r} n(\mathbf{r})$ ) vanishes (Landau & Lifshitz 1958), in which case the first derivative of the form factor vanishes identically for small arguments. Utilizing this fact for  $F(y/\Lambda \ll 1) = N_{e,j}$  and  $F_j(y \gg 1) = 0$ , we obtain

$$\begin{aligned} I_{1,j} &= 2Z_j N_{e,j} \ln y + 8Z_j \pi \int_0^\infty \rho_{e,j}(r) r^2 dr \underbrace{\int_0^\infty \frac{\ln q}{q} \left( \cos(qr) - \frac{\sin(qr)}{rq} \right) dq}_{=\gamma_E - 1 + \ln r} \\ &= 2Z_j N_{e,j} (\ln y - 1 + \gamma_E + \hat{I}_{1,j}), \end{aligned} \quad (\text{B } 4)$$

where we used  $4\pi \int r^2 \rho_{e,j}(r) dr = N_{e,j}$  and

$$\hat{I}_{1,j} \equiv \frac{4\pi}{N_{e,j}} \int_0^\infty \rho_{e,j}(r) r^2 \ln r dr. \quad (\text{B } 5)$$

Similarly, for the second term,

$$\begin{aligned} I_{2,j} &\equiv \int_{1/\Lambda}^1 \{F_j^2(q) - N_{e,j}^2\} \frac{dx}{x} \\ &= [\ln q [F_j(q)^2 - N_{e,j}^2]]_{y/\Lambda}^y - 2 \int_0^\infty \ln q F_j(q) F'_j(q) dq \end{aligned}$$

$$\begin{aligned}
&= -N_{e,j}^2 \ln y - (4\pi)^2 \int_0^\infty \rho_{e,j}(r) r^2 dr \int_0^\infty \rho_{e,j}(r_2) r_2^2 dr_2 \\
&\quad \times \int_0^\infty 2 \frac{\ln q \sin(qr_2)}{q qr_2} \left( \cos(qr) - \frac{\sin(qr)}{qr} \right) \\
&= -N_{e,j}^2 \ln y - (4\pi)^2 \int_0^\infty \rho_{e,j}(r) r^2 dr \int_0^\infty \rho_{e,j}(r_2) r_2^2 dr_2 \\
&\quad \times \left[ \gamma_E - \frac{3}{2} + \frac{(r+r_2)^2}{4rr_2} \ln(r+r_2) - \frac{(r-r_2)^2}{4rr_2} \ln|r-r_2| \right. \\
&\quad \left. + \frac{(r^2-r_2^2)}{4rr_2} \ln \left( \frac{r+r_2}{|r-r_2|} \right) [\ln(r^2-r_2^2) + 2(\gamma_E-1)] \right]. \quad (B 6)
\end{aligned}$$

In the integrand, the first term is straightforward to integrate with  $4\pi \int r^2 \rho_{e,j}(r) dr = N_{e,j}$ , while the last term must vanish upon integration since it is antisymmetric in  $r - r_2$ , leaving

$$I_{2,j} = -N_{e,j}^2 (\ln y - \frac{3}{2} + \gamma_E + \hat{I}_{2,j}), \quad (B 7)$$

where

$$\begin{aligned}
\hat{I}_{2,j} &\equiv \frac{(4\pi)^2}{4N_{e,j}^2} \int_0^\infty \int_0^\infty \rho_{e,j}(r) r \rho_{e,j}(r_2) r_2 [(r+r_2)^2 \ln(r+r_2) - (r-r_2)^2 \ln|r-r_2|] dr_2 dr \\
&= \frac{(4\pi)^2}{16N_{e,j}^2} \int_0^\infty ds \int_0^s dt (s^2 - t^2) \rho_{e,j} \left( \frac{s+t}{2} \right) \rho_{e,j} \left( \frac{s-t}{2} \right) [s^2 \ln s - t^2 \ln t]. \quad (B 8)
\end{aligned}$$

Adding the terms of (B 1) together yields (using  $2ZN_e - N_e^2 = Z^2 - Z_0^2$ )

$$\begin{aligned}
g_j(p) &= I_{1,j} + I_{2,j} \\
&= (Z_j^2 - Z_{0,j}^2) [\ln(2p/\alpha) - 1 + \gamma_E] + 2Z_j N_{e,j} \hat{I}_{1,j} + N_{e,j}^2 (\frac{1}{2} - \hat{I}_{2,j}). \quad (B 9)
\end{aligned}$$

Hence, the screening function  $g_j(p)$  grows logarithmically with momentum at high electron energies. This allows us to determine  $a_j$  so that the deflection frequency exactly matches the high-energy asymptote of the DFT results. Matching (B 9) with the high-energy asymptote of  $g_j(p)$  from (2.25),

$$g_j(p) \sim (Z_j^2 - Z_{0,j}^2) \ln(p\bar{a}_j) - \frac{2}{3} N_{e,j}^2, \quad p\bar{a}_j \gg 1, \quad (B 10)$$

we obtain

$$\bar{a}_j = \frac{2}{\alpha} \exp \left[ \gamma_E - 1 + \frac{2Z_j \hat{I}_{1,j} + N_{e,j}(7/6 - \hat{I}_{2,j})}{Z_j + Z_{0,j}} \right]. \quad (B 11)$$

The values of  $\bar{a}_j$  are given for many of the fusion-relevant ion species in table 1, of which the constants for argon and neon are illustrated in figure 2 as a function of  $Z_0$  in solid line.

### Appendix C. Partially screened avalanche-dominated runaway energy spectrum

We here generalize the derivation of the high electric field, avalanche-dominated distribution by Fülöp *et al.* (2006) to account for partially ionized impurities. In Fülöp *et al.* (2006), the kinetic equation is specialized to the case where  $E \gg E_c$ , which

gives a narrow pitch-angle distribution where the majority of the runaway electrons populate the region  $1 - \xi \ll 1$ , which is used as an expansion parameter. Note however, that assuming fast pitch-angle dynamics (Lehtinen *et al.* 1999; Aleynikov & Breizman 2015) is invalid when  $E \gg E_c^{\text{eff}}$ , where  $E_c^{\text{eff}}$  is the effective critical field (Hesslow *et al.* 2018).

Neglecting how the avalanche source term affects the shape of the distribution, we solve the coupled equations given by the avalanche growth rate (3.1) and the kinetic equation. In the kinetic equation, we utilize  $E \gg E_c^{\text{eff}}$  to replace the friction terms by  $E_c^{\text{eff}}$  in order to match the near-critical behaviour (Hesslow *et al.* 2018):

$$\begin{aligned} \tau_c \frac{\partial \bar{f}}{\partial t} = & \frac{\partial}{\partial p} \left[ \underbrace{\left( -\frac{\xi E}{E_c} + p v_s + F_{\text{br}} + \frac{p \gamma}{\tau_{\text{syn}}} (1 - \xi^2) \right) \bar{f}}_{\sim E_c^{\text{eff}}/E_c} \right] \\ & + \frac{\partial}{\partial \xi} \left[ (1 - \xi^2) \left( -\frac{1}{p} \frac{E}{E_c} \bar{f} + \frac{1}{2} v_D \frac{\partial \bar{f}}{\partial \xi} \right) - \underbrace{\frac{\xi (1 - \xi^2)}{\tau_{\text{syn}} \gamma} \bar{f}}_{\text{neglect}} \right]. \end{aligned} \quad (\text{C } 1)$$

Here,  $\bar{f} = p^2 f$ ,  $F_{\text{br}}$  describes bremsstrahlung losses and  $\tau_{\text{syn}}$  is a measure of the synchrotron losses. Assuming that the distribution is narrow,  $p_{\perp} \ll p_{\parallel} \simeq p$ , so that  $1 - \xi \ll 1$ , we integrate (C 1) over  $\xi$ . Together with (3.1), we obtain

$$\tau_c \Gamma(E) F + \frac{E - E_c^{\text{eff}}}{E_c} \frac{\partial F}{\partial p} = 0, \quad (\text{C } 2)$$

which has the solution

$$F(p, t) = n_{\text{RE}}(t) \frac{1}{p_0} e^{-p/p_0}, \quad (\text{C } 3)$$

where

$$p_0 = \frac{E - E_c^{\text{eff}}}{E_c \tau_c \Gamma(E)} = \frac{e}{m_e c} \frac{E - E_c^{\text{eff}}}{\Gamma(E)}. \quad (\text{C } 4)$$

Since  $\Gamma \propto E - E_c^{\text{eff}}$  for  $E/E_c^{\text{eff}} - 1 \ll 1$ , the term  $E_c^{\text{eff}}$  ensures that  $p_0 < \infty$  in the limit  $E \rightarrow E_c^{\text{eff}}$ . The average runaway momentum  $p_0$  can alternatively be interpreted as an average energy since  $p_0 \gg 1$  typically. Although  $p_0$  only depends on the effective charge in the fully ionized case, the average momentum acquires a significant  $E$ -dependence in the presence of partially screened ions, as shown in figure 5.

## REFERENCES

- ADAMO, C. & BARONE, V. 1999 Toward reliable density functional methods without adjustable parameters: the pbe0 model. *J. Chem. Phys.* **110** (13), 6158.
- AKAMA, H. 1970 Relativistic Boltzmann equation for plasmas. *J. Phys. Soc. Japan* **28**, 478.
- ALEYNIKOV, P. & BREIZMAN, B. N. 2015 Theory of two threshold fields for relativistic runaway electrons. *Phys. Rev. Lett.* **114**, 155001.
- ALEYNIKOV, P. & BREIZMAN, B. N. 2017 Generation of runaway electrons during the thermal quench in tokamaks. *Nucl. Fusion* **57** (4), 046009.
- BARYSZ, M. & SADLEJ, A. J. 2001 Two-component methods of relativistic quantum chemistry: from the Douglas–Kroll approximation to the exact two-component formalism. *J. Mol. Struct.: THEOCHEM* **573** (1), 181.

- BERGER, M., COURSEY, J., ZUCKER, M. & CHANG, J. 2005 ESTAR, PSTAR, and ASTAR: computer programs for calculating stopping-power and range tables for electrons, protons, and helium ions. <http://physics.nist.gov/Star>, [accessed: 2018, April 6].
- BERGER, M. J., INOKUTI, M., ANDERSON, H. H., BICHSEL, H., DENNIS, J. A., POWERS, D., SELTZER, S. M. & TURNER, J. E. 1984 4. Selection of mean excitation energies for elements. *J. Intl Commission Radiat. Units Measurements* **os19** (2), 22.
- BETHE, H. 1930 Zur theorie des durchgangs schneller korpuskularstrahlen durch materie. *Ann. Phys.* **397** (3), 325 (in German).
- BOOZER, A. H. 2015 Theory of runaway electrons in ITER: equations, important parameters, and implications for mitigation. *Phys. Plasmas* **22** (3), 032504.
- BRAAMS, B. J. & KARNEY, C. F. F. 1989 Conductivity of a relativistic plasma. *Phys. Fluids B* **1** (7), 1355.
- BREIZMAN, B. & ALEYNIKOV, P. 2017 Kinetics of relativistic runaway electrons. *Nucl. Fusion* **57** (12), 125002.
- CERCIGNANI, C. & KREMER, G. M. 2002 Relativistic Boltzmann equation. In *The Relativistic Boltzmann Equation: Theory and Applications*. Springer.
- CHIU, S., ROSENBLUTH, M., HARVEY, R. & CHAN, V. 1998 Fokker-Planck simulations mylb of knock-on electron runaway avalanche and bursts in tokamaks. *Nucl. Fusion* **38** (11), 1711.
- CONNOR, J. & HASTIE, R. 1975 Relativistic limitations on runaway electrons. *Nucl. Fusion* **15**, 415.
- DOUGLAS, M. & KROLL, N. M. 1974 Quantum electrodynamic corrections to the fine structure of helium. *Ann. Phys.* **82** (1), 89.
- DREICER, H. 1959 Electron and ion runaway in a fully ionized gas. I. *Phys. Rev.* **115**, 238.
- Dwyer, J. R. 2007 Relativistic breakdown in planetary atmospheres. *Phys. Plasmas* **14**, 042901.
- EMBRÉUS, O., STAHL, A. & FÜLÖP, T. 2018 On the relativistic large-angle electron collision operator for runaway avalanches in plasmas. *J. Plasma Phys.* **84** (1), 905840102.
- ERIKSSON, L.-G., HELANDER, P., ANDERSSON, F., ANDERSON, D. & LISAK, M. 2004 Current dynamics during disruptions in large tokamaks. *Phys. Rev. Lett.* **92**, 205004.
- FINKEN, K. H., WATKINS, J. G., RUSBÜLDT, D., CORBETT, W. J., DIPPEL, K. H., GOEBEL, D. M. & MOYER, R. A. 1990 Observation of infrared synchrotron radiation from tokamak runaway electrons in textor. *Nucl. Fusion* **30** (5), 859.
- FRISCH, M. J., TRUCKS, G. W., SCHLEGEL, H. B., SCUSERIA, G. E., ROBB, M. A., CHEESEMAN, J. R., SCALMANI, G., BARONE, V., PETERSSON, G. A., NAKATSUJI, H. et al. 2016 Gaussian 16 Revision B.01. Gaussian Inc. Wallingford CT.
- FÜLÖP, T., POKOL, G., HELANDER, P. & LISAK, M. 2006 Destabilization of magnetosonic-whistler waves by a relativistic runaway beam. *Phys. Plasmas* **13** (6), 062506.
- GULANS, A., KONTUR, S., MEISENBICHLER, C., NABOK, D., PAVONE, P., RIGAMONTI, S., SAGMEISTER, S., WERNER, U. & DRAXL, C. 2014 Exciting: a full-potential all-electron package implementing density-functional theory and many-body perturbation theory. *J. Phys.: Condens. Matter* **26** (36), 363202.
- HELANDER, P., ERIKSSON, L.-G. & ANDERSSON, F. 2002 Runaway acceleration during magnetic reconnection in tokamaks. *Plasma Phys. Control. Fusion* **44**, B247.
- HELANDER, P. & SIGMAR, D. 2005 *Collisional Transport in Magnetized Plasmas*. Cambridge University Press.
- HESS, B. A. 1986 Relativistic electronic-structure calculations employing a two-component no-pair formalism with external-field projection operators. *Phys. Rev. A* **33** (6), 3742.
- HESSLOW, L., EMBRÉUS, O., STAHL, A., DUBOIS, T. C., PAPP, G., NEWTON, S. L. & FÜLÖP, T. 2017 Effect of partially screened nuclei on fast-electron dynamics. *Phys. Rev. Lett.* **118**, 255001.
- HESSLOW, L., EMBRÉUS, O., WILKIE, G. J., PAPP, G. & FÜLÖP, T. 2018 Effect of partially ionized impurities and radiation on the effective critical electric field for runaway generation. *Plasma Phys. Control. Fusion* **60** (7), 074010.
- HOLLMANN, E. M., ALEYNIKOV, P. B., FÜLÖP, T., HUMPHREYS, D. A., IZZO, V. A., LEHNEN, M., LUKASH, V. E., PAPP, G., PAUTASSO, G., SAINT-LAURENT, F. et al. 2015 Status of research toward the iter disruption mitigation system. *Phys. Plasmas* **22** (2), 021802.

- HOPPE, M., EMBRÉUS, O., PAZ-SOLDAN, C., MOYER, R. & FÜLÖP, T. 2018a Interpretation of runaway electron synchrotron and bremsstrahlung images. *Nucl. Fusion* **58** (8), 082001.
- HOPPE, M., EMBRÉUS, O., TINGUELY, R., GRANETZ, R., STAHL, A. & FÜLÖP, T. 2018b SOFT: a synthetic synchrotron diagnostic for runaway electrons. *Nucl. Fusion* **58** (2), 026032.
- JACKSON, J. D. 1999 *Classical Electrodynamics*. Wiley.
- JAYAKUMAR, R., FLEISCHMANN, H. & ZWEBEN, S. 1993 Collisional avalanche exponentiation of runaway electrons in electrified plasmas. *Phys. Lett. A* **172**, 447–451.
- KIRILLOV, V. D., TRUBNIKOV, B. A. & TRUSHIN, S. A. 1975 Role of impurities in anomalous plasma resistance. *Sov. J. Plasma Phys.* **1**, 117.
- LANDAU, L. D. & LIFSHITZ, E. M. 1958 *Quantum Mechanics: Non-relativistic Theory*. Pergamon Press.
- LANDREMAN, M., STAHL, A. & FÜLÖP, T. 2014 Numerical calculation of the runaway electron distribution function and associated synchrotron emission. *Comput. Phys. Commun.* **185**, 847.
- LEHTINEN, N. G., BELL, T. F. & INAN, U. S. 1999 Monte Carlo simulation of runaway mev electron breakdown with application to red sprites and terrestrial gamma ray flashes. *J. Geophys. Res. Space Phys.* **104** (A11), 24699.
- MARTÍN-SOLÍS, J. R., LOARTE, A. & LEHNEN, M. 2015 Runaway electron dynamics in tokamak plasmas with high impurity content. *Phys. Plasmas* **22**, 092512.
- MOSHER, D. 1975 Interactions of relativistic electron beams with high atomic-number plasmas. *Phys. Fluids* **18**, 846.
- MOTT, N. F. & MASSEY, H. S. W. 1965 *The Theory of Atomic Collisions*, vol. 35. Clarendon Press.
- PARKS, P. B., ROSENBLUTH, M. N. & PUTVINSKI, S. V. 1999 Avalanche runaway growth rate from a momentum-space orbit analysis. *Phys. Plasmas* **6** (6), 2523.
- PUTVINSKI, S., FUJISAWA, N., POST, D., PUTVINSKAYA, N., ROSENBLUTH, M. & WESLEY, J. 1997 Impurity fueling to terminate tokamak discharges. *J. Nucl. Mater.* **241**, 316.
- REUX, C., PLYUSNIN, V., ALPER, B., ALVES, D., BAZYLEV, B., BELONOHY, E., BOBOC, A., BREZINSEK, S., COFFEY, I., DECKER, J. et al. 2015 Runaway electron beam generation and mitigation during disruptions at JET-ILW. *Nucl. Fusion* **55** (9), 093013.
- ROOS, B. O., LINDH, R., MALMQVIST, P.-Å., VERYAZOV, V. & WIDMARK, P.-O. 2004 Main group atoms and dimers studied with a new relativistic ano basis set. *J. Phys. Chem. A* **108** (15), 2851.
- ROOS, B. O., LINDH, R., MALMQVIST, P.-Å., VERYAZOV, V. & WIDMARK, P.-O. 2005 New relativistic ano basis sets for transition metal atoms. *J. Phys. Chem. A* **109** (29), 6575.
- ROSENBLUTH, M. & PUTVINSKI, S. 1997 Theory for avalanche of runaway electrons in tokamaks. *Nucl. Fusion* **37**, 1355–1362.
- ROSENBLUTH, M. N., MACDONALD, W. M. & JUDD, D. L. 1957 Fokker–Planck equation for an inverse-square force. *Phys. Rev.* **107**, 1.
- SAUER, S. P., ODDERSHEDE, J. & SABIN, J. R. 2015 Chapter three – the mean excitation energy of atomic ions. In *Concepts of Mathematical Physics in Chemistry: A Tribute to Frank E. Harris – Part A*, Advances in Quantum Chemistry, 71, p. 29. Academic Press.
- SMITH, H., HELANDER, P., ERIKSSON, L.-G., ANDERSON, D., LISAK, M. & ANDERSSON, F. 2006 Runaway electrons and the evolution of the plasma current in tokamak disruptions. *Phys. Plasmas* **13** (10), 102502.
- SOKOLOV, Y. 1979 ‘Multiplication’ of accelerated electrons in a tokamak. *JETP Lett.* **29**, 218–221.
- SOLODOV, A. A. & BETTI, R. 2008 Stopping power and range of energetic electrons in dense plasmas of fast-ignition fusion targets. *Phys. Plasmas* **15** (4), 042707.
- STAHL, A., EMBRÉUS, O., PAPP, G., LANDREMAN, M. & FÜLÖP, T. 2016 Kinetic modelling of runaway electrons in dynamic scenarios. *Nucl. Fusion* **56** (11), 112009.
- STAHL, A., LANDREMAN, M., PAPP, G., HOLLMANN, E. & FÜLÖP, T. 2013 Synchrotron radiation from a runaway electron distribution in tokamaks. *Phys. Plasmas* **20** (9), 093302.
- WESSON, J. 2011 *Tokamaks*, 4th edn. Oxford University Press.

- WIDMARK, P.-O., MALMQVIST, P.-Å. & ROOS, B. O. 1990 Density matrix averaged atomic natural orbital (ano) basis sets for correlated molecular wave functions. *Theor. Chim. Acta* **77** (5), 291.
- WILSON, C. T. R. 1925 The acceleration of  $\beta$ -particles in strong electric fields such as those of thunderclouds. *Math. Proc. Camb. Phil. Soc.* **22**, 534.
- ZHOGOLEV, V. & KONOVALOV, S. 2014 Characteristics of interaction of energetic electrons with heavy impurity ions in a tokamak plasma. *VANT or Problems of Atomic Sci. Tech. Series Thermonuclear Fusion* **37**, 71 (in Russian).

# Paper F

M. Hoppe, O. Embréus, R. A. Tinguely, R. S. Granetz, A. Stahl and T. Fülöp,

*SOFT: A synthetic synchrotron diagnostic for runaway electrons,*  
Nuclear Fusion **58**, 026032 (2018).

<https://doi.org/10.1088/1741-4326/aa9abb>  
arXiv:1709.00674 [physics.plasm-ph]

# SOFT: a synthetic synchrotron diagnostic for runaway electrons

M. Hoppe<sup>1</sup> , O. Embréus<sup>1</sup>, R.A. Tinguely<sup>2</sup> , R.S. Granetz<sup>2</sup>, A. Stahl<sup>1</sup> and T. Fülöp<sup>1</sup> 

<sup>1</sup> Department of Physics, Chalmers University of Technology, Göteborg, Sweden

<sup>2</sup> Plasma Science and Fusion Center, Massachusetts Institute of Technology, Cambridge, MA, United States of America

E-mail: [hoppe@chalmers.se](mailto:hoppe@chalmers.se)

Received 2 September 2017, revised 31 October 2017

Accepted for publication 13 November 2017

Published 9 January 2018



## Abstract

Improved understanding of the dynamics of runaway electrons can be obtained by measurement and interpretation of their synchrotron radiation emission. Models for synchrotron radiation emitted by relativistic electrons are well established, but the question of how various geometric effects—such as magnetic field inhomogeneity and camera placement— influence the synchrotron measurements and their interpretation remains open. In this paper we address this issue by simulating synchrotron images and spectra using the new synthetic synchrotron diagnostic tool SOFT (Synchrotron-detecting Orbit Following Toolkit). We identify the key parameters influencing the synchrotron radiation spot and present scans in those parameters. Using a runaway electron distribution function obtained by Fokker–Planck simulations for parameters from an Alcator C-Mod discharge, we demonstrate that the corresponding synchrotron image is well-reproduced by SOFT simulations, and we explain how it can be understood in terms of the parameter scans. Geometric effects are shown to significantly influence the synchrotron spectrum, and we show that inherent inconsistencies in a simple emission model (i.e. not modeling detection) can lead to incorrect interpretation of the images.

Keywords: runaway electron, synchrotron radiation, tokamak, synthetic diagnostic

(Some figures may appear in colour only in the online journal)

## 1. Introduction

Runaway acceleration of charged particles is one of the most interesting phenomena in plasmas. If the electric field exceeds a critical value, a fraction of particles can be detached from the bulk population and accelerated to relativistic energies [1]. Electrons are usually detached most easily and are then referred to as *runaway electrons*. In magnetic-fusion plasmas, runaway electrons can be generated during disruption events, in which a rapid cooling of the plasma takes place and a large electric field is induced in the toroidal direction in order to maintain the plasma current (which can be several megaamperes). A runaway-electron beam containing particles with energies of up to tens of MeV, carrying a significant fraction of the initial current, may form in such situations. If the density is sufficiently low, such a beam may also form during

start-up or flat-top operation. The potential for damage by such a localised beam of highly-energetic particles upon contact with the vessel wall is substantial, particularly in view of future large tokamaks, such as ITER, since the runaway generation rate increases exponentially [2] with the plasma current. This damage must be avoided or reduced using mitigation techniques [3] to make stable and reliable ITER operation possible. To this end, many dedicated experiments are performed on a number of existing tokamaks to study the dynamics of relativistic runaway-electron beams in both quiescent and disruptive plasmas.

One of the primary methods to experimentally diagnose runaway beams is to study the synchrotron radiation they emit. Synchrotron radiation is emitted by relativistic electrons as a consequence of their gyro motion and is an attractive means of diagnosing the runaways since it does not require

them to leave the plasma. In this paper we analyze the effects of geometry and the spatial distribution of runaway synchrotron radiation on synchrotron radiation images, which in typical runaway scenarios are experimentally observed in the visible and infra-red spectral ranges. The pioneering measurements of synchrotron radiation from runaway electrons were made already in the 1990's [4, 5] and since then such measurements have become a routine diagnostic used in many tokamaks around the world, including TEXTOR [6, 7], FTU [8, 9], Alcator C-Mod [10], ASDEX Upgrade [11], TCV [11], COMPASS [12] DIII-D [13], EAST [14], and KSTAR [15].

Although many observations of synchrotron radiation emitted by runaway electrons exist, obtaining useful information about the spatial and velocity distributions of the runaways requires careful interpretation of the diagnostics, which provide primarily line- and volume-integrated information (i.e. a camera photographing the plasma). In particular, modeling the synchrotron emission as coming from particles with a single energy and pitch angle is insufficient and can be misleading. Further complications are introduced by the geometry of the problem (in particular the twist of the magnetic field lines and the relativistic forward beaming of the synchrotron radiation); the pitch-angle, energy and radial distributions of runaway electrons; and the position and sensitivity of the camera. Theoretical descriptions of the relation between runaway and plasma parameters and the extent of the observed radiation spot have been considered previously [14, 16–18], however, with the exception of [18], these studies did not consider the synchrotron intensity distribution in the images (only the overall spot shape), and did not include effects of the velocity-space distribution of the runaway population.

Recently, a new synthetic synchrotron diagnostic taking full-orbit effects into account was presented in [18], where synchrotron images and spectra were also calculated and discussed with respect to the full-orbit effects. In contrast to [18], we derive a rigorous synthetic diagnostic theory expressed in terms of guiding-center quantities to reduce the numerical complexity of the problem. Using the simplified model we also analyze and discuss synchrotron images in terms of properties of the distribution function and detector.

The aim of the present paper is to analyze the synchrotron image and spectrum obtained from a population of relativistic electrons—with arbitrary spatial and velocity-space distributions—in an arbitrary tokamak magnetic geometry using the synthetic synchrotron diagnostic SOFT (Synchrotron-detecting Orbit Following Toolkit) [19, 20]. In section 2, the underlying theory used in the simulations is presented using a number of physically motivated approximations to reduce the computational cost of the problem. In section 3, a thorough investigation of the parameters that influence the final image is performed. The tool will also be used to analyze a specific image of synchrotron emission from a runaway beam, obtained in the Alcator C-Mod tokamak (section 4).

## 2. Synthetic synchrotron diagnostics

The basic idea of simulating the synchrotron radiation from runaway electrons is simple: place a detector in the tokamak,

follow a large number of particle trajectories in space, and at each point of space compute their contribution to the synchrotron image based on the particles' velocities at that point. In this section we will discuss the mathematical theory of this scheme. The angular and spectral distributions of synchrotron radiation will be introduced and discussed briefly, followed by a discussion of how a synchrotron image can be interpreted. In the discussion we will consider an ideal detector, i.e. we will assume that the detector has a uniform response function in a given spectral interval and directly measures the electromagnetic energy flux reaching the aperture.

### 2.1. Theory of synchrotron detectors

The radiated power detected at time  $t$  in the wavelength interval between  $\lambda$  and  $\lambda + d\lambda$  per unit surface area  $dA$  of a detector, per unit solid angle  $d\Omega_n$  centered on the vector  $\mathbf{n}$  by the observer, located at  $\mathbf{x}_0$ , is

$$\frac{d^3 P_0(\mathbf{x}_0, \mathbf{n}, \lambda, t)}{d\lambda dA d\Omega_n} = \int \delta^2(\mathbf{r}/r - \mathbf{n}) \frac{\mathbf{n} \cdot \hat{\mathbf{n}}}{r^2} \frac{d^2 P(\mathbf{x}, \mathbf{p}, \mathbf{x}_0, \lambda)}{d\lambda d\Omega} \times f(\mathbf{x}, \mathbf{p}, t - r/c) d\mathbf{x} d\mathbf{p}, \quad (1)$$

where  $f$  is the particle distribution function,  $\mathbf{x}$  is the particle's position,  $\mathbf{p} = m\mathbf{v}/\sqrt{1 - \beta^2}$  is the momentum,  $m$  is the particle's rest mass,  $\beta = |\mathbf{v}|/c$  is the particle's speed normalized to the speed of light in vacuum  $c$ ,  $d^3 P/d\lambda dA d\Omega_n$  is the emitted power per unit wavelength interval and solid angle [21, 22],  $\mathbf{r} = \mathbf{x} - \mathbf{x}_0$  is the relative position between particle and detector,  $\theta_p$  is the particle's pitch angle,  $\mu$  is the angle between the magnetic field and  $\mathbf{n}$  and  $\hat{\mathbf{n}}$  is the direction in which the detector is facing (i.e. the unit normal vector of the camera lens). The delta function singles out the radiation travelling along the specified line-of-sight  $\mathbf{n}$ , and  $d\Omega = \frac{\mathbf{n} \cdot \hat{\mathbf{n}}}{r^2} dA$  relates the solid angle element to detector surface area element.

Equation (1) describes the radiation reaching a point on the detector along a direction  $\mathbf{n}$  at a time  $t$  from all points in phase-space. The contribution to an individual pixel of the 2D grid of pixels making up the synchrotron image, which we label by the indices  $(i, j)$ , in a small wavelength interval  $d\lambda$ , is obtained by integrating over the finite surface of the detector and all lines-of-sight within the region  $N_{ij}$  corresponding to pixel  $(i, j)$ :

$$\frac{dI_{ij}}{d\lambda}(\mathbf{x}_0, t) = \int_A \int_{N_{ij}} \frac{d^3 P_0(\mathbf{x}_0, \mathbf{n}, \lambda, t)}{d\lambda dA d\Omega_n} dA d\Omega_n, \quad (2)$$

where  $A$  denotes the detector surface.

According to Liouville's theorem, the distribution function is constant along particle orbits when the system evolves slowly in time compared to the orbital time scale. Therefore, the distribution need only be specified at a single point along each orbit, from which it can be determined at all other points by integrating the equations of motion. By utilizing a particular orbit-coordinate set which we describe below (similar to the set introduced in [24]), we can describe the radiation from any distribution function in terms of a reduced 3D phase space.

The first coordinate transformation is a standard, zeroth-order, guiding-center transformation [25, 26], as it is

numerically more efficient to solve for the guiding-center orbit rather than a full particle orbit. We let  $\mathbf{X}$  denote the guiding-center position,  $p_{\parallel}$  the particle momentum parallel to the magnetic field,  $p_{\perp}$  the magnitude of the particle momentum perpendicular to the magnetic field, and  $\zeta$  the gyrophase of the particle. To zeroth order, the Jacobian for the spatial transformation is unity while for the momentum transformation it is just  $p_{\perp}$ , and we get

$$d\mathbf{x}dp \approx p_{\perp} d\mathbf{X} dp_{\parallel} dp_{\perp} d\zeta = |J_p| p_{\perp}^{(0)} d\mathbf{X} dp_{\parallel}^{(0)} dp_{\perp}^{(0)} d\zeta, \quad (3)$$

where  $\mathbf{p}^{(0)}$  is the particle momentum evaluated at any point  $\mathbf{X}^{(0)}$  along its orbit, and where the conservation of magnetic moment  $\mu = p_{\perp}^2/2m_e B$  yields a Jacobian

$$|J_p| = \frac{B(\mathbf{X})}{B(\mathbf{X}^{(0)})} \frac{|p_{\parallel}^{(0)}|}{\sqrt{(p_{\parallel}^{(0)})^2 - (p_{\perp}^{(0)})^2 \frac{B(\mathbf{X})}{B(\mathbf{X}^{(0)})}}}. \quad (4)$$

The use of guiding-center coordinates simplifies the computation since the integral over  $\zeta$  can be carried out explicitly, putting the integrand in (1) in a gyro-averaged form. In the limit of small gyro-radius, the vector  $\mathbf{r}$  will be independent of  $\zeta$ , allowing the delta function and geometrical factor  $\mathbf{n} \cdot \hat{\mathbf{n}}/r^2$  to be taken out of the  $\zeta$ -integral. Because of gyrotropy, the distribution function will be independent of the gyrophase  $\zeta$  and so can also be moved out of the  $\zeta$ -integral. The only factor for which a gyrophase dependence must remain is in the spectral power  $d^2P/d\lambda d\Omega$ , and as we will see later, the synchrotron power formulas can be analytically averaged over a gyro-period, allowing us to completely eliminate the gyrophase  $\zeta$  from the integral.

Secondly, we make a standard cylindrical coordinate transformation,  $(R, Z, \phi)$ , with  $R$  the radial distance to the particle from the axis-of-symmetry,  $Z$  the vertical offset of the particle from the midplane and  $\phi$  the toroidal angle. The spatial differential element  $d\mathbf{X}$  of (3) then becomes

$$d\mathbf{X} = R dR dZ d\phi. \quad (5)$$

So far we have only expressed the integral in terms of guiding-center coordinates, but we have still not fully taken the geometry of the magnetic field into account. Since the tokamak is an axisymmetric device, the equations of motion determine the guiding-center distribution in the poloidal plane, and because of toroidal symmetry the distribution will be identical in every such plane. In the third and final coordinate transformation we therefore change the poloidal guiding-center coordinates  $R$  and  $Z$  to the poloidal ‘trajectory coordinates’  $\rho$  and  $\tau$ . The coordinate  $\rho$  is the major radius at which the guiding-center is located at the start of its orbit (i.e. in the outer midplane), while  $\tau$  is the ‘orbit time’, defined such that  $\tau = 0$  corresponds to the outer midplane and  $\tau = \tau_0$  the point in the poloidal plane which it would take a time  $\tau_0$  for the guiding-center to reach, if starting in the midplane. The coordinate  $\tau$  can also be thought of as an alternative poloidal angle that takes the magnetic field geometry into account. The determinant of the Jacobian for this transformation depends

on the particular magnetic field used, and to allow for any (numerical) magnetic field to be used we will write the differential element as

$$dR dZ = |J| d\rho d\tau, \quad |J| = \left| \frac{\partial R}{\partial \rho} \frac{\partial Z}{\partial \tau} - \frac{\partial R}{\partial \tau} \frac{\partial Z}{\partial \rho} \right| \quad (6)$$

Equation (1) can now be cast into its final form,

$$\frac{d^3 P_0(\mathbf{x}_0, \mathbf{n}, \lambda, t)}{d\lambda d\Omega d\Omega_n} = \int d\rho dp_{\parallel}^{(0)} dp_{\perp}^{(0)} p_{\perp}^{(0)} f_{gc}(\rho, p_{\parallel}^{(0)}, p_{\perp}^{(0)}, t) \times d\phi d\tau |J_p| |J| R(\rho, \tau) \frac{\mathbf{n} \cdot \hat{\mathbf{n}}}{r^2} \delta^2(\mathbf{r}/r - \mathbf{n}) \left\langle \frac{d^2 P(\mathbf{X}, p_{\parallel}, p_{\perp}, \zeta, \lambda)}{d\lambda d\Omega} \right\rangle, \quad (7)$$

where the distribution of guiding-centers  $f_{gc}(\mathbf{X}, p_{\parallel}, p_{\perp}, t) \approx 2\pi f(\mathbf{x}, p_{\parallel}, p_{\perp}, t - r/c)$ ,  $\mathbf{p}^{(0)}$  denotes the guiding-center momentum at  $\tau = 0$  and the gyro-average  $\langle \dots \rangle$  of a quantity  $F = F(\zeta)$  is defined as

$$\langle F \rangle = \frac{1}{2\pi} \int_0^{2\pi} F(\zeta) d\zeta. \quad (8)$$

Given the distribution of guiding-centers  $f_{gc}$  in the outer midplane, i.e. at  $\tau = 0$ , the integral over  $\tau$  in (7) can be evaluated by solving the guiding-center equations of motion as an initial value problem in a set of points  $\{\tau_n\}$ , in order to obtain  $\mathbf{X}(\rho, \tau, \phi)$ ,  $p_{\parallel}(\rho, \tau, \phi)$  and  $p_{\perp}(\rho, \tau, \phi)$  at those points. Standard methods for solving the guiding-center equations of motion can therefore be applied—SOFT uses the familiar RKF45 scheme [27]—making the numerical solver very flexible when it comes to taking the magnetic field geometry of the simulated device into account.

A feature of equation (7) that can simplify computations is the fact that the integrand can be separated into one part consisting of the distribution function, and one part representing various geometric and emission effects, which we denote by  $\hat{I}_{ij}(\rho, p_{\parallel}^{(0)}, p_{\perp}^{(0)})$ :

$$I_{ij} = \int d\rho dp_{\parallel}^{(0)} dp_{\perp}^{(0)} f_{gc}(\rho, p_{\parallel}^{(0)}, p_{\perp}^{(0)}) \hat{I}_{ij}(\rho, p_{\parallel}^{(0)}, p_{\perp}^{(0)}). \quad (9)$$

By pre-computing and tabulating  $\hat{I}_{ij}$ , we may generate images or spectra by integrating over  $(\rho, p_{\parallel}^{(0)}, p_{\perp}^{(0)})$ , which reduces to a set of multiplications. For a particular detector setup and magnetic field configuration,  $\hat{I}_{ij}$  can be generated and used to quickly produce synthetic synchrotron data.

The model in (7) has the advantage of only assuming that the plasma is optically thin to the radiation, so while our studies are focused toward the synchrotron radiation emitted by runaway electrons, one could in principle use the same approach to simulate other types of radiation emitted by charged particle species in an axisymmetric plasma.

## 2.2. Expressions for the angular and frequency distributions of the radiation power

Synchrotron radiation is emitted almost entirely in the particle’s direction of motion, and the spectrum is practically a continuum in the IR or visible spectral ranges in scenarios relevant to magnetic fusion. The most general description of the

radiation received by a detector from a relativistic electron in helical motion in a homogeneous magnetic field is [28, 29]

$$\left\langle \frac{d^2P}{d\lambda d\Omega} \right\rangle = \frac{9e^2\beta^2\gamma^{12}\omega_B^3}{256\pi^3\epsilon_0 c^2\gamma_{\parallel}^2} \left( \frac{\lambda_c}{\lambda} \right)^4 \left( \frac{1 - \beta \cos \psi}{\beta \cos \psi} \right)^2 \times (1 - \beta \cos \theta_p \cos \mu) \left[ K_{2/3}^2(\xi) + \frac{(\beta/2) \cos \psi \sin^2 \psi}{1 - \beta \cos \psi} K_{1/3}^2(\xi) \right]. \quad (10)$$

Here,  $\langle \dots \rangle$  denotes a gyro-average as defined in (8),  $e$  is the elementary charge,  $\epsilon_0$  is the vacuum permittivity,  $m_e$  is the electron rest mass,  $\gamma = (1 - \beta^2)^{-1/2}$  and  $\gamma_{\parallel} = (1 - \beta_{\parallel}^2)^{-1/2}$ , where  $\beta_{\parallel}$  is the electron speed parallel to the magnetic field normalized to the speed of light,  $\omega_B = eB/\gamma m_e$  is the electron cyclotron frequency, and  $B$  is the magnetic field strength. The angle  $\psi$  is defined through the angle  $\mu$  between the velocity vector of the guiding-center and the observer's line-of-sight as  $\psi = \mu - \theta_p$ , where  $\theta_p = \arccos(v_{\parallel}/v)$  is the pitch angle. The functions  $K_{1/3}(\xi)$  and  $K_{2/3}(\xi)$  are modified Bessel functions, and their arguments are

$$\xi = \gamma^3 \frac{\lambda_c}{\lambda} \sqrt{\frac{(1 - \beta \cos \psi)^3}{(\beta/2) \cos \psi}}, \quad (11)$$

with  $\lambda_c = 4\pi m_e c \gamma_{\parallel} / 3\gamma^2 e B$  the critical wavelength, approximately corresponding to the peak of emission. The factor  $1 - \beta \cos \theta_p \cos \mu$  compensates for the difference between the observed and actual particle distribution, due to the finite speed of light [22] (effectively compensating for the apparent superluminal motion of relativistic particles approaching an observer, otherwise commonly associated with observation of relativistic jets from [23]).

Similar gyro-averaged expressions for the angular or spectral distributions of synchrotron radiation can be computed and are found to be [19]

$$\left\langle \frac{dP}{d\Omega} \right\rangle = \frac{e^4 B^2 \beta_{\perp}^2 \gamma_{\parallel}^2}{16\pi^2 \epsilon_0 \gamma^2 m_e^2 c} (1 - \beta \cos \theta_p \cos \mu) \left[ \frac{\kappa^3}{2} (3\eta^2 - 1) - \left( \frac{\sin \mu}{\gamma} \right)^2 \frac{\kappa^5}{8} (5\eta^2 - 1) \right], \quad (12)$$

and [28]

$$\left\langle \frac{dP}{d\lambda} \right\rangle = \frac{1}{\sqrt{3}} \frac{ce^2}{\epsilon_0 \lambda^3 \gamma^2} (1 - \beta \cos \theta_p \cos \mu) \int_{\lambda_c/\lambda}^{\infty} K_{5/3}(l) dl, \quad (13)$$

where  $\beta_{\perp}$  is the electron speed perpendicular to the magnetic field, and

$$\eta = \left[ 1 - \left( \frac{\beta \sin \mu \sin \theta_p}{1 - \beta \cos \mu \cos \theta_p} \right)^2 \right]^{-1/2}, \quad (14)$$

$$\kappa = \{(1 - \beta \cos \psi) [1 - \beta \cos(\psi + 2\theta_p)]\}^{-1/2}. \quad (15)$$

By integrating over all angular and spectral dependences in either of the formulas (10), (12) or (13), one obtains the total power received from an electron in helical motion as

$$P = \frac{e^4 B^2 \gamma^2 \gamma_{\parallel}^2}{6\pi \epsilon_0 m_e^2 c} \beta_{\perp}^2 (1 - \beta \cos \theta_p \cos \mu). \quad (16)$$

A number of properties of synchrotron radiation are interesting to note from these formulas. It can be shown that the angular width of the emitted radiation scales as

$$\psi_c = \frac{1}{\gamma} \left( \frac{2\lambda}{\lambda_c} \right)^{1/3}, \quad \lambda \gg \lambda_c, \quad (17)$$

$$\psi_c = \frac{1}{\gamma} \sqrt{\frac{2\lambda}{3\lambda_c}}, \quad \lambda \ll \lambda_c, \quad (18)$$

in the high and low wavelength limits, respectively. On average, the angular width of the emitted radiation scales as  $\psi_c \sim \gamma^{-1}$ , as is realized from the shaping factor  $(1 - \beta \cos \psi) \approx \frac{1}{2}(\gamma^{-2} + \psi^2)$  of (12). For a highly relativistic electron ( $\gamma \gg 1$ ), essentially all synchrotron radiation will be emitted in a very small angular interval around  $\psi = 0$ , and thus almost entirely in the particle's forward direction. In the guiding-center picture, this corresponds to a cone with opening angle  $\theta_p$  and lateral width  $\sim \gamma^{-1}$  being emitted around the guiding-center. This strong forward-beaming of synchrotron radiation, in combination with the fact that all runaways move in the same direction around the tokamak, also has the consequence that synchrotron radiation from runaway electrons is only detected on one side of the tokamak. This asymmetry in the detected synchrotron radiation between both sides of the tokamak is often used to confirm the presence of runaway electrons in an experiment.

Another interesting property of synchrotron radiation is that its spectrum consists of many closely spaced spectral lines near the peak wavelength  $\lambda_c$  and so is well described as a continuum by (13). Analyzing its asymptotic expressions reveals that the emitted power per wavelength decreases exponentially to short wavelengths ( $\lambda \ll \lambda_c$ ) and at a slower  $\lambda^{-2/3}$  rate to longer wavelengths.

Most of the synchrotron radiation will be emitted at wavelengths near  $\lambda = \lambda_c \sim 1/(\gamma B \sin \theta_p)$ . We thus see that the spectrum peak can be pushed towards shorter wavelengths in three different ways, namely by either increasing the particle energy, pitch angle or the magnetic field strength. During the transit of an electron in a tokamak, the particle energy will remain constant<sup>3</sup>, but both the magnetic field and pitch-angle will increase when the particle approaches the inboard side of the device. As such, the peak of the particle's synchrotron spectrum will vary during the course of an orbit, which will be demonstrated in section 3.5, and depending on where the spectrum peak  $\lambda_c$  is located relative to the visible spectral range of the camera, significantly different contributions of synchrotron radiation from the inboard and outboard sides of the device may be obtained.

### 2.3. Quantitative descriptions of synchrotron spots

While the theory presented so far can be used to study many aspects of synchrotron radiation from runaway electrons, this paper will focus mainly on synchrotron images and to some

<sup>3</sup>On the transit timescale, in which we are interested, both collisions and radiation losses are negligible.

extent also synchrotron spectra. The spots of synchrotron radiation observed in synchrotron images can take on many different shapes, and as was shown in [14] (and will be further demonstrated in section 3) the observed spot shape is strongly dependent on the placement of the synchrotron camera. In the literature, elliptical synchrotron spots appear to be the most common [4, 7, 13, 30, 31]; however, as is exemplified in sections 3 and 4, synchrotron spots in Alcator C-Mod tend to take on more crescent-like shapes. Our simulations suggest this is a combined effect due to camera placement and the fairly small pitch angles of the runaways, as will be discussed in section 3.1.

To gain a better understanding for how different synchrotron spot shapes arise, and to derive a computationally more efficient model of synchrotron radiation, we can use the strong beaming of synchrotron radiation into a cone of width  $\sim \gamma^{-1}$ . We let

$$\frac{d^2P}{d\lambda d\Omega} = \frac{1}{2\pi} \left\langle \frac{dP}{d\lambda} \right\rangle \delta(1 - \cos \alpha), \quad (19)$$

where  $\alpha$  is the angle between the particle's velocity vector and the observer direction. In terms of the angle  $\mu$  between the guiding-center velocity and observer direction, as well as pitch angle  $\theta_p$  and gyrophase  $\zeta$ , we can write  $\cos \alpha = \cos \mu \cos \theta_p + \sin \mu \sin \theta_p \cos \zeta$ . Representing the delta function in terms of Legendre polynomials  $P_l(x)$ , and utilizing the addition theorem for spherical harmonics, this implies

$$\begin{aligned} \frac{d^2P}{d\lambda d\Omega} = & \frac{1}{2\pi} \frac{dP}{d\lambda} \sum_{l=0}^{\infty} \frac{2l+1}{2} \left[ P_l(\cos \mu) P_l(\cos \theta_p) \right. \\ & \left. + 2 \sum_{m=1}^l \frac{(-1)^m (l-m)!}{(l+m)!} P_l^m(\cos \mu) P_l^m(\cos \theta_p) \cos m\zeta \right]. \end{aligned} \quad (20)$$

The gyro-average of this expression eliminates the sum over  $m$ , resulting in

$$\left\langle \frac{d^2P}{d\lambda d\Omega} \right\rangle = \frac{1}{2\pi} \frac{dP}{d\lambda} \delta(\cos \mu - \cos \theta_p). \quad (21)$$

This motivates the idea that the electron guiding-center emits synchrotron radiation in a cone of opening angle  $\theta_p$  around its direction of motion and gives a simple expression for the integral over the detector surface in (2). This simplified model of synchrotron radiation, which we call the *cone model*, has also been implemented in SOFT, and as will be demonstrated in the next section, shows good agreement with the full models. The model also brings computational benefits, and in typical runs it is commonly faster than the full models by a factor between 2–100<sup>4</sup>.

Aside from being a useful computational tool, the cone model provides insight into how to interpret the synchrotron spot observed in images. To zeroth order in the guiding-center approximation,  $\cos \mu = \mathbf{V} \cdot \mathbf{r} / Vr = \hat{\mathbf{b}} \cdot \mathbf{r} / r$ , where  $\mathbf{V} = V\hat{\mathbf{b}}$  is the guiding-center velocity and  $\mathbf{r}$  is the vector between the

<sup>4</sup>The large variation in time differences between the models is due to that the cone model allows a much stricter sorting algorithm to be employed, which efficiently excludes particles that cannot be detected. The different models therefore scale differently with resolution parameters.

detector and the guiding-center. For a guiding-center to emit towards the detector (which we temporarily consider to be a point), the equation

$$|\hat{\mathbf{b}} \cdot \mathbf{r} / r| = |\cos \theta_p|, \quad (22)$$

must therefore be satisfied. The solution to this equation is a surface in 3D space, which we will refer to as the *surface-of-visibility*, and its shape strongly depends on the detector position. In Alcator C-Mod, for pitch angles around 0.10–0.20 rad, it resembles a saddle or potato chip.

### 3. Elements and dependencies of the synchrotron image

Due to the strong dependence on energy, pitch-angle and particle location in both the synthetic detector equation (7) and synchrotron formulas (10), (12) and (13), we expect the synchrotron image observed by a camera to similarly depend strongly on these parameters. In this section we will vary a number of key parameters in order to illustrate the effect they have on the synchrotron spot. Specifically, we will use a set of mono-energetic and mono-pitch-angle distributions to study the effects of particle energy, pitch angle, radial distribution and camera vertical position. With the intent of applying the knowledge gained in this section to a more complete and realistic scenario in section 4, we use Alcator C-Mod parameters from discharge 1140403026 ( $t \sim 0.742$  s) in these parameter scans. The magnetic topology used is shown in figure 1(a) and unless otherwise noted, the synchrotron camera is located at major radius  $R \approx 107$  cm and  $\sim 20$  cm below the midplane, reflecting its actual position in the device. Figure 1(b) shows a typical synthetic Alcator C-Mod synchrotron image with flux surfaces and the wall cross-section superimposed, while figure 1(c) shows a top view of the tokamak, indicating the spatial extent of the synchrotron emission. Note, that the line-integration is in the vertical direction in the top view, which results in two separate bright features. The white line crossing the synchrotron spot in figure 1(c) is the plane orthogonal to the camera viewing direction (indicated by the red arrow), which is also the plane used for projecting the overlays in figure 1(b).

Unless otherwise stated, all particles in the following analysis are initiated in a radial interval spanning from the magnetic axis (located at major radius  $R = 68$  cm in the magnetic equilibrium used) and 16 cm outwards on the outboard side, so that the outermost particle considered is launched at  $R = 84$  cm. We will also separate the radial dependence from the overall distribution function so that the total distribution function can be written  $f(\rho, p_{\parallel}^{(0)}, p_{\perp}^{(0)}) = f_r(\rho) f_p(p_{\parallel}^{(0)}, p_{\perp}^{(0)})$ , where  $f_r(\rho)$  is the radial profile and  $f_p$  is the momentum-space distribution function. Particles are given an initial energy of  $E^{(0)} = 30$  MeV and pitch angle  $\theta_p^{(0)} = 0.15$  rad (i.e.  $f_p(E^{(0)}, \theta_p^{(0)}) = \delta(E^{(0)} - 30 \text{ MeV}) \delta[\cos \theta_p^{(0)} - \cos(0.15)]$ ), consistent with estimates made for runaways observed in Alcator C-Mod [10], and a uniform radial profile is used ( $f_r(\rho) = 1$

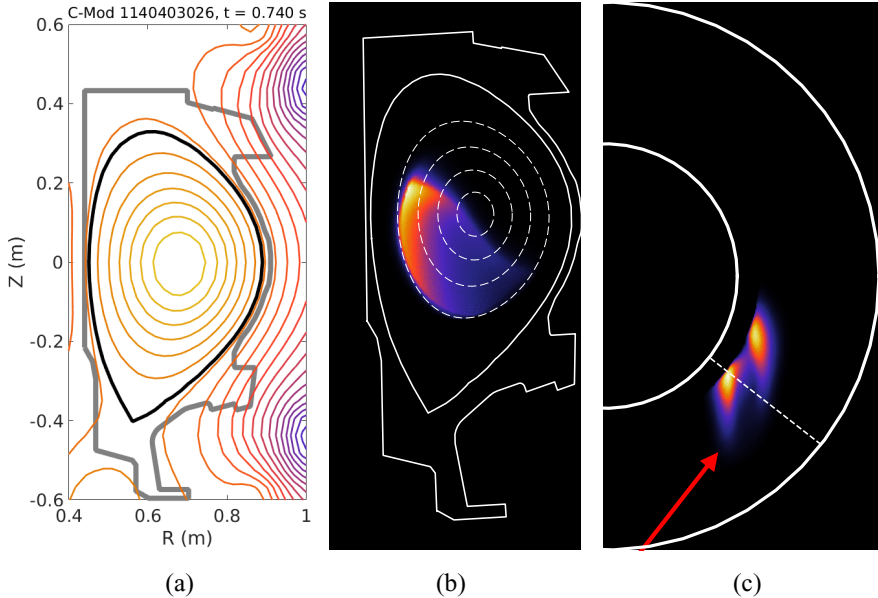


**Figure 1.** (a) Poloidal magnetic flux contours from EFIT [32] are shown on a poloidal cross-section of the Alcator C-Mod tokamak. The vacuum vessel wall is bolded grey and the plasma boundary bolded black. (b) Example of a synthetic synchrotron image with flux contours and vessel wall superimposed. (c) Top view of the tokamak, showing the spatial origin of the (synthetic) radiation. The white line crossing the synchrotron spot indicates the plane orthogonal to the camera viewing direction (red arrow), which is used as the projection plane in (b).

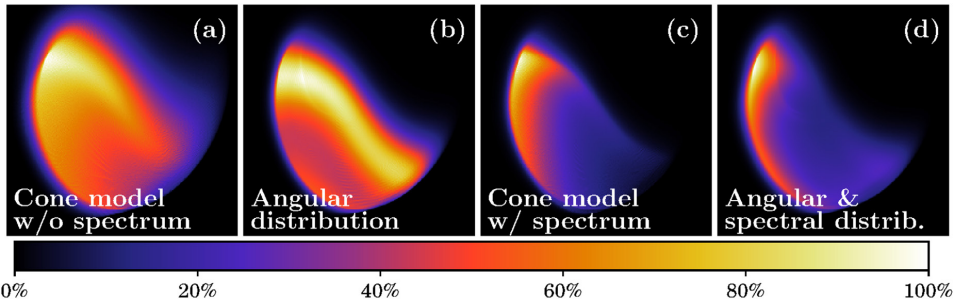


**Figure 2.** Comparison of synchrotron images using different emission models implemented in SOFT. The energies and pitch angles of particles are determined by a simulated distribution function, to be described in more detail in section 4.2, and launched on the radial interval  $r \in [68, 84]$  cm. Figure (a) was generated using the cone model by recording the radiation at all wavelengths. Figure (b) takes the angular distribution of radiation equation (12) into account, assumes the radiation to be emitted uniformly across all wavelengths, and records radiation at all wavelengths. Figure (c) shows the result of using the cone model but only registering radiation emitted at wavelengths between 500–1000 nm. Figure (d) takes the full angular and spectral distribution (10) into account, and only records radiation received at wavelengths between 500–1000 nm. The colors in the figures represent the intensity detected by the camera, normalized to the most intense pixel of each image.

for  $R < 84$  cm and zero otherwise). Only radiation emitted at wavelengths between  $\lambda = 500$  nm and  $\lambda = 1000$  nm is seen by the detector. The current runs in the counter-clockwise direction (when looking down on the tokamak from above), so that due to the strong forward-beaming of the synchrotron radiation, emission will only be seen on the right side of the tokamak. In most of the images to be presented, the camera will be zoomed in on the synchrotron spot, and the high-field side will be on the left side of the image.

### 3.1. Comparison of synchrotron images using different emission models

Figure 2 shows SOFT output generated using each of the radiation models discussed in section 2.2, simulated with the numerical distribution of runaway electrons to be described in section 4.2. Figures 2(a) and (c) were generated using the approximate cone model equation (21), with figure 2(c) taking the limited spectral range of the camera into account. Figures 2(b) and (d) take the full angular distribution of

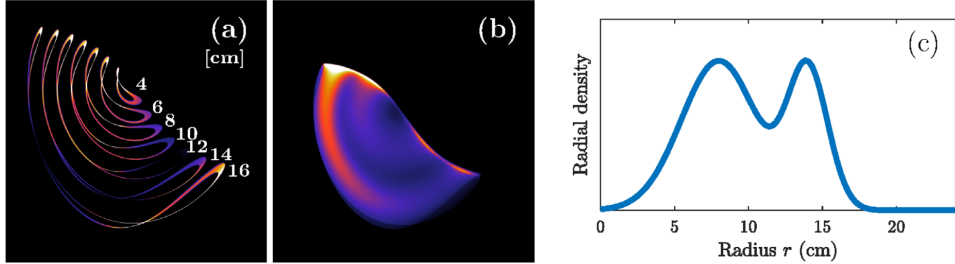


**Figure 3.** Radiation emission from particles launched at different radii. Figure (a) shows the result of launching particles from a set of eight uniformly spaced points from the magnetic axis ( $R = 68$  cm) and 16 cm outwards ( $R = 84$  cm). Contributions from the particles closest to the magnetic axis are not visible to the camera due to its vertical displacement. The numbers denote the distance, in cm, from the magnetic axis at which the particles were launched. In figure (b) the radial profile shown in figure (c), consisting of two Gaussian functions, was used to illustrate the effect of having a non-uniform spatial distribution of particles.

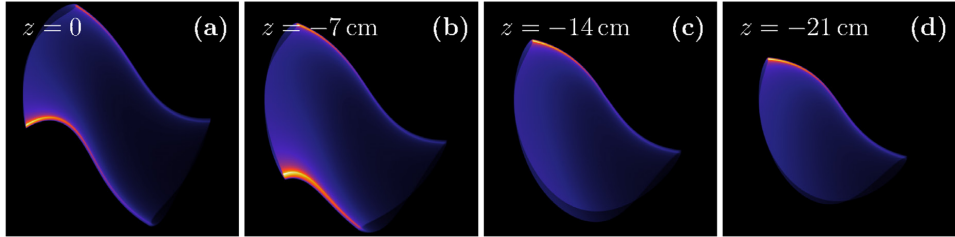


**Figure 4.** Comparison of synchrotron images using different vertical position of the camera. When the camera is placed in the midplane ( $z = 0$ ) the image becomes more symmetric compared to placing it  $z = -21$  cm below the midplane, as is done in Alcator C-Mod.

radiation into account, with the former using just the angular distribution formula (12) while the latter also respects the camera's limited spectral range with the angular and spectral distribution (10). As is evident from comparing the figures, taking the limited spectral range into account is important not just for obtaining the correct intensity distribution over the synchrotron spot, but also for obtaining the correct overall spot shape. Comparing figures 2(c) and (d) also reveals that the cone model is accurate in describing the emitted synchrotron radiation, and it will hence be used in the rest of this paper due to its computational efficiency.

### 3.2. Contributions from individual radii

As was discussed in section 2.1, the radial parameter in SOFT describes the major radius on the midplane at which the particle's guiding-center initiates its orbit, and because of the toroidal symmetry of the system and Liouville's theorem, it is the only spatial parameter of the distribution function. To reveal how contributions from a particle at a given radius appear in a synchrotron image, particles were initialized every 2 cm in the outer midplane, from the magnetic axis and 16 cm outwards, and the resulting image is shown in figure 3(a). Note that these results are specific to the case when the camera is located far below the midplane, although a similar but more symmetric behaviour is found when the camera is located in the midplane.

The contribution to the image from a particle launched at a single radius can be described as a closed ribbon, extending along a parabola, from the upper left of the image to the middle-right. Particles initialized at larger radii contribute

longer ribbons of radiation, each appearing further to the left (high-field side) in the image. The distinct radius plot figure 3(a) reveals how a radial distribution would affect the synchrotron spot, since each ribbon would be weighted differently, and in figure 3(b) a particular radial profile consisting of two Gaussian curves has been used, as shown in figure 3(c). The use of a radial profile consisting of two Gaussian functions illustrates how a peaked radial profile affects the synchrotron spot, which is of interest to the analysis of the experimental image in section 4.2.

Another interesting effect seen from figure 3 is that despite particles being initialized on the magnetic axis and at  $r = 2$  cm, contributions to the image from those radii do not appear in the image. This is a combined effect of the camera being located  $\sim 20$  cm below the midplane and the pitch angles of the particles being too small, so that particles moving close to the magnetic axis (which move essentially along it) never emit radiation towards the camera. While this effect is not necessarily significant in a camera image, it may strongly impact the observed synchrotron spectrum as, effectively, the *observed* runaway distribution function gets biased in favour of particles with large pitch angles.

### 3.3. Camera position

Because of the pitch angle's limiting effect on the extent of the synchrotron spot, the vertical displacement of the camera turns out to greatly impact the synchrotron image. In the images presented so far the camera was located  $\sim 20$  cm below the midplane, as in the Alcator C-Mod tokamak, and the resulting

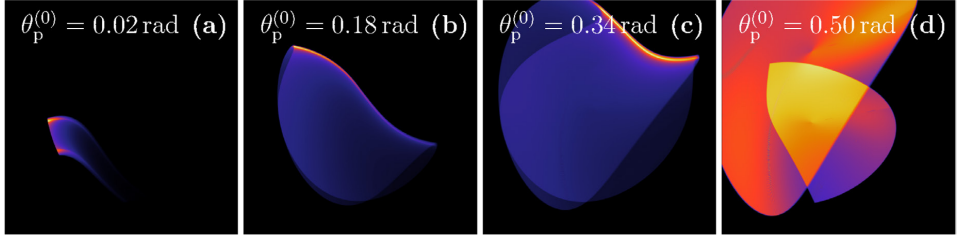


**Figure 5.** Comparison of synchrotron images using particles with the same energy  $E^{(0)} = 30$  MeV but different pitch angles. The pitch angle of the particles determines the ‘width’ of the synchrotron radiation spot. At small pitch angles, a saddle-like surface is observed, while at large pitch angles it separates into two distinct oval shapes. Note that all images are normalized to their maximum brightness. The brightest features of (a)–(c) are due to ‘line-integration’ effects of the surface-of-visibility, whereas (d) lacks this effect since it consists of two separated surfaces.

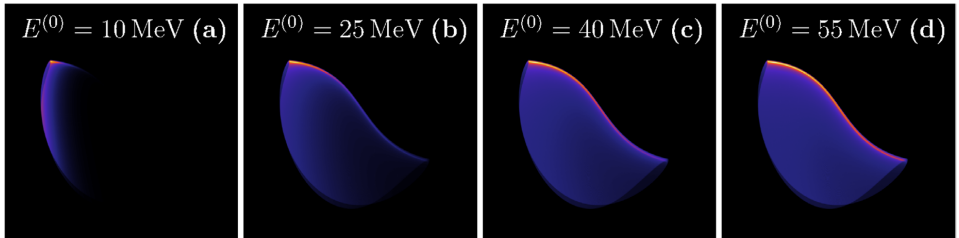


**Figure 6.** Comparison of synchrotron images from particles with different energies and the same initial pitch-angle  $\theta_p^{(0)} = 0.13$  rad. A particle’s energy determines both the focus of intensity in the image, as well as the maximum width of the synchrotron spot.

synchrotron radiation spot resembles a saddle. When we move the camera to the midplane we obtain the synchrotron radiation spot shown in figure 4(a), which has a more symmetric shape. What appeared to be a saddle when viewed from below the midplane now becomes a twisted cylinder.

The bright edges appearing on most single-particle synchrotron spots are results of the 3D extent of the synchrotron emission. As discussed in section 2.3, particles can only emit towards the detector in certain points of space, and we refer to this set of points as the *surface-of-visibility*. When the detector has a finite size, as is the case in our simulations, the surface turns into a thin volume with the same overall shape. Along certain edges of the volume, the volume curves, and a line-of-sight from the detector may for a small section of its path extend tangentially through the volume. These parts of the spot tend to be significantly brighter than any other parts.

### 3.4. Effect of pitch angle

The pitch angle of the particle mainly determines the width of the synchrotron spot, as shown in figure 5 and discussed in for example [4, 5, 16]. The spot shape can be understood by considering the cone model of synchrotron emission, which for small  $\theta_p$  suggests that the guiding-center should emit radiation in a very narrow cone in its direction of motion. The particle is only seen when a part of the cone surface intersects the camera, which is less likely to occur when the pitch-angle is small.

The shape of the synchrotron spot at small pitch angles is a saddle-like surface, as seen in figures 5(a)–(c). At large pitch angles, the saddle-like surface opens up along its upper

edge and separates into two distinct oval surfaces that start to move away slowly from each other as the pitch angle further increases, as shown in figure 5(d). The apparent brightness of figure 5(d) is due to that all images are normalized to their brightest point. Since the surface-of-visibility has split into two distinct surfaces in figure 5(d), it lacks a very bright line-integrated contribution which the surface-of-visibilities of figures 5(a) and (c) have along their upper edges.

### 3.5. Effect of energy

The main effect of the particle energy is related to the limited spectral range of the camera, since the energy does not appear explicitly in (21) which determines the spot shape. In figure 6(a), synchrotron radiation is only seen in the left part of the image, corresponding to the high-field side of the tokamak, and when the particle energy is increased more radiation starts to appear also from the right parts of the images. The cause of this is illustrated in figure 7, which shows the dependence of the synchrotron spectrum from a single particle located on the magnetic axis, on the energy of the particle. The spectral range of the camera considered here, with wavelengths between  $\lambda \in [500, 1000]$  nm, is marked in the plot with two vertical lines. At the lower energy,  $E^{(0)} = 10$  MeV, the spectrum peak lies at longer wavelengths than those observed by the camera, and the synchrotron emission depends exponentially on the magnetic field in this region, as shown in figure 7. As the energy is increased, the spectrum peak is pushed towards shorter wavelengths, and thus also closer to the spectral range of the camera.

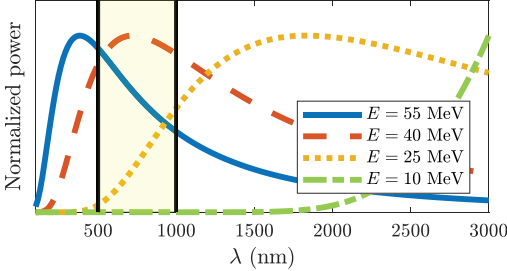


**Figure 7.** Synchrotron spectra, given by (13), for various particle energies, normalized to the maximum value of each spectrum. At fixed magnetic field  $B = 5.25$  T and pitch angle  $\theta_p = 0.13$  rad, the peak of the synchrotron spectrum is pushed to shorter wavelengths as the particle energy is increased. The spectral range visible to the camera is marked by two vertical black lines. The sharp fall-off of the spectrum in the visible range at low energy is the reason for the behaviour of the synchrotron spot observed in figure 6.

At the higher energies, particularly  $E^{(0)} = 55$  MeV, the spectrum peak is located at wavelengths much shorter than those detected by the camera so that radiation is emitted in the opposite limit,  $\lambda \gg \lambda_c$ . In this limit the amount of radiation emitted in the camera's spectral range scales roughly as  $(\lambda_c/\lambda)^{2/3} \sim B^{-1/3}$  (also taking the dependence of the particle's pitch angle on  $B$  into account), and no significant variation in the intensity over the synchrotron radiation spot is observed between the high- and low-field sides.

#### 4. Application: analysis of a synchrotron image in Alcator C-Mod

##### 4.1. Experimental observations

The Alcator C-Mod tokamak is a high field, compact fusion experiment with major and minor radii of 68 cm and 22 cm, respectively. Relativistic runaway electrons can be generated in low density C-Mod plasma discharges; however, they are not observed after disruptions, likely due to the fast break up of magnetic flux surfaces [33]. Instead, electrons will run away to relativistic speeds when the line-averaged electron density  $\bar{n}_e < 0.5 \times 10^{20} \text{ m}^{-3}$ , whereas normal operating densities are  $\bar{n}_e \sim 10^{20} \text{ m}^{-3}$ . Plasma parameters for a runaway-producing C-Mod discharge are shown in figure 8. In this particular experiment, the density was low during the first half of the flattop current ( $\sim 0.5$ –1 s); thus, the electric force driving plasma current was sufficient to overcome the collisional friction acting on a small fraction of electrons and accelerate these particles to relativistic energies. Figure 8(b) shows that the electric field at the magnetic axis,  $E_0$ , is approximately 5–10 times greater than the critical electric field required to generate runaway electrons [34],  $E_c = n_e e^3 \ln \Lambda / 4\pi_0^2 m_e c^2$ , which is consistent with empirical evidence [35] and theoretical predictions [36]. Note also that due to C-Mod's high magnetic field—5.4 T for this discharge—synchrotron radiation is an important power loss mechanism for runaways as indicated by the low values of  $\bar{\tau}_{\text{rad}}$ , the ratio between radiation and collisional timescales, in figure 8(b). As runaways

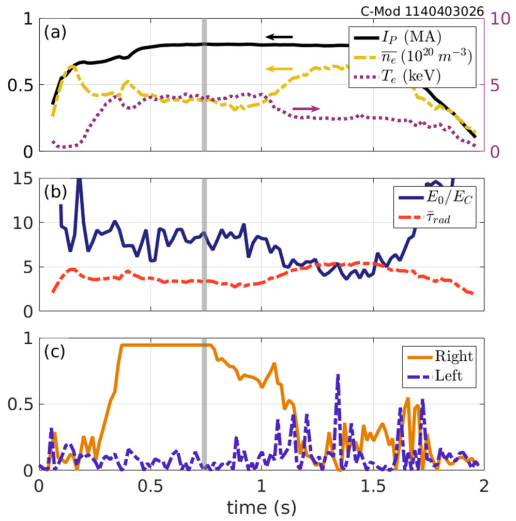


**Figure 8.** Time traces are plotted for C-Mod shot 1140403026 with time of interest  $t \sim 0.742$  s indicated by the grey vertical line: (a) Plasma current  $I_P$  (solid), line-averaged electron density  $\bar{n}_e$  (dashed), and central electron temperature  $T_e$  (dotted); (b) Ratios of the electric field at the magnetic axis  $E_0$  to the critical electric field  $E_c$  (solid) and radiation timescale to collision time  $\bar{\tau}_{\text{rad}} = \tau_{\text{rad}}/\tau_c$  (dashed); and (c) the intensities as measured by a camera on the right (solid) and left (dashed) sides of figure 9. The toroidal magnetic field on axis was 5.4 T.

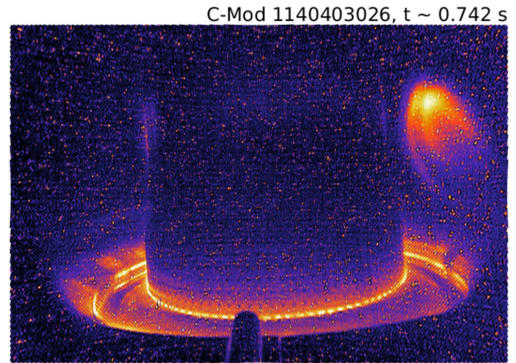


**Figure 9.** A camera inside C-Mod captures the spatial pattern of visible synchrotron emission during discharge 1140403026 at time  $t \sim 0.742$  s. Note that this image has been corrected for camera lens distortion, and a perceptually-uniform colormap has been applied to highlight details while conserving camera intensity. The plasma parameters and intensities measured by the camera are shown in figure 8.

are generated, a wide-view camera inside C-Mod measures increasing intensity of visible synchrotron emission from the counter-current direction, as seen in figures 8(c) and 9. At  $t \sim 1$  s, the density is ramped up, leading to a decrease in  $E_0/E_c$  and reduction of runaway electrons.

A visible-light camera with wide field of view captures images of each C-Mod plasma discharge at approximately 60 frames per second. Because C-Mod operates at high magnetic

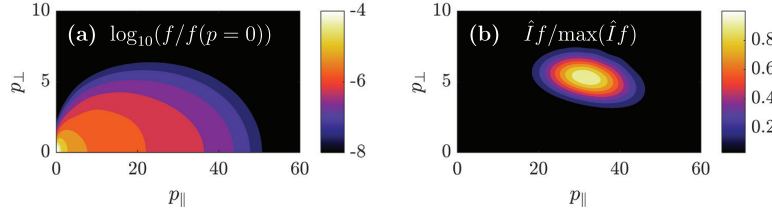


**Figure 10.** The momentum-space distribution function used in modelling figure 9 is shown in part (a), normalized to its peak value. In part (b), the distribution function has been weighted with the amount of synchrotron radiation  $\hat{I}$  emitted in the wavelength interval [500, 1000] nm from each point of momentum space, as given by (13). The resulting contour plot reveals which parts of momentum space will dominate the spectrum and image for this particular population of runaways.

fields (2–8 T), the peak emission of synchrotron spectra is shifted toward the visible wavelength range. Therefore, these images can provide important measurements of the spatial distribution and evolution of runaway electrons. The analysis is complicated by the interplay of the camera view and magnetic field geometries, as runaways emit synchrotron radiation primarily along their direction of motion. This camera is located at a major radius of 106.9 cm and vertical position of −22.655 cm (where the midplane is  $z = 0$ ). The viewing angle is approximately 3.4 degrees to the left of the axis of symmetry and 1.6 degrees upward from the horizontal. The hemispherical lens of the camera causes barrel distortion of the image, where straight lines in real space appear bent outward in the image. However, in-vessel calibrations were performed to correct for distortion and reproduce a rectilinear image, which can be compared to synthetic diagnostics.

The synchrotron emission patterns observed by the camera can display many interesting features. For example, in figure 9, two tilted parabolic structures appear to overlap each other, with the brightest emission at higher vertical position and smaller major radius. The magnetic flux surfaces on which runaway electrons form certainly impact the spatial distribution of runaway electrons and their observed radiation. Poloidal magnetic field coils and toroidal flux loops at many locations around the vacuum vessel are used in C-Mod to reconstruct the magnetic flux geometry inside the vessel and plasma. Contours of flux overlay a poloidal cross-section of the vacuum vessel in figure 1(a), where the plasma boundary is drawn in bolded black.

#### 4.2. Full distribution simulations with SOFT

In previous sections we considered radially uniform mono-energetic and mono-pitch-angle electron distributions, but the populations of runaway electrons in tokamaks are widely distributed in phase-space and typically far from mono-energetic. To model the image in figure 9, we use a momentum-space distribution of runaway electrons obtained from kinetic simulations. In this work, we use CODE [37, 38] to solve the spatially homogeneous kinetic equation for electrons in 2D momentum space, including electric-field acceleration, collisions, synchrotron-radiation reaction losses and the knock-on source term given by Chiu *et al* [39]. Figure 10 shows the runaway electron distribution function for the parameters at the time-slice indicated by the grey line in figure 8,  $t \sim 0.742$  s. Note that only parameters on the magnetic axis

have been used in generating the distribution function, and therefore the output is only an estimate of the distribution function. To more accurately calculate the distribution function, radial profiles of parameters such as temperature, electron density, electric field, etc would be needed.

As described in section 2.1, to utilize the physics of the system as much as possible, the distribution function in SOFT is specified in the outer midplane along the line  $\tau = \phi = 0$ . From this line, the guiding-center equations of motion are then used to evolve the distribution function in the poloidal plane, and particles are uniformly distributed in the toroidal direction. The integration regions for the variables  $\tau$  (orbit time) and  $\phi$  are constrained by the physics of the system to be  $\tau \in [0, \tau_{\text{pol}}(\rho, p_{\parallel}^{(0)}, p_{\perp}^{(0)})]$  and  $\phi \in [0, 2\pi]$ , where  $\tau_{\text{pol}}(\rho, p_{\parallel}^{(0)}, p_{\perp}^{(0)})$  denotes the time it takes for a particle beginning its orbit at major radius  $\rho$ , with initial momentum  $p_{\parallel}^{(0)}$  and  $p_{\perp}^{(0)}$  along and perpendicular to the magnetic field respectively, to return to its starting point in the poloidal plane. The only integration regions in phase-space that must be specified are therefore the runaway beam size (maximum radius  $\rho$ ), and the 2D momentum-space region from which to sample particles (for  $p_{\parallel}^{(0)}$  and  $p_{\perp}^{(0)}$ ). We choose a runaway beam size of 16 cm, placing particles in 100 points between  $\rho = 68\text{--}84$  cm; a total of 300 points for  $p_{\parallel}^{(0)} \in [10, 25] \text{ MeV c}^{-1}$  and 100 points for  $p_{\perp}^{(0)} \in [1.5, 4] \text{ MeV c}^{-1}$ , the latter two based on the region in figure 10(b) from which we expect the most significant contributions to the image. The detector is modeled as a square of side 6 mm and is assumed to only see radiation emitted at wavelengths between  $\lambda \in [500, 1000]$  nm, with a uniform response function.

The synthetic synchrotron images obtained from SOFT using the momentum-space distribution function and parameters just described, and with two different radial distributions, are presented in figure 11. In figure 11(a) a uniform radial profile was used, while in figure 11(b) a radial profile decreasing to zero linearly to the plasma edge at  $R = 84$  cm was considered. Despite using these rather basic models for the distribution function, the agreement of figures 11(a) and (b) with the experimentally obtained camera image figure 11(c) is quite good. The crescent shape is a result of the camera being located  $\sim 20$  cm below the midplane, in combination with the dominating pitch angle being  $\theta_p^{(0)} = 0.15$  rad, as indicated by

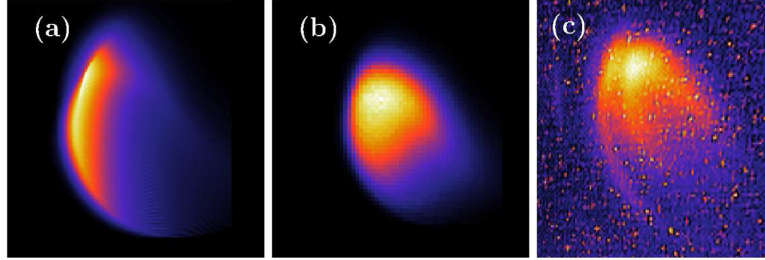


**Figure 11.** (a) Synchrotron image obtained with SOFT using the distribution of runaway electrons shown in figure 10 and a uniform radial profile. (b) The same momentum-space distribution as in (a), but with a linearly decaying radial profile. (c) Zoomed view of the camera image in figure 9.

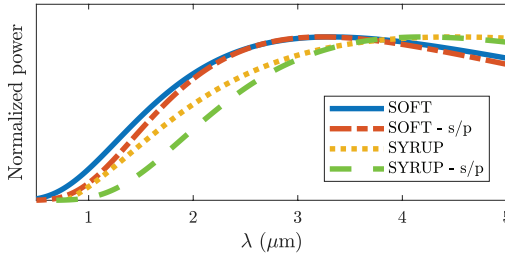


**Figure 12.** Comparison of synchrotron spectra for the Alcator C-Mod scenario using SOFT and the numerical tool SYRUP (described in [40]) respectively. The blue solid and yellow dotted lines are the spectra resulting from SOFT and SYRUP respectively when contributions from the entire runaway population is considered. The red dash-dotted and green dashed lines are ‘single particle’ (s/p) spectra, generated by locating the source of dominant emission in momentum-space ( $E^{(0)} \sim 14$  MeV,  $\theta_p^{(0)} \sim 0.15$  rad, see figure 10) and computing the corresponding spectra. It should be noted that the SYRUP spectra have been generated with the maximum magnetic field strength experienced by any particle,  $B = 7.13$  T, which clearly is not sufficient for agreement.

figure 10(b). While a linear radial profile significantly increases the similarity between the simulated and experimental image, the double crescent shape of figure 10(c) cannot be reproduced without a modulation of the linearly decreasing radial profile. An off-axis peak, combined with a near-linear decrease in the radial profile, could explain the experimentally observed spot shape. The effect of a spatially varying momentum-space distribution should also be explored.

Comparing the synchrotron spectra calculated with SOFT and the numerical tool SYRUP [40], respectively, from the distribution of runaways shown in figure 10 reveals that geometric effects significantly impact the spectrum. In figure 12, four spectra relevant to the Alcator C-Mod scenario described in this paper are shown—two with the full CODE distribution function of figure 10 and two for which the dominating particle of that distribution has been identified and the corresponding spectrum calculated.

While SOFT captures the geometry of the device, simulates the detector, and describes the spatial dependence of the radiation, SYRUP computes the synchrotron spectrum from a given momentum-space distribution function. Since the distribution is

initialized in the outer midplane in SOFT, as described in section 2.1, the pitch angles of all particles increase as they move in to the high field-side of the device, and correspondingly they emit more radiation at shorter wavelengths. SYRUP, on the other hand, does not account for this effect; thus, the SYRUP spectra are shifted toward longer wavelengths compared to the corresponding SOFT spectra. Furthermore, in certain scenarios where the spectrometer does not lie in the midplane and where particles with small pitch angles dominate emission, parts of the distribution function can be made completely invisible due to geometric effects, distorting spectra even further. Geometric effects are therefore essential and should always be taken into account when comparing simulations to experiments.

## 5. Discussion and conclusions

Synchrotron radiation is a powerful tool for diagnosing runaway electrons, but the analysis is complicated by the inhomogeneity of the tokamak magnetic field, the distribution of runaway electrons in phase-space and various geometric effects. It is therefore necessary to use a synthetic synchrotron diagnostic that takes into account the magnetic equilibrium and the properties of the detector used in experiments when studying the synchrotron radiation. SOFT is a flexible tool that computes synchrotron images and spectra by solving the guiding-center equations of motion in arbitrary magnetic geometry and calculating the emitted radiation. It can easily be coupled with Fokker-Planck solvers to simulate physically meaningful scenarios.

The region of the runaway electron distribution function in momentum-space that contributes significantly to the detected synchrotron radiation is typically large, yielding a rather complex image. The image is however linear in the sense that it can be considered a weighted superposition of images resulting from various radially localized mono-energetic and mono-pitch populations of runaways, with the distribution of runaways acting as the weight function. This permits study of the effect of mono-energetic and mono-pitch distributions on the synchrotron spot, and conclusions from these studies to be applied to more complex cases involving runaways that are continuously distributed in momentum-space.

Since the amount of synchrotron radiation emitted by a particle is proportional to  $p_{\perp}^2$ , particles with large pitch angles

tend to emit much more synchrotron radiation than those with small pitch angles, at a given energy. Conversely, particles with small pitch angles tend to be more numerous in the distribution function, and so the part of the distribution function that emits the most synchrotron radiation is a balance between these two properties. While a single particle mono-energy/mono-pitch angle spectrum or image can often be fitted to measurements, it is not useful in describing the actual distribution function, in which the fitted particle may only make up a vanishing fraction of the whole.

The synchrotron radiation spot shape and intensity distribution not only depends on the properties of the runaway electron population, but also on the placement of the synchrotron detector. This is an effect of the strong forward-beaming of synchrotron radiation, which must be emitted directly towards the detector for the particle to be seen. One of the more interesting consequences of this is that particles with small pitch angles, moving near the magnetic axis, will be invisible to the detector if the detector is placed too far from the midplane. While it may seem from this as though all synchrotron detectors should be placed in the midplane, it would be a good idea to distribute detectors both in, below and above the midplane, since this could further constrain the possible shape of the distribution function, which is the unknown quantity to be determined.

The great versatility of SOFT makes it possible to model experimental scenarios through forward modelling. This can be done with the use of a numerical kinetic-equation solver such as CODE [37, 38], LUKE [41–43] or NORSE [44], which allow for experimental parameters such as density, temperature and electric field to be given as input. The forward modelling approach would also allow verification of kinetic theory for runaway electrons in a direct way. Coupling SOFT with a numerical kinetic-equation solver to test whether any observed synchrotron images can be sufficiently constrained from measured quantities (that are of importance to runaway generation) is a useful way to model experiments.

While the framework developed in the beginning of this paper and leading up to equation (7) was applied specifically to synchrotron radiation, there is nothing preventing it from being applied to other forms of radiation. Of particular interest when studying runaway electrons are hard x-rays from bremsstrahlung emission. Since bremsstrahlung is also emitted almost entirely in the particle's direction of motion, much of the theory presented in this paper is directly applicable to such studies and could be used to build a synthetic bremsstrahlung diagnostic.

## Acknowledgments

The authors are grateful to G. Papp and I. Pusztai for fruitful discussions and the entire Alcator C-Mod team for excellent maintenance and operation of the tokamak. This work has been carried out within the framework of the EUROfusion Consortium and has received funding from the Euratom research and training programme 2014–2018 under grant agreement No 633053. The views and opinions expressed

herein do not necessarily reflect those of the European Commission. The authors also acknowledge support from Vetenskapsrådet and the European Research Council (ERC-2014-CoG grant 647121).

## ORCID iDs

M. Hoppe  <https://orcid.org/0000-0003-3994-8977>  
R.A. Tinguely  <https://orcid.org/0000-0002-3711-1834>  
T. Fülöp  <http://orcid.org/0000-0002-5898-0393>

## References

- [1] Dreicer H. 1959 *Phys. Rev.* **115** 238
- [2] Rosenbluth M.N. and Putvinski S. 1997 *Nucl. Fusion* **37** 1355
- [3] Hollmann E.M., Parks P.B., Commaux N., Eidietis N.W., Moyer R.A., Shiraki D., Austin M.E., Lasnier C.J., Paz-Soldan C. and Rudakov D.L. 2015 *Phys. Plasmas* **22** 056108
- [4] Finken K., Watkins J., Rusbüldt D., Corbett W., Dippel K., Goebel D. and Moyer R. 1990 *Nucl. Fusion* **30** 859
- [5] Jaspers R., Grewé T., Finken K., Krämer-Flecken A., Cardozo N.L., Mank G. and Waidmann G. 1995 *J. Nucl. Mater.* **220** 682–7
- [6] Jaspers R., Cardozo N.J.L., Donné A.J.H., Widdershoven H.L.M. and Finken K.H. 2001 *Rev. Sci. Instrum.* **72** 466–70
- [7] Wongrach K., Finken K., Abdullaev S., Koslowski R., Willi O., Zeng L. and The TEXTOR Team 2014 *Nucl. Fusion* **54** 043011
- [8] Esposito B., Martín-Solís J.R., Poli F.M., Mier J.A., Sánchez R. and Panaccione L. 2003 *Phys. Plasmas* **10** 2350–60
- [9] Esposito B. et al and FTU Team 2017 *Plasma Phys. Control. Fusion* **59** 014044
- [10] Tinguely R.A., Granetz R.S., Stahl A. and Mumgaard R. 2015 *Bull. Am. Phys. Soc.* **60** 19
- [11] Papp G. et al 2016 Runaway electron generation and mitigation on the european medium sized tokamaks ASDEX Upgrade and TCV *Preprint: 2016 IAEA Fusion Energy Conf.* (Kyoto, Japan, 17–22 October 2016) [EX9-4] (<https://nucleus.iaea.org/sites/fusionportal/Shared%20Documents/FEC%202016/fec2016-preprints/preprint0502.pdf>)
- [12] Vlainic M., Mlynar J., Cavalier J., Weinzettl V., Paprok R., Imrisek M., Ficker O., Varavin M., Vondracek P. and Noterdaeme J.-M. 2015 *J. Plasma Phys.* **81** 475810506
- [13] Yu J.H., Hollmann E.M., Commaux N., Eidietis N.W., Humphreys D.A., James A.N., Jernigan T.C. and Moyer R.A. 2013 *Phys. Plasmas* **20** 042113
- [14] Zhou R.J., Pankratov I.M., Hu L.Q., Xu M. and Yang J.H. 2014 *Phys. Plasmas* **21** 063302
- [15] Cheon M., Kim J., An Y., Seo D. and Kim H. 2016 *Nucl. Fusion* **56** 126004
- [16] Pankratov I.M. 1996 *Plasma Phys. Rep.* **22** 535–8
- [17] Entrop I., Jaspers R., Cardozo N.J.L. and Finken K.H. 1999 *Plasma Phys. Control. Fusion* **41** 377
- [18] Gomez L.C. and del-Castillo-Negrete D. 2017 *Plasma Phys. Control. Fusion* **59** 124001
- [19] Hoppe M. 2017 Synthetic synchrotron diagnostics for runaway electrons in tokamaks *Master's Thesis* Chalmers University of Technology
- [20] Hoppe M. 2017 Soft SOFT GitHub repository <https://github.com/hoppe93/SOFT>

- [21] Blumenthal G.R. and Gould R.J. 1970 *Rev. Mod. Phys.* **42** 237–70
- [22] Ginzburg V.L., Sazonov V.N. and Syrovatskii S.I. 1968 *Sov. Phys. Usp.* **11** 34
- [23] Pearson T.J., Unwin S.C., Cohen M.H., Linfield R.P., Readhead A.C.S., Seielstad G.A., Simon R.S. and Walker R. 1981 *Nature* **290** 365–8
- [24] Rome J.A. and Peng Y.M. 1979 *Nucl. Fusion* **19** 1193
- [25] Northrop T.G. 1961 *Ann. Phys.* **15** 79–101
- [26] Tao X., Chan A.A. and Brizard A.J. 2007 *Phys. Plasmas* **14** 092107
- [27] Ackleh A.S., Allen E.J., Kearfott R.B. and Seshaiyer P. 2009 *Classical and Modern Numerical Analysis: Theory, Methods and Practice* (Boca Raton, FL: CRC Press)
- [28] Schwinger J. 1949 *Phys. Rev.* **75** 1912–25
- [29] Bekefi G. 1966 *Radiation Processes in Plasmas* (New York: Wiley)
- [30] Zhou R.J. et al 2013 *Plasma Phys. Control. Fusion* **55** 055006
- [31] Tong R.H., Chen Z.Y., Zhang M., Huang D.W., Yan W. and Zhuang G. 2016 *Rev. Sci. Instrum.* **87** 11E113
- [32] Lao L., John H.S., Stambaugh R., Kellman A. and Pfeiffer W. 1985 *Nucl. Fusion* **25** 1611
- [33] Izzo V. et al 2011 *Nucl. Fusion* **51** 063032
- [34] Connor J. and Hastie R. 1975 *Nucl. Fusion* **15** 415
- [35] Granetz R.S., Esposito B., Kim J.H., Koslowski R., Lehnert M., Martin-Solis J.R., Paz-Soldan C., Rhee T., Wesley J.C. and Zeng L. 2014 *Phys. Plasmas* **21** 072506
- [36] Stahl A., Hirvijoki E., Decker J., Embréus O. and Fülöp T. 2015 *Phys. Rev. Lett.* **114** 115002
- [37] Landreman M., Stahl A. and Fülöp T. 2014 *Comput. Phys. Commun.* **185** 847–55
- [38] Stahl A., Embréus O., Papp G., Landreman M. and Fülöp T. 2016 *Nucl. Fusion* **56** 112009
- [39] Chiu S.C., Rosenbluth M.N., Harvey R.W. and Chan V.S. 1998 *Nucl. Fusion* **38** 1711
- [40] Stahl A., Landreman M., Papp G., Hollmann E. and Fülöp T. 2013 *Phys. Plasmas* **20** 093302
- [41] Peysson Y., Decker J., Harvey R.W. and Forest C.B. 2003 *AIP Conf. Proc.* **694** 495–8 (AIP)
- [42] Decker J. and Peysson Y. 2004 DKE: a fast numerical solver for the 3D drift kinetic equation *Technical Report EUR-CEA-FC-1736 Euratom-CEA*
- [43] Nilsson E., Decker J., Peysson Y., Granetz R., Saint-Laurent F. and Vlainic M. 2015 *Plasma Phys. Control. Fusion* **57** 095006
- [44] Stahl A., Landreman M., Embréus O. and Fülöp T. 2017 *Comput. Phys. Commun.* **212** 269–79